Newcastle University

Interactions between the Ubiquitin Proteasome System and Mitochondria in Ageing and Neurological Disorders

Emma Reynolds

This thesis is submitted in partial fulfilment of the requirements for the degree of Doctor of Philosophy

Newcastle University

Faculty of Medical Sciences

Institute of Neuroscience

September 2014

Abstract

Mitochondrial dysfunction and protein aggregation (which is partly due to the decline of the ubiquitin proteasome system, UPS), are two commonly observed features of aging and age-related neurodegenerative diseases. There has been considerable recent interest in the ways in which the UPS interacts with mitochondria, particularly in the area of mitochondrial dynamics and quality control. It is not known if the age-related decline in proteasome efficiency could disrupt mitochondrial dynamics and quality control, causing mitochondrial dysfunction.

In this study, I have used live-cell imaging to assess the effect of the UPS on mitochondrial dynamics in primary neurons. I found that complete disruption of the UPS greatly decreased mitochondrial motility, fission and fusion, whereas pharmacological inhibition of the deubiquitinase enzyme UCHL1 (which causes a physiologically relevant decline in the UPS) did not disrupt mitochondrial dynamics. Furthermore, I found that in UCHL1 knockout mice, mitochondria are not deficient in respiratory chain complexes I and IV; compromising the UPS does not cause mitochondrial dysfunction.

UCHL1 knockout mice have a neurodegenerative phenotype characterized by impaired hind-limb function, tremor and kyphosis. Using immunohistochemistry, I demonstrated synaptic and axonal loss at the distal regions of long sensory axons that target the brainstem and cerebellum. The neuropathology of UCHL1 knockout mice is characterized by axonal spheroids, large axonal swellings containing synaptophysin, mitochondria and neurofilaments, which share some characteristics with spheroids that occur during ageing in human brains. I also studied the progression of axonal dystrophy in UCHL1 knockout mice and found that the accumulation of synaptophysin transport vesicles is central to axonal spheroid formation. Furthermore, I investigated whether the UPS is impaired in patients with mitochondrial disease, however found no evidence to suggest this.

These findings indicate that the function of the UPS and mitochondria may be less tightly linked than previously thought.

Acknowledgments

Doing this PhD has definitely been a test of perseverance, and I am grateful to several people who have helped me along the way.

Firstly, I would like to thank Prof. Doug Gray, whose idea this project was, for all his help during the first year of the PhD, and in particular for generating and providing the UCHL1 mice, which are the subject of this thesis. I would like to thank Glyn Nelson for the many times he resolved problems with the somewhat temperamental spinning disk microscope, and Adele Kitching at the animal house who looked after the UCHL1 mice, performed the culling and perfusion fixing, and made a grim task bearable! I am also thankful to Dr. Lucy Craggs and Dr. Beth Stoll for their tips on dissection.

I would like to thank my supervisor Prof. Doug Turnbull for allowing me to become part of the MRG a year into my PhD, and for all of his guidance especially in terms of the aims and direction of this project. I would also like to thank Doug for being so prompt with reading through chapters and giving feedback and for being so understanding of my decision to move to the other end of the country a month before the PhD was finished! I would like to thank Dr. Nichola Lax for agreeing to become my supervisor in the first place, for her help in the lab especially where histology is concerned, and for always being willing to read through my work and give helpful thoughts and comments on it.

I would like to thank everyone at the MRG who has helped me with lab work or showed me how to do things, particularly Debbie Jones, Philippa Hepplewhite, who helped me get started with immunohistochemistry and Anna Smith, who cut an awful lot of tissue sections for me. I would also like to thank Dr. Alex Laude at the bioimaging unit for his help and advice on microscopy and image analysis.

I would like to thank my family, particularly my parents and in-laws, and my brothers; Tim for being so encouraging and Jonny for taking on the mammoth task of proof-reading this! Most of all, I would like to thank my husband Jim, for helping me to keep going with the PhD and to see the light at the end of the tunnel. Finishing this thesis is definitely a win for Team Reynolds – I couldn't have done it without you!

Author's Declaration

This thesis is submitted in partial fulfilment of the requirements for the degree of Doctor of Philosophy. The research described is my own work, and was performed at the Campus for Ageing and Vitality and the Wellcome Trust Centre for Mitochondrial Research within the Institute for Ageing and Health (now Institute of Neuroscience), Newcastle University. This research was carried out under the supervision of Professor D.A. Gray, Professor D.M. Turnbull and Dr. N.Z. Lax, between September 2011 and September 2014. I certify that none of the material in this thesis has been previously submitted for a degree or any other qualification at this or any other university.

Meetings and Conferences Attended

University College London, Crucible Centre for Lifelong Health & Wellbeing
Lifelong Health and Wellbeing Ageing Research Conference
London, UK. 6-8 November 2013
Poster Presentation: “The Role of Ubiquitin in Neurodegeneration”

Edinburgh University, Centre for Cognitive Ageing and Cognitive Epidemiology
Lifelong Health and Wellbeing Showcase Meeting
Edinburgh, UK. 4-5 December 2012
Poster Presented: “The Role of UCHL1 in Neurodegeneration and Mitochondrial Function”

Newcastle Centre for Brain Ageing and Vitality
XCAR Early Career Researcher Conference
Newcastle, UK. 7-8 November 2012
Poster Presented: “The Role of UCHL1 in Neurodegeneration and Mitochondrial Function”

Keystone Symposia
Mitochondrial Dynamics and Function
Banff, Alberta, Canada. 19 – 24 February 2012

Newcastle University, Centre for Brain Ageing and Vitality
‘Innovations for Lifelong Wellbeing’ – Research Showcase
Newcastle, UK. 16 November 2011
Oral Presentation: “The Role of Ubiquitin in Mitochondrial Dynamics and Quality Control”; Contribution to Poster: “The Ageing Brain”

Newcastle University, Faculty of Medical Sciences
North East Postgraduate Conference
Newcastle, UK. 21 October 2011
Poster presented: “The Role of Ubiquitin in Mitochondrial Dynamics”

Abbreviations

4-HNE	4-Hydroxynonenal
AD	Alzheimer's disease
ADP	Adenosine diphosphate
ALS	Amyotrophic lateral sclerosis
AMBRA1	Activating molecule in beclin-1 regulated autophagy
AMC	7-amino-4-methylcoumarin
ANOVA	Analysis of variance
APLIP1	APP-like interacting protein 1
APP	Amyloid precursor protein
ATP	Adenosine triphosphate
AU	Aribitrary units
Aβ	Amyloid β peptide
BAP1	BRCA-associated protein-1
Bcl-2	B-cell lymphoma 2
BER	Base excision repair
Blm10	Bleomycin resistance
C/EBPβ	CAAT enhancer-binding protein
CCCP	Carbonyl cyanide *m*-chlorophenyl hydrozone
CCT	Cuneocerebellar tract
CFV	Cresyl fast violet
CHOP	C/EBP homologous protein

CI	Confidence interval
CI-20	Complex I, subunit 20
CII-70	Complex II, subunit 70
CJD	Creutzfeldt-Jakob disease
ClpP	Caseinolytic protease
CMA	Chaperone mediated autophagy
CNS	Central nervous system
COX	Cytochrome *c* oxidase
COX-1	Complex IV, subunit I
CP	Core particle of the proteasome
CPEO	Chronic progressive external opthalmoplegia
CSU	Confocal scanning unit
Cy5	Cyanine 5/647nm/far red channel
Cys	Cysteine
DAB	Diaminobenzidine
D-loop	Displacement loop
*d*Mfn	Drosophila mitofusin
DMSO	Dimethyl sulphoxide
DNA	Deoxyribonucleic acid
DPX	Dibutyl phtalate xylene
DRG	Dorsal root ganglion
Drp1	Dynamin related protein 1
DSCT	Dorsal spinocerebellar tract

dsDNA	Double stranded DNA
DTT	Dithiothreitol
DUB	Deubiquitinase enzyme
E	glutamate
e-	Electron
EDTA	Ethylenediaminetetraacetic acid
EM	Electron microscope
EMCCD	Electron multiplying charge coupled device
ENS	Enteric nervous system
ER	Endoplasmic reticulum
FAD	Flavin adenine dinucleotide
FAT10	Human leukocyte antigen F associated
Fe-S	Iron-Sulphur
FEZ1	Fasciculation and elongation protein ζ(zeta) 1
FFPE	Formalin fixed, paraffin embedded
FITC	Fluorescein isothiocyanate/488nm/green channel
FMN	Flavin mononucleotide
fps	Frames per second
FUNDC1	FUN14 domain containing 1
GABA	Gamma-amino butyric acid
gad	Gracile axonal dystrophy
GAPDH	Glyceraldehyde phosphate dehydrogenase
GB	Gigabytes

GCL	Granular cell layer
GRIF1	GABA receptor interacting factor 1
GTP	Guanosine triphosphate
H&E	Haematoxylin and eosin
H+	Proton/Hydrogen ion
HDAC	Histone deacetylase
HECT	Homologous to the E6-AP C-terminus
HEPES	2-[4-(2-hydroxyethyl)piperazin-1-yl]ethanesulfonic acid
Het	Heterozygous
hFis1	Human fission protein 1
His	Histidine
HRP	Horseradish peroxidase
HSP	Heavy strand promoter
HSP60	Heat shock protein 60
HUWE1	HECT, UBA and WWE containing protein 1
I	Isoleucine
icp	Inferior cerebellar peduncle
IgG	Immunoglobulin type G
IHC	Immunohistochemistry
IMM	Inner mitochondrial membrane
IMS	Inter-membrane space
ISG15	Interferon stimulated gene
IVA	Isovaleric acidemia

JAMM	JAB1/MPN/Mov34 metalloenzyme
K	Lysine
kb	kilobase
KHC	Kinesin heavy chain C
KIF	Kinesin family member
KLP6	Kinesin-like protein
KO	Knockout
KSS	Kearnes-Sayre syndrome
LC3	Microtubule associated protein 1A/1B light chain 3
LRRK2	Leucine-rich repeat kinase 2
LSP	Light strand promoter
LTD	Long term depression
LTP	Long term potentiation
M	Methionine
M.O.M	Mouse on Mouse
MAD	Mitochondria associated degradation
MARCHV	Membrane Associated Ring Finger (C3HC4) V
MBP	Myelin basic protein
MCP	Middle cerebellar peduncle
MELAS	Mitochondrial encephalomyopathy with lactic acidosis and stroke-like episodes
MERRF	myoclonic epilepsy with ragged red fibres
Mff	Mitochondrial fission factor

Mfn	Mitofusin
MHC	Major histocompatibility complex
MIDD	Maternally inherited deafness and diabetes
MIEF1	Mitochondrial elongation factor 1
Miro	Mitochondrial rho
MITOL	Mitochondrial ubiquitin ligase
ML	Molecular layer
ML	Medial lemniscus
MNGIE	Mitochondrial neurogastrointestinal encephalomyopathy
MPP+	Metabolite of MPTP
MPTP	Mitochondrial permeability transition pore
MPTP	1-methyl-4-phenyl-1,2,3,6-tetrahydropyridine
mRNA	Messenger RNA
mSOD1	Mutant superoxide dismutase 1
mtDNA	Mitochondrial DNA
MTERF1	Mitochondrial termination factor 1
mtSSB	Mitochondrial single strand binding protein
MT-UPR	Mitochondrial unfolded protein response
MULAN	Mitochondrial ubiquitin ligase activator of NF-κB
MW	Molecular weight
NADH	Nicotinamide adenine dinucleotide (reduced)
NEDD8	Neuronal precursor cell expressed, developmentally down regulated 8
NF-κB	Nuclear factor κ light chain enhancer of B cells

NGS	Normal Goat's Serum
NMNAT	Nicotinamide mononucleotide adenine transferase
NRF	Nuclear Respiratory Factor
NTP	Nucleoside triphosphate
NTS	Nucleus tractus solaritii
OH	Origin of heavy stand replication
OIP106	O-linked N-acetylglucosamine transferase interacting protein
OL	Origin of light strand replication
OMA1	OMA1 zinc metallopeptidase protein
OMM	Outer mitochondrial membrane
Opa1	Optic atrophy 1
OUT	Ovarian Tumour Protease
OXPHOS	Oxidative phosphorylation
PARL	Presenilin-associated rhomboid-like protein
PBS	Phosphate buffered saline
PCL	Purkinje cell layer
PCR	Polymerase chain reaction
PD	Parkinson’s disease
PFA	Paraformaldehyde
PGC-1α	Peroxisome proliferator-activated receptor ɣ-coactivator 1α
PGPH	Post-glutamyl peptide hydrolysing
Pi	Inorganic phosphate
PI3K	Phosphatidylinositol-3 kinase

PINK-1	PTEN induced kinase 1
PM	Post-mortem
PML	Paramedian lobule
PNBM	Primary neuron basal medium
PNGM	Primary neuron growth medium
POLRMT	Mitochondrial RNA polymerase
POLγA	DNA polymerase γ, subunit A
POLγB	DNA polymerase γ, subunit B
PVDF	Polyvinylidine fluoride
Q	Ubiquinone
QH2	Ubiquinol
RanBP2	Ran-binding protein 2
RFP	Red fluorescent protein
RING	Really interesting new gene
RNA	Ribonucleic acid
RNAi	RNA interference
ROI	Region of interest
ROS	Reactive oxygen species
RP	Regulatory particle of the proteasome
Rpn	Regulatory particle non-ATPase
Rpt	Regulatory particle triple-A ATPase
rRNA	Ribosomal RNA
RT	Room temperature

S	Serine
SANDO	Sensory ataxic neuropathy, dysarthria and opthalmoparesis
SARM1	Sterile α and TIR motif containing 1
SD	Standard deviation
SDH	Succinate dehydrogenase
SDS	Sodium dodecyl sulphate
SOD1	Superoxide dismutase 1
SQSTM1	Sequestosome 1
ssDNA	single stranded DNA
SUMO	Small ubiquitin-like modifier
TBS	Tris-buffered saline
TBST	Tris-buffered saline + 0.2% (v/v) Tween 20
TCA	Tricarboxylic acid
TFAM	Mitochondrial transcription factor A
TFB2M	Transcription factor B2M
TIM	Translocase of the inner mitochondrial membrane
TIRF	Total internal resonant fluorescence
TMRE	Tetramethylrhodamine, ethyl ester
TOM	Translocase of the outer mitochondrial membrane
TRAK	Trafficking kinesin protein
TRITC	Tetramethylrhodamine isothiocyanate/541nm/red channel
tRNA	Transfer RNA
TWINKLE	T7 gp4-like protein with intramitochondrial nucleoid localisation

U	Uridine
UBA	Ubiquitin associated domain
UBE4B	Ubiquitination factor E4B
UBL	Ubiquitin-like protein
UCH	Ubiquitin C-terminal hydrolase
UCHL1	Ubiquitin C-terminal hydrolase L1
UCHL3	Ubiquitin C-terminal hydrolase L3
UPS	Ubiquitin Proteasome System
USP	Ubiquitin Specific Protease
VDAC	Voltage-dependent anion channel
W	tryptophan
Wlds	Wallerian degeneration (slow)
WT	Wild type
Y	Tyrosine
YME1L1	YME1-like 1
$\Delta\psi m$	Mitochondrial membrane potential

Table of Contents

List of Figures

List of Tables

Chapter 1.

Introduction

Chapter 1. **Introduction**

1.1 Protein Homeostasis

Mammalian cells have several systems by which they break down and recycle proteins, including the ubiquitin proteasome system (UPS), the autophagy/lysosome system and various cellular proteases. Protein degradation must be highly regulated in order to maintain cellular homeostasis and function. The ubiquitin proteasome system, which I will discuss in detail, is responsible for the degradation of the majority of soluble cytoplasmic and nuclear proteins (Rock *et al.*, 1994).

1.1.1 The Ubiquitin Proteasome System

1.1.1.1 Ubiquitin conjugation

Ubiquitin is a small, highly conserved protein which can become covalently attached to a target protein or substrate in a reaction catalysed by an E1-E2-E3 multi-enzyme cascade (Figure 1.1) (Schulman and Wade Harper, 2009). In order for ubiquitin conjugation to occur, ubiquitin must first be activated by an human ubiquitin activating enzyme (E1), in an ATP dependent reaction (Haas *et al.*, 1982). In this form, ubiquitin can then be transferred onto an E2 ubiquitin conjugating enzyme, and then attached to the substrate protein by an E3 ubiquitin ligase. There are hundreds of E3 ubiquitin ligases, and they introduce specificity into the ubiquitination process by recognizing specific substrate sequences (Hershko and Ciechanover, 1998). After ubiquitin ligation, E2 may then dissociate from the E3, allowing a second E2 charged with active ubiquitin to associate, thereby causing a second ubiquitin moiety to be added to the substrate. This cycle can be repeated several times until a polyubiquitin chain has formed on the substrate (Hochstrasser, 2006).

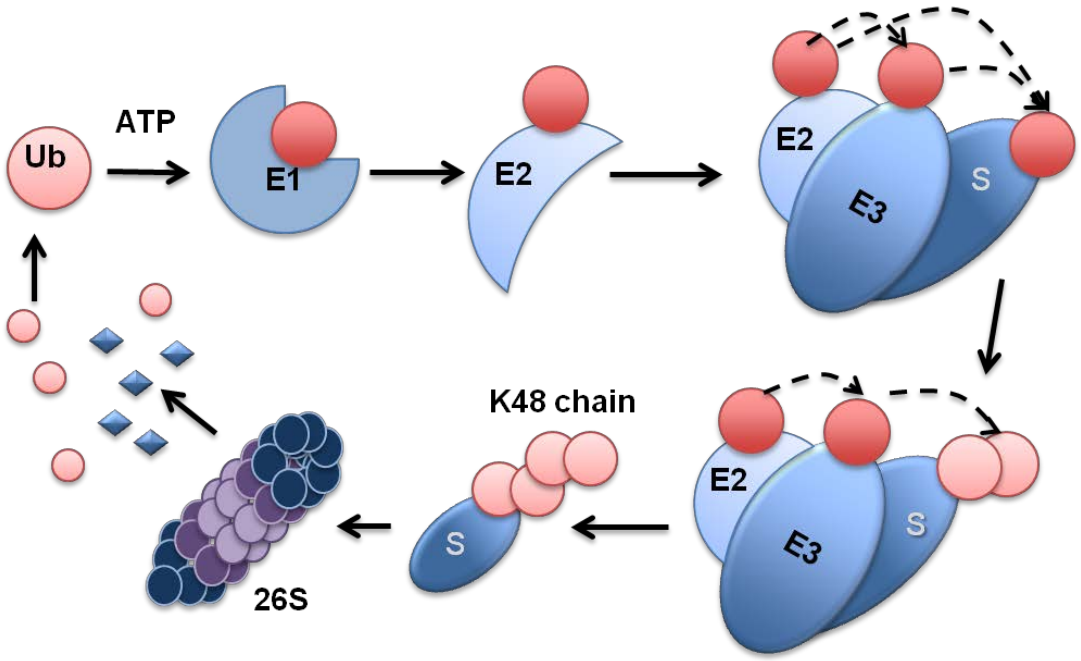

Figure 1.1: The Ubiquitin System.
Ubiquitin is activated by E1 ubiquitin activating enzyme in an ATP-dependent manner. Activated ubiquitin can then be passed onto an E2 ubiquitin conjugating enzyme, and then transferred to the substrate by an E3 ubiquitin ligase. The E2 can then dissociate from the E3, allowing a second E2 charged with active ubiquitin to associate, thereby allowing a second ubiquitin moiety to be added to the substrate. This cycle can be repeated several times until a polyubiquitin chain has formed on the substrate. A canonical ubiquitin 'tag' of four lysine-48 linked ubiquitin moieties targets substrates to the 26S proteasome, where the polyubiquitin chain is removed by 19S 'lid' and the substrate is broken down.

It was initially thought that a polyubiquitin chain of four lysine-48 (K48) linked ubiquitin moieties was the minimum signal for efficiently targeting proteins to the 26S proteasome (Thrower *et al.*, 2000). Indeed, a K48 linked ubiquitin chain of four is the minimum that could span the 70-80Å distance between the 26S proteasome's two ubiquitin receptors and be simultaneously removed from the substrate, allowing substrate processing (see section 1.1.3.2.1) (Lander *et al.*, 2012). The K48 tetra-ubiquitin tag is considered to be the principal proteasomal targeting signal, however there have been many reports demonstrating the degradation of proteins which have a variety of ubiquitination patterns and in reality, ubiquitin conjugation is far more complex than first thought (Ciechanover and Stanhill, 2014). Furthermore, conjugation of substrate proteins with ubiquitin can also have non-proteolytic consequences, such as the activation or stabilisation of a protein (see section 1.1.1.1.3). The variety of consequences of ubiquitination, combined with the vast range of proteins that are ubiquitinated means that ubiquitin regulates many cellular processes, including DNA damage repair, cell cycle control and apoptosis.

1.1.1.1.1 The heterogeneity of ubiquitin chain formation

Ubiquitin has 76 amino acids, of which 7 are lysine residues – these are at positions 6, 11, 27, 29, 33, 48 and 63. Although the 'canonical' proteasomal tag consists of four ubiquitin moieties linked via the lysine at position 48 (K48) (Chau *et al.*, 1989), ubiquitin chains that are assembled via almost all of the other lysine residues (apart from K63) are also broken down by the 26S proteasome (Xu *et al.*, 2009). Upon proteasome inhibition, the increase in levels of K48 linked ubiquitin chains is the greatest (8.2 fold), followed by K11, K29, K6, K27 and K33 (Xu *et al.*, 2009), demonstrating that K48 linked ubiquitin chains are the most efficient proteasome targeting signal, but ubiquitin chains linked via other lysine residues are also capable of targeting substrates to the proteasome.

Furthermore, different forms and lengths of ubiquitin chains have been reported to target proteins to the proteasome, for example monoubiquitination (Shabek *et al.*, 2012) and multiple monoubiquitination (!!! INVALID CITATION !!!). The ubiquitin moieties in the canonical tetraubiquitin signal are linked by angular isopeptide bonds, however linear tetraubiquitin chains are also recognised by the proteasome and can target proteins for degradation (Zhao and Ulrich, 2010). Most commonly, ubiquitin moieties are conjugated to lysine residues in target proteins, however ubiquitination of cysteine and threonine residues can also be recognised by the proteasome (Vosper *et al.*, 2009). The vast range of proteasome-targeting signals have different 26S binding affinities, and it is therefore thought that the type of signal a protein has may determine its 'priority level' for degradation (Ciechanover and Stanhill, 2014). Therefore, the great complexity and variety of ubiquitin tags adds a further level of regulation to protein degradation.

1.1.1.1.2 Ubiquitin-like proteins

In addition to ubiquitin, proteins can also be modified by the attachment of ubiquitin – like proteins (UBLs), for example NEDD8, SUMO (Small ubiquitin-like modifier), ISG15 (Interferon stimulated gene 15) and FAT10. There are several UBLs, which are conjugated to substrate proteins via an E1-E2-E3 enzyme cascade, in much the same way as ubiquitin itself (Hochstrasser, 2000). However, these ubiquitin like proteins do not form polymers on target proteins (Passmore and Barford, 2004), and with the exception of FAT10, do not directly target substrates for proteolysis (Schmidtke *et al.*, 2014). However, modification of substrates with a UBL can have a broad range of downstream effects, including promoting or inhibiting the formation of polyubiquitin

chains, and thereby indirectly controlling the substrate's stability (Passmore and Barford, 2004).

1.1.1.1.3 Ubiquitin mediated signalling

In addition to targeting substrate proteins to the 26S proteasome, ubiquitination constitutes a signalling mechanism in its own right; it can cause changes in localisation or activity of substrate proteins (Chan *et al.*, 2011). Ubiquitin signalling via residues other than lysine 48 (e.g. K63 and K11) is particularly important in cell cycle control (Bremm and Komander, 2011; Wickliffe *et al.*, 2011; Meyer and Rape, 2014), the DNA damage response (Ramaekers *et al.*, 2014; Xu *et al.*, 2014), and cell signalling (Dynek *et al.*, 2010; Hay-Koren *et al.*, 2011), thus having a huge influence over cellular function.

1.1.2 Deubiquitinase enzymes

The removal of ubiquitin from a polyubiquitin chain or substrate, known as deubiquitination, is catalysed by deubiquitinating enzymes (DUBs). By editing or removing ubiquitin chains from substrate proteins, DUBs may protect substrates from proteolysis, promoting their stability, and thereby regulating a diverse range of cellular functions (Clague et al., 2012). DUBs recycle ubiquitin by disassembling polyubiquitin chains and salvage ubiquitin from small adducts, thereby replenishing pools of free monomeric ubiquitin and maintaining ubiquitin homeostasis. As I will discuss in further detail later (section 1.2.1.2), the deubiquitinase enzyme UCHL1 (Ubiquitin C-terminal hydrolase – 1) also has an ubiquitin stabilisation function. The functions of deubiquitinase enzymes are outlined in Figure 1.2.

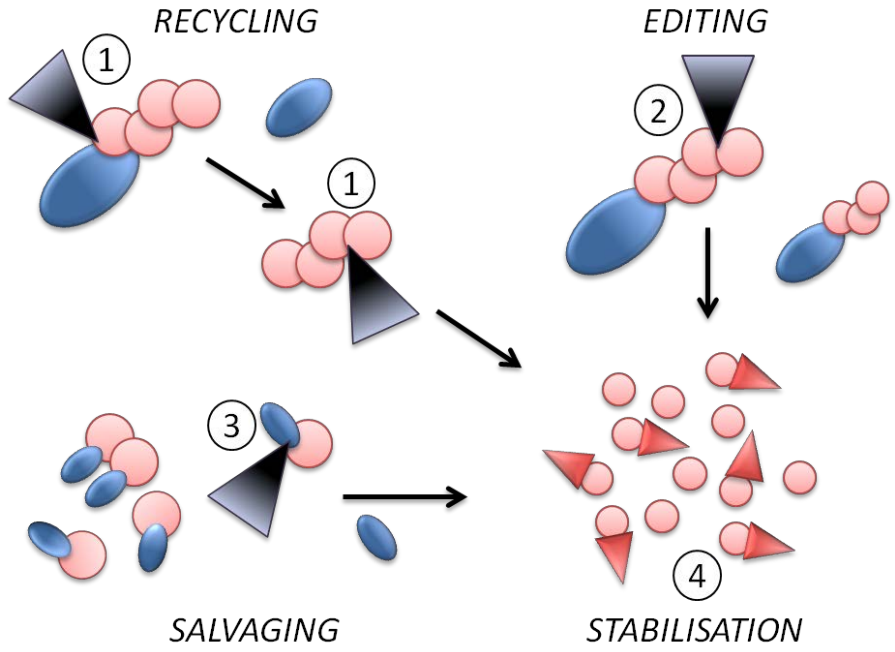

Figure 1.2: Functions of deubiquitinase enzymes.
1) Ubiquitin recycling can occur by removing the whole ubiquitin chain (eg. removal of the chain at the proteasome by the Rpn11 subunit of the 19S regulatory particle). This can rescue the substrate from proteolysis, or allow it to be broken down. DUBs can also disassemble polyubiquitin chains. 2) Editing the length or linkage of a polyubiquitin chain can also alter the substrate's fate. 3) DUBs (Such as the UCHs) can salvage ubiquitin from small peptides or adducts. Recycling and editing polyubiquitin chains, as well as salvaging ubiquitin can replenish pools of monoubiquitin. The DUB UCHL1 can bind to monoubiquitin (4), thus stabilising monoubiquitin pools.

There are approximately 84 active human DUBs (Ye *et al.*, 2009), which can be classified into five families, according to their catalytic domains; Ubiquitin Specific Proteases (USPs), Ubiquitin Carboxy-terminal hydrolases (UCHs), Josephin domain proteases, Ovarian Tumour Proteases (OTUs), and JAMM Motif Proteases (Nijman *et al.*, 2005).

The USP family is the most common subset of DUBs, of which there are approximately 56 members. Their catalytic core ranges in size from 295 to 800 amino acids, but invariably contains Cys-His boxes, which are essential for catalysis (Ye *et al.*, 2009). Not all USPs have been characterized, but several are able to cleave or remove poly-Ub chains (Ye *et al.*, 2009).

There are only four Ubiquitin C-terminal hydrolase DUBs (UCHs); they are thiol proteases that contain a 230-residue catalytic domain at the N-terminus. The two smaller UCH enzymes (UCHL1 and UCHL3) cleave ubiquitin from small peptides and amino acids, however are not capable of disassembling poly-Ub chains or ubiquitin conjugates (Larsen *et al.*, 1998), however the two larger UCHs (BAP1 and UCH37) are capable of cleaving poly-Ub chains. It was later determined that this difference is due to the length of a loop that crosses over the active site of the UCH, limiting access to larger conjugates (Zhou *et al.*, 2012). Since UCHL1 and UCHL3 can only cleave ubiquitin from small leaving groups, it is thought that their role may be to recycle ubiquitin after it has been conjugated to intracellular nucleophiles such as the antioxidant glutathione (Nijman *et al.*, 2005).

Of the four proteins that constitute the Josephin domain family of DUBs, the most studied is Ataxin-3, due to its association with spinocerebellar ataxia type-3, also known as Machado Joseph Disease. Ataxin-3 binds to and cleaves ubiquitin from long K48 and K63 chains, indicating a role for Josephin domain DUBs in editing ubiquitin chains of varying lengths (Eletr and Wilkinson, 2014).

Ovarian Tumour Proteases (OTUs) are a family of cysteine proteases consisting of 15 members. Each member of the OTU DUB family that has been characterized specifically cleaves the poly-Ub chain of one or two particular linkages (eg. K63, K48, K11, K29, K33) (Eletr and Wilkinson, 2014).

Finally, there are eight JAMM domain proteases, many of which are highly specific for K63 polyubiquitin chains (Cooper *et al.*, 2009). Rpn11, the subunit of the proteasome's 19S regulatory particle (RP) is a JAMM domain proteasome, and it functions by removing whole K48 or K63 polyubiquitin chains from substrates to allow or prevent (respectively) substrate proteolysis (Yao and Cohen, 2002).

DUBs can prevent proteasomal degradation of substrates, but are also instrumental in degradation by the 26S proteasome. They recycle ubiquitin to replenish the monomeric

ubiquitin pool, and are involved in regulating the components of the ubiquitin conjugation cascade, often acting in complexes with E3 ubiquitin ligases (Cummins and Vogelstein, 2004). The vast number of deubiquitinating enzymes, each with their different specificities and functions adds another level of complexity and regulation to the ubiquitin proteasome system.

1.1.3 Proteasome Structure

In mammalian cells, there are several forms of proteasome, made up of different subunits, which have different functions.

1.1.3.1 The 20S Core Particle

The crystal structure of the 20S core particle was first determined from the archaeon, *Thermoplasma acidophilum*. It has a well-organised barrel-shaped structure made up of four rings; two outer α rings, and two inner β rings (Lowe *et al.*, 1995). Each of these rings is heptameric, consisting of seven distinct but structurally related subunits, α_{1-7} and β_{1-7} (Groll *et al.*, 1997). Each of the inner β rings contains three catalytically active subunits (β1, β2, β5), which encode post-glutamyl peptide hydrolyzing (PGPH)/caspase-like, trypsin-like and chymotrypsin-like activities, respectively. The β1, β2 and β5 subunits each possess the ability for the cleavage of peptide bonds at the C-terminal side of acidic, basic and hydrophobic amino acid residues, respectively. Their active sites face the interior of the cylinder, therefore proteolysis takes place at the centre of the barrel-shaped proteasome (Tanaka *et al.*, 2012), and proteins must enter through the two outer α rings. The crystal structure of the 20S proteasome shows that there is only a small (13Å diameter) pore at the centre of the heptameric α rings, which limits the entry of unstructured proteins (Lowe *et al.*, 1995). Furthermore, the N-terminal polypeptides of the seven α subunits form an additional barrier to the entry of proteins (Förster *et al.*, 2003); the 20S proteasome is normally in an inactive form, and must be activated by opening the α-ring 'gates' in order for proteolysis to occur.

Activation of the 20S proteasome and opening of the α-ring 'gates' takes place when protein complexes bind to the α rings at either end of the barrel structure. Such activators include the 19S, 11S and Blm10 complexes. Although the biochemical mechanisms of activation for both the 11S and Blm10 complexes have been elucidated through their crystal structures, their biological functions remain unclear (Kish-Trier and Hill, 2013), and therefore we will focus on the 19S regulatory particle (RP).

The 26S proteasome is assembled from the 20S 'core particle' (CP), in addition to the 19S regulatory particle (RP), either bound to both ends of the 20S CP, or bound to only one end, whilst an 11S or Blm10 proteasome activator binds the other end (Kish-Trier and Hill, 2013).

1.1.3.2 The 19S Regulatory Particle

The function of the 19S regulatory particle has been well characterised; it recognises polyubiquitinated substrate proteins, removes polyubiquitin chains, unfolds substrate proteins and feeds them into the central chamber of the 20S CP for proteolysis (Ehlinger and Walters, 2013).

The structure of the 19S regulatory particle however is somewhat complex; it consists of 19 subunits, which can be divided into 'base' and 'lid' sub-complexes. The base links the 19S RP to the CP, and is sufficient to activate the CP, recognise ubiquitinated proteins and translocate them into the 20S catalytic chamber (Prakash *et al.*, 2004; Rabl *et al.*, 2008; Schreiner *et al.*, 2008), whilst the lid stabilises the 26S proteasome complex and catalyses the removal of polyubiquitin chains from substrate proteins (Yao and Cohen, 2002; Vilchez *et al.*, 2012).

1.1.3.2.1 The 10-subunit 'base' complex

The base of the 19S regulatory particle has a total of ten subunits: six ATPases (Rpt 1-6), regulatory particle non-ATPase (Rpn) proteins 1 and 2, and the two ubiquitin receptors, Rpn10 and Rpn13 (Young *et al.*, 1998; Husnjak *et al.*, 2008; Schreiner *et al.*, 2008).

The six ATPase subunits form a heterohexameric ring at the core of the 19S RP in the order Rpt1-Rpt2-Rpt6-Rpt3-Rpt-4-Rpt5 (Tomko Jr *et al.*, 2010). The C-terminal domains of the six ATPase subunits bind to the 20S CP at regions in-between the α subunits, inducing a rotation in the α subunits that causes an 'open gate' conformation (Rabl *et al.*, 2008). The N-terminal domains of these subunits recognise unstructured regions in substrate proteins that act as initiation sites (Prakash *et al.*, 2004). They unravel the substrate proteins, starting from the initiation site, and translocate them into the proteolytic chamber (Prakash *et al.*, 2004; Djuranovic *et al.*, 2009). The two regulatory particle non-ATPase subunits (Rpn 1 and 2) are the largest subunits of the 19S RP, and they serve as platforms for binding various shuttle ubiquitin receptors, deubiquitinating enzymes and proteasome adaptors (Kish-Trier and Hill, 2013). Rpn10

and Rpn13 recognise the polyubiquitin tag that designates substrate proteins for proteolytic degradation (Young *et al.*, 1998; Husnjak *et al.*, 2008; Schreiner *et al.*, 2008).

1.1.3.2.2 The 10-subunit 'lid' complex

The 'lid' of the 19S RP is made up of 9 subunits; Rpn3, 5-9, 11, 12 and 15. Rpn12 is responsible for linking the 'lid' and 'base of the 19S RP (Tomko and Hochstrasser, 2011). The 9 subunits form a horseshoe conformation, and the 'lid' sub-complex sits on the side of the 19S RP rather than on top. This arrangement allows Rpn6 and 5 to contact the α1 and α2 subunits of the 20S CP, thus stabilising the 26S proteasome complex (Vilchez *et al.*, 2012). The Rpn11 subunit is the only enzymatically active subunit of the 19S RP, and its function is to remove the polyubiquitin tag from substrate proteins (Yao and Cohen, 2002), which is required for substrate proteolysis (Verma *et al.*, 2002). Rpn11 is positioned above and in contact with the ATPase ring pore, which is likely to stabilize the active conformation of Rpn11 and allow the coupling of substrate processing and deubiquitination (Pathare *et al.*, 2014).

1.1.3.3 The immunoproteasome

In addition to the standard 26S and 20S proteasomes, cells also have immunoproteasomes, which break down proteins into oligopeptidases for antigen presentation by the major histocompatibility complex (MHC class 1). Immunoproteasomes are structurally very similar to the 26S proteasome, apart from the inclusion of alternative catalytic subunits in the 20S core particle (CP). The immunocytokine interferon y˙induces the expression of these subunits (β1i, β2i and β5i), which are then incorporated into the core particle in place of the standard β1, β2 and β5 subunits (Tanaka *et al.*, 1997; Unno *et al.*, 2002).

1.1.3.4 Proteasomal Degradation

The ubiquitin proteasome system is responsible for the degradation of the majority of soluble cytoplasmic and nuclear proteins (Rock *et al.*, 1994), and the vast majority of this occurs via the ATP-dependent, ubiquitin-dependent pathway, whereby a polyubiquitin 'tag' targets substrates to the 26S proteasome for proteolysis, which is an ATP-dependent process. Since the ubiquitin proteasome system is responsible for the degradation of many cellular proteins, whether long-lived, short-lived or damaged, it is unsurprising that the proteasome is implicated in diverse cellular functions such as apoptosis, cell cycle regulation, transcription, DNA damage repair and the immune response.

In addition to the 'housekeeping' functions of the UPS in the normal turnover of proteins, the UPS is also responsible for the proteolysis of damaged and oxidised proteins, and in the response to oxidative stress. In response to mild oxidation, cells upregulate intracellular proteolysis (Gieche *et al.*, 2001), however it has been demonstrated that the activity of the 26S proteasome greatly declines after oxidative stress, and ubiquitin activation and conjugation enzymes are downregulated by glutathione (Jahngen-Hodge *et al.*, 1997; Reinheckel *et al.*, 1998). Furthermore, cells which do not have functional ubiquitin activation and conjugation enzymes are still able to remove oxidized proteins (Shringarpure *et al.*, 2003), suggesting that the mechanism by which oxidised proteins are broken down is independent of the ubiquitination cascade and the 26S proteasome.

Conversely, the 20S proteasome is far more resistant to oxidative stress than the 26S proteasome (Reinheckel *et al.*, 1998), and remains active under conditions of mild oxidative stress in vitro (Davies, 2001). Because of this, and its independence from ATP or ubiquitin, it is generally accepted that the 20S proteasome is responsible for the proteolysis of oxidised proteins (Grune *et al.*, 2004). Indeed, is thought that when damaged proteins, which have hydrophobic surface patches, bind to the α ring 'gates', it can cause them to open, allowing access to the catalytic centre of the 20S proteasome (Jung and Grune, 2008). Furthermore, it is thought that approximately 20% of proteins are broken down by the 20S or 26S proteasome in a ubiquitin-independent manner, these proteins are termed 'intrinsic proteasome substrates', and are thought to be recognised by the proteasome by extended disordered regions (Baugh *et al.*, 2009).

The efficiency of the ubiquitin proteasome system declines with age; this is outlined in section 1.10.2.

1.1.4 The Autophagy/Lysosome Pathway

The autophagy/lysosome pathway is responsible for the degradation of long lived proteins, organelles, and extracellular proteins, and can be categorised into three different autophagy pathways: macroautophagy, microautophagy and chaperone mediated autophagy.

Macroautophagy involves the formation of a double membrane vesicle, termed an autophagosome, which sequesters a whole region of the cytosol, including soluble proteins and organelles. Autophagosomes then fuse with lysosomes, leading to the degradation of the cargo by lysosomal enzymes (Mizushima *et al.*, 2008). This pathway

does have basal activity in some cell types, but is often activated as a stress response. Macroautophagy can be activated in response to starvation to maintain levels of amino acids for protein synthesis (Kuma *et al.*, 2004), in defence against intracellular microbes (Deretic, 2009), or as part of cellular remodelling (Tsukamoto *et al.*, 2008).

Microautophagy also results in the degradation of a non-specific region of the cytosol, but in this case the cytosol is captured by invagination of the lysosomal membrane, forming intralysosomal vesicles. These vesicles are then degraded, along with their cytosolic contents in the lysosomal lumen (Ahlberg and Glaumann, 1985).

Chaperone mediated autophagy (CMA) is a selective form of autophagy, in which substrate proteins are directly transported across the lysosomal membrane (Cuervo, 2010) as a result of recognition of a pentapeptide targeting motif (Dice, 1990). Like macroautophagy, in most cell types there is some basal CMA activity, and CMA is activated in response to cellular stress, such as oxidative stress or starvation (Cuervo, 2010); these two forms of autophagy often act in a synchronized way. This allows selected proteins that have been altered with the pentapeptide motif to be broken down to release amino acids for protein synthesis, whilst keeping other more essential proteins intact (Orenstein and Cuervo, 2010).

Like the ubiquitin proteasome system, the autophagy/lysosome system becomes less efficient in its degradative capacity with age. A decrease in the activity of macroautophagy has been reported in several mammalian tissues (Cuervo *et al.*, 2005) and CMA activity is also decreased with ageing in rodents and in senescent human fibroblasts (Cuervo and Dice, 2000).

1.1.5 Cellular Proteases

The cell contains various proteases, such as calpain, which break down proteins in a calcium-dependent manner (Kolchinskaya and Malysheva, 2004). Some organelles contain their own proteases, such as ER-60 in the endoplasmic reticulum (Rutledge *et al.*, 2013), and the AAA proteases in mitochondria (Koppen and Langer, 2007).

1.2 UCHL1

UCHL1 (Ubiquitin Carboxy-terminal Hydrolase 1) is a DUB that is expressed exclusively in the nervous system, testes and ovaries (Saigoh *et al.*, 1999). It is one of the most abundant proteins in the brain, representing 1-2% of soluble protein (Wilkinson *et al.*, 1989) and, importantly, is involved in the maintenance of monomeric ubiquitin pools (Osaka *et al.*, 2003).

1.2.1 Molecular functions of UCHL1

1.2.1.1 C-terminal Hydrolase Activity

UCHL1 cleaves small protein adducts from the C terminal end of ubiquitin by its hydrolase activity, generating free monomeric ubiquitin (Larsen *et al.*, 1998). The group attached to the C terminal end of ubiquitin must be small; like UCHL3, there is a loop covering the catalytic site of UCHL1, restricting the group attached to the C-terminus of ubiquitin to less than 10Å (Das *et al.*, 2006). Therefore, it is thought that UCHL1 serves to cleave ubiquitin from the polyubiquitin gene product or from small protein adducts such as the antioxidant glutathione (Nijman *et al.*, 2005). However, it is thought that hydrolysis is not the most important activity of UCHL1, as this activity is weak in relation to UCHL3 and the other DUBs (Kabuta *et al.*, 2008).

1.2.1.2 Monoubiquitin Stabilisation

UCHL1 has been shown to stabilize free monomeric ubiquitin (monoubiquitin) in neurons by binding to ubiquitin and inhibiting its degradation. Overexpression of UCHL1 increases levels of monoubiquitin in cultured cells and mouse brains, whereas levels of monoubiquitin are reduced in mice not expressing functional UCHL1 (Osaka *et al.*, 2003). A reduction in ubiquitin levels has also been observed by immunohistochemistry in the brains of UCHL1 knockout mice (Gray *et al.*, 2003). UCHL1 mediated ubiquitin stabilisation has also been shown in cultured podocytes; there was a marked increase in mono- and poly-ubiquitin levels upon UCHL1 expression, and vice versa (Meyer-Schwesinger *et al.*, 2011).

1.2.1.3 Regulation of UCHL1by Ubiquitination

In addition to the above functions, it has also been demonstrated that UCHL1 is regulated by post-translational modification with ubiquitin. UCHL1 can be monoubiquitinated at lysine residues near the active site, thus inhibiting its hydrolytic activity and its monoubiquitin binding and stabilisation activity. However, UCHL1 is

capable of auto-deubiquitination, therefore this modification is reversible (Meray and Lansbury Jr, 2007).

1.2.1.1 E3 Ubiquitin Ligase Activity

It has also been reported that UCHL1 has a dimerisation dependent E3 ubiquitin ligase function, which does not require ATP, although this activity has only been demonstrated *in vitro* (Liu *et al.*, 2002), and there is no indication that UCHL1 exists as a dimer in solution, although the crystal structure of dimeric ubiquitin has been solved (Das *et al.*, 2006).

1.2.2 UCHL1 in Disease

1.2.2.1 Neurodegeneration

It has been recently reported that a homozygous missense mutation in the UCHL1 gene ($UCHL1^{Glu7Ala}$) causes early-onset, progressive neurodegeneration in three siblings. This mutation is predicted to be within the ubiquitin binding domain of UCHL1, and causes at least a 7-fold decrease in ubiquitin binding activity, and almost complete loss of UCHL1 hydrolase activity. Neurodegeneration is early onset, beginning around 5 years of age, and leading to blindness, cerebellar ataxia, nystagmus and titubation (Bilguvar *et al.*, 2013). These cases indicate the requirement of the human nervous system for UCHL1, and the phenotype of UCHL1 null mice is further evidence for this in mammals (see Section 1.3.2 and Chapter 4)

Furthermore, several studies have suggested the involvement of UCHL1 in some forms of adult-onset neurodegeneration, in particular in Alzheimer's disease (AD) and Parkinson's disease (PD).

UCHL1 has been identified both in the brains of AD subjects (Castegna *et al.*, 2002; Butterfield *et al.*, 2006) associated with neurofibrillary tangles, and in the brains of Parkinson's disease patients (Choi *et al.*, 2004) incorporated into Lewy Bodies (Lowe *et al.*, 1990). Full length UCHL1 undergoes oxidative modification in both AD and PD (Choi *et al.*, 2004), causing it to lose between 40% and 80% of its activity (Nishikawa *et al.*, 2003). Furthermore, levels of UCHL1 protein are decreased in brains of those with AD, PD (Choi *et al.*, 2004), and Dementia with Lewy Bodies (Barrachina *et al.*, 2006), possibly due to damaged UCHL1 being sequestered in inclusions. In the AD brain, levels of soluble UCHL1 are inversely proportional to the number of plaques (Choi *et al.*, 2004).

In addition, two UCHL1 mutations have been associated with PD; the gene encoding UCHL1 is designated as *PARK5*. The I93M mutation was linked to Parkinson's through a sibling pair with a strong family history of PD, however this association is controversial, since the siblings' father (the presumed carrier of the mutation) did not have PD (Leroy *et al.*, 1998). The S18Y mutation was suggested to be protective against PD (Maraganore *et al.*, 1999), although evidence for this is inconclusive and epidemiological studies have only been able to offer moderate evidence for an association in some populations (Ragland *et al.*, 2009; Snapinn *et al.*, 2011; Wang *et al.*, 2011b). Structural studies have revealed that the S18Y mutation may have reduced E3 ligase activity (Liu *et al.*, 2002), has little effect on hydrolase activity (Liu *et al.*, 2002; Nishikawa *et al.*, 2003) and is only slightly less structurally stable than the wild type (WT) protein (Andersson *et al.*, 2011), again indicating that it is unlikely that the S18Y mutation has a strong protective effect against PD.

In contrast, I93M mutant UCHL1 has approximately 55% less catalytic activity than the WT protein (Leroy *et al.*, 1998; Nishikawa *et al.*, 2003), and the I93M mutation induces structural rearrangements around the mutation site, causing a hydrophobic surface area to become exposed (Andersson *et al.*, 2011). Interestingly, it has been shown that oxidatively modified UCHL1 undergoes structural changes similar to the I93M mutant (Kabuta *et al.*, 2008), implicating UCHL1 in both familial and sporadic forms of Parkinson's disease. The loss of UCHL1 hydrolase activity caused by oxidative modification or by the I93M mutation may contribute to the pathogenesis of PD, since UCHL1 hydrolase activity generates monoubiquitin from small protein adducts (Larsen *et al.*, 1998), although since the hydrolase activity of UCHL1 is significantly lower than that of other DUBs (Kabuta *et al.*, 2008) it is unlikely that this is the sole mechanism. The structural changes in $UCHL1^{I93M}$ may play a role in the pathogenesis of PD by inducing UCHL1 aggregation, since UCHL1 is an abundant brain protein (Wilkinson *et al.*, 1989) and is present in Lewy bodies (Lowe *et al.*, 1990).

1.2.2.2 Cancer

Since the ubiquitin pathway and UCHL1 are known to regulate the degradation of proteins involved in cell signalling and cell cycle regulation, it is not surprising that UCHL1 has been implicated in several forms of cancer. UCHL1 has been proposed to play a role in oncogenesis through the β-catenin signalling pathway, through interactions with cell signaling protein p27 and by inactivation of NF-κB (Fang *et al.*, 2010). Furthermore, UCHL1 overexpressing mice are prone to developing lymphomas

and lung tumours, possibly mediated through the PI3K signaling pathway (Hussain *et al.*, 2010) and recently, UCHL1 has been identified as a potential driver of cancer cell invasiveness (Jang *et al.*, 2011).

1.3 UCHL1 null mouse models

1.3.1 Genetics

There are three UCHL1 null mouse models that have been characterised in the literature. The first, known as the gracile axonal dystrophy (*gad*) mouse originated from a spontaneous in-frame deletion of 3.5kb spanning exons 7 and 8 of the *UCHL1* gene (Saigoh *et al.*, 1999) The *gad* allele predicts a truncated version of UCHL1 which lacks a 42 amino acid fragment, including histidine 161, a catalytic residue required for UCHL1's hydrolase activity (Larsen *et al.*, 1996; Saigoh *et al.*, 1999) However, western blot did not detect any truncated or full length UCHL1 protein in homozygous *gad* mice. Expression of *UCHL1* mRNA in *gad* mice was not significantly different from the wild type, suggesting that the truncated *gad* mRNA is degraded after transcription (Saigoh *et al.*, 1999), therefore the *gad* mice can essentially be regarded as UCHL1 null.

Similarly, the UCHL1 knockout mice characterised by Lin's group (Chen *et al.*, 2010a) resulted from a targeted deletion in a region containing exons 6-8, along with the first few base pairs of exon 9. It was verified that UCHL1 was not present as a protein by western blot (Chen *et al.*, 2010a). The nm3419 mouse model originated from a spontaneous 795 bp deletion in the BALB/cJ mouse line, which deletes the final 24 base pairs of exon 6 the first 771 base pairs of intron 6 of the UCHL1 gene. Once again, no UCHL1 protein was detected by western blot (Walters *et al.*, 2008), and therefore all three of these mouse models can be regarded as UCHL1 null. The UCHL1 mice studied in this thesis were generated by the homologous recombination of the UCHL1 gene with a pgk-neo-pgk cassette, as described previously (Coulombe *et al.*, 2014).

1.3.2 Onset and Progression of the UCHL1 null Phenotype

In all three mouse models, the characteristic phenotype is hind limb impairment, accompanied by tremor and kyphosis.

The *gad* mice exhibit ataxia from around 80 days of age (11 weeks), followed by a tremor and immobility. These symptoms become progressively more severe, and death occurs around 5 or 6 months (140-170 days) (Yamazaki *et al.*, 1988). The progression and survival of UCHL1 knockout mice was more robustly described by Lin's group.

Mice first demonstrated a phenotype at 50 days, when they showed clasping movements of their hind limbs when suspended by the tail, and developed a kyphosis and gait problems at 3 months (approx. 80 days). Furthermore, hind limbs became paralyzed between 4 and 6 months (approx. 120-170 days) and fore limbs were also affected, becoming paralysed by 8 months. The majority (~80%) of mice survived at least 6 months, and mostly died between 7 and 10 months of age (196 – 280 days) (Chen *et al.*, 2010a). The nm3419 mice begin to display motor ataxia by 4 weeks of age (28 days), earlier than both the UCHL1 knockout and *gad* mice. Their viability, however is in-between the two other UCHL1 null mouse models, with most mice dying between 160 and 200 days (approx. 6-7 months) (Walters *et al.*, 2008).

1.3.3 Neuropathology of UCHL1 null mice

The neuropathology of UCHL1 null mice has been most extensively studied in *gad* mice, however there have been more recent studies on the UCHL1 knockout and nm3419 mice.

The first neuropathological finding in the *gad* mouse, and the hallmark of UCHL1 neuropathology, was the presence of axonal swellings (spheroids) in the gracile nucleus of the medulla oblongata and gracile fasciculi of the spinal cord (Yamazaki *et al.*, 1988). Further studies showed that this axonal dystrophy also occurs in the spinocerebellar tract at the level of the cerebellum, inferior cerebellar peduncle, medulla, and spinal cord. (Kikuchi *et al.*, 1990). The *gad* mouse displays 'dying back' type axonal degeneration, where axonal degeneration starts distally, at presynaptic nerve terminals, and then spreads caudally down the gracile fasciculus to more proximal regions of the axon, and is particularly prominent in long axons (Mukoyama et al., 1989; Oda et al., 1992). *Gad* mice also show axonal degeneration at the distal ends of descending motor neurons. The presynaptic muscle terminals retract from the distal end plates, and degeneration progresses towards more proximal regions of the axon (Miura et al., 1993). This observation was confirmed by Chen *et al* who also showed that this is accompanied by the accumulation of tubulovesicular structures and loss of synaptic vesicles at presynaptic nerve terminals of motor neurons (Chen *et al.*, 2010a). An *in vitro* study also indicates a link between UCHL1 and synapses; inhibition of UCHL1 ubiquitin-binding activity caused a decrease in the number of PSD-95 (pre-synaptic density-95) positive synapses, whilst each one of these synapses was larger. The authors found that this defect was rescued by exogenous ubiquitin expression and that NMDA receptor activation upregulates UCHL1 hydrolase activity, increasing levels of free

monomeric ubiquitin (Cartier *et al.*, 2009). Furthermore, a small fraction of UCHL1 (2-5%) coimmunoprecipitates with synaptic vesicles, along with synaptic markers α-synuclein, synapsin I, synaptotagmin I and synaptophysin (Liu *et al.*, 2002), suggesting that UCHL1 may function at synapses and/or synaptic vesicles.

There is no indication of any pathology in the hippocampus and cortex of the *gad* mice, but Sakurai *et al* find that 6 week old *gad* mice display learning and memory deficits, and have deficient long term potentiation (LTP) at CA3-CA1 synapses (Sakurai *et al.*, 2008). Conversely, Walters *et al* found no difference in short term synaptic plasticity, LTP or LTD (long term depression) in 4-6 week old nm3419 mice in the hippocampus (Walters *et al.*, 2008).

Ultrastructural examination of spheroids, the large axonal swellings that characterise gracile axonal dystrophy, revealed that they were full of neurofilaments, mitochondria, and tubulovesicular and membranous structures (Mukoyama et al., 1989). An examination of ubiquitin immunoreactivity in the CNS of *gad* mice revealed ubiquitinated foci in the gracile nucleus, spinocerebellar tract and the white matter of the cerebellum after 9 weeks. Ubiquitinated foci were primarily localized to spheroids, and ubiquitin immunoreactivity at the distal ends of dystrophic axons was either negative or very diffuse (Wu et al., 1996). Axonal degeneration in *gad* mice is concomitant with an increase in APP (amyloid precursor protein) immunoreactivity, and subsequent deposition of the amyloid β protein, indicating blocked axonal transport (Ichihara et al., 1995). β and y˙synucleins also accumulate over time within axonal spheroids, however the pathogenic α synuclein was not shown to accumulate (Wang et al., 2004). A more recent study also observed an age-related increase of the oxidative stress markers sulfonated GAPDH (Glyceraldehyde phosphate dehydrogenase) and 4-HNE (4 hydroxy-nonenal) (Goto et al., 2009). Together, these studies implicate the reduced degradation of proteins (including those that are oxidatively damaged) in axonal dystrophy in *gad* mice. Interestingly, crossing *gad* mice with Wld_s (Wallerian degeneration, slow) mice, which are resistant to Wallerian degeneration reduces axonal spheroid pathology in the resulting offspring. This indicates that Wld_s acts downstream of ubiquitin, and that axon swelling may be a programmed response to axon damage (Mi et al., 2005).

UCHL1 null mice fail to gain weight after 12 weeks of age; their weight plateaus whilst the weight of WT mice increases (Coulombe *et al.*, 2014). This has been attributed to

axonal dystrophy in the NTS (Nucleus Tractus Solitarii, or Solitary Tract), which receives sensory input from the tongue and gut, mediating taste and swallowing. Doug Gray's group also observed the failure of UCHL1 mice to gain weight, and found morphological and functional abnormalities in neurons of the enteric nervous system (ENS) which innervate the gut, such as swellings of neurites and decreased transit time of food through the gut (Coulombe *et al.*, 2014). This demonstrates the vulnerability of long axonal processes to axonal swelling in UCHL1 null mice.

1.4 Mitochondria

Mitochondria are cytosolic organelles, whose primary function is the generation of ATP by oxidative phosphorylation. Mitochondria are unique in being the only organelles to have their own genome; mtDNA is a maternally inherited, 16.6kb double stranded loop of DNA. Mitochondria are a dynamic network of organelles, constantly undergoing fission, fusion, and movement around the cell using the cytoskeleton as tracks.

1.4.1 Structure of Mitochondria

Early work to elucidate the structure of mitochondria was carried out by Palade, using electron microscopy (Palade, 1953). He observed that each mitochondrion has a limiting membrane (the outer mitochondrial membrane; OMM), a mitochondrial matrix, and a system of internal ridges, termed '*cristae mitochondriale'*, which are formed by the folding of a continuous internal membrane (the inner mitochondrial membrane IMM). This was known as the 'baffle model'. Whilst these observations were largely true, more advanced 3D electron microscopic (EM) tomography studies showed that Palade's 'baffle model' was somewhat inaccurate: cristae are in fact distinct tubular membranes which connect to the inner boundary membrane by structures named crista junctions that have a diameter of 28nm (Frey and Mannella, 2000). The key components of mitochondrial structure are demonstrated in Figure 1.3.

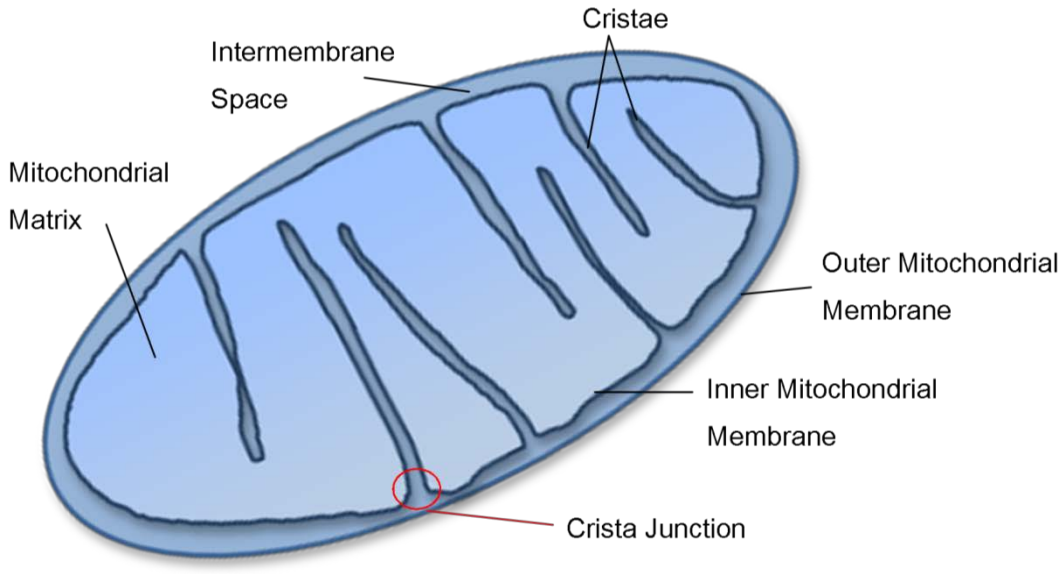

Figure 1.3: Diagram of mitochondrial structure.
Mitochondria are enclosed by an outer mitochondrial membrane (OMM). Cristae are tubular structures that attach to the inner mitochondrial membrane (IMM) via 28nm cristae junctions and are therefore continuous with the intermembrane space (IMS). The mitochondrial matrix contains many copies of mtDNA.

The outer mitochondrial membrane is similar in composition to the cell membrane, and separates the intermembrane space from the cytosol. The most abundant integral membrane protein of the OMM is the voltage-dependent anion channel (VDAC), also known as porin. VDAC forms hydrophilic pores in the OMM, and regulates the exchange of metabolites such as adenosine nucleotides to and from the IMS, as well as taking part in key mitochondrial processes, such as apoptosis and calcium homeostasis (Shoshan-Barmatz *et al.*, 2010). The transport of polypeptides and proteins across both mitochondrial membranes is facilitated by TOM (translocase of the outer mitochondrial membrane) and TIM (Translocation machineries in the Inner mitochondrial Membrane) complexes, which recognise mitochondrial proteins by their mitochondrial targeting sequences (Wagner *et al.*, 2009). Mammalian mitochondria contain around 1000-1500 proteins; of these only 13 are encoded by the mitochondrial genome, therefore the remainder are nuclear encoded and imported from the cytoplasm (Milenkovic *et al.*, 2007).

The two primary functions of the inner mitochondrial membrane are to act as the scaffold for the mitochondrial respiratory chain complexes (Section 1.5.5.1), and to act as a barrier between the intermembrane space and the mitochondrial matrix, maintaining the electrochemical gradient between these two compartments, which is essential for the generation of ATP by the F_1F_0ATPase (Mitchell, 1966; Mannella *et al.*, 2013). As such, the IMM is impermeable to small molecules and ions. As previously mentioned, TIM complexes facilitate the transport of proteins across the IMM, and specialized metabolite carrier proteins allow the translocation of metabolites. The most abundant of these is the ADP/ATP carrier protein. The mitochondrial matrix is a dense, protein rich environment, which contains enzymes involved in several metabolic processes, such as the tricarboxylic acid cycle and oxidative phosphorylation, the β-oxidation of fatty acids and the urea cycle. Importantly, the mitochondrial matrix is also contains multiple copies of mtDNA and is the site of mtDNA replication, transcription and translation.

1.5 Functions of Mitochondria

In addition the generation of ATP by oxidative phosphorylation, mitochondria also play a central role in the formation of iron-sulphur clusters, calcium handling, reactive oxygen species (ROS) production and apoptosis.

1.5.1 Iron-Sulphur Cluster formation

Mitochondria are the major site of iron-sulphur (Fe-S) cluster formation within the cell (Lill *et al.*, 1999). Fe-S clusters are not only essential within mitochondria (they facilitate electron transfer at complexes I, II and III of the respiratory chain), but also act as cofactors for a variety of cellular processes (gene expression, enzyme catalysis, DNA repair and maintenance) (Lill *et al.*, 1999).

1.5.2 Calcium handling

Whilst the endoplasmic reticulum (ER) is the primary cellular calcium store, mitochondria also play an important role in calcium buffering (Kaufman and Malhotra, 2014), thereby contributing to the regulation of intracellular calcium levels, which are important for a wide array of cell signalling pathways (Jacobson and Duchen, 2004). This is particularly important in neurons, where calcium levels are a key determinant of presynaptic activity and neurotransmitter release (Sandoval, 1980), and play a role in regulating levels of mitochondrial motility (MacAskill *et al.*, 2009). The influx of calcium into mitochondria causes the upregulation of the tricarboxylic acid cycle, increasing ATP production and ROS generation (Jacobson and Duchen, 2004), whilst calcium overloading signals apoptosis via the MPTP (Mitochondrial Permeability Transition Pore) opening and cytochrome *c* release (Orrenius *et al.*, 2003). Interestingly, it has also been reported that the influx of calcium into mitochondria can activate mitophagy (Kaufman and Malhotra, 2014).

1.5.3 Apoptosis

Mitochondria have long been considered the central regulators of apoptosis (Susin *et al.*, 1998). The influx of calcium into mitochondria from the ER or cytosol in response to apoptotic signals is an important mediator of apoptosis, leading to the opening of the mitochondrial permeability transition pore (MPTP), release of cytochrome *c*, formation of the apoptosome and caspase activation (Jeong and Seol, 2008). Mitochondrial fragmentation (mediated by increased mitochondrial fission and decreased fusion) is an important apoptotic process; overexpression of a component of the mitochondrial fission machinery causes apoptosis (James *et al.*, 2003), whereas inhibition of mitochondrial fission prevents or delays cell death by apoptosis (Lee *et al.*, 2004).

1.5.4 Oxidative Phosphorylation

Oxidative phosphorylation occurs on the mitochondrial respiratory chain, a group of 92 polypeptides organised into 5 multi-subunit transmembrane complexes (Complexes I –

V) on the inner mitochondrial membrane. 79 of the polypeptides of the respiratory chain are encoded by nuclear DNA, whilst 13 are encoded by Mitochondrial DNA (mtDNA) (DiMauro and Schon, 2003). The movement of electrons along complexes I – IV provides enough energy to pump protons across the inner mitochondrial membrane from the matrix to the inter-membrane space, creating an electrochemical gradient. This gradient enables the fifth complex, ATP synthase, to catalyse the phosphorylation of ADP, forming ATP. This is termed the chemiosmotic theory (Mitchell, 1966). This process is summarised in Figure 1.4.

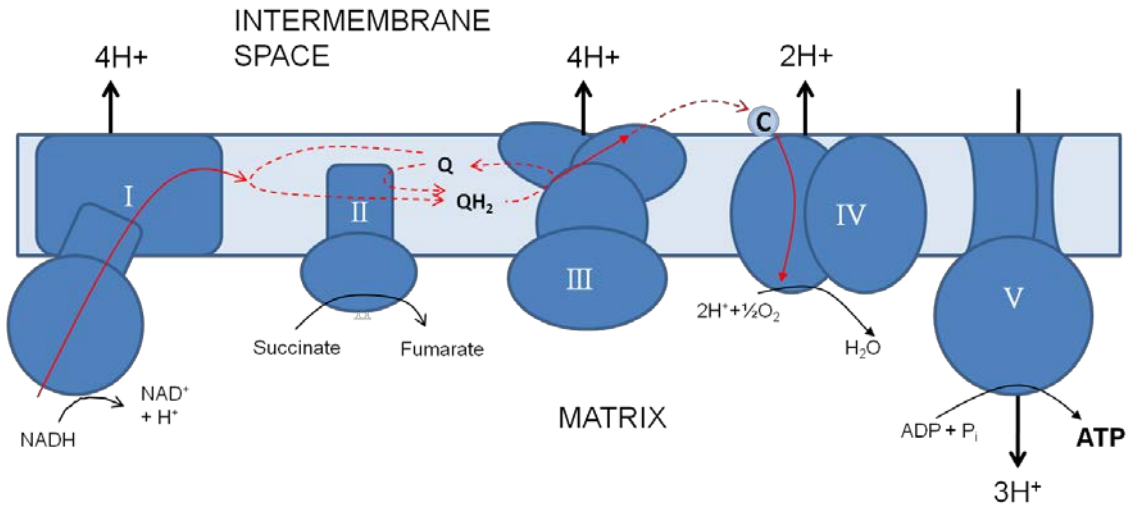

Figure 1.4: Oxidative Phosphorylation:
Complex I: NADH releases two electrons to the electron acceptor FMN (flavine mononucleotide), which are passed through a series of Fe-S clusters to ubiquinone (Q), which is reduced to ubiquinol, QH_2 in the Q cycle. Two hydrogen ions are pumped across the IMM for every electron transferred (Wikström, 1984). Complex II catalyses the oxidation of succinate to fumarate as part of the tricarboxylic acid cycle. This is coupled to the reduction and re-oxidation of FAD, and results in the reduction of ubiquinone. *Complex III:* By a process known as the Q cycle (Mitchell, 1976), 2 electrons are transferred from ubiquinol to cytochrome c , and two protons are released into the IMS. Cytochrome *c* then transfers electrons to *complex IV*, which catalyses the reduction of O_2 to H_2O, through a cycle involving two haem groups and copper centres; this is coupled to the pumping of protons across the IMM , at a rate of $1H^+/e^-$. *Complex V*, the F_0F_1 ATP synthase, uses the electrochemical gradient to couple the transfer of H_+ ions through the F_0 subunit to the synthesis of ATP from ADP and P_i (Papa *et al.*, 2012). Thick black arrows indicate the transfer of protons across the IMM, red arrows indicate the passage of two electrons, red dashed arrows show the Q cycle. C=Cytochrome *c*. Based on (Parikh *et al.*, 2008)

1.5.5 Production of Reactive Oxygen Species

As a necessary by-product of oxidative phosphorylation, mitochondria produce the superoxide anion ($O_2^-\bullet$) (Adam-Vizi and Chinopoulos, 2006), which can be converted to other forms of reactive oxygen species (ROS) within mitochondria ($\bullet OH$, H_2O_2). The implications of ROS generation within mitochondria will be discussed further within the context of the mitochondrial theory of ageing (Sections 1.10.1).

1.5.5.1 Mitochondrial Respiratory Chain Complexes

Complex I (NADH - Ubiquinone reductase) is the largest enzyme of the oxidative phosphorylation system and consists of 45 different subunits; 7 of these are encoded by the mitochondrial genome, whilst the remainder are encoded by nuclear DNA. Complex I is the main site of ROS generation within the respiratory chain (Boveris *et al.*, 1976). Complex II (Succinate Dehydrogenase) is the smallest complex of the respiratory chain, is entirely nuclear encoded, and does not pump protons across the IMM. Complex III (Ubiquinone – Cytochrome *c* Oxidoreductase) is the second site of ROS generation within the mitochondrial respiratory chain (Turrens and Boveris, 1980). It consists of 11 different subunits and contains cytochrome *b*, cytochrome *c*, and an Fe-S cluster known as the Rieske centre. Cytochrome *b* is the only mitochondrially encoded subunit of complex III. Complex IV (Cytochrome *c* Oxidase) contains four redox centres: two copper groups and two Haem groups. 3 of the 13 Complex IV subunits are mitochondrially encoded (COX I, II and III) (Anderson *et al.*, 1981). Complex V, the F_1F_0 ATP Synthase has 16 subunits, of which only 2 are encoded by the mitochondrial genome (Papa *et al.*, 2012).

1.6 Mitochondrial DNA

Mitochondria are unique in being the only organelles to have their own genome. MtDNA is a 16,569bp, double stranded loop of DNA that encodes 13 polypeptides, 22 transfer RNAs and 2 ribosomal RNAs (Anderson *et al.*, 1981; Andrews *et al.*, 1999). All of the 13 polypeptides are components of respiratory chain complexes (the remainder of the ~80 subunits are encoded by the nuclear genome), whilst the 22 tRNAs and 2 rRNAs comprise the necessary machinery for protein synthesis (Kyriakouli *et al.*, 2008). MtDNA consists of an outer heavy (H-) strand and an inner light (L-) strand (depicted in Figure 1.5), and is highly efficient in terms of coding. The only non-coding region of the mitochondrial genome is the displacement (D) loop, which contains two hypervariable regions in addition to the control regions for mtDNA transcription and replication (Anderson *et al.*, 1981).

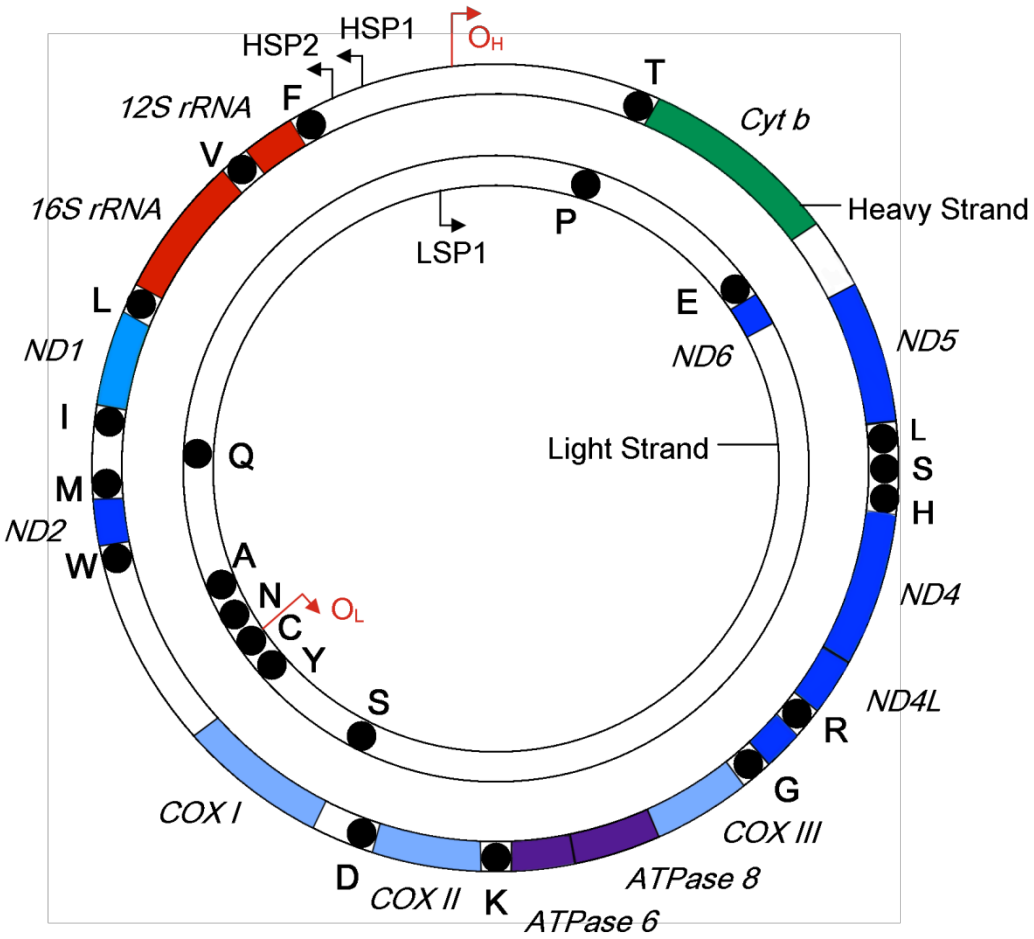

Figure 1.5: The Human Mitochondrial Genome.
Complex I NAD Hydrogenase genes (ND), dark blue; Complex III Cytochrome B gene, green; Complex IV Cytochrome *c* oxidase (COX) genes, light blue; Complex V ATP Synthase (ATPase) genes, purple; rRNA genes, red; tRNA genes, black circles. O_H: Origin of heavy strand replication, O_L: Origin of light strand replication. LSP: Light strand promoter, HSP: Heavy strand promoter Based on (Kyriakouli *et al.*, 2008; Wanrooij and Falkenberg, 2010).

When extended, a mtDNA molecule is around 5µm in length (Nass, 1966; Van Bruggen *et al.*, 1966), longer than the typical mitochondrion. However, mtDNA is coated in proteins *in vivo* (predominantly TFAM, Mitochondrial Transcription Factor A) and highly compacted to form nucleoids, which have a mean diameter of approximately 100nm (Kukat and Larsson, 2013), and reside in the mitochondrial matrix in close proximity to the IMM. Many studies have attempted to quantify the number of mtDNA molecules per nucleoid, with estimates ranging from 1 to 7.5 copies per nucleoid (Gilkerson *et al.*, 2008; Bogenhagen, 2012). There are multiple copies of mtDNA present in all nucleated cell types.

1.6.1 Transcription and Translation

Transcription of the mitochondrial genome is bidirectional, and originates from three promoters: HSP1 and HSP2 (Heavy strand promoters 1 and 2) on the heavy strand, and LSP1 (Light strand promoter 1) of the light strand (Figure 1.5) (Montoya *et al.*, 1983).

The transcription machinery of mitochondrial DNA has been reviewed in detail (Bestwick and Shadel, 2013), however for the purposes of this thesis I will discuss it only briefly. The three main components of the mitochondrial transcription machinery are Mitochondrial Transcription Factor A (TFAM), the Mitochondrial RNA Polymerase (POLRMT), and Transcription Factor B2M, (TFB2M) (Falkenberg *et al.*, 2002; Shi *et al.*, 2012). In addition to its role of packaging mtDNA into nucleoids, TFAM binds to mtDNA at specific sites upstream of promoters, bending the DNA and thus activating transcription (Shi *et al.*, 2012). Transcription is carried out by POLRMT, which is capable of recognising promoter sequences in the presence of TFAM (Gaspari *et al.*, 2004). In order for transcription to occur, POLRMT must form a heterodimer with TFB2M, which is thought to carry out promoter melting (Sologub *et al.*, 2009), thus facilitating transcription. Site-specific termination of transcription is thought to be mediated by MTERF1 (Mitochondrial Termination Factor 1) (Yakubovskaya *et al.*, 2010).

Translation is a very complex process, which has been reviewed recently (Christian and Spremulli, 2012). Translation follows the transcription and post-translational modification of mRNA, and is carried out by mitochondrial ribosomes, which contain the two rRNAs encoded by mtDNA (Anderson *et al.*, 1981). Translation requires 22tRNAs, which read mRNA codons and transfer the appropriate amino acid onto the nascent polypeptide chain. Mitochondrial translation uses fewer tRNA species than predicted by Crick's 'Wobble hypothesis'(Crick, 1966); this is enabled by the use of a 'U' (Uridine) in the first position of the anticodon (known as the wobble base), allowing for a single tRNA to recognise four codons rather than one (Barrell *et al.*, 1980). The translation of mRNA transcripts into proteins consists of four phases: initiation, elongation and termination, which are regulated by initiation, elongation, recycling and release factors (Christian and Spremulli, 2012). Since the 22tRNAs that are necessary for mitochondrial protein synthesis are encoded by mtDNA (Anderson *et al.*, 1981), it is not surprising that mutations of these genes are common causes of mitochondrial disease. Amongst the types of mitochondrial disease caused by tRNA mutations are MELAS (Mitochondrial encephalopathy with lactic acidosis and stroke-like episodes) (Kirino *et al.*, 2004) and MERRF (Myoclonic epilepsy with ragged red fibres) (Shoffner *et al.*, 1990), which are commonly caused by m.3243 A>G and m.8344 A>G point mutations, respectively. m.3243A>G and m.8.344 A>G tRNA point mutations are discussed in more detail in the introduction to chapter 7.

1.6.2 Replication of Mitochondrial DNA

The basic machinery for the replication of mtDNA has been characterized (Falkenberg *et al.*, 2007), although the exact mode of mtDNA replication is controversial, with two modes of mtDNA replication being postulated (Clayton, 2000; Holt and Reyes, 2012), reviewed in (Wanrooij and Falkenberg, 2010).

Only five proteins are necessary for the replication of mtDNA: the mitochondrial DNA helicase TWINKLE (T7 gp4-like protein with intramitochondrial nucleoid localization), both subunits of mitochondrial DNA polymerase γ (POLγA and POLγB), mitochondrial single stranded binding protein (mtSSB) and POLRMT.

TWINKLE unwinds dsDNA in an NTP-dependent manner moving in a 5' to 3' direction (Spelbrink *et al.*, 2001). It's DNA unwinding activity is enhanced by the presence of mtSSB (Korhonen *et al.*, 2003). Mitochondrial DNA polymerase γ (POLγ) is an RNA dependent DNA polymerase (Fridlender *et al.*, 1972), which consists of one catalytic subunit (POLγA) and two accessory subunits (POLγB) (Yakubovskaya *et al.*, 2006). POLγA possesses polymerase, 3'-5' exonuclease and 5'deoxyribose phosphate lyase activities, whilst the accessory subunit POLγB binds to dsDNA of >45bp, and is capable of substantially increasing POLγA activity (Falkenberg *et al.*, 2007). mtSSB plays a key role in mtDNA replication by binding ssDNA, preventing it from refolding and protecting it against nucleolytic attacks (Yang *et al.*, 1997). mtSSB also aids the replication of mtDNA by enhancing primer recognition, as well as stimulating the activities of TWINKLE and POLγ (Wanrooij and Falkenberg, 2010). POLRMT plays an important role in DNA replication by transcribing the RNA primers necessary for POLγ to bind to mtDNA and initiate replication, both at the origin of heavy strand replication (O_H) and at the origin of light strand replication (O_L) (Wanrooij and Falkenberg, 2010).

1.7 Mitochondrial Genetics

1.7.1 Damage and Repair of Mitochondrial DNA

The frequency of point mutations that occur in mitochondrial DNA is 10-fold higher than that of nuclear DNA (Brown *et al.*, 1979). The vulnerability of mtDNA to mutations, deletions and insertions is thought to be due to its proximity to damaging reactive oxygen species. mtDNA is packaged into nucleoids, which are either attached to or in close proximity with the inner mitochondrial membrane (Kopek *et al.*, 2012),

which is the site of oxidative phosphorylation and concomitant ROS generation (Adam-Vizi and Chinopoulos, 2006). In addition, mtDNA is not protected by the histone proteins that protect nuclear DNA, however it has been demonstrated that nucleoid proteins can shield mtDNA from damage (Guliaeva *et al.*, 2006). Quality control of mitochondria and mtDNA occurs at several levels (outlined in section 1.9); however the first line of defence is the repair of mtDNA damage. The primary mechanism by which DNA damage repair occurs in mitochondria is base excision repair (BER) (LeDoux *et al.*, 1992), although other repair mechanisms (nucleotide excision repair, mismatch repair, recombination and non-homologous end-joining) have been demonstrated in mitochondria on occasion, but the in vivo relevance of these observations is unclear (Graziewicz *et al.*, 2006). Mitochondrial BER takes place via a similar mechanism to nuclear BER, however since POLγ is the only DNA polymerase present in mitochondria, it is an essential part of the mitochondrial BER machinery (Longley *et al.*, 1998) .

1.7.2 Heteroplasmy, the Threshold Effect and Maternal Inheritance

In healthy cells there are many identical copies of mtDNA; this is known as homoplasmy. However a situation known as heteroplasmy can arise whereby one or more different species of mtDNA (for example those with deletions or mutations) exist within the cell. The proportion of mutant mtDNA copies within a cell or tissue can increase over time, by a process known as clonal expansion. There are several theories of how this may occur (De Grey, 1997; Kowald and Kirkwood, 2000; Elson *et al.*, 2001), yet none of these has been proven as yet. If a species of mutant mtDNA rises above a certain threshold, this can cause mtDNA disease (Rossignol *et al.*, 2003), a broad group of diseases with predominantly neurological and neuromuscular symptoms. Over 250 mutations in mitochondrial DNA have been shown to cause various forms of mtDNA disease (Tuppen *et al.*, 2010), two of which are discussed in the introduction to chapter 7. Mitochondrial DNA is strictly maternally inherited (Giles *et al.*, 1980); paternal mitochondria are selectively degraded by proteolysis shortly after fertilisation (Sutovsky *et al.*, 2000) so that only maternal mtDNA remain. Therefore, all transmission of mtDNA disease is maternal, apart from in the case of mitochondrial disease caused by a nuclear mutation.

1.8 Mitochondrial Dynamics

Mitochondria form a dynamic network of organelles, and constantly undergo fission, fusion, and movement around the cell using the cytoskeleton as tracks. This is outlined in Figure 1.6

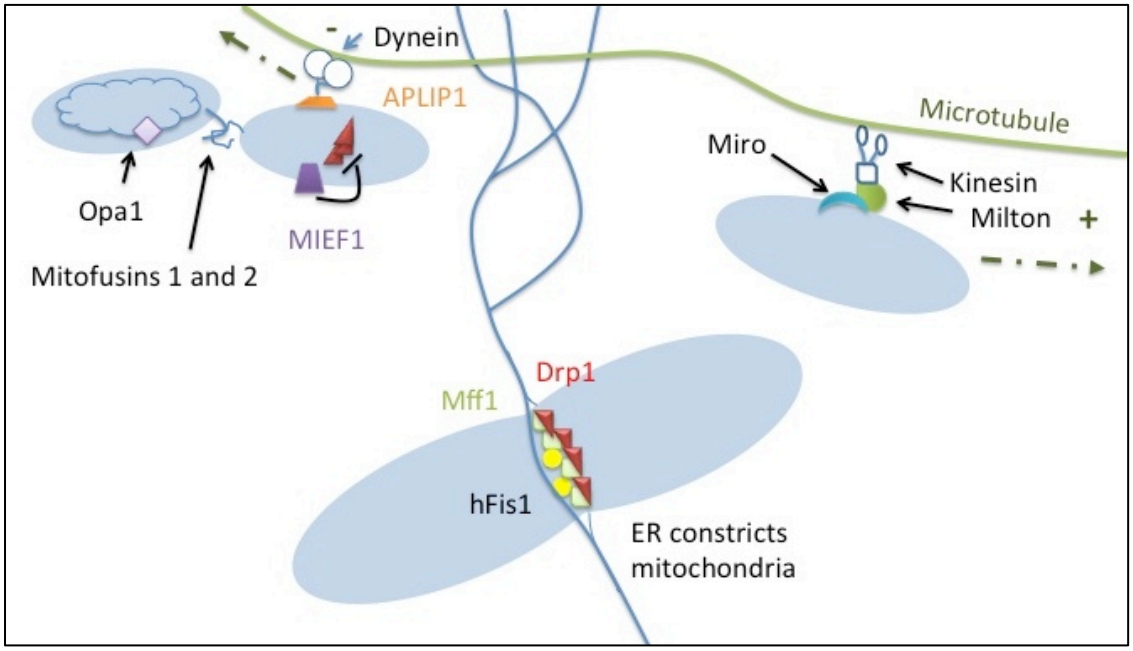

Figure 1.6: Mitochondrial Fission, Fusion and Motility.
Fusion: Opa1, Mfn1 and Mfn2 co-ordinate the simultaneous fusion of inner and outer mitochondrial membranes. MIEF1 induces elongation by inhibiting Drp1 activity. *Fission:* The ER constricts mitochondria at fission sites; Mff1 recruits Drp1, the GTPase responsible for fission to the OMM. hFis may prevent MIEF1 inhibition of Drp1, promoting fission. *Motility:* Kinesin proteins mediate anterograde mitochondrial transport along microtubules, facilitated by receptor and adaptor proteins; shown here are Miro and Milton/TRAK1/2. Dynein mediates retrograde axonal transport, APLIP1(APP-like interacting protein1) has been proposed at a mitochondria-dynein linker protein.

1.8.1 Fusion

Mitochondrial fission and fusion are outlined in Figure 1.6. Complete mitochondrial fusion requires the co-ordinated fusion of both inner and outer mitochondrial membranes. The large GTPases mitofusin 1 (Mfn 1) and mitofusin 2 (Mfn2) are responsible for the fusion of the outer mitochondrial membrane, whilst Opa1 (Optic Atrophy 1) resides in the IMM and IMS and is responsible for the fusion of the IMM (Misaka *et al.*, 2002; Song *et al.*, 2009). Mitofusins self-assemble, and are anchored to the OMM by two transmembrane domains, with their N- and C-termini exposed to the cytoplasm; interactions between these terminal domains are essential for the process of fusion (Rojo *et al.*, 2002). The i-AAA ATPases YME1L1 and OMA1 are responsible for the cleaving Opa1 to short isoforms, thus maintaining the balance between mitochondrial fission and fusion (Anand et al., 2014). Fusion is also regulated by phosphorylation and ubiquitination of the mitofusins, the latter of these is discussed in the introduction to chapter 3.

1.8.2 Fission

Mitochondrial fission is a complex process involving several stages. The large GTPase Drp1 is necessary for mitochondrial fission (Smirnova *et al.*, 2001). Drp1 accumulates at fission points, forming rings around mitochondria and causing scission by its GTPase activity. It has recently been shown that mitochondrial fission occurs at points of endoplasmic reticulum (ER) to mitochondria contact (Friedman *et al.*, 2011). The ER wraps tightly around the mitochondrial network, causing it to constrict. Constriction of mitochondrial tubules by the ER is thought to be a prerequisite for the formation of Drp1 rings around mitochondria, since mitochondria are typically 500-1000nm in diameter, whereas Drp1 rings have a mean reported diameter of 129nm in vitro (Friedman *et al.*, 2011). Drp1 is predominantly a cytosolic protein (Smirnova *et al.*, 2001), and for fission to occur, it must first be recruited to the OMM. Human fission protein 1 (hFis1) localizes to the OMM by a transmembrane domain (James *et al.*, 2003), and was originally thought to be the molecular adaptor for the recruitment of Drp1 to the OMM (Yoon *et al.*, 2003). However, Mitochondrial fission factor 1 (Mff1), a tail anchored OMM protein that is similar in localisation and topology to hFis1, is necessary for the formation of Drp1 foci, interacts with Drp1 on the OMM, and is sufficient to recruit Drp1 to the plasma membrane (Otera *et al.*, 2010). This data poses Mff1 as the essential molecular adaptor for mitochondrial Drp1 recruitment. The novel OMM protein MIEF1 (Mitochondrial Elongation Factor 1) was independently identified by two groups (Palmer et al., 2011; Zhao et al., 2011); it directly recruits the fission protein Drp1 (Dynamin Related Protein 1) to mitochondria, and inhibits Drp1 by reducing its GTPase binding activity, thus inducing mitochondrial elongation (Zhao et al., 2011). It is currently thought that hFis1 promotes mitochondrial fission by binding to MIEF1, thereby preventing it from inhibiting Drp1 GTP hydrolysis activity (Zhao *et al.*, 2011). In addition to hFis1/MIEF1 mediated regulation, Drp1 is also regulated by a variety of post-translational modifications, such as phosphorylation, glycosylation, S-nitrosylation, SUMOylation and ubiquitination (Elgass *et al.*, 2013). The regulation of mitochondrial fission by ubiquitination is discussed further in the introduction to chapter 3.

1.8.3 Mitochondrial Motility

When viewed by fluorescence microscopy, mitochondria can be seen moving along neuronal processes. This movement is bidirectional, and mitochondria can pause, change direction, or dock and stop moving completely. Mitochondria predominantly use

microtubules as a track to move along and this is mediated by the binding of receptor-adaptor-motor protein complexes to the OMM.

Microtubules are polarised, and in neurons they are arranged with minus (-) ends towards the cell body, and plus (+) ends towards synapses. Kinesin motor proteins KIF5B (Kinesin family member 5B, also known as Kinesin heavy chain C (KHC)) (Tanaka et al., 1998), KIF1Bα (Nangaku et al., 1994) and KLP6 (Kinesin like protein 6) (Tanaka et al., 2011) have been shown to mediate transport in the anterograde (+) direction, whilst the motor protein dynein mediates retrograde axonal transport, probably in association with linker protein APLIP1 (APP-like Interacting Protein 1) (Horiuchi et al., 2005). It is thought that KHC is the primary kinesin motor protein responsible for the anterograde axonal transport of mitochondria in neurons (Birsa et al., 2013)

Several proteins have been identified as adaptors for the binding of mitochondria to kinesin motor proteins, including the *Drosophila* and mammalian Miro and Milton proteins, Syntabulin, FEZ1 (fasciculation and elongation protein ζ 1), RanBP2 (Ran-binding protein 2) and APLIP1 (For review, see (Sheng and Cai, 2012; Birsa *et al.*, 2013)). Of these, there has been the most interest in Milton and Miro.

Milton was originally identified as a protein necessary for the axonal transport of mitochondria to synapses in *Drosophila*; Milton colocalizes with mitochondria and coimmunoprecipitates with KHC (Stowers et al., 2002) and mediates KHC recruitment by interacting with Miro (Mitochondrial Rho) (Glater et al., 2006). Miro's mammalian orthologues Miro1 and 2 (Mitochondrial atypical Rho GTPases) were identified, and shown to induce perinuclear aggregation of mitochondria upon overexpression, thus indicating role in anterograde mitochondrial trafficking (Fransson et al., 2003). The mammalian orthologues of Milton, huMilt1/TRAK1 and huMilt2/TRAK2 (Stowers et al., 2002), were also identified as GRIF1 (GABA Receptor Interacting Factor 1) and OIP106 (O-linked N-acetylglucosamine transferase Interacting Protein 106) respectively (Brickley et al., 2005). Both TRAK1 and TRAK2 coimmunoprecipitate with KHC (Brickley et al., 2005; Smith et al., 2006), and interact with Miro1 and 2 (Fransson et al., 2006). Furthermore, depletion of Miro1 or TRAKs in neurons significantly reduces the number of motile mitochondria (Birsa et al., 2013), providing strong evidence for their roles as receptor and adaptor proteins.

As well as acting as a receptor protein, Miro plays a key role in the regulation of mitochondrial trafficking. Miro consists of a transmembrane domain (responsible for its interaction with the OMM), two GTPase domains, and two calcium-binding EF hands (Fransson et al., 2003). It is known that calcium entry into neurons reduces mitochondrial motility (Rintoul et al., 2003), and it has been demonstrated that Miro1 stops mitochondrial movement upon Ca^{2+} binding by uncoupling mitochondria from motor proteins (MacAskill et al., 2009). Mitochondrial motility and trafficking is also regulated by ubiquitin, as discussed in chapter 3.

1.9 Mitochondrial Quality Control

Mitochondria are the main site of ROS generation (Adam-Vizi and Chinopoulos, 2006), and are thus vulnerable to mtDNA damage (Brown *et al.*, 1979), which can accumulate in cells by clonal expansion (Elson *et al.*, 2001), causing deleterious effects at the level of the cell, tissue and organism, such as ageing and neurodegeneration. Therefore, it is essential that cells maintain the integrity of mitochondria. There are several mechanisms of mitochondrial quality control, which I have outlined with a particular focus on the involvement of the UPS.

1.9.1 The Mitochondrial Unfolded Protein Response

The mitochondrial unfolded protein response (MT-UPR) is the mechanism by which mitochondria detect and respond to misfolded proteins within mitochondria (Zhao *et al.*, 2002). The presence of unfolded proteins within mitochondria causes the upregulation of nuclear transcription factors C/EBPβ (CAAT enhancer-binding protein) and CHOP (C/EBP homologous protein), mediated by c-Jun phosphorylation (Horibe and Hoogenraad, 2007). C/EBPβ and CHOP activate the transcription MT-UPR target genes such as the mitochondrial AAA protease ClpP (Caseinolytic protease) and mitochondrial chaperone proteins HSP60 (Heat shock protein 60) and MPPβ (Mitochondrial processing peptidase β subunit) (Bernales et al., 2012), thus causing mitochondrial unfolded proteins to be refolded or degraded and maintaining protein homeostasis. It is though that the MT-UPR may be involved in triggering apoptosis, however this link has not yet been characterised (Bernales *et al.*, 2012).

1.9.2 Mitochondrial Associated Degradation (MAD)

Whilst the mitochondrial AAA proteases are instrumental in the proteolysis of mitochondrial proteins (Koppen and Langer, 2007), a role for the UPS in mitochondrial protein turnover is now becoming widely accepted (Karbowski and Neutzner, 2012).

Mitochondrial associated degradation (MAD) involves the ubiquitination of OMM associated proteins by transmembrane E3 ubiquitin ligases, such as Parkin and MITOL (Mitochondrial Ubiquitin Ligase), which have RING domains that confer E3 ligase activity facing the cytosol (Neutzner *et al.*, 2007). This process requires the AAA-ATPase p97 for the retrotranslocation of ubiquitinated proteins into the cytosol for degradation (Tanaka *et al.*, 2010; Xu *et al.*, 2011).

The degradation of mutant SOD1 (Superoxide Dismutase 1) by OMMAD serves as an example of the importance of this process in maintaining mitochondrial integrity. MITOL, an OMM-localised E3 ubiquitin ligase ubiquitinates mutant SOD1 causing it to be degraded (Yonashiro *et al.*, 2009). Whilst SOD1 is an antioxidant, mutant SOD1 (mSOD1) is a misfolded protein that localises to mitochondria, impairing their function; this process is involved in the pathogenesis of ALS (Amyotrophic Lateral Sclerosis). MITOL overexpression increases mSOD1 degradation, thereby decreasing its accumulation on mitochondria, and decreasing mSOD1 induced ROS generation. MITOL depletion on the other hand increases mitochondrial mSOD1 accumulation, leading to increased ROS generation and cell death (Yonashiro *et al.*, 2009).

MAD is also an important mediator of mitochondrial quality control by mitochondrial dynamics and mitophagy; it is by this mechanism that E3 ligases MITOL, Parkin and HUWE1 (HECT, UBA and WWE containing) regulate fusion/fission proteins Mfn1/2, hFis1 and Drp1 (Nakamura *et al.*, 2006; Yonashiro *et al.*, 2006; Park *et al.*, 2010)(Leboucher *et al.*, 2012, and that Parkin induces mitophagy (Chan *et al.*, 2011).

1.9.3 Mitochondrial Dynamics

Mitochondrial fission and fusion dynamics constitute a quality control mechanism that is instrumental in conserving mitochondrial integrity.

Inhibition of mitochondrial fission causes mitochondrial dysfunction, characterized by RC uncoupling and decreased ATP production, loss of mtDNA, increased ROS and protein oxidation, decreased mitochondrial membrane potential ($\Delta\Psi m$) and increased mitophagy (Parone *et al.*, 2008). The homozygous knockout of Drp1 in mice results in early embryonic lethality, and neuron specific Drp1 knockout causes developmental defects in the brain, abnormal mitochondrial morphology, and death 1 day postpartum (Wakabayashi *et al.*, 2009) Cells lacking mitochondrial fusion proteins Mfn1 and Mfn2 showed decreased oxygen consumption and respiration, and decreased $\Delta\Psi m$ (Chen *et al.*, 2005). Furthermore, null mutations in Mfn1 and Mfn2 are embryonic lethal (Chen *et*

al., 2003), whilst conditional Mfn1/2 mutants (in which Mfn1/2 are not expressed in skeletal muscle) display mtDNA depletion to the extent that at 2 months, mtDNA levels in conditional mutant mice were only 7% of wild-type levels (Chen *et al.*, 2010b).

Mitochondrial fusion allows the exchange of nuclear encoded mitochondrial proteins (including those involved in mtDNA maintenance) between mitochondrial units with different requirements (Kowald and Kirkwood, 2011), thereby sustaining mtDNA integrity (Sato *et al.*, 2006; Chen *et al.*, 2010b). Fusion also facilitates functional complementation by transfer of mtDNA transcripts in situations where mtDNA is heteroplasmic (Gilkerson *et al.*, 2008), allowing mitochondria to tolerate low levels of mtDNA mutations, and improving the overall quality of the mitochondrial population. Mitochondrial fission preserves mitochondrial function and mtDNA integrity by segregating damaged sections of mitochondria from the rest of the network, preventing further oxidative damage (Parone *et al.*, 2008). Furthermore, mitochondrial fission precedes and initiates mitophagy; by tracking individual mitochondria it was demonstrated that fusion triggers fission, and fission produces 'daughter' mitochondria with decreased $\Delta\psi m$, which are more likely to undergo mitophagy (Twig *et al.*, 2008).

1.9.4 Mitophagy

Mitochondrial autophagy, also known as mitophagy, is the process by which mitochondria are broken down by engulfment in autophagosomes, either to regulate the number of mitochondria within a cell, or to remove defective mitochondria. The ubiquitin-dependent PINK1/Parkin pathway for the clearance of dysfunctional and depolarised mitochondria has been extensively characterised (Section1.9.4.1), although it's physiological relevance is questioned, since most studies involve the use of mitochondrial uncoupler CCCP (Carbonyl Cyanide *m*-chlorophenyl hydrozone) which completely collapses $\Delta\psi m$. It is not known whether PINK1 and Parkin function during the clearance of mitochondria in physiologically-relevant situations (Campello *et al.*, 2014). Programmed mitophagy, which occurs in situations such as red blood cell development, occurs via an alternative mechanism involving Nix, a Bcl-2 related OMM protein with an LC3 binding motif (Novak and Dikic, 2011), which acts as an autophagosome receptor. It has been suggested that Nix may also function in alternative situations, such as mitochondrial depolarisation and in hypoxia, in concert with the novel protein FUNDC1 (Campello *et al.*, 2014). Interestingly, autophagy initiation protein AMBRA1 (Activating molecule in beclin-1 regulated autophagy) localizes to mitochondria (Strappazzon *et al.*, 2011), and may initiate mitophagy in association with

the E3 ligase TRAF6 via a positive-regulation cycle involving K63-linked ubiquitination (Nazio *et al.*, 2013). Furthermore, AMBRA1 associates with Parkin, and is crucial for mitochondrial clearance (van Humbeeck *et al.*, 2011). AMBRA1 also associates with the CUL4-DDB (Cullin 4 DNA binding protein) E3 ubiquitin ligase (Behrends *et al.*, 2010). Therefore, it is tempting to speculate that AMBRA1 may initiate mitophagy by the recruitment of autophagic machinery, by associating with E3 ubiquitin ligases that are capable of ubiquitinating OMM proteins.

1.9.4.1 The PINK1/Parkin-dependent pathway

In healthy mitochondria, mitochondrial IMM protease PARL (Presenilin-associated rhomboid like protein) cleaves full length PINK1, and a truncated version is imported into the mitochondria. However, upon mitochondrial depolarisation by CCCP, full length PINK1 accumulates on the OMM (Jin *et al.*, 2010; Matsuda *et al.*, 2010; Vives-Bauza *et al.*, 2010), and this is both necessary and sufficient for the translocation of Parkin to the OMM (Narendra *et al.*, 2010). Parkin was originally identified as a cause of autosomal recessive juvenile Parkinson's Disease (Kitada *et al.*, 1998), and it was later shown that Parkin is an E3 ubiquitin ligase (Shimura 2000). Upon translocation to the OMM, Parkin promotes mitophagy by inducing a pro-fission state (Yu *et al.*, 2011), inhibiting mitochondrial motility (Wang *et al.*, 2011c) and finally recruiting autophagosomes (Narendra *et al.*, 2008). Ubiquitination is necessary for PINK1/Parkin dependent mitophagy. A strong ubiquitination signal is observed upon Parkin translocation to mitochondria (Matsuda *et al.*, 2010; Sarraf *et al.*, 2013), resulting in the degradation of OMM proteins (Chan *et al.*, 2011). Parkin mutants that do not have ubiquitin ligase activity fail to induce mitophagy of CCCP induced depolarisation (Lee et al., 2010), and inhibition of the 26S proteasome also prevents mitophagy (Chan *et al.*, 2011). Mitochondrial ubiquitination is necessary for the recruitment of HDAC6 and p62/SQSTM1 to mitochondria; p62 is an adaptor for LC3, a key component of the autophagic machinery, whilst HDAC6 indirectly promotes autophagosome-lysosome fusion (Lee et al., 2010). It has been demonstrated that recruitment of HDAC6 and p62 is necessary for mitophagy (Geisler *et al.*, 2010; Lee *et al.*, 2010). Interestingly, it has recently been shown that the deubiquitinase enzyme USP30 antagonises Parkin-induced mitophagy, by removing ubiquitin from OMM proteins, thus inhibiting mitophagy (Bingol *et al.*, 2014).

1.9.5 Mitochondrial Biogenesis

Mitochondrial biogenesis can be upregulated by a number of stimuli, including endurance exercise, and the associated increase in intracellular calcium levels (Holloszy and Booth, 1976), reactive oxygen species (Yoboue *et al.*, 2014), and nitrous oxide (Nisoli *et al.*, 2003). There are, therefore, multiple mechanisms by which the master regulator of mitochondrial biogenesis, peroxisome proliferator-activated receptor ɣ-co-activator 1α (PGC-1α), is expressed or activated, including by CREB-mediated transcription (Wu *et al.*, 2006), phosphorylation (Wright *et al.*, 2007), and deacetylation (Lerin *et al.*, 2006). Mitochondrial biogenesis requires the coordinated expression of mitochondrial genes encoded by both nuclear and mitochondrial DNA, and this is orchestrated by PGC-1α, a transcriptional co-activator which binds to and activates nuclear transcription factors, such as NRF1 and 2 (Nuclear Respiratory Factors 1 and 2) (Scarpulla, 2002). This stimulates the expression of nuclear-encoded mitochondrial genes, including those that are required for the replication and transcription of mtDNA, such as TFAM (Scarpulla, 2002).

It is known that the rate of mitochondrial biogenesis decreases with aging, further contributing to the decline in mitochondrial function with age (López-Lluch *et al.*, 2008). Interestingly, mitochondrial biogenesis is often upregulated in mitochondrial disorders as a compensatory mechanism, giving rise to the ‘ragged red fibres’, which are characteristic of muscle sections from patients with mitochondrial disorders (DiMauro and Schon, 2003).

(Lerin *et al.*, 2006)

1.10 Ageing

Ageing can be seen as the progressive decline of multiple biological functions, causing increased vulnerability to disease and death, and it is generally accepted that it is a complex multifactorial process. Some of the key features of ageing are the decline of the ubiquitin proteasome system and accumulation of damaged and aggregated proteins, mitochondrial dysfunction, oxidative stress and associated oxidative damage, and DNA damage and telomere shortening, all of which are intrinsically linked to the other. For the purposes of this introduction, I will focus on the roles that mitochondrial dysfunction and the decline of the ubiquitin proteasome system play in ageing, since this thesis attempts to define whether these two features of ageing and neurodegeneration are mechanistically linked.

1.10.1 Mitochondrial Dysfunction in Ageing

One of the early ageing theories, known as the 'Rate of Living Hypothesis', stated that longevity is inversely proportional to the rate of energy expenditure during life (Pearl, 1928). Once it was demonstrated that respiration, and therefore 'energy expenditure' entails the generation of reactive oxygen species, Harman theorised that ageing is caused by the deleterious effects of these free radicals on cells and tissues; the 'Free Radical Theory of Ageing' (Harman, 1956). This theory was later updated to the 'Mitochondrial Theory of Ageing' (Harman, 1972), since mitochondria are the primary site of ROS generation. The 'Vicious Cycle hypothesis' (Fleming *et al.*, 1982; Wei, 1998) built on this theory and has been one of the most prominent theories of ageing (Wei *et al.*, 2001), although is now widely discredited since the link between mitochondrial dysfunction and ROS production has been questioned. The vicious cycle hypothesis proposes that mtDNA accumulates mutations due to its proximity to the site of ROS generation, and thus a vicious cycle ensues whereby mtDNA mutations compromise the respiratory chain, increasing the rate at which it generates ROS and accelerating further damage to mtDNA (Mandavilli *et al.*, 2002). However, manipulations of ROS levels (by altering the function of antioxidants) did not affect the lifespan of Drosophila flies and mice (Huang, 2000; Van Remmen *et al.*, 2003; Miwa *et al.*, 2004; Van Remmen *et al.*, 2004) as would be predicted by the vicious cycle hypothesis. Furthermore, the assumption that increased mitochondrial respiration will increase ROS production was shown to be unfounded; when the rate of mitochondrial respiration increases, the rate of ROS production usually decreases (Kushnareva *et al.*,

2002), and there is little experimental support for the tenet that mitochondrial dysfunction increases ROS generation (Trifunovic and Larsson, 2008).

More recent studies favour the theory that somatic mtDNA mutations occur earlier in life, and increase in prevalence by clonal expansion until they cause mitochondrial dysfunction and lead to a mosaic pattern of respiratory chain deficiency, resulting in a bioenergetic deficiency at the level of the tissue or organ.

It is known that mtDNA acquires damage such as deletions and point mutations, with age (Krishnan *et al.*, 2007), and that levels of mtDNA deletions increase linearly with age (Bender *et al.*, 2006). As discussed earlier (Section 1.7.2), pathogenic forms of mtDNA must exceed a certain threshold level in order to cause respiratory chain deficiency (Moraes *et al.*, 1992; Sciacco *et al.*, 1994); single copies of mutated mtDNA will have very little effect on the overall function of a cell, due to the very high copy number of mtDNA present in most cell types. Mutated forms of mtDNA that originate from childhood or early adult years increase in frequency with age by the process of clonal expansion; one theory is that this occurs by random intracellular drift (Elson *et al.*, 2001). Interestingly, it has been hypothesised that mitochondrial fission and fusion dynamics may allow clonal expansion of mtDNA mutations to take place (Kowald and Kirkwood, 2011). In mitotic tissues, heteroplasmic mtDNA mutations are randomly distributed amongst daughter cells during cell division, this can lead to some daughter cells which have higher levels of mutated mtDNA than others (Trifunovic and Larsson, 2008). This, in addition to the clonal expansion of mutated mtDNA can lead to the mosaic pattern of respiratory deficiency that is often observed in ageing tissues, such as muscle, colon, heart and brain (Larsson, 2010). The link between mtDNA deletions, respiratory chain deficiency and ageing was demonstrated by a mouse model (the *PolgA* mtDNA-mutator mouse) which accumulates mtDNA mutations and deletions due to defects in mtDNA replication and repair, and displays a premature ageing phenotype (Trifunovic *et al.*, 2004).

Along with respiratory chain deficiency, there are further changes that occur in mitochondria with age; in general, electron microscope studies of mitochondria in ageing tissues demonstrate that mitochondria are fewer and generally larger, sometimes extremely large. Mitochondria in aged tissues have decreased ultrastructural organisation, for example a decrease in the number of cristae (Miquel *et al.*, 1980;

Beregi *et al.*, 1988) Ageing mitochondria have decreased membrane potential, produce less ATP and therefore produce more ROS (Ozawa, 1997; Kushnareva *et al.*, 2002)

The recent progress of research into mitochondrial dynamics has opened up the intriguing possibility that the dysregulation of mitochondrial fission and fusion dynamics with age may be involved in the accumulation of dysfunctional mitochondria (Seo *et al.*, 2010). This is supported by the important roles that mitochondrial dynamics play in mitochondrial quality control and mitophagy (section 1.9) and in apoptosis (section 1.5.3). RNA interference of the mitochondrial fission protein hFis1 has been shown to cause mitochondrial elongation, decreased $\Delta\psi m$, increased ROS, and to induce a senescence associated phenotype (Lee *et al.*, 2007). Furthermore, a recent study in which Parkin was upregulated in Drosophila flies demonstrated a decrease in levels of *Drosophila* mitofusin (*d*Mfn) (which normally increases in abundance with age), and increased mitochondrial fragmentation and activity. This was associated with an increase in both mean and maximum lifespan in Parkin overexpressing *Drosophila* flies. These studies indicate that mitochondrial quality control through fission and fusion dynamics may be important factors in the process of ageing and the accumulation of dysfunctional mitochondria. It is also tempting to speculate that mitochondrial fission and fusion (or perhaps their dysregulation) could explain the accumulation of mtDNA mutations by the clonal expansion, as hypothesised by (Kowald and Kirkwood, 2011). However, further experimental evidence is required before a conclusion can be made as to the role of mitochondrial dynamics in ageing.

1.10.2 The Ubiquitin Proteasome System in Ageing

It is generally accepted that damaged and oxidized proteins accumulate with age (Petropoulos *et al.*, 2000b; Löw, 2011) and the age-related accumulation of ubiquitinated proteins has also been demonstrated in *Drosophila* flies (Tonoki *et al.*, 2009), in rat heart (Bulteau *et al.*, 2002) and mouse brain (Gray *et al.*, 2003). It is thought that the decreased turnover of proteins with age is not only caused by increased levels of oxidative stress and protein damage, but also by a decrease in the activity of the 20S and 26S proteasomes.

An age –related decrease in the activity of the 20S proteasome has been demonstrated in a variety of model systems and tissues, invariably by monitoring the breakdown of fluorogenic peptide substrates which are specific for the three activities of the proteasome (Dahlmann, 2007). In humans, proteasome activities have been shown to

decline with age in the lens (Viteri *et al.*, 2004), lymphocytes (Carrard *et al.*, 2002), epidermis (Bulteau *et al.*, 2000; Petropoulos *et al.*, 2000a) and dermis (Jung *et al.*, 2007). Studies examining proteasome activity in the brain of several species have had equivocal results, however all but one study (Abd El Mohsen *et al.*, 2005) report a general decrease in the activities of the 20S and/or 26S proteasome, but to varying degrees in different areas of the brain (Zeng *et al.*, 2005; Gavilán *et al.*, 2012).

1.10.2.1 Mechanisms of age-related proteasome impairment

There are several mechanisms that could cause the age-related decline in function of both the 20S and 26S proteasomes: the decreased expression of proteasome subunits with age, impaired assembly of the proteasome from its subunits, inhibition of the proteasome by damaged proteins, or a rate-limiting decline in the availability of ATP.

In human epidermal cells, the decline in the chymotrypsin-like and PGPH-like activities of the 20S proteasome is accompanied by a decrease in overall proteasome content (Petropoulos *et al.*, 2000a). However in studies that determine specific proteasome activity by purifying the 20S proteasome, decreases in PGPH, chymotrypsin-like and trypsin-like (Orenstein and Cuervo, 2010) activity are still detected, demonstrating intrinsic changes to the 20S proteasome with age, independent of its level of expression (Wagner and Margolis, 1995; Conconi *et al.*, 1996; Bulteau *et al.*, 2000; Bulteau *et al.*, 2002).

Furthermore, an age-related decline in the chymotrypsin-like activity of the 26S proteasome has also been observed in human lymphocytes, accompanied by increased post-translational modifications (glycation, conjugation with 4-hydroxy-2-nonenal, and ubiquitination). Strikingly, the vast majority of post-translational modifications were observed on the 20S α and β subunits, rather than the 19S regulatory particle, and the abundance of these modifications, indicative of damage, increased with age (Carrard *et al.*, 2002). It was later shown that the decline in the activity of the 26S proteasome is associated with an interruption of its assembly from 20S and 19S proteasome subunits (Chondrogianni *et al.*, 2003; Tonoki *et al.*, 2009), therefore the decline in function of both the 20S and 26S proteasomes may be caused by decreased expression of proteasome subunits or by impaired assembly of the proteasome from its subunits.

Another mechanism by which the activity of the proteasome may decline with age is by the action of ‘inhibitory damaged proteins’, or protein aggregates. Cross-linked protein aggregates, for example HNE-cross linked protein, are resistant to proteolysis and

furthermore, are able to non-competitively inhibit the proteasome (Friguet and Szweda, 1997). Proteasome activity drastically declines in cells that are fed with lipofuscin, the protein material that accumulates in ageing (Sitte *et al.*, 2000), and mutated, aggregation-prone proteins are able to cause a similar decline in proteasome activity and cause ubiquitinated proteins to accumulate (Bence *et al.*, 2001). Strikingly, by breaking up protein aggregates in a yeast model system, not only did the level of protein inclusions decline, the activity of the 26S proteasome also increased (Andersson *et al.*, 2013). These studies demonstrate the vulnerability of the proteasome to damaged, oxidised or aggregation-prone proteins.

Finally, since ATP is required for the activation of ubiquitin (Bacik *et al.*, 2010), for the assembly of the 26S proteasome (Kim *et al.*, 2013), and for the recognition of the polyubiquitin signal and subsequent unfolding and translocation of the substrate proteins (Lam *et al.*, 2002), it is thought that proteasome impairment may be caused indirectly by mitochondrial dysfunction and the resulting lack of ATP availability (Martins-Branco *et al.*, 2012).

1.10.2.2 UPS Function is linked to Longevity

It is widely accepted that the decline of the ubiquitin proteasome system is a contributory factor in ageing (Kevei and Hoppe, 2014) and in the development of age-related neurodegenerative disorders, and it is thought that proteasomal function is tightly linked to lifespan.

Enhanced proteasome activity has been associated with increased lifespan in several ways; naked mole rats have an extremely long lifespan and have very high levels of proteasomes and considerably increased proteasome activity compared to mice (Rodriguez *et al.*, 2012). Furthermore, proteasomes isolated from fibroblasts of centenarians have functional proteasomes, and their activity is more comparable to that of younger controls, rather than elderly controls. It has also been demonstrated that activation of the 26S proteasome can increase replicative lifespan in yeast (Kruegel *et al.*, 2011). Knockdown of 19S subunit *rpn11* reduces 26S proteasome levels, enhances the age-related accumulation of ubiquitin conjugates and shortens the lifespan of *Drosophila,* whilst the overexpression of *rpn11* prevents the age-related accumulation of ubiquitin conjugates with age and increases the lifespan of Drosophila (Tonoki et al., 2009).

1.11 Neurodegeneration

The most robust risk factor for the development of neurodegenerative diseases is ageing, and therefore it is perhaps not surprising that the mechanistic features involved in neurodegeneration are very similar to that of ageing. Whilst it is clear that there are many types of neurodegenerative disease involving different neuronal subgroups and with varying phenotypes, it is striking that many of them share the same pathophysiological features, namely proteasomal dysfunction and protein aggregation, mitochondrial dysfunction, oxidative stress, disruption of axonal transport, neurotrophin dysfunction and neuroinflammatory processes. For the purposes of this thesis, I will concentrate on the roles of the ubiquitin proteasome system and mitochondrial dysfunction in neurodegeneration, and in particular in Parkinson's disease and Alzheimer's disease.

1.11.1 Mitochondrial Dysfunction in Neurodegeneration

The role of mitochondria in neurodegeneration has become increasingly recognized in recent years, and has been recently reviewed (Schon and Przedborski, 2011). Neurodegenerative diseases such as Alzheimer's and Parkinson's diseases are comprehensively different from primary mitochondrial diseases (e.g. MELAS, MERRF), due to their late onset and multifactorial nature. Bioenergetic deficiency may still play a role in common neurodegenerative disorders, although generally as a consequence rather than a cause. For example, it is well known that complex I defects are associated with Parkinsonism and Parkinson's disease (PD); this association was first made when heroin contaminated with the complex I inhibitor MPTP induced parkinsonism in humans (Opeskin and Anderson, 1997). In sporadic PD, Complex I deficient neurons are present in the substantia nigra (Schapira *et al.*, 1990), accompanied by high levels of mtDNA mutations (Bender *et al.*, 2006).

The identification of a number of PD-related genes that locate to or interact with mitochondria (for example PINK1, Parkin, α-synuclein, LRRK2 (Leucine-rich repeat kinase 2) and DJ-1) further illustrate the importance of mitochondrial dysfunction in PD, and indicate that disrupted mitochondrial dynamics and quality control are key to PD pathogenesis (Santos and Cardoso, 2012). Several studies have demonstrated that mitochondrial fragmentation occurs upon Complex I inhibition with a variety of toxins (Santos and Cardoso, 2012), however the strongest evidence for mitochondrial dynamics dysregulation in PD arises from PD-associated genes. LRRK2 and DJ-1 are both associated with mitochondrial fragmentation (Irrcher *et al.*, 2010; Thomas *et al.*,

2011; Wang *et al.*, 2012). PINK1 and Parkin, notably, are part of a pathway that regulates mitochondrial morphology (inducing a pro-fission state) (Yu *et al.*, 2011), and also act together to bring about mitophagy, as has been discussed previously in this introduction (section 1.9.4.1). For a more detailed discussion on the regulation of mitochondrial fission and fusion by Parkin, see the introduction to chapter 3. Therefore, advances in the genetics of Parkinson's disease indicate that the dysregulation of mitochondrial dynamics are part of the pathogenesis of Parkinson's disease.

It is also increasingly accepted that mitochondria play an important role in Alzheimer's disease, especially late-onset forms of the disease. The 'mitochondrial cascade hypothesis' places mitochondria at the centre of the AD pathological cascade, which, though controversial, highlights the importance of mitochondrial dysfunction to this disease (Swerdlow *et al.*, 2014). Early indicators of mitochondrial dysfunction in AD included altered mitochondrial morphology and COX deficiency in the brain (Parker Jr *et al.*, 1990; Kish *et al.*, 1992). The mitochondrial cascade hypothesis states that a person's nuclear and mitochondrial genes determine the baseline function and durability of their mitochondria, and the rate of decline of mitochondrial function (driven by both genetics and environmental changes) determines the onset of Alzheimer's disease. Support for this hypothesis includes data that indicates that COX inhibition increases production of the pathogenic amyloid β42 peptide, perhaps mediated by oxidative stress (Gabuzda *et al.*, 1994; Gasparini *et al.*, 1997), although it has also been shown that amyloid β (Aβ) reduces COX activity (Pereira *et al.*, 1998; Canevari *et al.*, 1999); the causality of this relationship is controversial (Swerdlow *et al.*, 2010). There is also evidence for the involvement of mitochondrial dynamics dysregulation in AD (Su *et al.*, 2010). For example mitochondrial dynamics are significantly altered in AD patient fibroblasts (Wang *et al.*, 2008) and $A\beta_{25-35}$ aggregates disrupt mitochondrial axonal transport in primary hippocampal neurons (Rui *et al.*, 2006). Furthermore, the expression of mitochondrial fusion proteins is reduced in the hippocampus of Alzheimer's cases compared to controls (Wang *et al.*, 2009), and the abnormal distribution of mitochondria in pyramidal neurons (Wang *et al.*, 2009) and synaptic vulnerability in AD is consistent with disruptions to mitochondrial transport and dynamics.

1.11.2 The Ubiquitin Proteasome System in Neurodegeneration

As I have previously described, it is widely accepted that the ubiquitin proteasome system declines with age (Section 1.10.2) and as such, is also one of the primary

mechanisms involved in age-related neurodegenerative disorders. The main indicator of the malfunction of the ubiquitin proteasome system in most adult-onset neurodegenerative diseases is the presence of intracellular or extracellular protein aggregates of various forms, furthermore, the enrichment of ubiquitin in these inclusions is a clinical diagnostic feature of these diseases (Tanaka and Matsuda, 2014). Extracellular and intracellular amyloid beta (Aβ) plaques are the hallmark of Alzheimer's disease, whilst Lewy bodies containing α-synuclein are found in neurons of patients with Parkinson's disease. The accumulation of these proteins as aggregates or oligomers may disrupt neuronal function, eventually leading to neurodegenerative disease.

In Parkinson's disease, the evidence for the involvement of the UPS is comprehensive (reviewed here: (Cook and Petrucelli, 2009)); however it is not clear whether UPS dysfunction is a cause or consequence of the disease. Several studies have demonstrated that proteasomal activity is decreased in the brain of PD patients (McNaught and Jenner, 2001; Furukawa *et al.*, 2002; McNaught *et al.*, 2003), and ubiquitinated proteins as well as components of the UPS (including proteasomes, UCHL1 and Parkin) accumulate within Lewy Bodies (Lennox *et al.*, 1989; Lowe *et al.*, 1990; Ii *et al.*, 1997; Schlossmacher *et al.*, 2002). Interestingly, mice administered with the complex I inhibitor MPTP develop a PD like phenotype, along with α-synuclein and ubiquitin-positive inclusions, and decreased proteasome activity (Fornai *et al.*, 2005), indicating that ubiquitin proteasome dysfunction in PD may be potentiated by mitochondrial dysfunction. Further indications of the involvement of the UPS in PD are given by the functions of the proteins encoded by the genes related to familial PD. α-synuclein (*SNCA*) is a natively unfolded presynaptic protein, whose function has not been fully characterized, but is thought to aggregate and thus impair proteasomal function (Cook and Petrucelli, 2009). Parkin (*PARK 2*) was originally identified as a cause of autosomal recessive juvenile Parkinson's Disease (Kitada *et al.*, 1998), and it was later shown that Parkin is an E3 ubiquitin ligase (Shimura 2000). As described in detail earlier, it associates with Parkinson's associated protein PINK1 (*PARK6*) to regulate mitochondrial dynamics and mitophagy via ubiquitination (section 1.9.4.1). As described earlier, the deubiquitinase enzyme UCHL1 (*PARK5*), has also been linked to Parkinson's disease (section 1.2.2.1).

Similarly, there is substantial evidence for the involvement of the UPS in Alzheimer's disease; one of the primary hypotheses for AD is the amyloid β cascade hypothesis. The

initial association between the UPS and Alzheimer's disease was made when the tau proteins that make up neurofibrillary tangles (NFTs) were found to be ubiquitinated (Mori *et al.*, 1987), indicating the failure of the ubiquitin proteasome to remove NFTs. Furthermore, Paired helical filaments (composed of ubiquitinated tau) may inhibit the proteasome; proteasomes are less efficient in brain regions where NFTs form abundantly than in unaffected areas (Keller *et al.*, 2000). Furthermore, a mutant form of ubiquitin (UBB^{+1}), which becomes polyubiquitinated and inhibits proteasome activity (Lam *et al.*, 2000) is also found in AD brains. In addition to this, UCHL1 is associated with Alzheimer's disease, since oxidatively modified forms of UCHL1 are found in the AD brain, and levels of soluble UCHL1 are inversely proportional to the number of NFTs (Choi *et al.*, 2004). Interestingly, one study found that UCHL1 expression can reverse synaptic dysfunction and memory loss that occurs in mice overexpressing APP and Presenilin 1 (PS1) (Gong *et al.*, 2006). It has also been observed that pathogenic soluble Aβ oligomers inhibit the proteasome, thus promoting further accumulation of Aβ and tau (Tseng *et al.*, 2008). Therefore, it is widely accepted that the UPS is involved in the pathogenesis of AD; however it is unknown whether UPS dysfunction is causative or secondary to other factors.

1.12 Aims of this thesis

The aim of this thesis is to examine the interactions between the ubiquitin proteasome system and mitochondria, particularly in relation to mitochondria. My initial aim was to investigate the hypothesis outlined in Figure 1.7, and this is done both *in vitro*, by using UCHL1 inhibitors, and *in vivo*, by assessing levels of mitochondrial respiratory chain complexes immunohistochemically in UCHL1 knockout mice. The reasoning behind this hypothesis is explained in the introduction to chapter 3.

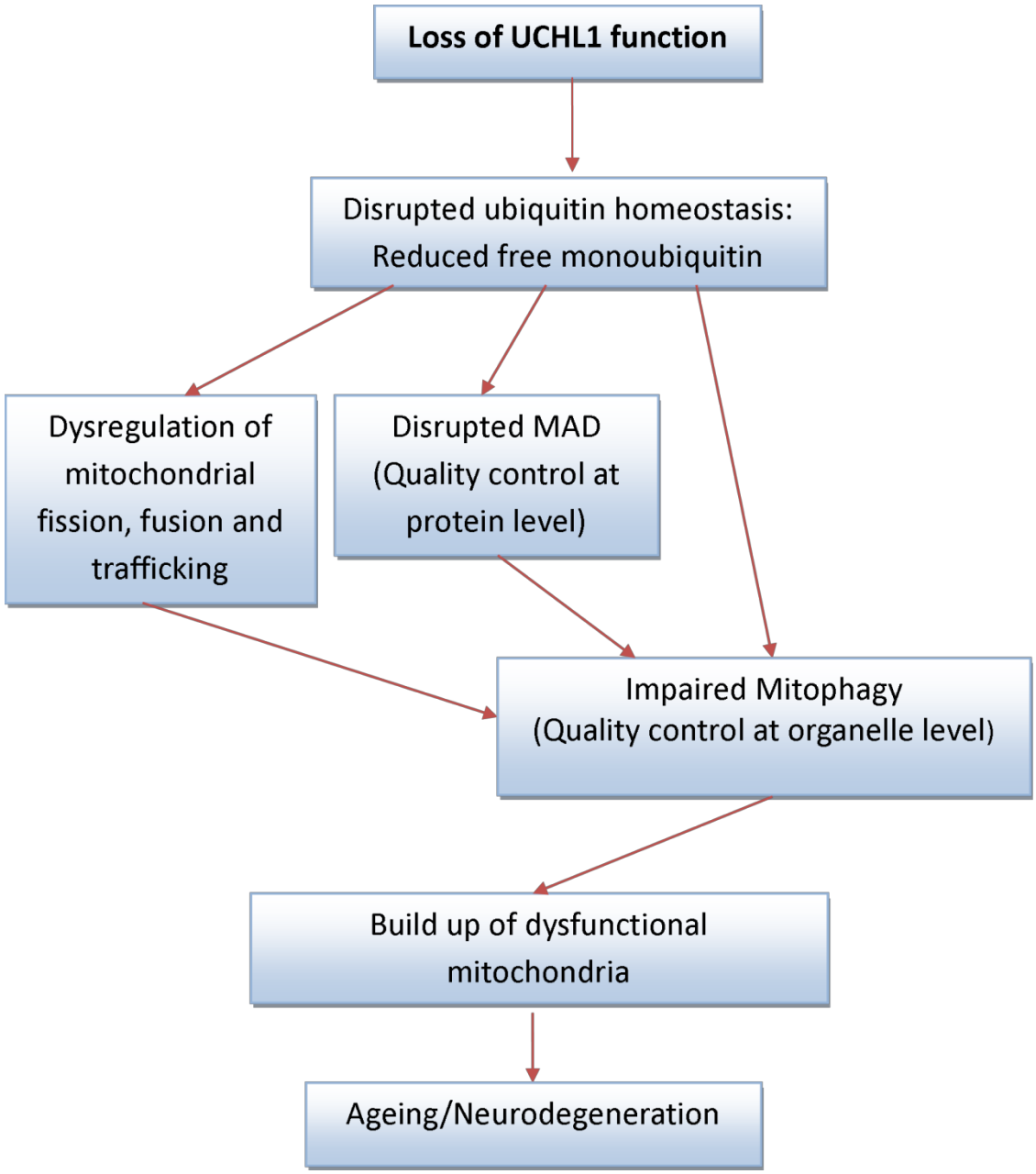

Figure 1.7: Hypothesis Model.
'Ubiquitin depletion caused by UCHL1 inhibition or knockout will disrupt mitochondrial trafficking, fission and fusion and cause the accumulation of dysfunctional mitochondria' MAD=Mitochondria Associated Degradation

In addition to this, I aimed to characterize the phenotype and neuropathology of UCHL1 mice, and assess the suitability of these mice as a model of the decline of the UPS with age. I then aim to further understand how the loss of UCHL1 function causes neuropathological changes and the formation of axonal spheroids. My final aim was to examine whether mitochondrial dysfunction causes UPS dysfunction in the context of mitochondrial disease.

Chapter 2.

Materials and Methods

Chapter 2. **Materials and Methods**

2.1 Reagents and Materials

2.1.1 Materials: Equipment and Consumables

2.1.1.1 Equipment

2100 retriever	Aptum Biologics
Adventurer OHAUS Balance	Jencons-PLS
Autoclave	Astell
Bench-top Centrifuge 5417 R	Eppendorf
Bench-top Centrifuge 5418	Eppendorf
C1000 Thermal Cycle PCR Machine	Bio-Rad
ChemiDoc MP Imaging System	Bio-Rad
ELx895 absorbance microplate reader	BioTEK
Fluorimeter: PolarStar Omega	BMG Labtech
Heraus Incubator	Thermo Scientific
Laminar Flow Hood	Jencons PLS
MenaPath Access Retrieval Unit	A Menarini Diagnostics
Microflow Biological Safety Cabinet	Bioquell
Microtome	MICROM
Mini Protean Tetra Cell and Blotting Module	BioRad
MP-250V Power supply	Cleaver Scientific
Neubauer Improved Haemocytometer	Millipore
Pipetman Classics: P10, P20, P200, P1000, P5000	Gilson
pH Meter (3510)	Jenway
Polytron P1600 E Bench-top Homogeniser	Kinematica
Sonics Vibra-CellTM Ultrasonic Processor	Sonics®
Sprout® Mini-Centrifuge 220/230 Vac	Heathrow Scientific
Vortex Genie	Scientific Industries
WS-6 Downflow Workstation	Labcaire
Zeiss Cell Observer Spinning Disk (Live Cell Imaging)	Zeiss
Confocal Scanning Unit – X1	Yokogawa
Quant EM:512SC camera	Photometrics

x100 Plan apochromat oil objective, NA=1.4	Zeiss
Axiovision	Zeiss
Nikon TIRF / Spinning Disk (TIRF live cell study)	Nikon
Evolve 512 EM CCD camera	Photometrics
60X CFI Apochromat TIRF oil objective, NA=1.49	Nikon
Argon 457-514 65mW laser	CVI Melles Griot
NIS-Elements	Nikon
Nikon A1R Confocal	Nikon
Nikon A1R Confocal Imaging System	Nikon
60x Plan Apochromat VC oil objective, NA=1.4	Nikon
405nm 100mW laser; 561nm 20mW laser	Coherent
Argon 457-514 nm 65mW, 647nm 50mW laser	CVI Melles Griot
NIS-Elements	Nikon
Olympus BX51 light microscope	
MAC 6000 Modular Automation Controller System	Ludl Electronic Products
Picture Frame Software	Optronics
Stereo Investigator Software	MBS Bioscience
Image Analysis Software	
Image J	NIH
Volocity 6.0	Perkin Elmer
IMARIS 7.7	Bitplane

2.1.1.2 Consumables

1.5 ml Eppendorf tubes	Eppendorf
2 ml Eppendorf tubes	Eppendorf
10ml Syringe	BD Plastipak
18G needle. 1.2mm x 40mm	BD Plastipak
72 Superfrost® Plus Slides 25 x 75 x 1.0mm	VWR International
Cellview™ cell culture dish with glass bottom, 35mm	Advanced TC, Greiner Bio One
Cellstar® disposable pipettes: 5ml, 10ml	Greiner
Cellstar® Tissue Culture Flasks: T25, T75	Greiner
Colourcoat^{+} adhesion positively charged microscope slides 26 x 76mm, 1.0-1.2mm	Cell Path Ltd.
Coverglass 20 x 20mm, 20 x 40mm	VWR International
Falcon tubes: 15ml and 50ml	BD Biosciences
Flat-bottom 96 well plates	Greiner Bio One
Immobilon Transfer Membranes PVDF	Millipore
Millex-GP 0.22µm, polyethersulfore, 33mm sterile filter.	Merck Millipore™
Pasteur Pippettes	VWR International
Pippette Tips	Starlab
Whatman Grade1 Filter paper	Merck

2.1.2 Solutions and Reagents

2.1.2.1 Solutions

Buffers and solutions were prepared with nanopure (18 mega-ohms (Ω) measured activity) water.

0.1M Phosphate Buffered Saline, pH7.4 (filtered)	5.75g Disodium Hydrogen Phosphate Anhydrous 1.311g Sodium Dihydrogen Phosphate 1L dH_2O
10x Transfer Buffer	60g Trizma Base 288g Glycine 4g SDS 2L dH_2O
10x $CaCl_2$ Transfer Buffer	30g Trizma Base 144g Glycine 2.94g Calcium Chloride 1L dH_2O
4% Iron Alum	20g Ammonium Ferric Sulphate 500ml dH_2O
4% Paraformaldehyde , pH7.4	40g Paraformaldehyde 4ml 1N Sodium Hydroxide Make up to 1L with dH_2O
Acetate Buffer, pH4.5	13.5ml Acetic Acid 23.5g Sodium Acetate Make up to 2L with dH_2O
Coomassie Blue	135ml Methanol 135ml dH_2O 30ml Glacial Acetic Acid 0.75g Coomassie Dye

Coomassie de-staining solution	80ml Acetic Acid 400ml Ethanol 320ml dH_2O
Cresyl Fast Violet Staining Solution	50ml Cresyl Fast Violet stock solution 500ml Acetate Buffer 500ml dH_2O
Cresyl Fast Violet Stock Solution	0.2g Cresyl Fast Violet 100ml dH_2O
Eosin	10g Eosin ‘yellowish’ 250mg Erythrosin B 250mg Phloxine B
Haematoxylin	5g Haematoxylin 50ml Ethanol 450ml dH_2O 10ml Saturated Lithium Carbonate 1L dH_2O
HEPES Buffer, pH7.5	5.96g HEPES 746mg Potassium Chloride 508mg Magnesium Chloride 77mg Dithiothreitol 500ml dH_2O Add 10% glycerol
Ponceau Red	2% Ponceau S 30% Trichloroacetic Acid 30% Sulfosalicyclic Acid dH_2O

Running Buffer, pH8.8	15g Trizma Base 72g Glycine 5g SDS 1 litre dH_2O
Sample Buffer	10ml Stacking Buffer 4ml Glycerol 4ml 20% (w/v) SDS 0.02g Bromophenol Blue 2ml dH_2O
Scott's Tap Water	2g Sodium Bicarbonate 20g Magnesium Sulphate A few crystals of Thymol 1L dH_2O
Stacking Buffer, pH6.8	30.275 Trizma Base 500ml dH_2O
Sudan Black	0.3% Sudan Black 70% Ethanol dH_2O
Tris-HCl Lysis buffer, pH7.5	2.428g Trizma Base 1L dH_2O

2.1.2.2 Reagents

Acetic Acid	Sigma Aldrich
Ethanol, absolute	Fischer Scientific
Dimethyl Sulfoxide (DMSO)	Anala®
Methanol, absolute	Fischer Scientific
Phosphate Buffered Saline tablets (Dulbecco A)	OXOID Limited
Sodium Chloride	Sigma-Aldrich®
Trizma® Base	Sigma® Life Science
Tween® 20	Sigma-Aldrich®

2.1.2.2.1 Cell Culture & Live Cell Imaging

Calbiochem® UCHL1 inhibitor LDN-57444	Merck Chemicals Ltd.
Calbiochem® UCHL1 inhibitor LDN-91946	Merck Chemicals Ltd.
Cell Light Mitochondria RFP BacMam 2.0	Life Technologies™
Laminin	Sigma
PNGM Singlequot® Kit	Lonza Clonetics®
Poly-L lysine hydrobromide	Sigma
Poly-L-lysine solution	Sigma
PR-619 Ubiquitin, ubiquitin like isopeptidase and deubiquitinase inhibitor	Tebu-bio
Primary Neuron Basal Medium without L-Glutamine, 200mL	Lonza Clonetics®

2.1.2.2.2 PCR

Agarose, Molecular grade	Bioline
Extract-N-Amp™ Tissue PCR Kit	Sigma
Gel Loading Dye 6x	New England BioLabs
GelRed™ Nucleic Acid gel stain, 10,000x in water	Biotium
GeneRuler™ 1kb plus DNA ladder	New England BioLabs
Pgk Reverse Primer 2	Sigma
Quick Load® 1kb ladder	New England BioLabs
UCHL1 Reverse Primer 5' CTGGACCACCATCTGCTTAC	Sigma
UCHL1 Forward Primer	Sigma
Pgk Reverse Primer 2	Sigma

2.1.2.2.3 Mouse Dissection

Dolethal 200mg/ml solution (Pentobarbital Sodium)	Vétoquinol UK Limited
Sodium Hydroxide	Sigma-Aldrich®
Sodium Phosphate Dibasic	Sigma-Aldrich®
Sodium Phosphate monobasic monohydrate	Sigma-Aldrich®
Paraformaldehyde	Sigma-Aldrich®

2.1.2.2.4 Histology, Immunohistochemistry and Immunofluorescence

Acetic Acid	Sigma-Aldrich
Ammonium Ferric Sulphate	BDH
Avidin/Biotin Blocking Kit	Vector Laboratories, Inc.
Catalase (from bovine liver) 2000-5000 units/mg protein	Sigma®
Cresyl Violet	Sigma®
Cytochrome C	Sigma®
Diaminobenzidine (DAB)	Sigma®
DPX Mounting Medium	Cell Path Ltd.
EDTA Tetrasodium Salt, Dihydrate, Ultrapure	USB Corporation, Cleveland
Eosin Yellowish – Acid Red 87	Raymond A. Lamb

Erythrosin B	Raymond A. Lamb
EDTA dipotassium salt	BDH
Haematoxylin	Raymond A. Lamb Ltd.
Histoclear™	National Diagnostics
Hoechst 33342, Trihydrochloride, Trihydrate	Life Technologies™
HRP Polymer	CellPath
Hydrogen Peroxide, 30% w/w.	Sigma® Life Science
Lithium Carbonate	BDH
M.O.M™ Kit	Vector Laboratories, Inc.
Magnesium Sulphate, anhydrous.	Sigma-Aldrich®
Nitro Blue Tetrazolium (NBT)	Sigma®
Normal Goat's Serum (NGS)	Sigma-Aldrich®
Paraformaldehyde Solution, 4% in PBS	Santa Cruz Biotechnology inc.
Phenazine Methosulphate (PMS)	Sigma®
Phloxine B	Raymond A. Lamb
ProLong® Gold Antifade Reagent 5 x 2mL	Life Technologies™
SIGMAFAST™ 3,3' – Diaminobenzidine tablets	Sigma® Life Science
Sodium Acetate Anhydrous	BDH
Sodium Azide	Sigma®
Sodium Bicarbonate	Sigma®
Sodium Succinate	Sigma®
Sudan Black B	Reactifs RAL
Thymol, min. 99.5%	Sigma-Aldrich®
Universal Probe	CellPath
Vectastain® ABC Kit Elite® Standard	Vector Laboratories, Inc.

Primary Antibodies	
Anti Myelin-Basic Protein (SMI-94)	MitoSciences® Abcam®
Anti-Neurofilament H (Rabbit Polyclonal)	Millipore™
COX IV	MitoSciences® Abcam®
GRIM19 (Complex I-19)	MitoSciences® Abcam®
MBP-4	Dako
Monoclonal Mouse Anti-Synaptophysin	Dako
Mouse Anti-Alzheimer precursor protein A4 (APP) monoclonal antibody	Millipore™

MT-CO1 (Complex IV-I)	MitoSciences® Abcam®
NDUFB8 (Complex I-20kDa)	MitoSciences® Abcam®
NDUFS3 (Complex I-30kDa)	MitoSciences® Abcam®
Neurofilament H Non-Phosphorylated (SMI-32) Monoclonal Antibody, Purified	Covance
Neurofilaments, Phosphorylated (SMI-31) Monoclonal Antibody	Covance
SDHA (Complex II-70kDa)	MitoSciences® Abcam®

Secondary Antibodies and Fluorophores	
Alexa Fluor® 488 Goat Anti-Mouse IgG2a	Life Technologies™
Alexa Fluor® 647 Goat Anti-Rabbit IgG (H+L)	Life Technologies™
Alexa Fluor® 647 Streptavidin	Life Technologies™
Biotin-SP-conjugated AffiniPure Goat Anti-Mouse IgG Fc Subclass 1	Jackson Immunoresearch laboratories
Biotin-SP-conjugated AffiniPure Goat Anti-Mouse IgG Fc Subclass 2a	Jackson Immunoresearch laboratories
Biotin-SP-conjugated AffiniPure Goat Anti-Mouse IgG Fc Subclass 2b	Jackson Immunoresearch laboratories
Biotinylated Anti-Rabbit IgG (H+L)	Vector Laboratories
Streptavidin, AlexaFluor® 488 conjugate	Life Technologies™
Streptavidin, Tetramethylrhodamine conjugate	Life Technologies™

2.1.2.2.5 Western Blotting

8-16% Mini – PROTEAN TGX Precast Gel	Bio-Rad UK
AmershamTM ECLTM Prime Western Blot Detection Reagent	GE Healthcare
Bio – Rad Protein Assay Dye Reagent Concentrate	Bio-Rad UK
Bromophenol Blue	Sigma-Aldrich
Calcium Chloride	Sigma-Aldrich
cOmplete ULTRA protease inhibitor tablets	Roche Applied Science
Coomassie Brilliant Blue	Fluka
DL- Dithiothreitol	Sigma-Aldrich
Glycerol anhydrous	Sigma®
Glycine	Sigma®
Immobilon®-P Transfer Membrane	Millipore
Ponceau S	Sigma-Aldrich
Purified Bovine Serum Albumin 100X (10mg/ml)	Life Technologies
Skimmed, powdered milk	Marvel
Sodium dodecyl sulphate	Sigma-Aldrich
Sulfosalicyclic acid	Sigma-Aldrich
Trichloroacetic acid	Sigma-Aldrich

Antibodies	
Anti-alpha tubulin [DM1A] antibody – Loading control	Abcam®
Anti-VDAC1/Porin	Abcam
Polyclonal Rabbit Anti-Mouse Immunoglobulins/HRP	Dako
Polyclonal Rabbit Anti-Ubiquitin	Dako
Polyclonal Swine Anti-Rabbit Immunoglobulins/HRP	Dako

2.1.2.2.6 Proteasome Activity Assay

Boc-Leu-Arg-Arg-AMC	Boston Biochem
HEPES	Sigma Aldrich
Lactacystin	Santa Cruz Biotech
MG132	Sigma Aldrich
Magnesium Chloride	Anala®
Potassium Chloride	Sigma
Suc-Leu-Leu-Val-Tyr-AMC	Calbiochem
Z-Leu-Leu-Glu-AMC	UBP Bio

2.2 Methods:

2.2.1 Primary Neuron Culture and Live Cell Imaging

2.2.1.1 Cell Culture:

Cellview™ quartered 35mm glass-bottom dishes were coated with Laminin and Poly-L-Lysine. Each well was incubated for 1 hour with 2µg/ml Laminin (Sigma®) and 30µg/ml Poly-L-Lysine (Sigma®), before rinsing in dH_2O and leaving to dry for 2 hours before use. Lonza Mouse Cortex Neuronal Cells stored in liquid nitrogen were thawed quickly in a 37^{o}c waterbath. Each vial contained approximately 4 million viable cells. Pre-warmed Primary Neuron Basal Medium (PNBM) (plus L-Glutamine, GA-1000 and 2% NSF-1) was then added to the cells drop-wise. On each occasion, the cell suspension was divided equally between 3 Cellview ™ 35mm cell culture dishes by pipette. Cell culture medium was changed 2 hours after initiating cell culture, after 7 days, and subsequently every 3 days. Cells were kept in an incubator at 37^{o}c, 5% CO_2 and 20% O_2 and at constant humidity.

UCHL1 hydrolase inhibitor LDN-91946 (Calbiochem®) was used at a concentration of 25µM (justified in Section 3.2.1.3), and added to cells by pipette 1 hour before the start of live cell imaging. DUB inhibitor PR-619 (Tebu-bio) was used at a concentration of 50µM, and added to cells 1 hour before image acquisition (See section 3.2.1.3). Primary neurons were incubated with UCHL1 ubiquitin binding inhibitor LDN-57444 (Calbiochem®) (See section 3.2.1.3) at 5µM for 12 hours before the start of image acquisition, since immediately after LDN-57444 is added to cells it causes mitochondrial dyes to become diffuse and blurry (Appendix 1), although staining intensity recovers over time. Previous studies using LDN-57444 confirm that it is still active 12 hours after addition to cells and causes transcriptional and morphological changes to neurons (Cartier *et al.*, 2009; Zhang *et al.*, 2012). In all cases DMSO was added to control wells in the same volume (ie. to a final concentration of 1 in 750 (0.1%) or 5 in 750 (0.7%)), and for the same amount of time as the inhibitor. CellLight™ reagent Mitochondria RFP BacMam 2.0 (Invitrogen™, Oregon, USA) was used as a mitochondrial marker; 5µl was added to each well at least 16 hours before imaging. To image LDN-57444 treated cells and controls, neurons were incubated with Mitotracker Green at 50nM, since LDN-57444 quenches MitoRFP fluorescence in an unknown manner (see Appendix 1).

2.2.1.2 Microscopy

Live cell imaging of LDN-91946 and PR-619–treated neurons and controls was carried out using a Zeiss Cell Observer spinning disc microscope at high magnification (100X Plan Apochromat oil objective, NA=1.4) and low laser intensity (5%), with a 561nm laser. Neurons were fully enclosed in a heated environmental chamber, maintained at 37^{o}c, 20% O_2, 5% CO_2. Z stacks consisting of 3 z-planes 0.260µm apart were taken at 3 second intervals for the 10 minute imaging duration.

Live cell imaging of neurons treated with LDN-57444 and corresponding controls was carried out using the Nikon TIRF (Total Internal Resonance Fluorescence) microscope, using the 60x oil objective with the perfect focus system. Neurons were maintained in an environmental chamber at constant humidity, temperature and O_2 and CO_2 conditions.

2.2.2 UCHL1 mouse genotyping

The generation of the UCHL1 mice studied in this thesis is described in detail by Doug Gray's group (Coulombe *et al.*, 2014). Briefly, a region of the fourth exon of the UCHL1 gene (cloned from a 129sv phage library), including the catalytic cysteine, was replaced by homologous recombination with a pgk-neo-pgk cassette. This vector was than transfected into ES cells by electroporation, and properly recombined clones were aggregated with CD-1 morulas. The original 129 line was then backcrossed with C57BL/6J mice for 10 generations to establish a line of UCHL1 knockout mice on the C57BL/6J background (Coulombe *et al.*, 2014).

Mice were genotyped, using Sigma® Extract-N-Amp TM Tissue PCR Kit to extract DNA from ear notches taken from each mouse. DNA was extracted by adding 100µl extraction solution and 25µl tissue preparation solution to each sample, and leaving at room temperature for 10 minutes before incubating at 95^{o}c for 3 minutes. 100µl neutralization solution was then added to each sample, and samples were stored at 4^{o}c for further use. The solution for PCR amplification was made up of 10µl Extract-N-Amp PCR reaction mix, 0.5µl of each primer (3 primers total) and 4.5µl PCR grade water per sample. 4µl of each sample was added to 16µl of pre-mixed PCR amplification solution. PCR was performed using a C1000 Thermal Cycle (BioRad) PCR machine, on the cycle outlined in Figure 2.1. A 1% agarose gel was poured, and each PCR product was loaded onto the gel, along with gel loading dye, with GeneRuler^{TM} 1kb plus DNA ladder at each end of the gel. Gels were run at 80V for 1-2 hours.

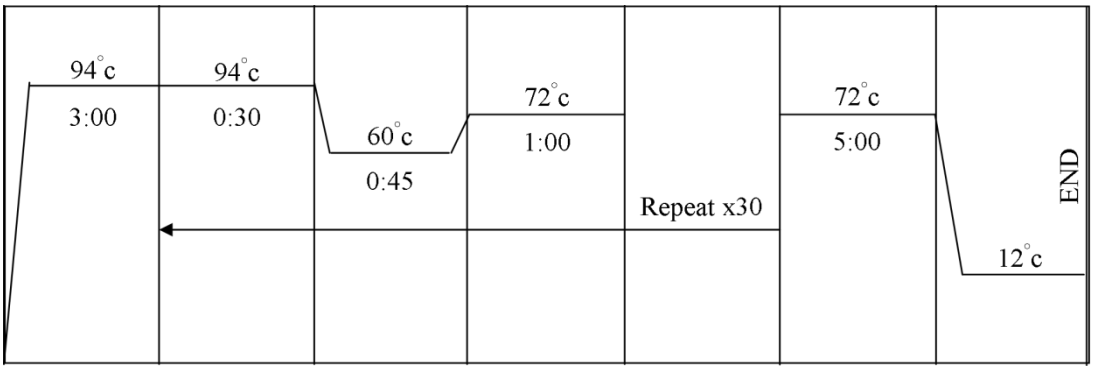

Figure 2.1: PCR Cycle for genotyping UCHL1 mice

2.2.3 Behavioural testing

The onset and progression of hind limb impairment in UCHL1 KO mice was assessed by suspending mice by the tail for 5 seconds, and scoring hind limb function on a scale of 0 – 2, as follows: 0 = Hind limbs splayed, 1 = Hind limbs not splayed, but held hip distance apart, 2 = Hind limbs crossing over or held together. Mice were identified according to cage number and by the positioning of ear notches, and scoring was done on a blinded basis; the genotype of the mice was not known at the time of testing. Mice aged between 7 and 22 weeks were assessed on a weekly basis using this method.

2.2.4 Mouse Dissection

Brain and spinal cord tissues were collected from mice at an early stage of pathology (9-12 weeks) and at and advanced stage of pathology (16 – 21 weeks), in order to assess the progression of pathology in UCHL1 KO mice. Dissections are summarised in Table 4.1 and a comprehensive list of mice dissected is given in Table 8.1, Appendix B.

2.2.4.1 Frozen Tissue

Frozen brain and spinal cord tissue was obtained directly from UCHL1 WT and KO mice. Mice were given isofluorane anaesthetic gas until unconscious and euthanized by a lethal injection of Dolethal 200mg/ml solution (Pentobarbital Sodium) by Adele Kitching. Transcardial perfusion with 0.1M PBS, pH 7.4 was also carried out by Adele Kitching. Mice were perfused until the liver had cleared of blood. I then carried out a dissection of the brain and spinal cord. One cut was made with a large pair of scissors in order to remove the head, cutting cleanly through the spinal cord at the base of the brainstem. The skin was then pulled back over the head, and using sharp tweezers and small scissors, excess muscle was removed from the back of the neck. The brain was then disarticulated by cutting through the middle of the skull, starting at the base of the brainstem and working upwards. The skull was then taken off from the middle outwards, using curved serrated tweezers, entirely exposing the brain. Using a small metal scoop to break through the circle of Willis, the brain was gently encouraged out onto a piece of foil. The brain was then transferred on the foil into an aluminium boat, and frozen over liquid nitrogen. Meanwhile, a cut was made through the spinal column and surrounding tissue at the level of the hips. The skin was cut parallel to the vertebral column and pulled back out of the way. The cervical and sacral end of the spinal cord were then inspected to ensure they had been cut cleanly, and if not fresh cuts were made as required. An 18 Gauge needle had previously been trimmed with wire cutters and blunted by filing. This was attached to a 10ml BD Plastipak syringe, filled with 0.1M

PBS. The needle was inserted into the spinal column at the sacral end, and firm pressure was applied to the syringe. This caused the whole spinal cord to shoot out of the cervical end of the spinal column onto the foil. The spinal cord was straightened out carefully, and placed on the foil into the aluminium boat for freezing over liquid nitrogen. Once brain and spinal cord samples had frozen sufficiently, they were transferred into tubes kept on dry ice, and after that stored in a -80^{o} c freezer until needed.

2.2.4.2 Formalin Fixed, Paraffin Embedded Tissue

UCHL1 KO and WT mice were perfusion fixed, before dissection of the brain and spinal cord. Two dissection methods were used, as a improved method was found after the dissection of the first seven perfusion fixed mice.

2.2.4.2.1 Perfusion Fixing:

Mice were euthanized by giving isofluorane anaesthetic gas until unconscious and then a lethal injection of Dolethal 200mg/ml solution (Pentobarbital Sodium). Once mice were dead, they were perfused with 0.1M PBS, pH 7.4 and then 4% PFA, using a perfusion pump. Mice were perfused with 4% PFA until a good fix was achieved (both head and tail were stiff), and then kept at 4^{o}c for 1 – 2 hours before dissecting. Euthanizing and perfusion fixing the mice was carried out by Adele Kitching.

2.2.4.2.2 Dissection (method 1):

Brains dissection was carried out using the method described in section 2.2.4.1. Brains were then each placed in a generous volume of 4% PFA in a sample pot, and kept on a rocker at 4^{o}c overnight. To remove the spinal cord, firstly a cut was made through the skin down the middle of the back, parallel to the spinal column, and the skin was pulled apart to either side. Using a scalpel, muscle was cleared from the spinal column. Starting at the cervical end, small scissors were used to cut the vertebrae either side of the spinal cord, and one at a time the vertebrae and associated muscle were pulled off with tweezers, gradually exposing the spinal cord. The whole spinal column was then removed and placed in 4% PFA overnight, on a rocker at 4^{o}c. The next morning, the spinal cord was carefully separated from the remaining bones and muscle, starting from the sacral end. Underlying nerves were cut in order to free the spinal cord and save the dorsal root ganglion (DRG). Spinal cords were then placed in tissue processing cassettes and incubated in 30% sucrose solution at 4^{o} c overnight. Simultaneously, mouse brains were also placed in yellow cassettes in 30% sucrose solution, kept at 4^{o}c.

2.2.4.2.3 Dissection (method 2)

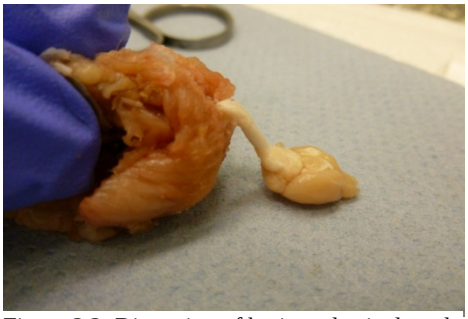

Figure 2.2: Dissection of brain and spinal cord as a whole unit

Mice were euthanized and perfusion fixed as previously described. The brain and spinal cord were then dissected as one unit, using a method adapted from Kennedy et al (Kennedy et al., 2011). After perfusion fixing, mice were kept at 4^{o}c for at least half an hour. The first cut was made through the skin across the back, perpendicular to the spinal column, and the skin was then pulled back in either direction as far as possible. Forelimbs were removed using large scissors, and a scalpel was used to remove the fat and muscle from the spinal column, particularly at cranial and caudal ends. Using large scissors the abdominal viscera were removed from underneath, and a clean cut was made across the spinal column at the level of the hips, revealing the sacral end of the spinal column. Using very small, strong scissors, two cuts were made through each vertebra parallel to, and on either side of, the spinal cord. This left bone and muscle that was pulled away using tweezers to reveal a section of spinal cord. Starting at the caudal end, this process was undertaken one vertebra at a time, until reaching the cervical end of the spinal cord. The skull was disarticulated in the same way as described in section 2.2.4.1. With a small metal scoop, the brain was gently taken out, starting underneath the occipital lobes and working backwards, cutting through the circle of Willis. Once the brain was disconnected from all bone and connective tissue, it was allowed to hang backwards, acting as a weight to pull the spinal cord from the surrounding vertebrae (Figure 2.2).

The spinal cord was removed, working from the cervical end to the caudal end, by cutting away nerves and connective tissue with small scissors. Nerves were cut as far away from the spinal cord as possible in order to leave the dorsal root ganglia (DRG) attached to the spinal cord. Once the brain and spinal cord were completely detached, they were laid out flat onto a piece of plastic, and tied on loosely. This was then placed in a sample pot filled with 4% PFA and left at room temperature for approximately 24 hours to fix. Sections were then given to Mrs. Lynn Ramsay for further processing, and subsequently embedded in hot paraffin wax, oriented so that sections cut from these blocks would be coronal.

2.2.5 Preparation of Tissue Sections

2.2.5.1 Cryosectioning

Brain and spinal cord samples were transferred from the -20°c freezer to the cryostat on dry ice, and then placed in the cryostat at an ambient temperature of around -20°c. Prior to cryosectioning, whole spinal cords were divided into 4mm long portions using a sharp scalpel. Each of these portions was mounted vertically onto a small piece (approx 1x1cm square) of filter paper, with OCT (Optimal Cutting Temperature Compound), over dry ice. Mounted spinal cord portions were held over liquid nitrogen, and then attached onto a metal chuck with a small amount of water. To cut sections, the chuck was inserted into the cryostat. Sections were cut 10µm thick, and taken up onto Superfrost® Plus Slides (VWR™ International). Sections were cut and stained in the following order: H&E, COX/SDH, COX, COX/SDH, SDH, COX/SDH

2.2.6 Microtomy

Paraffin embedded brains and spinal cords were cut into sections using a microtome. Sections intended for immunohistochemistry or immunofluorescence were cut at a 5µm thickness. Sections intended for Haematoxylin & Eosin (H&E) and Loyez Haematoxylin staining were cut at 10µm thickness, and those sections to be stained with Cresyl Fast Violet (CFV) were cut at 20µm thickness. Before cutting 5µm sections, blocks were placed on ice to cool, whereas blocks were placed in a 37°c incubator before cutting 10 and 20µm sections to allow the wax to soften. Sections were taken up onto Colourcoat+ adhesion microscope slides, and then left to dry at room temperature. In order to prevent the fragmentation of the sections, 10µm and 20µm sections were left at room temperature for approximately 48 hours before placing in the 37°c incubator, whilst 5µm sections were left at room temperature for only 2-3 hours prior to this. If tissue sections were not to be used immediately, they were placed in the cold room (4°c) for longer term storage. Tissue sections from the advanced stage pathology UCHL1 mice and controls were cut by myself, whilst tissue sections from the early stage mice were cut by Anna Smith.

2.2.7 Human Tissue

2.2.7.1 FFPE Tissue Sections

Tissue blocks from cases 2013-0823 and 2010-0195 were supplied by Dr. Tuomo Polvikoski and the Department of Cellular Pathology at the Royal Victoria Infirmary, Newcastle; tissue sections were taken from these blocks by Anna Smith. Subsequent

human aged control cases (2007-0049, 2005-0053, 2008-0005) were obtained from the Newcastle Brain Tissue Resource (NBTR), under ACATU number 2014026, and tissue sections were taken by Anna Smith. This project had received ethical approval (number LREC 2002/205).

2.2.7.2 Frozen Samples

Frozen tissue samples were obtained from the NBTR under the ACATU number 2013084, and 2013084 (amended). Details of these cases are listed in Table 7.1and Table 7.2. This project had received ethical approval (number LREC 2002/205).

2.2.8 Histology

2.2.8.1 Neuropathology Markers

2.2.8.1.1 Cresyl Fast Violet (Nissl)

20µm sections on Colourcoat+ Adhesion glass slides were placed in a 60^{o}c incubator for 20 minutes to melt the wax. Sections were then deparaffinised with Histoclear HS-202, and rehydrated through a graded ethanol series. Meanwhile, the CFV staining solution was pre-heated in the 60^{o}c incubator. Sections were then placed in 1% acid alcohol (1% HCl, 85% EtOH) for 5 minutes before rinsing in distilled water. The sections are then incubated in the pre-heated CFV at 60^{o}c for 10 – 15 minutes, and left to cool in the CFV for a further 5 minutes. Finally, sections are rinsed in distilled water, dehydrated by moving quickly through a graded ethanol series, cleared in Histoclear and mounted in DPX (Dibutyl phthalate xylene)

2.2.8.1.2 Loyez Haematoxylin

10µm sections on Colourcoat+ adhesion glass slides were deparaffinised and rehydrated to water, as described above. They are then placed in 4% iron alum mordant for approximately 6 hours. After this, sections are washed well in distilled water before leaving to stain in freshly prepared haematoxylin (1% Haematoxylin, 10% EtOH, 2% Saturated Li_2CO_3) overnight. The next morning, sections are washed in distilled water and then dehydrated, cleared in histoclear and finally mounted in DPX.

2.2.8.1.3 Haematoxylin and Eosin

Firstly, formalin fixed, paraffin embedded (FFPE) sections were deparaffinised by heating at 60^{o}c for 20 minutes, then washing twice in Histoclear, for 10 minutes total. Sections were then rehydrated through an ethanol series: 5 minutes in 100% ethanol twice, then 5 minutes in 95% (v/v) ethanol and 5 minutes in 70% (v/v) ethanol. Sections

were washed well in distilled water before immersing in Mayer's haematoxylin for 5 minutes. Sections were washed in distilled water again, and placed in Scott's Tap Water for 1 minute to 'blue' the nuclei, before immersing in eosin for 10 minutes. The sections were dehydrated in another ethanol series: 3 minutes in 70% (v/v) ethanol, 3 minutes in 95% (v/v) ethanol, 2x 5 minutes in 100% ethanol, and finally 2x 5minutes in Histoclear^{TM}. Sections were finally mounted in DPX.

2.2.8.2 COX/SDH Histochemistry in frozen tissue

Before COX/SDH sequential histochemistry, spinal cord sections on VWR Superfrost® Plus slides were left to air dry for one hour after being removed from the -80^{o}c freezer or immediately after cryosectioning. The COX medium (100µM cytochrome *c* and 4mM DAB) was prepared by adding 200µl cytochrome *c* to 800µl Diaminobenzine (DAB), and vortexing with a few crystals of catalase. This was applied to the sections, and incubated for 35 minutes at 37^{o}c. Sections were then washed twice with 0.1M PBS, pH7, before application of the SDH medium (800µl Nitro Blue Tetrazolium, 100µl Sodium Succinate, 100µl Phenazine Methosulphate and 10µl Sodium Azide), which sections were incubated with for 40 minutes at 37^{o}c. Finally, sections were washed twice with PBS and dehydrated in an ethanol series (70% (v/v), 95%, (v/v) 100% and a final 10 minutes in 100% ethanol) before mounting in DPX.

2.2.9 Immunohistochemistry

2.2.9.1 Avidin-Biotin method:

Formalin fixed, paraffin embedded sections on Colourcoat+ adhesion slides were firstly deparaffinised in Histoclear™ (Two 5 minute incubations) and rehydrated in a graded ethanol series (2 x 5 minutes in 100% ethanol, 5 minutes in 95% (v/v) ethanol, 5 minutes in 70% (v/v) ethanol, water). Sections were then subject to antigen retrieval (See section 2.2.8.3 for further detail). After antigen retrieval, sections were cooled by washing well in distilled water. All sections were incubated in 3% H_2O_2 (v/v) for 30 minutes, in order to block any endogenous peroxidise activity. The tissue sections were encircled by a hydrophobic pen before sections were washed once in TBS, pH7.4 and once in TBS + 0.2% (v/v) Tween®20, pH7.4. Sections were then blocked for endogenous avidin and biotin with an Avidin/Biotin blocking kit (15 minutes of each solution, with two washes in TBS in-between). Sections were blocked for 1 hour in 5% normal goat serum (NGS) in 2.5ml TBS with two drops of M.O.M (Mouse On Mouse) blocking solution, to prevent binding to endogenous mouse immunoglobulin. Sections are then incubated for 5 minutes with a working solution of M.O.M. diluents (600µl M.O.M. Protein Concentrate from the M.O.M kit in 7.5ml TBS, pH7.4). Primary antibodies were made up in M.O.M. diluents at the appropriate dilution (Table 1), and applied to the sections for the optimal incubation time (Table 1). At this stage the ABC solution is made up from the Vectastain® ABC Kit, according to instructions, to allow the avidin-biotin-complex to form. After washing sections twice with TBS, secondary antibodies, made up at 1:200 dilution in 5% NGS with M.O.M. diluents, were applied for 10 minutes. Sections were again washed twice with TBS, and then incubated with the ABC complex for 30 minutes. After washing sections in TBS and then distilled water, sections were incubated with DAB chromogen (SIGMAFAST) for 5 minutes. Sections were washed well in distilled water to eliminate any unbound chromogen, and then counterstained with haematoxylin for 5 minutes and Scott's tap water for 15 seconds. All sections were then dehydrated through a graded ethanol series (5 minutes in 70% (v/v), 5 minutes in 95%, 2 x 5 minutes in (v/v) 100%), cleared in Histoclear™ and mounted in DPX.

This protocol was also used for immunohistochemistry with human tissue sections; however it was not necessary to use the M.O.M kit in this case. Therefore, addition of M.O.M blocking solution to NGS and incubation of sections with M.O.M diluents were

omitted. Primary and secondary antibodies were made up in TBS and 5% NGS, respectively. All other steps remain the same.

2.2.9.2 Universal Probe Method:

For immunohistochemistry to APP and synaptophysin antibodies on human tissue sections, the universal probe method was followed. As in Section 2.2.8.1, tissue sections were firstly deparaffinised and rehydrated, and then underwent antigen retrieval. Sections were then incubated in 3% H_2O_2 for 10 minutes, and subsequently outlined with a hydrophobic pen and incubated with TBS and then TBST for 2 minutes each. Next, sections were incubated with the appropriate primary antibody made up in TBS for 1 hour, at room temperature. After rinsing sections twice in TBS, the universal probe was applied for 30 minutes. Sections were then rinsed twice in TBS again, before incubating with the HRP polymer for 30 minutes. Sections are finally washed twice in TBS before applying the DAB chromogen for 5 minutes, then rinsed well in distilled water and counterstained with Mayer's Haematoxylin for 5 minutes. Sections were immersed in Scott's tap water for 15 seconds in order to 'blue' nuclei, and finally sections are dehydrated and mounted in DPX.

2.2.9.3 Methods of Antigen Retrieval:

2.2.9.3.1 Complex I-20kDa, Complex IV-1, Complex II-70kDa, SMI-32P, MBP-4, Synaptophysin:

Sections to be stained with the above primary antibodies underwent antigen retrieval as follows. 1mM EDTA (USB), pH8 was brought to the boil by microwaving in a plastic box with the lid on at 70% power for 6 minutes. After this 12 slides/sections (double-spaced in a plastic rack) were placed in the box, with the lid on. This was then microwaved for a further 5 minutes at 50% power. The box and slides were left to cool for 5 minutes, before removing the lid, and allowing to cool by washing thoroughly in distilled water.

Human tissue sections require harsher antigen retrieval conditions than mouse sections, therefore when doing IHC to CII-70 and SMI-94, sections were retrieved using the 2100 retriever antigen retrieval machine. 750ml water was placed in the body of the machine, and slides were double spaced in plastic chambers containing a combined total of 500ml EDTA, pH8. The 2100 retriever then increases the internal pressure and brings the temperature to 120^{o}c; slides are left in the machine for a further 20 minutes after the cycle has finished before rinsing in cold water.

2.2.9.3.2 APP, Synaptophysin:

Sections for immunohistochemistry with the APP antibody were placed in 500ml 10mM sodium citrate, and microwaved at 70% power for 10 minutes with the lid on. Sections were then left for a further 10 minutes with the lid on to cool, before washing with distilled water. Human gracile nucleus sections were also retrieved in this way for IHC to synaptophysin.

2.2.10 Immunofluorescence

2.2.10.1 Dual Synaptophysin and COX-1 Immunofluorescence

Formalin fixed, paraffin embedded sections on Colourcoat+ adhesion slides were firstly deparaffinised in histoclear and rehydrated in a graded ethanol series, as described in section 2.2.8.1. Sections were then subject to antigen retrieval (as in section 2.2.8.3.1). After antigen retrieval, sections were cooled by washing well in distilled water. All sections were incubated in 3% H_2O_2 (v/v) for 30 minutes, in order to block any endogenous peroxidise activity. The tissue sections were encircled using a hydrophobic pen before sections were washed once in TBS, pH7.4 and once in TBS + 0.2% (v/v) tween20, pH7.4. Sections were then blocked for endogenous avidin and biotin with an avidin/biotin blocking kit (15 minutes of each solution, with two washes in TBS in-between). Sections were blocked for 1 hour in 5% normal goat serum (NGS) in 2.5ml TBS with two drops of M.O.M blocking solution, to prevent binding to endogenous mouse immunoglobulin. Sections are then incubated for 5 minutes with a working solution of M.O.M. diluents (600µl M.O.M. protein concentrate from the M.O.M kit in 7.5ml TBS, pH7.4). The synaptophysin primary antibody was made up in M.O.M. diluents (1:800) and applied to the sections. Sections were incubated with the primary antibody overnight at 4^{o}c.

After washing sections once with TBS, pH7.4 and once with TBST, pH7.4, the secondary antibody was diluted 1:100 in 5% NGS with M.O.M diluents and applied to sections for 30 minutes at room temperature. Sections were then washed twice in TBS, before incubating with streptavidin tetramethylrhodamine conjugate (TRITC) (1:100 in 5% NGS with MOM diluents) for 30 minutes at room temperature. Sections were washed twice with TBS, and another mouse IgG block (5% NGS with two drops of M.O.M blocking solution) was applied for 1 hour. Sections are then incubated for 5 minutes with a working solution of M.O.M. diluents, as before, and the COX-1 primary antibody is made up in M.O.M. diluents (1:400) and applied to the sections. Sections

were incubated with the primary antibody overnight at 4°c. The next morning, the secondary antibody (biotinylated Goat anti Mouse IgG2a) was diluted 1:100 in 5% NGS with M.O.M diluents, and applied to sections for 30 minutes at room temperature. Sections were then washed twice with TBS before incubating with Streptavidin AlexaFluor® 488 (FITC) (diluted 1:100 in 5% NGS with M.O.M diluents) for 30 minutes at room temperature. After two washes with TBS, Hoechst (a stock solution of 10mg/ml in PBS, further diluted 1:1200 in TBS) was applied for 15 minutes, in order to stain nuclei blue. A 0.3% (w/v) sudan black solution was prepared by dissolving 150mg sudan black B powder in 50ml 70% ethanol. This requires the solution to be mixed for a couple of hours. The sudan black solution was always syringe filtered before applying to sections to reduce the incidence of precipitates forming on slides. Application of sudan black to immunofluorescent sections for 10 minutes eliminates the autofluorescence intrinsic to brain tissue. Sections are subsequently washed well in a coplin jar of distilled water, again to prevent the formation of sudan black precipitates. Sections are then mounted by applying a drop of ProLong® Gold Antifade Reagent and covering with a cover slip. After the mounting solution has dried, the coverslip can be secured with nail varnish. Immunofluorescent sections were stored at -20°c to minimise the fading of fluorophores.

2.2.10.2 Triple Neurofilament – H, Synaptophysin and COX-1 Immunofluorescence

The protocol explained in detail in section 2.2.9.1 was modified in the following ways in order to visualise neurofilaments, mitochondria and synaptophysin together:

After overnight incubation with the synaptophysin antibody (1:800), and subsequent washes in TBS, sections were incubated with goat anti-mouse IgG1 AlexaFluor 546 secondary antibody, diluted 1:100 in 5% NGS with M.O.M diluents for 30 minutes at room temperature.

Sections are incubated with both COX-1 and Neurofilament-H antibodies simultaneously (1:400 and 1:800 respectively in M.O.M diluents)

After this incubation and subsequent rinses, sections are incubated with biotinylated goat anti-rabbit IgG (1:100 in 5% NGS/M.O.M diluents) for 30 minutes at room temperature. After 2x 2minute washes in TBS, they are then incubated for 30 minutes at room temperature with goat anti-mouse IGg2a AlexaFluor 488 and streptavidin AlexaFluor 647 simultaneously; both diluted 1:100 in 5% NGS.

In order to ensure that there was no interference from autofluorescence, background or cross-reactivity, the following control sections were carried out:

- No primary antibody, no secondary antibody, no sudan black
- No primary antibody, no secondary antibody, with sudan black
- No primary antibody, goat anti-mouse IgG1 AlexaFluor546
- No primary antibody, goat anti-mouse IgG2a AlexaFluor488
- No primary antibody, biotinylated goat anti-rabbit IgG, streptavidin AlexaFluor 647
- Synaptophysin primary antibody, goat anti-mouse IgG2a AlexaFluor488
- COX-1 primary antibody, goat anti-mouse IgG1 AlexaFluor 546

2.2.10.3 Microscopy

Microscopy of immunofluorescence staining was carried out using the Nikon A1R microscope at high magnification (60x oil objective, magnified x1.5). Galvano scanning mirrors were utilised to allow for high resolution images, with a pixel dwell time of 1.9ms to prevent photobleaching, pinhole diameter of 1.2 AU and image size of 512x512 pixels. In order to visualise Hoescht nuclear staining, as well as FITC, TRITC and Cy5, 405nm, 457-514nm, 541nm and 647nm lasers were used with the appropriate filter sets. Image acquisition was carried out using NIS elements software (Nikon).

2.2.11 Western Blotting and Proteasome Assay

2.2.11.1 Preparing homogenates from UCHL1 mouse cerebellum

Mouse brains were sub-dissected so that each sample was half a cerebellum, weighing approximately 100mg. Samples were homogenized in 2ml ice cold lysis buffer (20mM Tris-HCl, pH7.5), supplemented with cOmplete ULTRA protease inhibitor tablets (inhibit serine, cysteine, aspartic and metallo-proteases, and contain EDTA). Homogenates were briefly kept on ice before performing the Bradford Assay, and subsequently stored at -80^{o}c.

2.2.11.2 Preparing homogenates from human brain tissue

For western blotting, human brain tissue samples were homogenized in ice cold lysis buffer (20mM Tris-HCl, pH7.5), supplemented with cOmplete ULTRA protease inhibitor tablets; approximately 500µl lysis buffer was added to each 30mg tissue, to result in an eventual protein concentration of approximately 4µg/µl. Tissue samples were homogenized with a Polytron P1600 E benchtop homogeniser (Kinematica), at

30,000 rpm for at least 10 seconds, and then immediately sonicated using Sonics Vibra-Cell™ ultrasonic processor, at 20 kHz for 10 seconds, to ensure complete homogenization of each sample. This was done in a class III biological safety cabinet. After 1µl of each sample was taken for the Bradford assay, samples were frozen and stored at -80°c until use.

For the proteasome activity assay, samples were homogenized in the same way, but in HEPES buffer (50mM HEPES, 20mM KCl, 5mM $MgCl_2$, 1M DTT plus 10% Glycerol, pH7.5), and were stored at -80°c until use.

2.2.11.3 Bradford Assay

In order to produce a standard curve, from which to determine the sample protein concentrations, standards of known protein concentrations (0, 2, 5, 10, 15 and 20µg/µl) were prepared using 1mg/ml purified bovine serum albumin, dH_2O and 20% (v/v) Bradford reagent (Bio – Rad protein assay dye reagent concentrate). Samples were prepared for the Bradford Assay by adding the sample 1 in 1000 to 20% (v/v) Bradford reagent in dH_2O. 200µl of each of the protein standards were loaded onto a 96 well optic plate in duplicate and 200µl of each sample was loaded in triplicate. Absorbance of the protein standards and samples was read at 595nm by a BioTEK ELx895 absorbance microplate reader.

The values produced were averaged to give a concentration (µg/µl) for each sample, and used to ensure that equal amounts of protein from each sample were loaded onto gels for electrophoresis.

2.2.11.4 Electrophoresis

The volume of each sample was calculated so that 20µg total protein was used to visualise levels of monoubiquitin, and 40µg of each was used to visualise ubiquitin conjugates. For human samples, only 10µg total protein was required for the visualisation of the ubiquitin monomer. Sample buffer (250mM Tris, 25% Glycerol, 0.4% SDS, 0.1% Bromophenol Blue) plus 20% DTT was added in a 1:1 ratio to the largest sample (by volume), and added in excess to the other samples to equal the same volume as the largest sample. Samples were then heated at 95°c for 5 minutes in order to linearise proteins uniformly, and subsequently loaded onto a precast 8-16% gradient gel, and electrophoresed at 100V for 90 minutes, in running buffer (15% (w/v) Tris, 17% (w/v) glycine, 5% (w/v) SDS).

2.2.11.5 Protein Transfer

2.2.11.5.1 For the visualisation of ubiquitin conjugates:

10x transfer buffer (250mM Tris, 1.9M Glycine, 0.2% (w/v) SDS) was diluted 1in10 plus 20% methanol, and cooled to 4^{o}c. Filter paper and sponges were soaked in ice cold transfer buffer before assembling the cassette for a wet transfer of proteins from the gel onto an Immobilon®-P PVDF transfer membrane (activated by rinsing in methanol for 15 seconds), using the Mini-Protean Blotting module (Bio Rad). The transfer cassette was prepared as follows: sponge, filter paper, gel, activated PVDF membrane, filter paper, sponge. This was assembled in the transfer apparatus with cooled transfer buffer and a freezer-block, so that the gel was closest to the negative cathode. Proteins were electroblotted to the PVDF membrane at 100V for 1 hour.

2.2.11.5.2 For the visualization of ubiquitin monomers:

10x $CaCl_2$ transfer buffer (250mM Tris, 1.9M glycine, 20mM $CaCl_2$) was diluted 1 in 10 plus 20% methanol, and cooled to 4^{o}c. The positively charged calcium ion encourages the binding of small proteins (including the ubiquitin monomer) to the PVDF membrane, but prevents the transfer of larger proteins (McKeon and Lyman, 1991). The transfer cassette and apparatus were assembled as previously described, and proteins were electroblotted to the PVDF membrane at 100V for 50 minutes at 4^{o}c.

2.2.11.6 Coomassie Blue and Ponceau Red Stains

In order to determine the efficiency of protein transfer from the gel to the membrane, coomassie blue and ponceau red stains were undertaken, to visualise proteins on the gel and membrane, respectively.

After the transfer was complete, the gel was transferred into a small amount of coomassie blue dye (45% (v/v) methanol, 10% (v/v) glacial acetic acid 0.25% (w/v) Coomassie Brilliant Blue), and agitated on a shaker for 1-2 hours. It was then rinsed in coomassie de-stain solution (50% (v/v) ethanol, 10% (v/v) acetic acid), and incubated in the de-staining solution overnight on a shaker at 4^{o}c.

To visualise the proteins on the membrane, Immobilon®-P PVDF transfer membranes were transferred to a dish of Ponceau Red (2% Ponceau S, 30% Trichloroacetic acid, 30% Sulfosalicyclic acid) and agitated for approximately 5 minutes. Membranes were then rinsed several times in water until protein bands became clear.

2.2.11.7 Immunoblotting

Immobilon®-P PVDF transfer membranes were blocked by incubating for 1 hour with 5% (w/v) skimmed milk in TBST, and then incubated with DAKO anti-ubiquitin (1:750) and anti-α tubulin (1:5000), diluted in 5% (w/v) milk overnight at 4^{o}c. Membranes were rinsed 3x 10 minutes in TBST at room temperature, before incubating with Swine anti-Rabbit Polymerase secondary antibody (1:1000) in 5% (w/v) milk for 1 hour at room temperature. Blots were developed using Amersham^{TM} ECL^{TM} Prime western blot detection reagent, and imaged using the Bio Rad ChemiDoc System. Membranes were then rinsed again in TBST, before blocking once more in 5% (w/v) milk for 1 hour at RT, and incubating with polyclonal rabbit anti-mouse immunoglobulins/HRP (1in1000 in 5% w/v milk) for 1 hour. After rinsing 3x 10 minutes in TBST, the membrane was developed a second time with the Amersham^{TM} ECL^{TM} Prime reagent, in order to visualise the α-tubulin loading control. α-tubulin was selected as a loading control due to its ubiquitous presence as a structural protein in eukaryotic cells; its sensitivity to changes in protein concentration was assessed in Section 7.2.1.

For human samples, this protocol was extended in order to determine levels of ComplexI-20 and Porin/VDAC-1. The concentration of α-tubulin antibody was also reduced to 1:10000 on conjugates blots. Following development of blots to visualise ubiquitin conjugates, membranes were rinsed in TBST and blocked once more in 5% milk for 1 hour at RT. They were then incubated with CI-20 (1:1000) and Porin (1:1000) in 5% milk/TBST at RT for 3 hours, before rinsing 3x 10 minutes in TBST. Subsequently, polyclonal rabbit anti-mouse immunoglobulins/HRP was applied to membranes (1in1000 in 5% w/v milk) for 1 hour. Membranes were rinsed again (3x10 minutes in TBST), developed using the ECL^{TM} Prime reagent, and finally imaged using the Chemi-Doc system (Bio-Rad).

2.2.11.8 Assessment of Proteasome Activity

Optimisation of the proteasome assay was carried out using a mouse brain, homogenised in ice- cold HEPES buffer plus 10% glycerol. On the morning of the experiment, samples were removed from the -80^{o}c freezer, put on wet ice until melted, and then centrifuged at 10,000g for 30 minutes at 4^{o}c. The supernatant was then separated from the pellet, and 1µl of each sample was taken to perform the Bradford Assay, as described in section 2.2.10.3, to determine protein concentration. The assay was set up in a flat-bottom 96 well plate (Greiner Bio-One) on ice, each well contained the following components:

20S Trypsin Activity	20S PGPH Activity	20S Chymotrypsin Activity
HEPES buffer (to make total volume 250µl)		
Sample (10µg)	Sample (30µg)	Sample (30µg)
10µl 875µM MG 132 or 10µl DMSO	10µl 875µM MG 132 or 10µl DMSO	10µl 250µM lactacystin or 10µl DMSO
10µl 1.25mM Boc-LRR-AMC	10µl 2.5mM Z-LLE-AMC	10µl 1.25mM Suc-LLVY-AMC

Table 2.1: Outline of proteasome assay

Each 96 well plate was set up in the following order, and kept on wet ice at all times:

1. HEPES buffer is added to each well in the appropriate volume
2. The calculated volume of each sample is added to the appropriate wells
3. 10µl proteasome inhibitor (MG132 or lactacystin) is added to every other columns; 10µl DMSO is added to the alternate columns. The plate is then left for half an hour before starting the experiment
4. 10µl of the appropriate fluorogenic substrate is added to each well immediately before the beginning of the experiment.

The plate is then placed in a fluorimeter, kept at 37^{o}c and fluorescence (between 395–514nm) is read every 90 seconds for 1 hour.

2.2.12 Statistics

The D'Agastino-Pearson omnibus normality test was used to determine whether data fits a Gaussian distribution, whilst the F-test was used to determine whether variances are significantly different. Means of two groups of normal data were compared using a student's unpaired t-test (α=0.05); if the two groups were sampled from populations with unequal variances, Welch's correction was employed, and the Mann-Whitney test was used if data was non-parametric. In Figure 6.17, it was appropriate to use a paired t-test. The means of three groups were compared using an ordinary one-way ANOVA, with Dunnett's multiple comparisons test, or using the Kruskal Wallis test with Dunn's post-hoc test if the data was not normally distributed. To compare more than three groups, I used multiple t-tests with the Holm-Sidak correction. Frequency distributions were compared using a Mann-Whitney test, whilst Kolmogorov-Smirnov tests were used to compare cumulative frequency distributions. In general, data was graphically

represented as the mean ± standard deviation, however in Figure 4.12, data is shown as the mean ± standard error of the mean.

Chapter 3.

Mitochondrial Dynamics

Chapter 3. **Mitochondrial Dynamics**

3.1 Introduction

Mitochondrial dysfunction and the decline of the ubiquitin proteasome system are two commonly observed features of ageing and age-related neurodegenerative diseases, as described in the introduction (Sections 1.10 and 1.11).

Dysfunctional mitochondria accumulate with age, characterised by increased size and decreased ultrastructural organisation (Miquel et al., 1980; Beregi et al., 1988), along with decreased membrane potential and ATP production and increased ROS generation (Ozawa, 1997; Kushnareva et al., 2002). It is known that the number of mtDNA mutations increases in a linear fashion with age due to clonal expansion (Elson *et al.*, 2001; Bender *et al.*, 2006). The ubiquitin proteasome system also declines in function with age; both 20S and 26S proteasomes have been demonstrated to become less efficient with age in several species and tissues (Dahlmann, 2007), and consequently, damaged and oxidized proteins accumulate with age (Petropoulos *et al.*, 2000b; Löw, 2011).

I aim to determine whether these two features of ageing and neurodegeneration occur concomitantly but by different mechanisms, or whether the decline of the ubiquitin proteasome system may cause mitochondrial dysfunction, and by what mechanism this may occur.

There are many instances in which the UPS does interact with mitochondria, most notably in regulating the proteins that control mitochondrial fission, fusion and trafficking, and in mitochondrial quality control (Escobar‐Henriques and Langer, 2014).

3.1.1 Regulation of Mitochondrial Fission and Fusion by the UPS

There are many proteins and molecules that interact with and regulate the fission and fusion machinery of mitochondria (Elgass *et al.*, 2013; Escobar-Henriques and Anton, 2013), however it is clear that ubiquitination has a central role in the regulation of mitochondrial dynamics. The ubiquitination of fission and fusion proteins by mitochondrial E3 ubiquitin ligases can result in their stabilisation or proteasomal degradation, depending on the mode of ubiquitination.

Drp1, the key executor of mitochondrial fission is regulated by ubiquitination carried out by two mitochondrial E3 ubiquitin ligases, Parkin and MITOL; however the effects

of these ubiquitination events are unclear. MITOL (Mitochondrial Ubiquitin Ligase), also known as MARCHV (Human Membrane Associated RING finger C3HC4 V), also interacts with and ubiquitinates Drp1 (Nakamura *et al.*, 2006; Yonashiro *et al.*, 2006; Park *et al.*, 2010). However the effect of this ubiquitination event is debated, since MITOL has no effect on Drp1 protein levels (Karbowski *et al.*, 2007; Park *et al.*, 2010) and has been shown to both inhibit (Nakamura *et al.*, 2006; Yonashiro *et al.*, 2006) and promote (Karbowski *et al.*, 2007; Park *et al.*, 2010) mitochondrial fission. MITOL RING mutants (which have no ubiquitin ligase activity) form high molecular weight complexes on the OMM, and abnormal Drp1 clusters colocalise with these complexes. This is accompanied by mitochondrial elongation, suggesting that MITOL may be a pro-fission protein, involved in the correct formation of Drp1 scission complexes (Karbowski *et al.*, 2007). The E3 ubiquitin ligase Parkin was also shown to ubiquitinate Drp1, targeting it to the proteasome for degradation (Wang *et al.*, 2011a), however, a further study convincingly demonstrated that Parkin promotes mitochondrial fission in rat hippocampal neurons (Yu *et al.*, 2011). Therefore, whilst ubiquitination is clearly involved in the regulation of mitochondrial fission by MITOL and Parkin, the exact mechanisms behind this are disputed and further studies are required. Interestingly, it has also been shown that the cell cycle protein and E3 ubiquitin ligase APC/C^{Cdh1} ubiquitinates Drp1, which in part causes the formation of a hyperfused giant mitochondrial network in G1/S phase of the cell cycle (Horn *et al.*, 2011).

Mitochondrial fusion is also regulated by ubiquitination. Mitofusins can either be activated, thus promoting fusion, or targeted for degradation by ubiquitination, in particular in response to cellular stress.

Studies on the function of Parkin in the model system *Drosophila* originally indicated that Parkin promotes mitochondrial fission by ubiquitinating *Drosophila* Mitofusin (*d*Mfn) (Poole *et al.*, 2010; Ziviani *et al.*, 2010), and this was also observed in mammals (Gegg *et al.*, 2010; Tanaka *et al.*, 2010; Rakovic *et al.*, 2011; Yu *et al.*, 2011). Therefore the consensus is that Parkin-mediated ubiquitination of mitofusins has a pro-fission role, in response to conditions of cellular stress, such as mitochondrial depolarisation and mitophagy induction. Furthermore, the ER-targeted E3 ligase gp78, has also been shown to ubiquitinate Mfn1 and 2 upon the induction of mitophagy (Fu *et al.*, 2013). The E3 ubiquitin ligase HUWE1 ubiquitinates Mfn2 in response to cell stress and Mfn2 phosphorylation, causing it to be degraded by the proteasome, and causing mitochondrial fragmentation and inducing apoptosis (Leboucher *et al.*, 2012). Another

E3 ubiquitin ligase known as MAPL (Mitochondrial anchored protein ligase) similarly targets Mfn2 for proteolysis, although in response to muscle-wasting stimuli (Lokireddy *et al.*, 2012). Finally, MITOL ubiquitinates Mfn1 during the G2/M phase of the cell cycle leading to mitochondrial fragmentation and allowing mitochondria to be segregated between daughter cells (Park and Cho, 2012).

There is also evidence that ubiquitination activates Mfn1 and Mfn2, promoting mitochondrial fission. The deubiquitinase enzyme USP30 localises to the mitochondrial OMM (Nakamura and Hirose, 2008), and regulates mitochondrial morphology. USP30 deubiquitinates ubiquitinated forms of Mfn1 and Mfn2, thereby inhibiting mitochondrial fusion. Furthermore, USP30 inhibition rescues the mitochondrial fusion defects in Mfn1 and Mfn2 single knockout cell lines (Yue *et al.*, 2014). This indicates that mitofusin ubiquitination permits mitochondrial fusion in mammals, as has previously been demonstrated in yeast (Anton *et al.*, 2013).

3.1.2 Regulation of Mitochondrial Motility by Ubiquitin

As has been described in the introduction (section 1.83), mitochondrial transport is mediated by adaptor proteins Miro1/2 and TRAK1/2. Miro can alter mitochondrial motility in response to calcium levels (MacAskill *et al.*, 2009), however it is also thought to be regulated by ubiquitination in response to mitochondrial membrane potential ($\Delta\psi m$) (Liu *et al.*, 2012). PINK1 (PTEN Induced Kinase 1), a kinase that acts upstream of the E3 ligase Parkin, is present in a protein complex with Miro and Milton on the OMM (Weihofen *et al.*, 2009; Wang *et al.*, 2011c; Liu *et al.*, 2012), and it is proposed that PINK1 phosphorylates Miro, dependent on mitochondrial membrane potential ($\Delta\psi m$). This activates the ubiquitination and proteasomal degradation of Miro in a Parkin-dependent manner (Liu *et al.*, 2012; Sarraf *et al.*, 2013). The degradation of Miro disconnects receptor-adaptor-motor protein complexes, so that mitochondria become stationary. Since mitochondrial movement is necessary for fusion, this may serve to quarantine damaged and depolarised mitochondria for degradation by mitochondrial autophagy (mitophagy). This is supported by the observation that the loss of Miro promotes the removal of depolarised mitochondria by mitophagy (Liu et al., 2012).

It has also been proposed that the E3 ubiquitin ligase MULAN (Mitochondrial Ubiquitin Ligase Activator of NF-κB) plays a role in the regulation of mitochondrial trafficking by ubiquitination. MULAN knockdown causes the perinuclear aggregation

of mitochondria (Li *et al.*, 2008), similar to phenotypes observed upon the disruption of mitochondrial trafficking proteins KIF5B (Tanaka *et al.*, 1998) and Miro (Fransson *et al.*, 2003). This indicates that MULAN may regulate mitochondrial trafficking by the ubiquitination of OMM proteins. However, to confirm this, it would be necessary to identify the OMM substrate proteins of MULAN that mediate this effect.

3.1.3 Mitochondrial Quality Control

Mitochondrial dynamics are important not only in maintaining mitochondrial morphology, but also in maintaining the integrity of mitochondrial DNA (Parone *et al.*, 2008; Chen *et al.*, 2010b). Furthermore, both ubiquitination and mitochondrial dynamics are key players in mitochondrial quality control (Section 1.9.3). Therefore, if both the ubiquitin proteasome system and consequently mitochondrial dynamics are compromised, it is reasonable to hypothesise that mitochondrial will become increasingly dysfunctional.

3.1.4 UCHL1

As I have described in the introduction, UCHL1 is a deubiquitinase enzyme, which has the capacity to generate monomeric ubiquitin through its C-terminal hydrolase activity (Larsen et al., 1998), and stabilise monomeric ubiquitin by binding to it (Osaka et al., 2003). Complete inhibition of UCHL1 C-terminal hydrolase activity will cause a moderate disruption to ubiquitin homeostasis, mimicking oxidatively modified UCHL1 and the UCHL1^{I93M} mutation associated with Parkinson's disease, which lose between 40 and 80%, and around 55% of their hydrolase activity, respectively (Nishikawa *et al.*, 2003).

Inhibition of UCHL1's monoubiquitin binding activity will cause a more profound depletion of monoubiquitin (reducing ubiquitin levels by around 40%), thereby creating an *in vitro* situation that is physiologically relevant to the decline of the ubiquitin proteasome system with age.

In this thesis I will examine the following hypothesis: 'Ubiquitin depletion caused by UCHL1 inhibition or knockout will disrupt mitochondrial trafficking, fission and fusion and cause the accumulation of dysfunctional mitochondria'

This chapter will focus on the assessment of mitochondrial trafficking, fission and fusion *in vitro,* and chapter 4 will assess whether mitochondrial are dysfunctional *in vivo* in UCHL1 knockout mice.

3.1.5 Aims of this study

The primary aim of this study is to investigate whether the compromise of the ubiquitin proteasome system, which is often observed in ageing and neurodegenerative diseases of ageing, is causally related to the mitochondrial dysfunction that often accompanies it. I will aim to answer the following questions: Is the ubiquitin proteasome system required for the proper functioning of mitochondrial dynamics? Does the inhibition of UCHL1 C-terminal hydrolase activity or ubiquitin stabilisation activity cause a decrease in levels of mitochondrial motility, fission or fusion, or affect mitochondrial morphology?

3.2 Effects of UCHL1 and DUB Inhibition on Mitochondrial Dynamics

3.2.1 Methodology and Methods Development

3.2.1.1 Mouse Cortex Neuronal Cells

This study was done using neurons from the cortex of mouse brains, in order to ensure that it is physiologically relevant to both UCHL1 knockout mice and the ageing human brain. In order to assess mitochondrial dynamics, it is essential that the mitochondrial network is simple and that individual mitochondria can be clearly distinguished. Therefore the selection of neurons is beneficial in this respect; long, thin neuronal processes force mitochondria to separate and move bi-directionally up along the axon or dendrite. This is far easier to accurately quantify than the movements of mitochondria in the complex networks observed in fibroblasts, for example.

3.2.1.2 Mitochondrial Probe: MitoRFP

Dyes for the visualisation of mitochondria can be categorised into two groups: mitochondrial membrane potential ($\Delta\Psi m$) dependent, eg. Rhodamine dyes such as TMRE (Tetramethylrhodamine, ethyl ester); and $\Delta\Psi m$ independent, for example Mitotracker Green. Another option is to use mitochondria–targeted fluorescent proteins, known as mitochondrial probes. It is thought that mitochondrial probes show less photobleaching than mitochondrial dyes, and lack the side effects on mitochondrial function that dyes are thought to cause when interacting with photons from the laser, such as inhibition of the respiratory chain and oxidative damage (Twig *et al.*, 2006). Additionally, the fluorescence of mitochondrial probes such as Mito RFP is far more stable that mitochondrial dyes such as Mitotracker Green and Mitotracker Red, as fluorescence can last several days, as opposed to several hours. Therefore, for my experiments I have chosen to use CellLight™ reagent Mitochondria RFP BacMam 2.0

(Invitrogen), which I will refer to as MitoRFP. MitoRFP is a baculovirus coupled to a mammalian promoter that drives the expression of red fluorescent protein (RFP) with a mitochondrial targeting sequence.

Since the expression of mitochondrial probes at high levels may affect mitochondrial structure and cell viability (De Vos and Sheetz, 2007), I firstly determined the optimal volume of MitoRFP to maximise visibility of mitochondria, whilst reducing adverse effects on mitochondrial structure and cell viability. This was done by trying various levels of MitoRFP, centred on the suggested concentration from the manufacturer's instructions, and assessing the levels of cell death in the neuronal culture, as well as the transfection efficiency of MitoRFP. Based on these results, 5µl MitoRFP/well was taken to be optimal.

3.2.1.3 UCHL1 and Deubiquitinase Inhibitors

In order to characterise the effects of ubiquitin on mitochondrial motility, fission, fusion and morphology, mitochondria were tracked in neurons treated with three different inhibitors (two inhibitors of UCHL1 activity and one general deubiquitinase inhibitor).

LDN-91946 inhibits the C-terminal hydrolase catalytic activity of UCHL1 in an uncompetitive manner, by binding to the Michaelis complex (a complex between a form of the enzyme and the substrate) (Mermerian *et al.*, 2007). LDN-91946 has an IC_{50} between 2-3µM, and inhibits 80% of UCHL1 hydrolase activity at 10µM. Furthermore, no cytotoxicity was observed upon treatment of N2A neuroblastoma cells with up to 100µM LDN-91946 (Mermerian *et al.*, 2007). Therefore I used this inhibitor at a concentration of 25µM, in order to ensure complete inhibition of UCHL1 C-terminal hydrolase activity. A previous study showed that in fibroblasts, 25µM LDN-91946 causes a significant reduction in levels of the antioxidant glutathione (Coulombe *et al.*, 2014).

Neurons were also treated with the inhibitor PR-619 at 50µm, to demonstrate the necessity of deubiquitination to mitochondrial dynamics. PR-619 is a reversible inhibitor of deubiquitinase enzymes and ubiquitin-like isopeptidases. It inhibits a broad range of deubiquitinase enzymes, including UCHL1, UCHL3, and UCHL5 as well as many USPs (Ubiquitin Specific Proteases) and other forms of DUB, however has limited off-target effects on other families of proteases, including cysteine proteases (Altun *et al.*, 2011). Treatment of cells with PR-619 results in the accumulation of both ubiquitin and SUMO-conjugated proteins, since ubiquitin is not being recycled or

salvaged due to deubiquitinase inhibition. PR-619 is effective between 25 and 50μm, and only exhibits cytotoxicity after 6 hours incubation at concentrations higher than 50μm in human embryonic kidney cells (Altun *et al.*, 2011).

Inhibition of UCHL1's hydrolase activity (using LDN–91946), which salvages monomeric ubiquitin from small ubiquitin adducts, did not cause any disruption to mitochondrial dynamics, however general deubiquitinase inhibition did have an effect. Therefore, I also wanted to assess whether the ubiquitin-binding function of UCHL1 may have a role in maintaining mitochondrial dynamics, as this function of UCHL1 has a much greater effect on levels of monomeric ubiquitin. This experiment was performed much later on in the course of the PhD, due to a change of circumstances meaning limited access to the microscope and facilities used for the initial experiment. The effect of UCHL1 monoubiquitin stabilisation was assessed using the UCHL1 inhibitor LDN-57444. LDN-57444 is a potent, reversible and competitive active site-directed inhibitor of UCHL1, with IC_{50} = 0.88μM. It is thought to protect the catalytic cysteine which is required for the binding and stabilisation of monomeric ubiquitin (Liu *et al.*, 2003), and has been demonstrated to cause a reduction of ubiquitin levels in cultured neurons by approximately 40% (Cartier *et al.*, 2009). This is comparable to the reduction in monomeric ubiquitin I observed in UCHL1 knockout mice (Chapter 4, section 1.22).

LDN 57-444 was used at 5μM; this concentration ensures that at least 90% of UCHL1 enzymatic activity is inhibited, without causing inhibition of UCH-L3 (Liu *et al.*, 2003) . LDN 57-444 was also trialled at 10μM, as this would inhibit 95% of UCHL1 enzymatic activity; however LDN-57444 at this concentration appeared to cause cell death in primary neurons. A study on the cytotoxicity of LDN-57444 in human neuroblastoma cells (SK-N-SH) revealed that treatment of cells with 5μM LDN-57444 for 24 hours does not reduce cell viability, however doses of 25μM or more cause cell death (Tan *et al.*, 2008).

3.2.1.4 Microscopy

Live cell imaging was undertaken using a Zeiss Cell Observer Spinning Disk microscope, with an environmental chamber, allowing cells to be maintained at constant humidity, 37°C, 20% O_2 and 5% CO_2 during imaging. This microscope utilises the Yokogawa CSU-X1 Spinning Disk (Confocal Scanning Unit), which makes it possible for emission light from multiple points on the sample to be collected simultaneously. This not only means that images can be collected with relatively low exposure to laser

light (compared to confocal laser scanning microscopy, for example), but also enables a very high rate of image capture. Therefore spinning disk microscopy is ideal for live cell imaging, particularly for samples that have weak signal or that are prone to photobleaching. This system was used with the QuantEM:512SC EMCCD (Electron Multiplying) Camera. This system enabled me to take one z-stack image (3 z-planes) every three seconds, the limiting factor being the exposure time of the EMCCD camera required to give the best signal to noise ratio. Images were taken using a 561nm laser, and a 100X plan apochromat oil objective, and recorded using Zeiss Axiovision 4.8 image processing software. At each time-point, images were taken on three focal planes to aid the analysis of mitochondrial fission and fusion events; by using z-stack images it is possible to distinguish between two mitochondria that have fused, and two mitochondria that are in the same x-y plane but different z planes. Z-stacks were taken at an interval of 3 seconds, as this is sufficient for tracking mitochondria and thus assessing mitochondrial motility (De Vos and Sheetz, 2007).

3.2.1.5 Assessment of Laser Phototoxicity and Photobleaching

Since laser exposure is known to decrease mitochondrial motility (Ligon and Steward, 2000) and cause photobleaching, assays were carried out in order to determine live cell imaging conditions whereby mitochondria may be imaged every 3 seconds without adverse effects on signal intensity, and without causing phototoxicity. Live cell imaging was carried out for periods of 10 minutes at varying laser intensity (5%, 25%, 50%, 75%, 100%); 3 videos were captured under each condition. The imaging area was spread over 4 wells of primary neurons cultured under the same conditions, to limit the effects of cumulative laser exposure resulting from taking multiple time lapse videos in a small area of cells. All cells imaged had been transfected with 5µl MitoRFP.

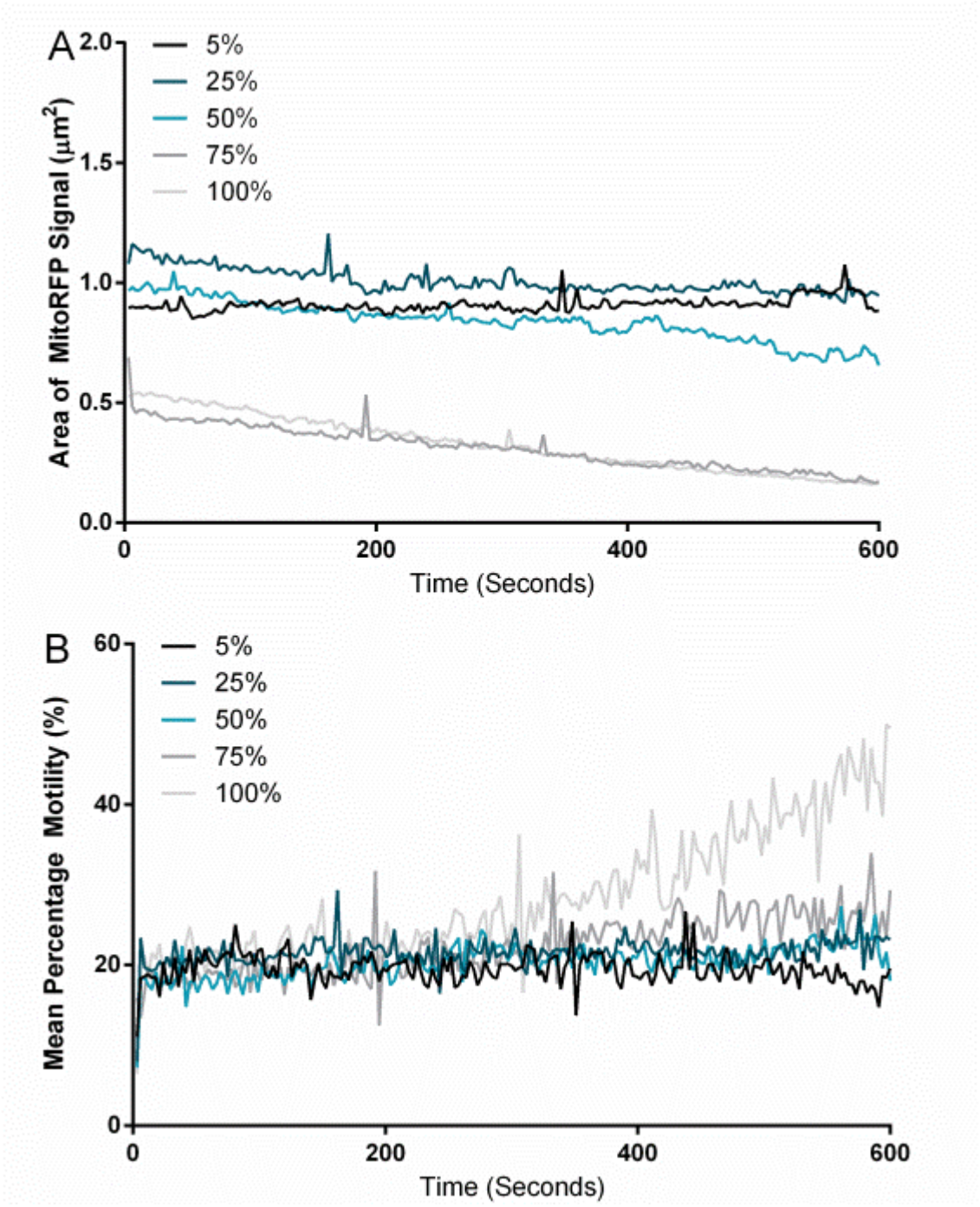

Figure 3.1: Photobleaching and Laser Phototoxicity Assay.
A) Lines represent the mean area of MitoRFP signal (n=3). B) Lines represent mean percentage motility of mitochondria, defined in section 3.2.1.6 (n=3). Images were captured at an interval of 3 seconds over a 10 minute imaging period at varying laser intensities (5% - 75%), see legend.

Figure 3.1A demonstrates that photobleaching occurs when neurons transfected with MitoRFP are imaged every 3 seconds with a laser intensity of 25% or more, using the Zeiss Cell Observer Spinning Disk system. This is shown by a progressive decrease in the area of MitoRFP signal that is over the image analysis threshold over the time-course of imaging, due to bleaching of the RFP flourophore. When live-cell imaging is carried out using the 561nm laser at 5% intensity, the area of MitoRFP signal remains

constant over the 10 minute imaging period. Therefore, it is acceptable to image mitochondria at an interval of 3 seconds for 10 minutes without causing photobleaching.

In order to ensure that the level of laser exposure is not causing phototoxicity, which is known to decrease mitochondrial motility, (Ligon and Steward, 2000) the percentage mitochondrial motility was also assessed for each level of laser intensity. This is determined by working out the percentage area of MitoRFP signal that has moved between imaging time points, and is explained in detail in Section 3.2.1.6. Figure 3.1B shows that there is no decrease in the level of mitochondrial motility over the imaging time-course, and therefore the level of laser exposure is suitable for assessing mitochondrial motility without causing phototoxicity.

Interestingly, percentage mitochondrial motility (defined as the area of mitochondria that moves as a percentage of the total mitochondrial area) appears to increase over the course of live cell imaging at 75% and 100% laser intensity. However, upon more careful examination of the time lapse videos, and data shown in Figure 3.1A, this effect is due to photobleaching. The area of MitoRFP signal decreases over the course of live cell imaging (indicating photobleaching), whilst the mitochondrial area that has moved between timeframes stays relatively constant.

So, considering:

$$\%\, Motility = \frac{Area_t{}^{moved}}{Area_t{}^{total}} \times 100$$

As the denominator ($Area_t^{total}$) tends towards 0, % Motility tends towards infinity, as $1/0 = \infty$ Therefore, as $Area_t^{total}$ decreases, and $Area_t^{moved}$ remains relatively constant, "% motility" increases reflecting photobleaching caused by the laser.

This highlights the importance of carefully optimising image acquisition conditions, to avoid misleading results. This analysis of mitochondrial motility would not be suitable for a situation where photobleaching occurs over the imaging time course, but it is valid when images are taken in conditions that prevent photobleaching.

In conclusion, in order to prevent photobleaching and to avoid phototoxicity, imaging was conducted using a 561nm laser at 5% intensity.

3.2.1.6 Development of Percentage Mitochondrial Motility Analysis

Percentage Mitochondrial Motility is defined as:

$$\%\, Motility = \frac{Area_t{}^{moved}}{Area_t{}^{total}} \times 100$$

Equation 1: Mitochondrial Motility (De Vos and Sheetz, 2007)

The following method was developed to determine mitochondrial motility in time lapse videos using NIH Image J, based on a method outlined in the text book 'Mitochondria' (De Vos and Sheetz, 2007)

Z-stack images comprising the time lapse videos are converted into single images, using the grouped Z project function, 'Sum slices'. Brightness and contrast are then adjusted and a threshold is applied to include maximal levels of mitochondrial signal, whilst minimising noise. Using this thresholded stack, each frame is subtracted from the next to create a 'subtracted stack' – this displays only the pixels that have moved, and so accurately represents the area of mitochondria that has moved in the interval between images being taken . This is done by running the 'subtract stack' macro (Pruess). The measurements function of Image J is used to determine the proportion of white pixels (moving mitochondria) in each timeframe, and the percentage motility is calculated using Equation 1.

3.2.1.7 *Development of Kymograph Analysis*

Kymographs offer an accurate way to determine the number of motile and stationary mitochondria. I developed a method to make kymographs from my live cell imaging data , based on methods in 'Mitochondria'(De Vos and Sheetz, 2007), and using the image analysis program, NIH Image J. Since judging whether a mitochondrion has moved could become fairly subjective, I imposed criteria for 'motile' and 'stationary' mitochondria that would remain consistent for the analysis of all videos. The consensus in the literature was that a mitochondrion can be classified as motile if it is displaced by 5µm (Kang *et al.*, 2008; Sheng and Cai, 2012). Therefore, I used the following criteria for mitochondrial movement: Mitochondria are defined as motile if the centre of the mitochondria has been displaced by at least 5µm during the course of the 10 minute time lapse video.

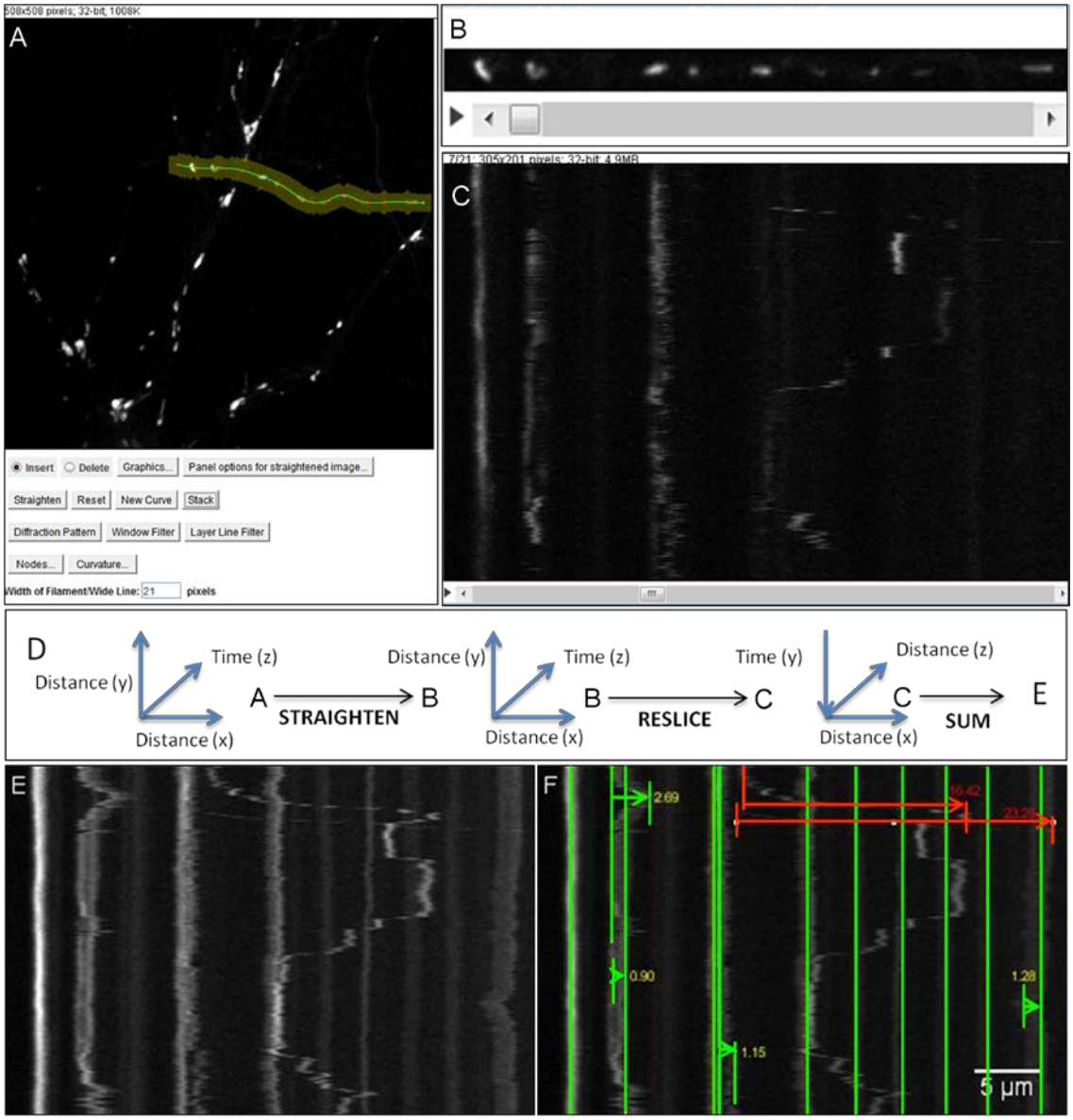

Figure 3.2: Kymograph analysis of live cell imaging to determine differences in mitochondrial motility.

A: Neuronal processes were straightened using the NIH Image J 'Straighten' Plugin (Kocsis *et al*, 1991) to form a straightened stack (B). D: Straightened stacks were 'resliced', so that time is along the y axis (C). The slices in these stacks (C) were then 'Summed', to form a kymograph (E), with time along the Y axis, and distance along the neuronal process along the x axis. Stationary mitochondria appear as vertical lines, whereas motile mitochondria appear as diagonal, or near-horizontal lines. Numbers of motile and stationary mitochondria were quantified (F). Mitochondria whose approximate centre was displaced 5µm or more during the 10 minute recording period were classed as motile (red lines), whereas mitochondria whose centre was not displaced by 5µm were classed as stationary (green lines).

3.2.2 Results

3.2.2.1 Effects of LDN-91946 and PR-619 on Mitochondrial Motility

In order to determine the effect of inhibition of UCHL1 C-terminal hydrolase activity on mitochondrial motility, live cell imaging was carried out in both control (0.1% DMSO), LDN-91 946 treated and PR-619 treated primary neurons.

Kymograph analysis was carried out in order to quantify the number of motile mitochondria (displaced ≥ 5µm) in neurons treated with DMSO, LDN-91946 and PR-619, and the percentage mitochondrial motility was also quantified in all cases.

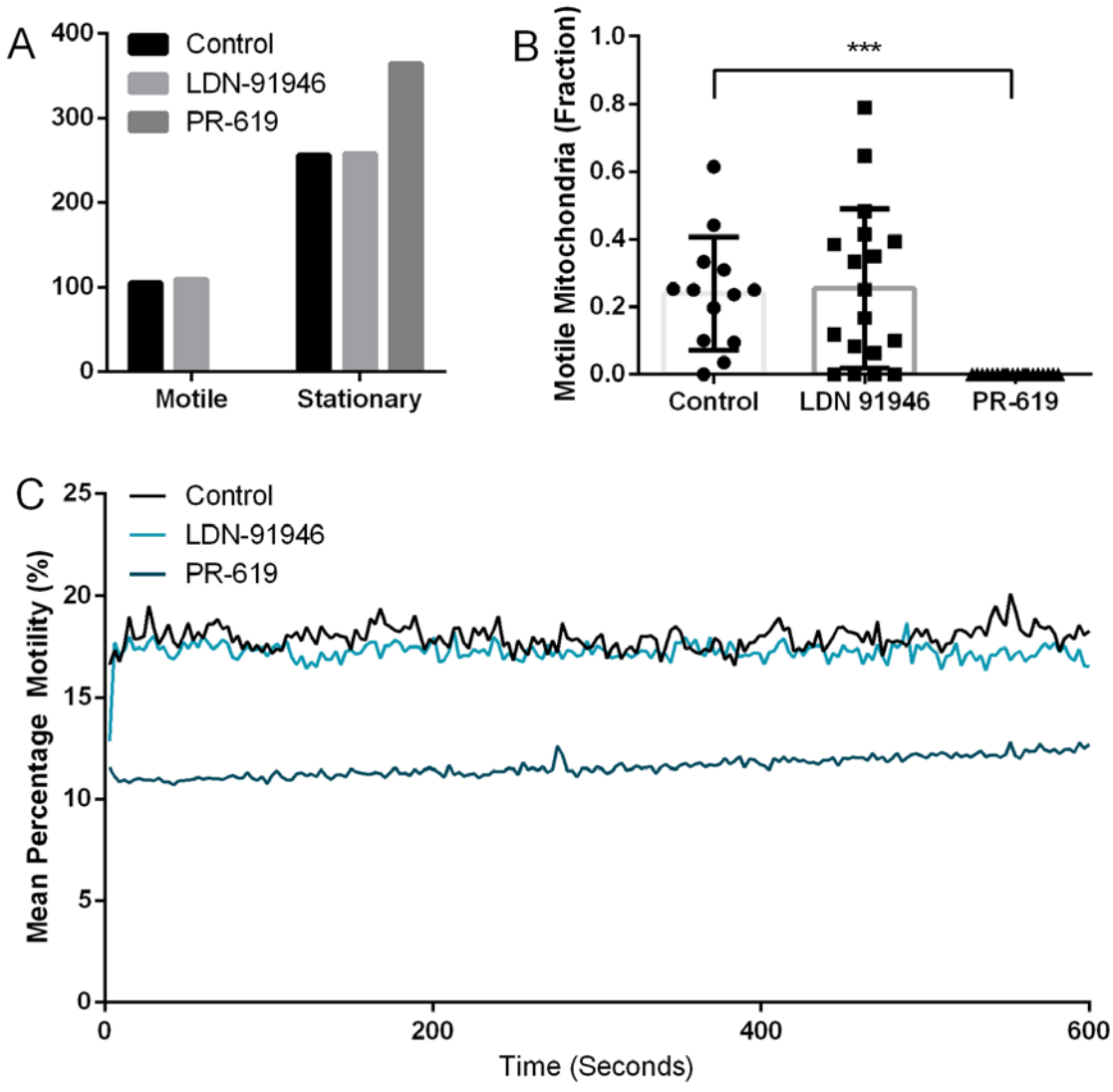

Figure 3.3: Inhibiting UCHL1 hydrolase activity does not disrupt mitochondrial movement.
A) Bar graph showing the total number of motile and stationary mitochondria observed in Control, LDN-91946 treated and PR-619 treated neurons. B) Dot-plot showing the proportion of motile mitochondria in each live cell imaging video. Bars represent mean ± SD. P < 0.0001, ordinary one-way ANOVA with Dunnett's multiple comparisons test. Control vs. LDN-91946: not significant. Control vs. PR-619, ***. N=13, 18, 20 respectively. C) Mean percentage motility of mitochondria for Control, LDN-91946 and PR-619 treated neurons. P=0.0011, ordinary one way ANOVA with Dunnett's multiple comparisons. Control vs. LDN-91946: ns. Control vs. PR-619: **, n=16, 16, 20.

Results show that there is no difference in the number of motile mitochondria in neurons treated with DMSO (Control) and neurons treated with LDN-91946. Numbers of motile and stationary mitochondria are very similar under both conditions (Figure 3.3A), and there is very little difference in the proportion of motile mitochondria between the two conditions, with control and LDN-91946 treated neurons having a mean proportion of motile mitochondria of 0.24 and 0.25 respectively (Figure 3.3B). The broad range DUB inhibitor, PR-619, however, has a dramatic effect on mitochondrial motility, with no motile mitochondria being observed in any of 20 live cell imaging videos, out of a total of 384 mitochondria. The difference in the mean proportion of motile mitochondria in PR-619 treated neurons, compared to control and LDN-91946 treated neurons is highly significant, $p < 0.0001$ (one way ANOVA). In addition, Figure 3.3C shows that the percentage motility of PR-619 treated mitochondria is consistently and significantly lower than control and LDN-91946 treated mitochondria ($p=0.0011$). This demonstrates that, whilst deubiquitinase activity is required for mitochondrial motility, UCHL1 C-terminal hydrolase activity is not.

3.2.2.2 Effects of LDN-91946 and PR-619 on mitochondrial morphology

As shown in Figure 3.4, there is no obvious difference between the morphology of mitochondria in control neurons, and mitochondria in neurons that have been treated with LDN-91946. Mitochondrial morphology is heterogeneous; some mitochondria appear elongated and well-networked, whilst others are shorter and more isolated. There is variation in mitochondrial morphology even within cells, however there is no consistent difference in mitochondrial morphology between control and LDN-91946 treated neurons.

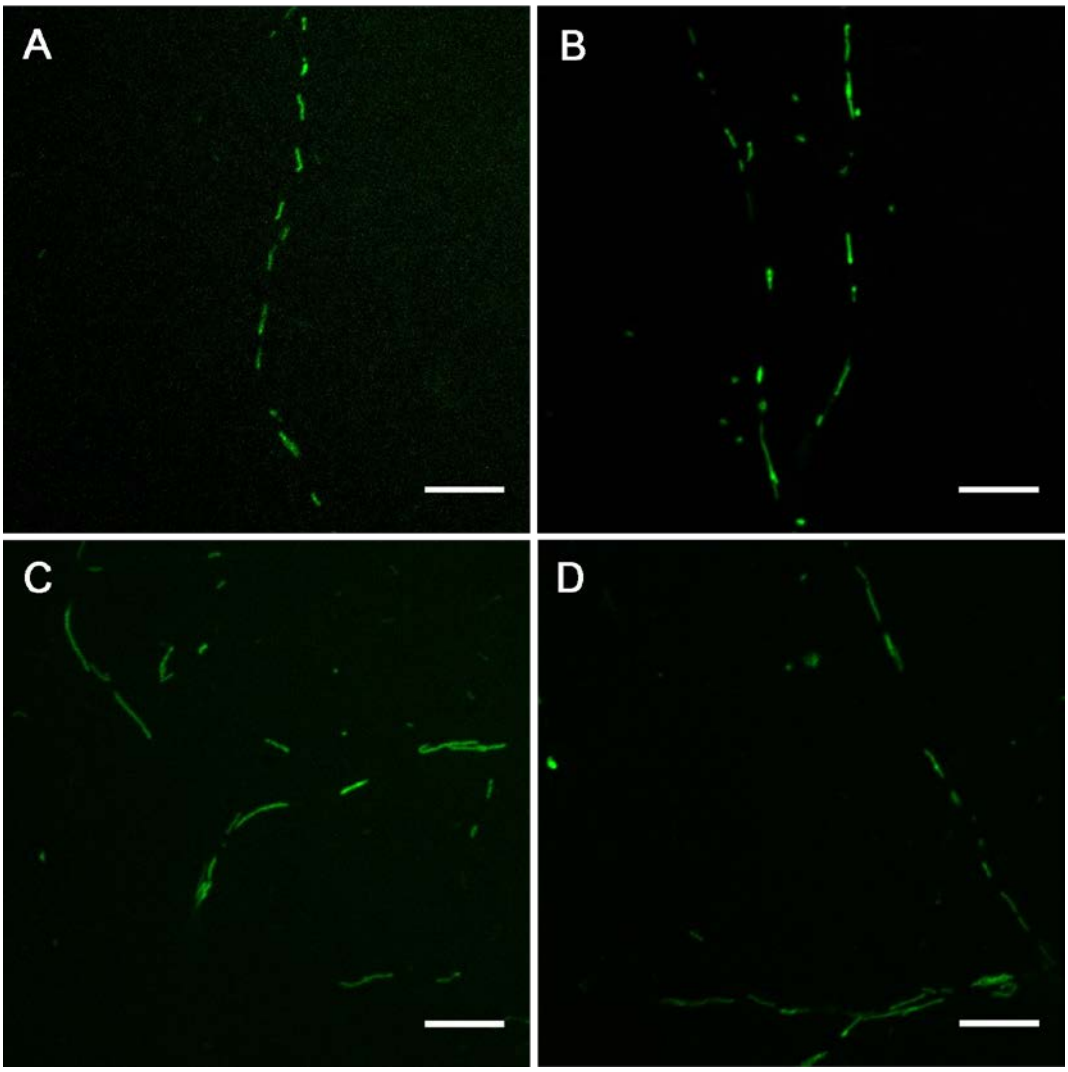

Figure 3.4: Comparison of mitochondrial morphology in neurons with and without UCHL1 inhibitor LDN-91946. A,B) Control (DMSO), C,D) 25μM LDN-91946. Scale bars = 10μm.

The broad-range DUB inhibitor PR-619 has an immediate effect on mitochondria however; after addition of the inhibitor mitochondria do not move (as has been demonstrated in Figure 3.3), furthermore, there is no mitochondrial fission or fusion apparent, as will be discussed in section 3.2.3. This demonstrates that the activity of deubiquitinase enzymes is essential to all processes of mitochondrial dynamics. PR-619 also changes mitochondrial morphology, however this effect is not immediate but occurs gradually over 3-4 hours, as is demonstrated in Figure 3.5. After 1 hour, mitochondria are mostly shorter than mitochondria in control neurons, (Figure 3.4A, B), although there are exceptions, and some have become short and rounded (Figure 3.5A). After neurons have been incubated with PR-619 for 3 hours, all of the mitochondria are rounded in shape, and there are none that are thin and elongated (Figure 3.5C, D).

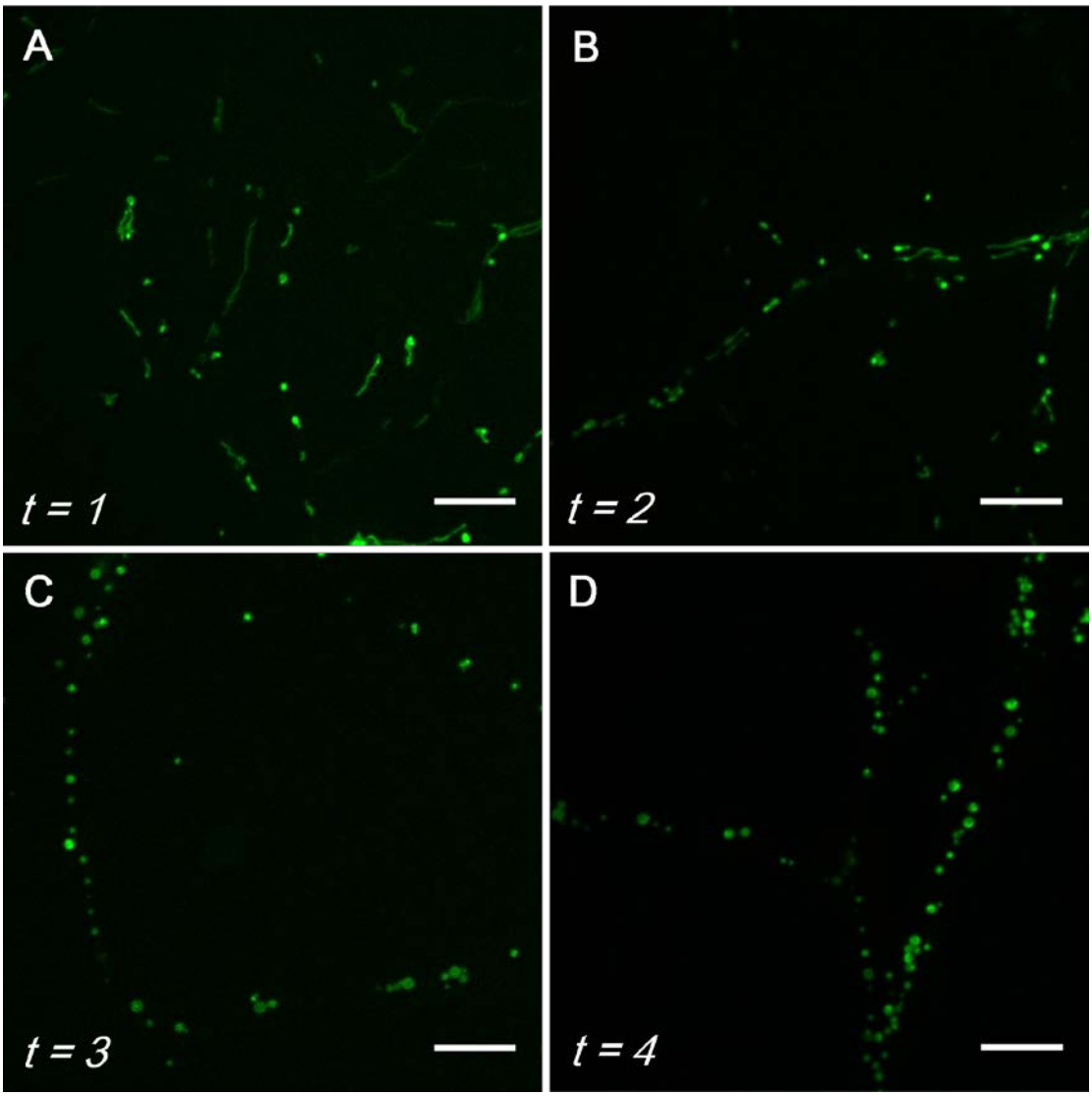

Figure 3.5: Broad- range DUB inhibitor PR-619 causes mitochondria to become rounded and globular in morphology. A-D, images of mitochondria after 1, 2, 3 and 4 hours of treatment with PR-619, respectively. Scale bars=10μm.

To quantify changes in mitochondrial morphology, the Feret's diameter and circularity of each mitochondrion was measured using Image J (NIH). Feret's diameter is defined as the longest linear distance between any two points on the boundary of an object, and is also known as the maximum calliper. Therefore, it is a reliable measure of the length of a mitochondrion. In subsequent studies, mitochondrial length was taken as the 'skeletal length', which is a more accurate measure of length for irregular shapes. This was due to the availability of a more advanced image analysis program, Volocity 6.0.

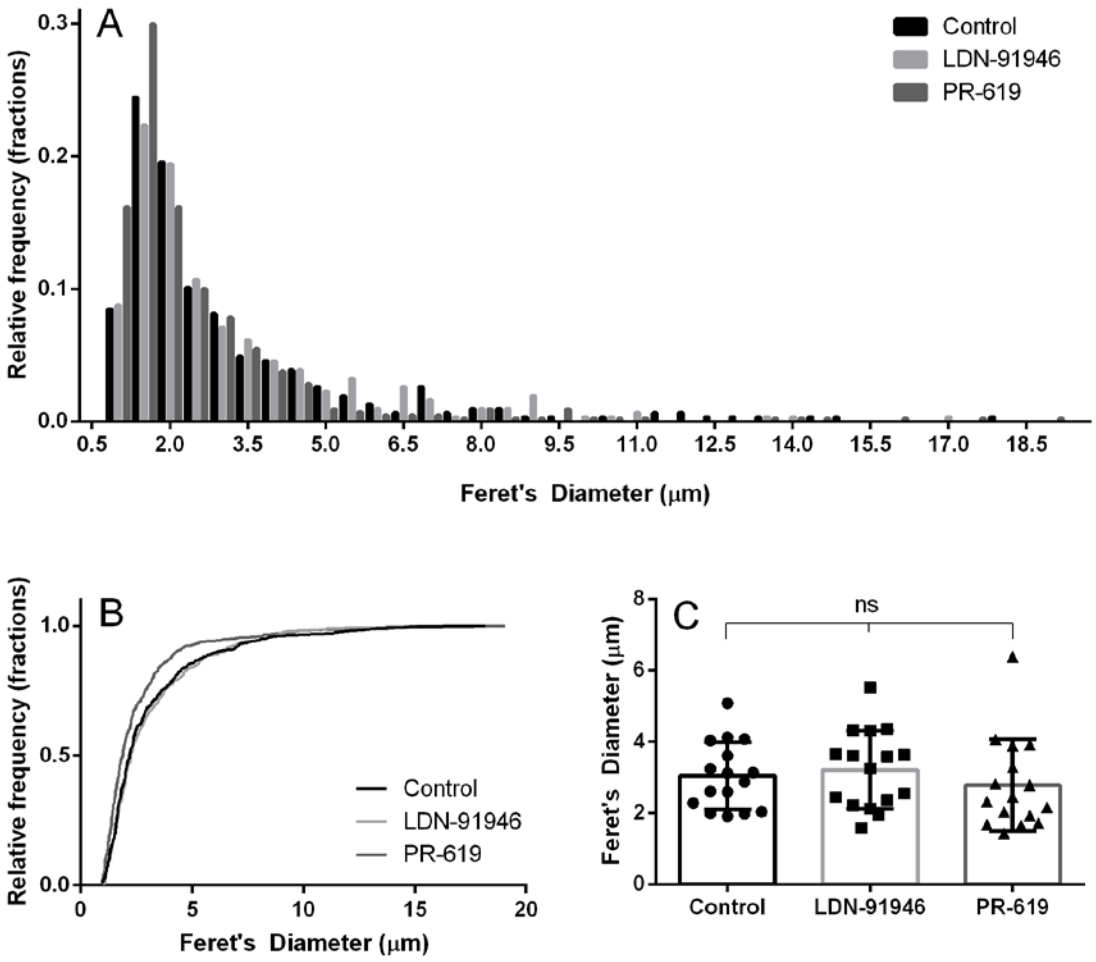

Figure 3.6: Feret's Diameter of mitochondria in control neurons, and those treated with LDN-91946 and PR-619. A) Frequency distribution of the mitochondrial length (μm) B) Cumulative frequency distribution of mitochondrial length (μm), p<0.0001, Kruskal Wallis test with Dunn's post-hoc test: Control vs. LDN-91946 ns, Control vs. PR-619 ****, n=307, 309, 421 respectively. C) Bar graphs of the mean Feret's diameter for mitochondria in each live cell imaging video. Bars represent mean ± SD. Differences between means are not significant, p=0.5500, n=16, ordinary one-way ANOVA with Dunnett's tests for multiple comparisons.

There is little difference in the distribution of mitochondrial length between control and LDN-91946 treated neurons, however Figure 3.6A (dark grey bars) indicates that neurons treated with PR-619 have relatively more short mitochondria, with a Feret's diameter >2μm, compared to control and LDN-91946 treated neurons. The cumulative frequency distributions of Feret's diameter confirm this observation; the PR-619 cumulative frequency distribution is clearly distinguishable from the other two conditions (dark grey), and is significantly different, p<0.0001, according to a Kruskal Wallis test with Dunn's post-test. However, when comparing the mean length of mitochondria for each independent live cell imaging video, the difference between means is not significant, p=0.550, although the data for PR-619 neurons is skewed negatively. This is probably since the PR-619 inhibitor only gradually changes mitochondrial morphology over 3 hours; the data set includes several videos that have

been acquired only 1-2 hours after the addition of the inhibitor, and therefore do not show a dramatic shortening of mitochondria.

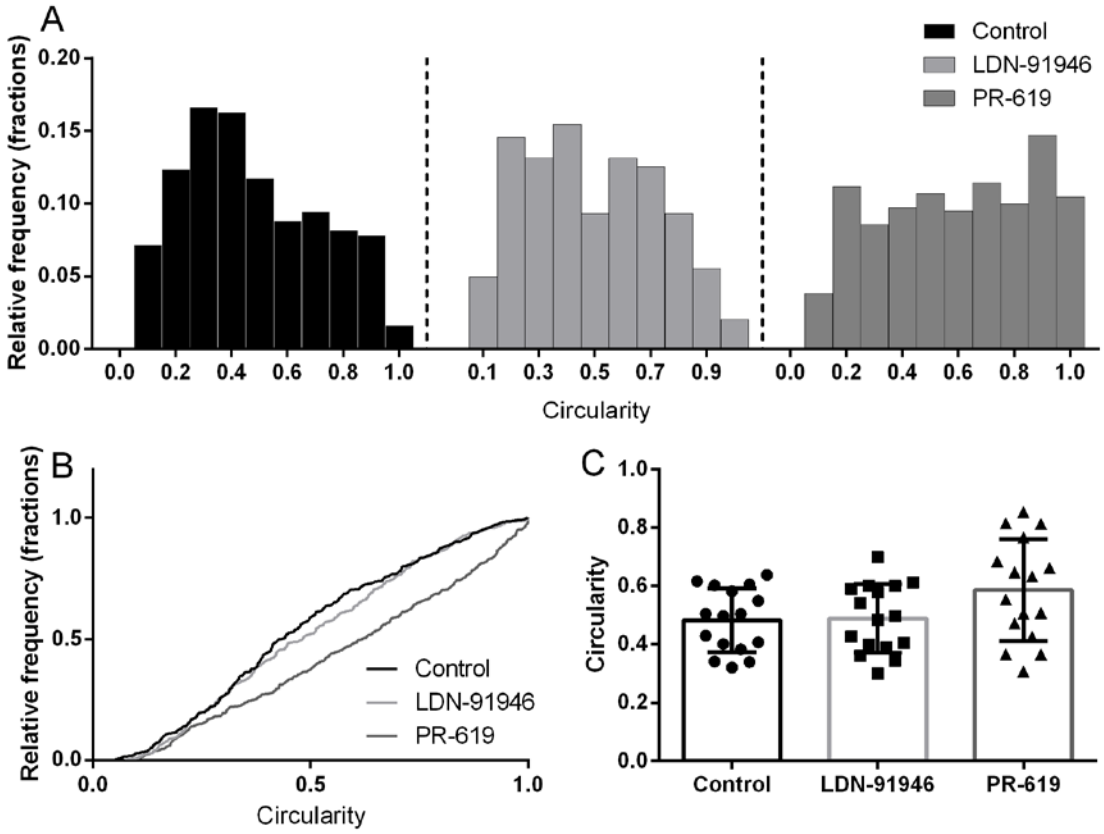

Figure 3.7: Effects of LDN-91946 and PR-619 on mitochondrial morphology.
A) Histograms of the distribution of mitochondrial circularity for control neurons, and neurons treated with LDN-91946 and PR-619. B) Cumulative frequency distributions of mitochondrial circularity, $p < 0.0001$, Kruskal Wallis test with Dunn's post-hoc test: Control vs.LDN-91946 ns, Control vs. PR-619 ****, n=307, 309, 421 respectively. C) Each data point represents the mean circularity of mitochondria of one independent live-cell imaging video. Difference between means is not significant, p=0.0672 one way ANOVA with Dunnett's multiple comparisons test.

Circularity is a mathematical measure of the shape of an object, where a value of 1 represents a perfect circle, and 0 represents an infinitely elongated polygon. It is defined by the formula:

$$Circularity = 4\pi \frac{[Area]}{[Perimeter]^2}$$

Therefore, the circularity of mitochondria was measured using Image J (NIH), to assess whether inhibition of UCHL1 hydrolase activity or inhibition of a broad range of DUBs affects mitochondrial morphology.

Figure 3.7A indicates that the distributions of mitochondrial circularity are fairly similar for both control and LDN-91946 treated neurons; both are negatively skewed, indicating that mitochondria are generally more elongated than they are circular.

However the distribution of mitochondrial circularity is slightly positively skewed for neurons that have been treated with the broad-range DUB inhibitor PR-619, indicating that mitochondria tend to be more circular, and there are less elongated mitochondria. The cumulative frequency distribution also reflects this difference, and a Kruskal Wallis test confirms that the distribution of mitochondrial circularity is significantly different in PR-619 treated neurons compared to controls ($P<0.0001$), and that there is no significant difference between controls and LDN-91946 treated neurons. However, an ordinary one way ANOVA, with Dunnett's post- tests comparing the mean mitochondrial circularity for each independent live cell imaging video finds that the difference between means is not significant, again this is probably due to the data-set including several videos that were taken only 1-2 hours after the addition of the inhibitor.

Holding these results together with the videos from live cell imaging, I can conclude that treatment of neurons with LDN-91946 does not change mitochondrial morphology; both the length and circularity of mitochondria are comparable to controls. Treatment of neurons with the broad-range DUB inhibitor PR-619, however, gradually causes mitochondria to become shorter and rounder, over the course of 3-4 hours. This is reflected in a tendency for PR-619 mitochondria to have a shorter Feret's diameter, and increased circularity.

3.2.3 Effect of LDN-91946 and PR-619 on Mitochondrial Fission and Fusion

In order to determine the effects of UCHL1 C-terminal hydrolase inhibition and broad range DUB inhibition on mitochondrial fission and fusion, kymographs were used to quantify the number of fission and fusion events, which were normalised to neurite length. Results demonstrated that there is no difference between the mean number of fission and fusion events that take place per 100µm neurite length in control and LDN-91946 treated neurons. However, there is a reduction in the number of both fission and fusion events that take place in neurons that have been treated with PR-619, as compared to controls (p~0.0005, p~0.0016, respectively). These results indicate that the C-terminal hydrolase activity of UCHL1 is not required for mitochondrial fission or fusion, whereas deubiquitinase activity is required for mitochondrial fission and fusion.

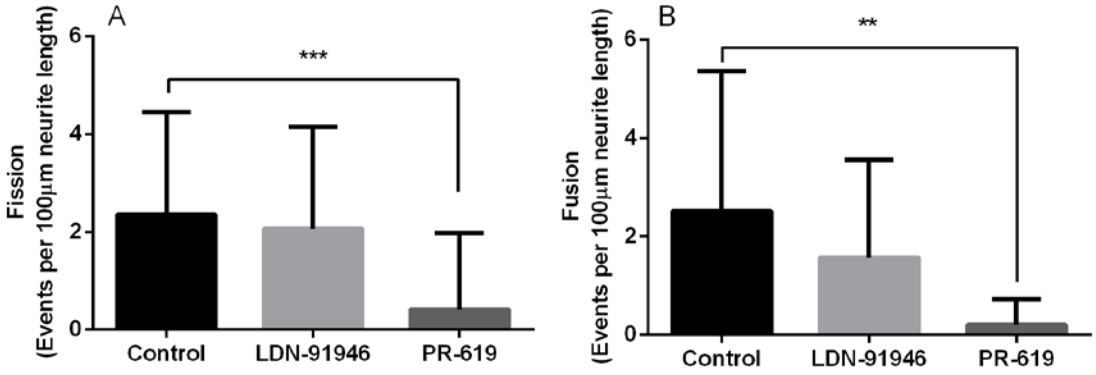

Figure 3.8: Fission and fusion events in control, LDN-91946 and PR-619 treated neurons.
A) Bar graph showing the mean + SD fission events per 100µm neurite length. Difference between means is significant, p ~ 0.0005, control vs. LDN-91946 ns, control vs. PR-619 ***, Kruskal Wallis test with Dunn's post- test for multiple comparisons, n=13, 18, 20 respectively. B) Bar graph showing the mean + SD fusion events per 100µm neurite length. Difference between means is significant, p ~ 0.0016, control vs. LDN-91946 ns, Control vs. PR-619 **, Kruskal Wallis test with Dunn's post- test for multiple comparisons, n=13, 18, 20 respectively.

3.2.4 Inhibition of UCHL1-mediated ubiquitin stabilisation

In order to determine whether inhibition of the ubiquitin-binding function of UCHL1 affects mitochondrial dynamics, a live cell imaging experiment was undertaken, using the inhibitor LDN-57444 in cultured neurons.

Due to an unknown interaction between LDN-57444 and MitoRFP (Appendix1, Figure1), I was unable to continue to use MitoRFP for this experiment and therefore used Mitotracker Green, which is a dye that accumulates in mitochondria regardless of mitochondrial membrane potential. Mitotracker Green is relatively photostable, especially compared to rhodamine dyes such as TMRE; TMRE was ruled out as a mitochondrial dye for this experiment due to its susceptibility to photobleaching. Mitotracker Green was selected over Mitotracker Red as it gives a clearer, brighter, more mitochondria-specific signal, probably as Mitotracker Green is effectively non-fluorescent in aqueous solution, and only becomes fluorescent upon being taken up into mitochondria.

3.2.4.1 Microscopy

In order to perform complicated analyses such as the tracking of mitochondria, it is essential that images are of good quality and have a high signal to noise ratio, and a sufficiently small interval between frames. Although spinning disk microscopy had previously given images of high enough quality for this kind of analysis, imaging for this experiment was carried out on the Nikon TIRF microscope, using TIRF (Total Internal Resonant Fluorescence) microscopy, as this technology was available at the time and more convenient. TIRF microscopy is equally as suitable for live cell imaging and mitochondrial tracking as spinning disk microscopy. TIRF works by restricting the depth of excitation light to around 100nm from the coverslip, thus only capturing fluorescence very close to the coverslip and cell membrane, both limiting out of focus signal from outside of this range, and limiting the amount of light exposure to cells.

Imaging was undertaken using a Nikon 60X CFI Apochromat TIRF oil objective (NA=1.49), in addition to a 1.5X zoom, and using the Photometrics Evolve 512 EMCCD (Electron multiplying charge coupled device) camera to enable the resolution of mitochondria. The perfect focus system was also utilised during the course of imaging to prevent focal drift. Cells were maintained in an enclosed environmental chamber at constant humidity, temperature and O_2 and CO_2 conditions.

3.2.4.2 Development of Image Analysis using IMARIS 7.7

Live cell imaging data was analysed using IMARIS 7.7.1 (Bitplane Scientific Software); the protocol for tracking mitochondria is outlined in Figure 3.9.

Since TIRF requires images to be acquired at a rate of 5 frames per second (fps) at least, live cell videos consisted of 10,000 frames and were very large (approx. 0.7 GB), and therefore could not be analysed by IMARIS. Therefore images were resampled so that they consisted of only 300 frames, were a more reasonable size (0.03 GB) and could be analysed by IMARIS. Resampling time resulted in videos of 0.5 fps (one image every 2 seconds), which is sufficient in order to analyse mitochondrial speed and motility (De Vos and Sheetz, 2007), and for tracking mitochondria in IMARIS.

Since neurons were confluent and Mitotracker Green is taken up into all mitochondria, there were often hundreds of mitochondria per frame. In addition to this, it was often difficult to avoid imaging complex regions such as cell bodies or areas where several neuronal processes cross over, making it difficult for IMARIS to identify and track individual mitochondria. For this reason, images were cropped, so that only a smaller area was selected for analysis. In all cases, the simplest region of the image was chosen (see Figure 3.9A, B), allowing for the accurate measurement of mitochondrial movement and speed.

Mitochondria were tracked using the 'autoregressive motion' protocol. Prior to analysis of all of the data, the protocol was optimised and trialled on several videos to ensure that the tracks and data output were accurate, i.e. a visual estimate of motile mitochondria was compared to the number of motile mitochondria as determined by IMARIS.

In order to create 'surfaces' for mitochondria, 'background subtraction' was enabled, and the minimum diameter for an object to be recognised as a mitochondrion was given as 0.3μm, based on the minimum diameter of mitochondria in the literature (Gerencser *et al.*, 2008). A threshold based on signal intensity was then applied using the interactive histogram. In order to include all mitochondria in the threshold, occasionally small areas of 'noise' were also included, however these were subsequently excluded from the analysis by introducing a filter which excludes anything smaller than 6 voxels (volumetric pixels). Due to normal variations in signal intensity and background between videos, each video was given a threshold manually, so mitochondria were identified accurately. All other elements of the image analysis protocol were kept

constant for all analyses so that the data is directly comparable. The ‘autoregressive motion’ algorithm also allows the user to identify a maximum distance over which a surface can jump, and a maximum ‘gap size’ (the number of frames for which a surface can disappear), which were set as 3 and 2, respectively. The minimum track duration was determined as 4 seconds. These parameters were identified by an iterative procedure whereby a value was estimated and then adjusted based on how representative the track was of the data.

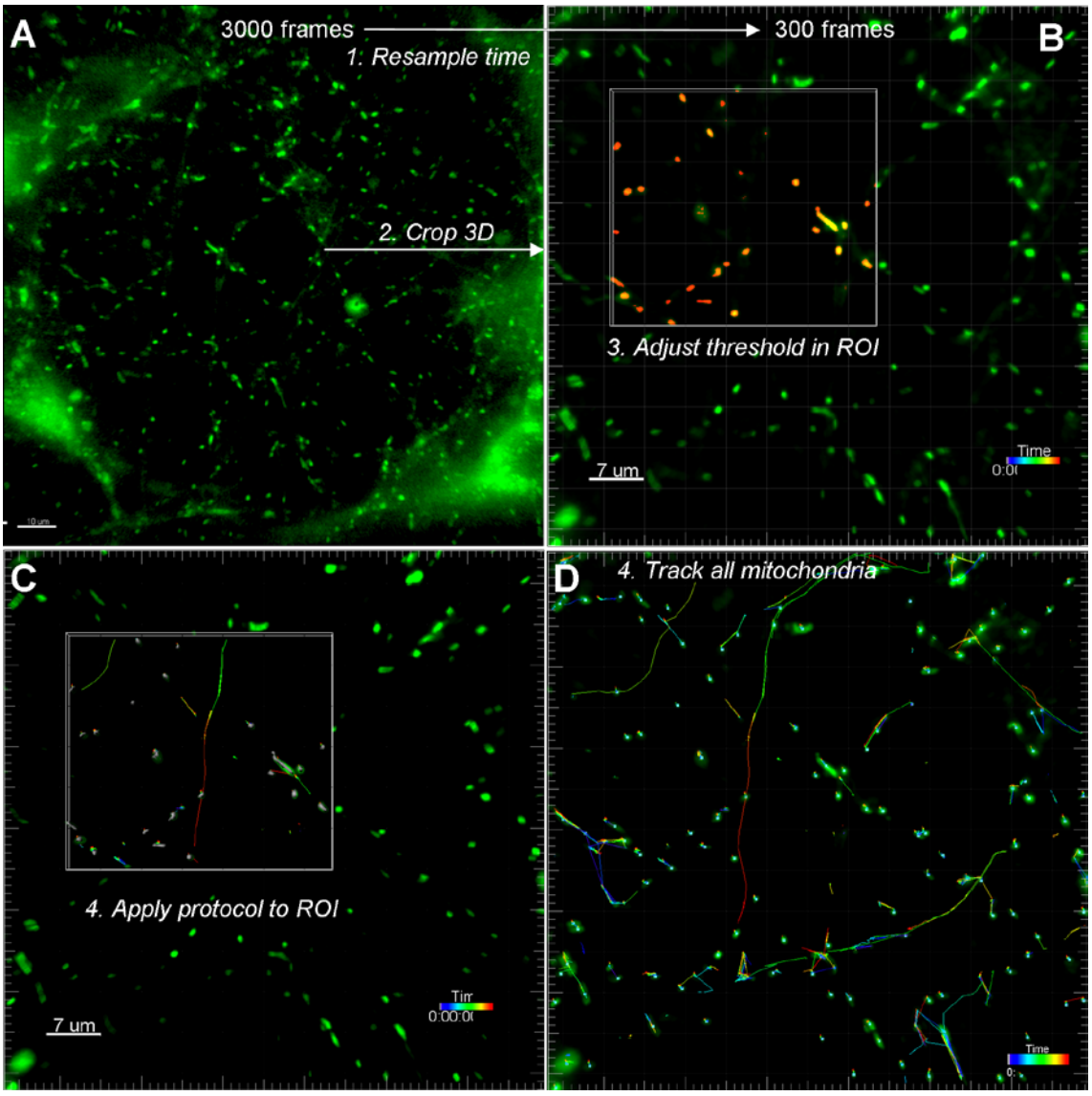

Figure 3.9: IMARIS Image analysis protocol.
A) Images consisting of 3000 frames (5 fps) were resampled to 300 frames (0.5fps), and also cropped to an area of 257x257 pixels. Scale bar = 12µm B) A threshold was applied to mitochondria in an ROI. Scale bars = 7µm (B, C). C) Surfaces are tracked using the ‘autoregressive motion’ protocol, firstly for an ROI, and then for the whole image (D).

3.2.4.3 LDN-57444 does not change mitochondrial morphology

There is no visible difference in mitochondrial morphology or size between neurons that have been treated with LDN-57444 and controls, as is apparent from Figure 3.10.

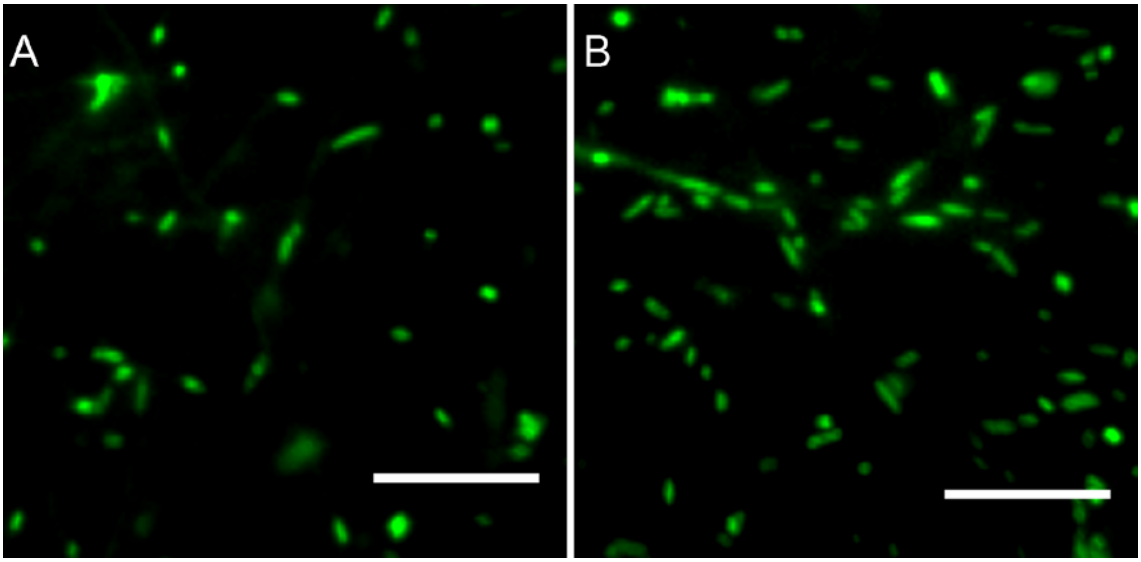

Figure 3.10: LDN-57444 does not change mitochondrial morphology.
A) Mitochondria in control neurons, B) Mitochondria treated with 5μM LDN-57444. Scale bars = 10μm.

In addition, the area of each mitochondrion was monitored throughout the length of the live cell imaging period by IMARIS. Figure 3.11 demonstrates that the area of mitochondria is not significantly changed after treatment with 5μM LDN-57444 for 12 hours (unpaired t-test, p=0.6109, n=4 wells); mitochondria do not become larger or smaller on addition of LDN-57444.

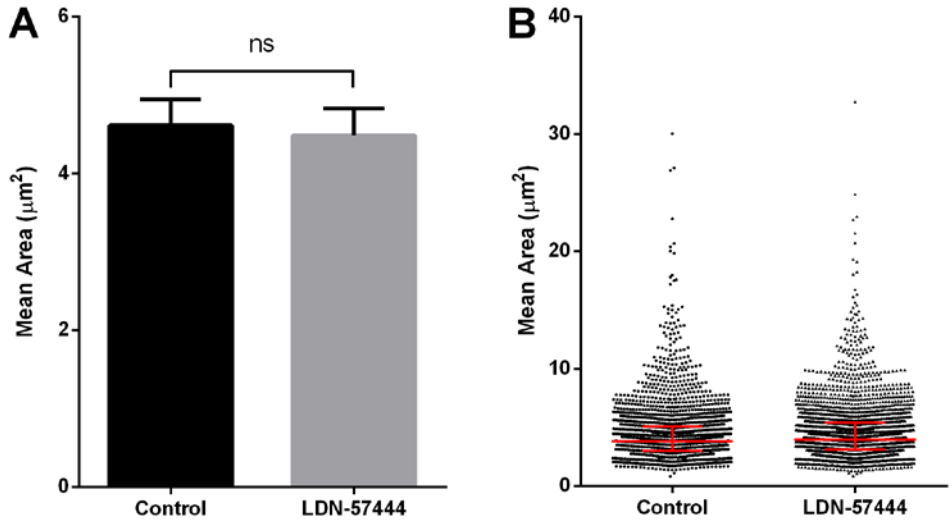

Figure 3.11: Area of mitochondria treated with LDN 57 444.
A) Data represents the median mitochondrial area for each well (n=4), bars show the mean +SD. Difference is not significant, unpaired t-test, p=0.6109. B) Each data point represents the mean area of a single mitochondrion over the duration of the 10-minute imaging period. Bars represent median ± interquartile range.

3.2.4.4 LDN -57444 does not decrease mitochondrial motility

In order to determine whether inhibition of UCHL1 ubiquitin binding activity with 5μM LDN-57444 affects mitochondrial motility, the distance moved by each mitochondrion (track length) was assessed for the duration of live cell imaging, using IMARIS 7.7. As in previous studies, mitochondria were classified as motile if they moved 5μm or more, and stationary if they moved less than 5μm. Figure 3.12B shows the percentage of motile mitochondria for each repeat of the experiment, for both control and LDN-57444. Figure 3.12A shows the mean and standard deviation of the independent repeats (n=4), which do not differ significantly (p= 0.5737, unpaired t-test with Welch's correction). Therefore we can accept the null hypothesis that the UCHL1 inhibitor LDN-57444 does not change the number of mitochondria that move more than 5μm in 10 minutes.

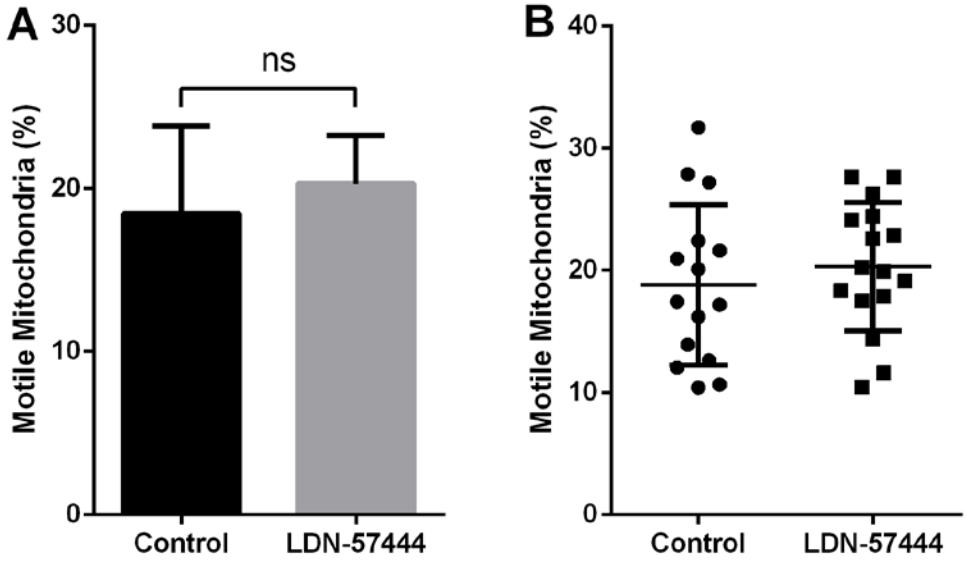

Figure 3.12: LDN 57-444 does not change mitochondrial motility.
A) The number of motile mitochondria (track length > 5μm) expressed as a percentage of the total; bars show the mean for four independent repeats plus standard deviation. Difference between means is not significant (p= 0.5737, n=4, unpaired t-test with Welch's correction) B) The number of motile mitochondria (track length > 5μm) expressed as a percentage of the total; each data point represents one live-cell imaging video, bars show the mean and standard deviation.

3.2.4.5 LDN -57444 does not decrease mitochondrial track length

Figure 3.13 shows the first frame of two live cell imaging videos, along with the mitochondria (green), surfaces (small blue squares) and tracks generated by IMARIS. For both control and LDN-57444 treated neurons there was a wide variation in the degree of mitochondrial motility demonstrated in videos, i.e. in some many mitochondria were moving, in others very few. Figure 3.13 shows tracks of videos which have a near-average level of moving mitochondria.

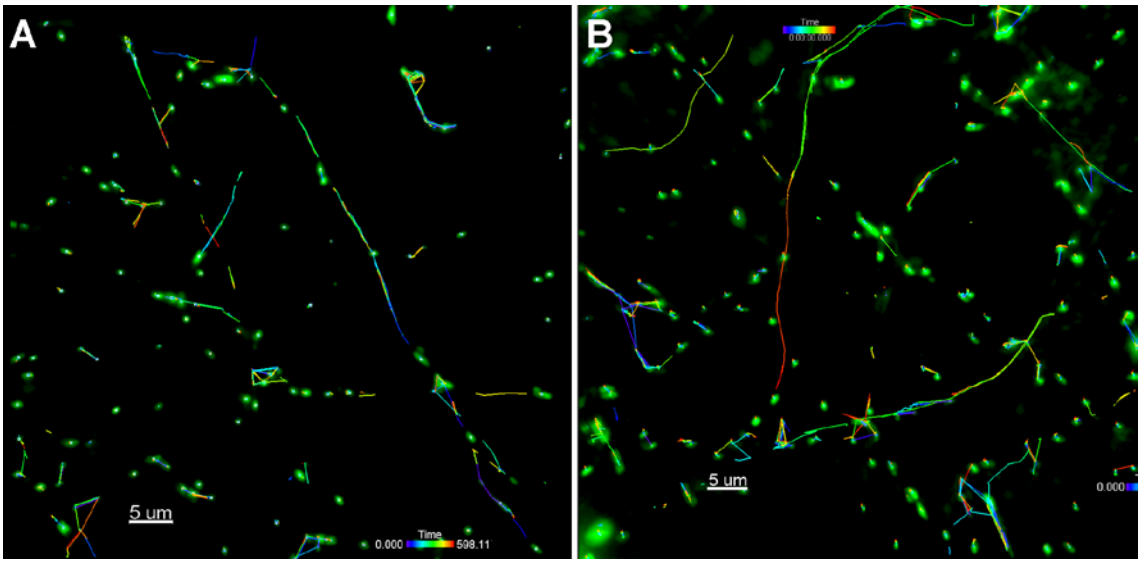

Figure 3.13: IMARIS surfaces and tracks.
A) Control (DMSO), B) 5µm LDN 57-444. The centre of surfaces assigned to mitochondria by IMARIS 7.7 are displayed as blue squares. Tracks are displayed as lines; their colour indicates the time-point when the surface was tracked in that position. Scale bars = 5µm

There is no significant difference between the mean track length for all mitochondria ($p= 0.7708$, unpaired t-test, $n=4$), and for the mean track length of motile mitochondria ($p= 0.9917$, unpaired t-test, $n=4$), Figure 3.14A, B.

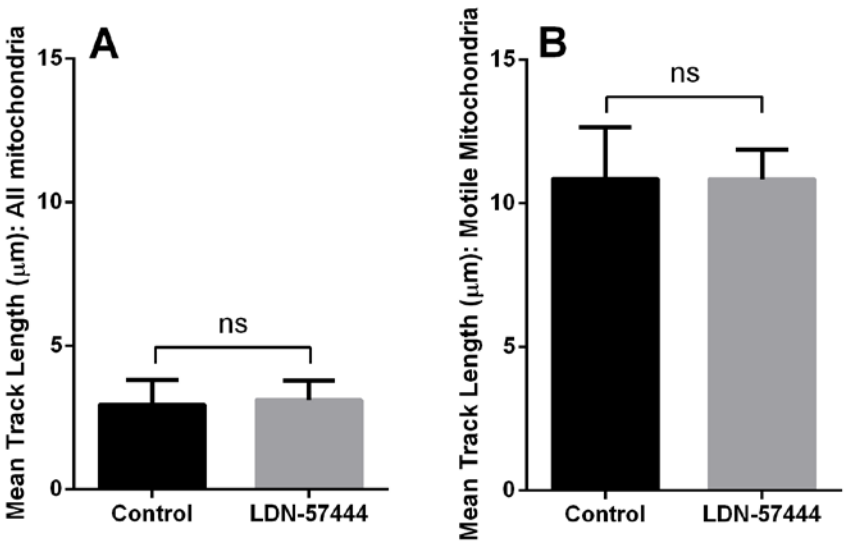

Figure 3.14: Track Length of mitochondria.
A) All mitochondria. Difference not significant, p=0.7708, unpaired t-test, n=4, 95% CI. B) Motile mitochondria. Difference not significant, p=0.9917, unpaired t-test, n=4, 95% CI. Data represent the mean of 4 independent repeats and error bars represent the standard deviation.

Further analysis was carried out on the track lengths of motile mitochondria, to determine whether there is any difference in the movement characteristics of mitochondria after treatment with LDN-57444, such as mitochondria moving, but only over shorter distances.

The frequency distributions of the track lengths of motile mitochondria are very similar for both control and LDN-57444 treated neurons, although it appears that there are slightly more mitochondria with longer tracks after treatment with in the LDN-57444 population (Figure 3.15A). However, there is no difference in the cumulative distributions of the two populations (p= 0.2788, Kolmogorov-Smirnov test), and a Mann-Whitney test demonstrates that there is no difference in the median track length of mitochondria (p=0.4897). In addition, the cumulative frequency distributions are very similar and almost indistinguishable by sight (Figure 3.15B). Therefore we can conclude that depletion of ubiquitin, after treatment with LDN-57444 does not cause mitochondria to move for shorter or longer distances.

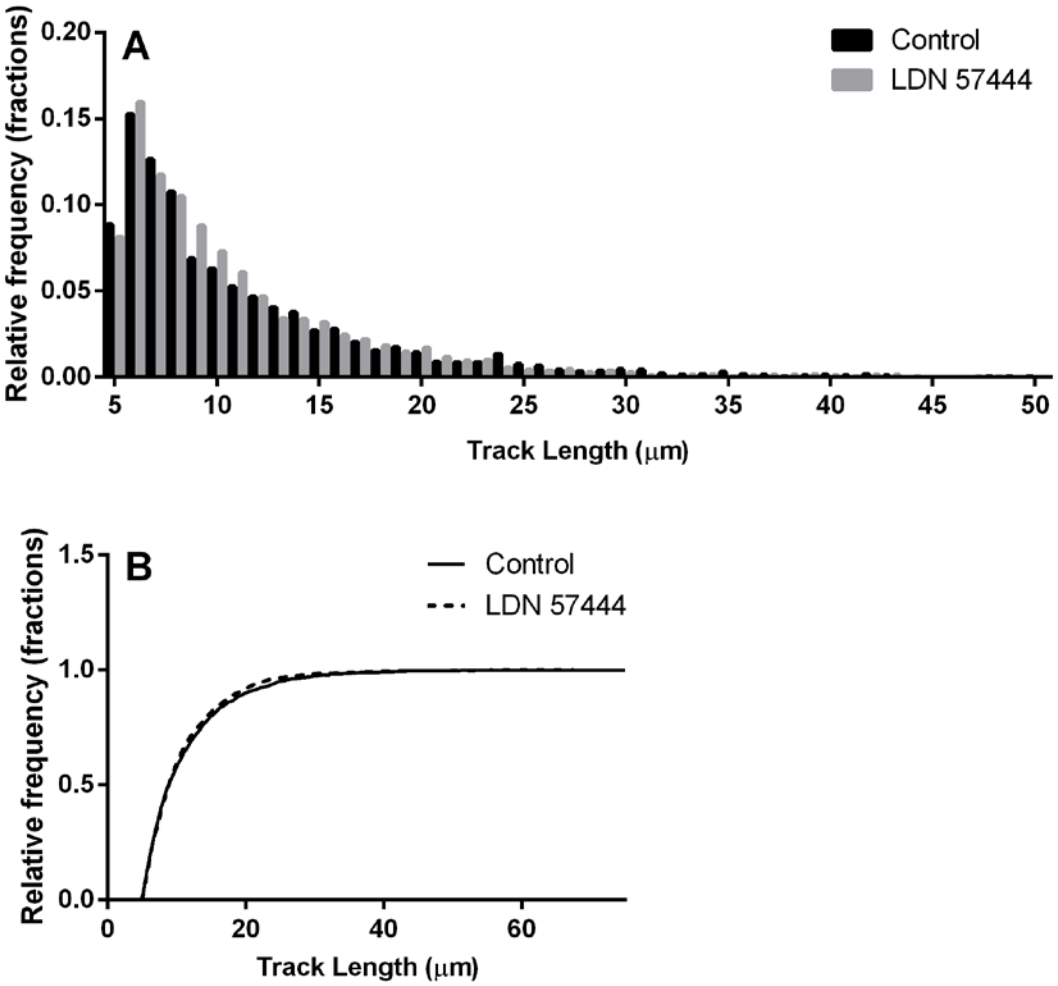

Figure 3.15: Distribution of track lengths of motile mitochondria.
A) Histogram showing the distribution of the track lengths of motile mitochondria. No significant difference between the median of the control and LDN-57444 populations, p=0.4897, Mann Whitney test, 95% CI. B) Cumulative frequency distributions of the track lengths of mitochondria from both control and LDN-57444 –treated neurons. No difference between distributions, p=0.2788, Kolmogorov-Smirnov test to compare cumulative distributions.

3.2.4.6 LDN-57444 does not affect the speed of mitochondria

In order to fully determine whether ubiquitin depletion caused by UCHL1 inhibition has any effect on mitochondrial motility, I also assessed the speed of mitochondria over the 10 minute imaging period. Results show that the average speed of all mitochondria does not differ between control neurons and LDN-57444 treated neurons (p=0.9772, n=4, unpaired t-test). Since the inclusion of stationary mitochondria, or mitochondria that move only very slightly (<5μm in 10 minutes), may have a skewing effect on the data and mask subtle differences in the speed of motile mitochondria, I also determined whether there are any differences in the average speed of motile mitochondria. The mean speed of motile mitochondria in control neurons is 0.500 ± 0.046 μm/second, whereas the mean speed in LDN-57444 treated mitochondria is 0.516 ± 0.036 μm/second. The difference between the two means is not significant (unpaired t-test, p=0.7854, n=4, unpaired t-test), demonstrating that LDN-57444 does not affect the speed at which mitochondria move.

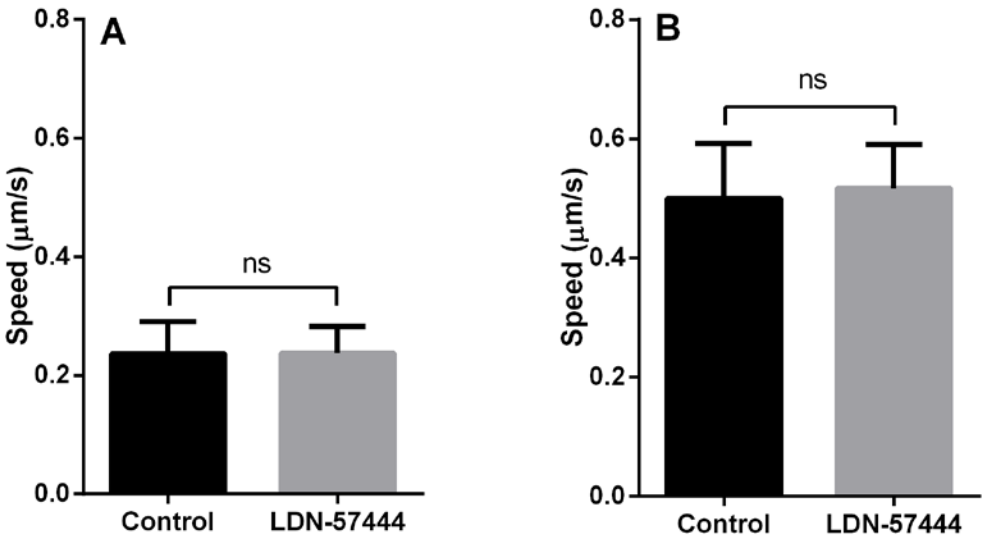

Figure 3.16: Speed of control and LDN-57444 mitochondria.
A) Mean speed of both stationary and motile mitochondria. No significant difference, p= 0.9772, n=4, CI=95%, unpaired t-test. B) Mean speed of only motile mitochondria (track length ≥ 5μm). No significant difference, p=0.7854, n=4, CI=95%, unpaired t-test. Data represents the maximum speed of each mitochondrion during the imaging period, averaged over 4 repeats of 4 independent experiments. Bars represent the mean + SD.

In order to further investigate whether UCHL1 inhibition has any effect on the speed of mitochondria and to examine the data set more thoroughly, I also plotted the frequency and cumulative frequency distributions of the speed of motile mitochondria. From the frequency distribution, it appears that the control population may contain more 'slow' mitochondria (< 0.5μm/second), whilst the LDN-57444 treated population may contain more 'fast' mitochondria (> 0.5μm/second). A Mann Whitney test to compare medians

detected that this difference is significant (p=0.0100). However the medians of the two populations are very similar (Control = 0.4179 μm/s, LDN-57444 = 0.4669 μm/s), and the 95% confidence interval of the difference is very small (0.005406 to 0.04225), therefore the difference is considered statistically significant due to the number of mitochondria in each population being so large (Control, n=2445, LDN-57444, n=2696). Similarly, a Kolmogorov-Smirnov test to compare the cumulative distributions was carried out, and found that the difference in distributions are statistically significant (p=0.0073), although the cumulative distributions plotted in Figure 14B are very similar. It is doubtful that the statistically significant differences in medians and cumulative distributions are biologically significant, especially since the velocity of neuronal mitochondria has generally been shown to fall within the range of 0.3 to 1.0μm/s in the literature (Birsa *et al.*, 2013); these figures show that a difference between 0.4179 and 0.4669μm/s is physiologically irrelevant. It is likely that this small difference has occurred by the chance selection of faster mitochondria when imaging LDN-57444 treated neurons.

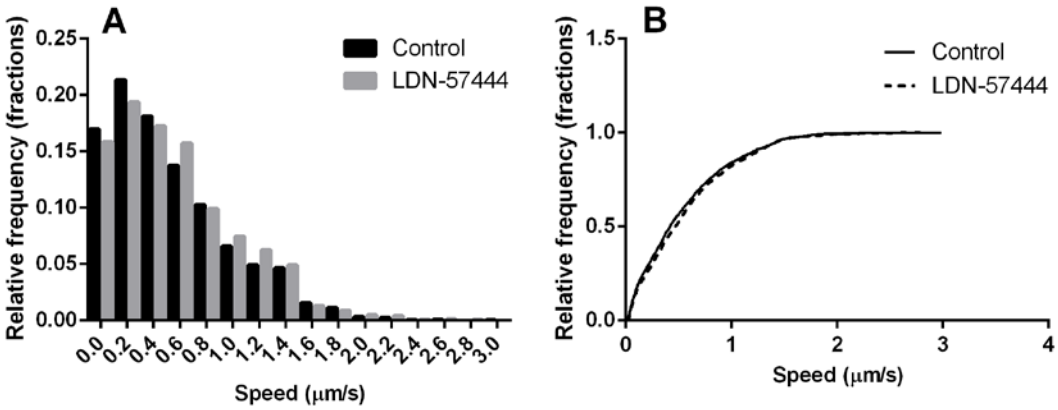

Figure 3.17: Distribution of the speed of motile mitochondria.
A) Frequency distribution, B) Cumulative Frequency distribution. The difference between the median speed of control and LDN-57444 populations is significant, p=0.0100, n=2445, 2696 respectively, Mann-Whitney test. The difference between cumulative distributions is significant, p=0.0073, Kolmogorov-Smirnov test.

3.2.4.7 LDN-57444 does not Alter the Rate of Mitochondrial Fission or Fusion

In order to determine whether treatment of neurons with 5µM LDN-57444 affects mitochondrial fission and fusion dynamics, the rates of fission and fusion events were estimated. The number of 'disconnected components' at each time point (ie. the number of mitochondria) was quantified, and the change in the number of mitochondria, given as a percentage of the total number was taken as the rate of mitochondrial fission or fusion, where a negative value indicates fusion, and a positive value indicates fission:

$$\%\ Change = \frac{Number\ of\ mitochondria_{t=2} - Number\ of\ mitochondria_{t=1}}{Number\ of\ mitochondria_{t=2}}\ x\ 100$$

Figure 3.18 shows the mean rate of change in the number of mitochondria for each time-point of 4 independent repeats (each independent repeat being a mean of 4 live cell imaging videos). The rate of fission and fusion is evenly distributed around 0, and there is no difference between the mean rate of change LDN-57444 treated neurons, as compared to control (p=0.8415). Since averaging the data for each independent repeat has an effect of smoothing the data, I also plotted a histogram of the rate of mitochondrial fission and fusion for each time-point in all 36 live cell imaging videos (Figure 3.19). This shows that the distribution of fission and fusion rates for both control and LDN-57444-treated neurons is normally distributed around 0, and is neither negatively skewed (favouring fusion) or positively skewed (favouring fission). Furthermore, there is no significant difference between the distributions (p=0.5144), or between the medians (p=0.8662), showing that inhibition of the ubiquitin-stabilising activity of UCHL1 does not affect mitochondrial fission or fusion.

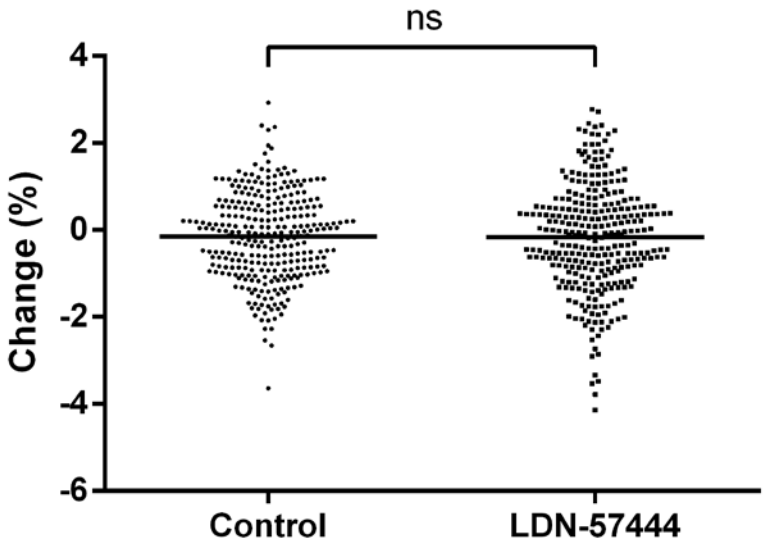

Figure 3.18: Mean rate of change in number of mitochondria.
Difference between means is not significant, p=0.8415, n=4, unpaired t-test with Welch's correction.

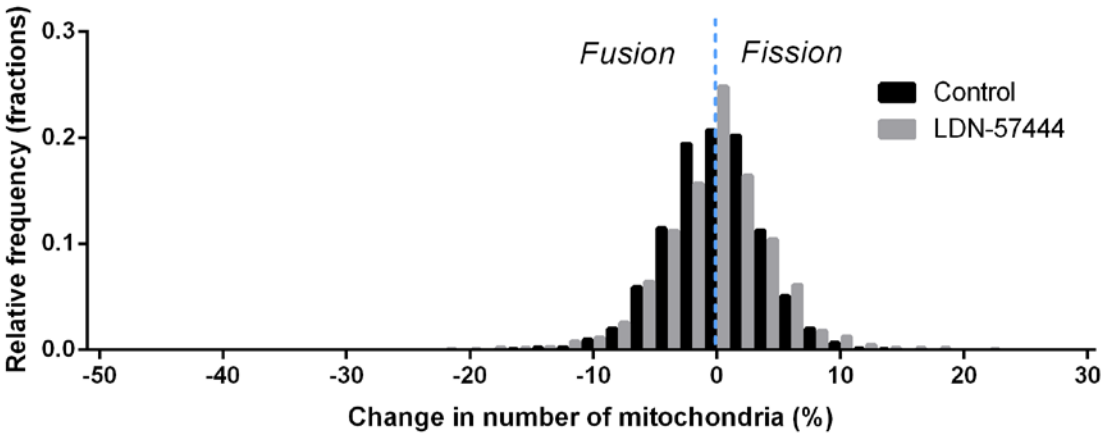

Figure 3.19: Rate of Mitochondrial Fission and Fusion:
Data represents the percentage change in the number of mitochondria, for 300 time-points, for 36 live cell imaging videos. Difference between medians is not significant, p=0.8662, Mann-Whitney test. Difference in cumulative distributions is not significant, p=0.5144, Kolmogorov Smirnov test.

3.3 Discussion

This study aimed to determine whether the inhibition of the deubiquitinase enzyme UCHL1 would disrupt mitochondrial morphology and dynamics. I have found that the inhibition of UCHL1 with inhibitors LDN-91946 and LDN-57444 does not have any effect on mitochondrial motility, fission, fusion or morphology. However, the broad-range inhibitor of deubiquitinase enzymes, PR-619, prevents mitochondrial trafficking in neurons, and greatly decreases mitochondrial fission and fusion. Furthermore, it has a gradual effect on mitochondrial morphology, causing mitochondria to transition from elongated tubules to rounded puncta, over the course of approximately 3 hours. I will discuss each of these findings in turn, in the context of the literature.

3.3.1 Inhibition of UCHL1 Hydrolase Activity does not affect Mitochondrial Dynamics or Morphology

UCHL1 is thought to recycle ubiquitin by catalysing the hydrolysis of bonds between small adducts and the C-terminus of ubiquitin, thus replenishing cellular monomeric ubiquitin (Larsen *et al.*, 1998; Nijman *et al.*, 2005), although it has been previously suggested that this activity is functionally redundant; UCHL1 hydrolase activity is weak in relation to other DUBs, such as UCHL3 (Kabuta *et al.*, 2008). However, the UCHL1 I93M mutation is associated with Parkinson's disease, and UCHL1^{I93M}'s hydrolase activity is reduced by around 55%; this is also true of oxidatively modified UCHL1, which loses between 40 and 80% of its catalytic activity (Nishikawa *et al.*, 2003) and is present in Lewy bodies in PD (Lowe *et al.*, 1990; Choi *et al.*, 2004). My findings show that complete inhibition of UCHL1 hydrolase activity does not disrupt mitochondrial dynamics, including mitochondrial trafficking, fission, fusion and morphology. This finding indicates that the decreased hydrolase activity of UCHL1^{I93M} and oxidatively modified UCHL1 would not have sufficient impact to cause the disruption in mitochondrial dynamics and function observed in Parkinson's disease. It is more likely that the pathological I93M mutant contributes to protein aggregation within neurons. The I93M mutation causes a hydrophobic surface area to become exposed (Andersson *et al.*, 2011), increasing the likelihood of aggregation as is predicted by mathematical modelling (Proctor *et al.*, 2010), and conferring risk of Parkinson's disease.

3.3.2 Inhibition of UCHL1-Mediated Ubiquitin Stabilisation does not affect Mitochondrial Dynamics or Morphology

LDN-57444 causes a decrease of approximately 40% in levels of monomeric ubiquitin, which has been shown to decrease proteasomal degradation by around 50% (Cartier *et*

al., 2009). There has been much interest in recent years in the role of ubiquitin in regulating mitochondrial dynamics and quality control, in particular relating to mitochondrial E3 ubiquitin ligases such as Parkin and MITOL (Escobar‐Henriques and Langer, 2014). However, my results demonstrate that a 40% decrease in monomeric ubiquitin is not sufficient to impair mitochondrial trafficking, fission and fusion in neurons. This indicates that the ubiquitination and deubiquitination enzymes that regulate mitochondrial dynamics are still functional after UCHL1 inhibition; there is sufficient monoubiquitin present for ubiquitin ligation to take place, and the proteasome is still able to degrade mitochondrial dynamics proteins efficiently.

Since the function of the ubiquitin proteasome system declines with age, these results are also physiologically relevant to the ageing brain, and to age-related neurodegeneration. LDN-57444 decreases proteasomal degradation by 50% in hippocampal neurons (Cartier *et al.*, 2009), whilst proteasomal function declines by between 33% and 55% in aged mice, depending on the brain area assessed (Zeng *et al.*, 2005), and by a similar proportion in rats (Gavilán *et al.*, 2012). The decline in UPS function with age has not been quantified in human brain, but has been observed in other tissues (Bulteau *et al.*, 2000; Petropoulos *et al.*, 2000a; Carrard *et al.*, 2002; Viteri *et al.*, 2004; Jung *et al.*, 2007).

I have shown that inhibiting UCHL1's monoubiquitin binding function (which has previously been shown to decrease UPS activity by 50% in hippocampal neurons, (Cartier *et al.*, 2009)) is not sufficient to disrupt mitochondrial fission and fusion dynamics. This suggests that the decline of mitochondrial function with age in the human brain is not caused by the decline of the ubiquitin proteasome system and mediated by dysfunctional mitochondrial dynamics and quality control as hypothesised:

"Ubiquitin depletion caused by UCHL1 inhibition or knockout will disrupt mitochondrial trafficking, fission and fusion and cause the accumulation of dysfunctional mitochondria"

There are various alternative methods that could be used to confirm these results, and further assess the hypothesis above; these are outlined in section 8.2 of this thesis.

My data does not support the first part of my original hypothesis, however I will go on to assess whether UCHL1 knockout causes the accumulation of dysfunctional

mitochondria in Chapter 4 by assessing levels of respiratory chain complexes in UCHL1 knockout mice.

3.3.3 DUB Inhibition disrupts Mitochondrial Dynamics and Morphology

Treatment of neurons with the broad-range DUB inhibitor PR-619 resulted in a striking decrease in the motility of mitochondria; no mitochondria were observed to move more than 5µm (and therefore be classified as motile) after 1 hour of treatment with PR-619. In addition to this, mitochondrial fission and fusion rates were greatly reduced, and mitochondrial morphology was altered, as mitochondria became shorter and more rounded.

These results demonstrate that the activity of deubiquitinase enzymes is essential for mitochondrial trafficking, fission and fusion to take place, and for mitochondria to maintain their elongated and tubular morphology. This finding is in accordance with the literature describing the role of ubiquitin in mitochondrial dynamics. As is highlighted in the introduction, ubiquitin is required for mitochondrial fusion (Nakamura and Hirose, 2008; Anton *et al.*, 2013; Yue *et al.*, 2014) and E3 ubiquitin ligase enzymes (which utilise ubiquitin) are required for mitochondrial fission, fusion, trafficking and mitophagy (Escobar‐Henriques and Langer, 2014). Deubiquitinase enzymes are an important part of the ubiquitin-proteasome system, and have roles in editing polyubiquitin chains, as well as recycling and salvaging ubiquitin. Thereby, deubiquitinase enzymes are essential for replenishing cellular pools of monomeric ubiquitin. PR-619 does not affect the activity of the 20S proteasome, however upon treatment of cells with PR-619, polyubiquitinated proteins accumulate (Altun *et al.*, 2011). Since the proteasome is still active, this observation is because deubiquitinase activity is inhibited to the point where ubiquitin is not recycled from polyubiquitin chains, or salvaged from small adducts, quickly causing pools of monomeric ubiquitin to be depleted.

Although the inhibitor PR-619 has been well characterised previously and was found to be specific to DUBs whilst not affecting the activity of other proteases, (Altun *et al.*, 2011), it would be useful to confirm this result via an alternative method, such as inhibiting or knocking out the E1 enzyme that is required for ubiquitin activation.

Therefore, I can conclude that mitochondrial motility, fission and fusion are processes that rely on the presence of monomeric ubiquitin, which is quickly depleted without the activity of deubiquitinase enzymes. However, neither inhibition of UCHL1 hydrolase

activity, or depleting monomeric ubiquitin to a level that is physiologically relevant to aging, are sufficient to disrupt mitochondrial dynamics.

Chapter 4.

Phenotypic and Neuropathological Assessment of the UCHL1 Knockout Mouse Model

Chapter 4. Phenotypic and Neuropathological Assessment of the UCHL1 Knockout Mouse Model

4.1 Introduction

4.1.1 UCHL1 Null Mouse Models

As discussed in the introduction (Section 1.3), there are three UCHL1 null mouse models that have been characterised in the literature. They are all caused by either spontaneous or targeted intragenic deletions in UCHL1, and in all three mouse models UCHL1 is not detectable by western blot (Saigoh *et al.*, 1999; Walters *et al.*, 2008; Chen *et al.*, 2010a). The characteristic phenotype of UCHL1 null mice is sensory and motor ataxia, accompanied by tremor and kyphosis. Onset of the phenotype occurs at anything from 4 to 11 weeks, and is progressive, resulting in eventual paralysis of both hind- and fore-limbs. UCHL1 null mice have not been reported to live longer than 10 months (Yamazaki *et al.*, 1988; Walters *et al.*, 2008; Chen *et al.*, 2010a). UCHL1 null mice display axonal dystrophy, which progresses in a distal to proximal direction, and is characterised by axonal spheroids (swellings in axons containing neurofilaments, mitochondria and tubulovesicular structures). Axonal dystrophy occurs predominantly in long axonal tracts, namely the ascending dorsal column and dorsal spinocerebellar tract and the descending corticospinal tract (Miura *et al.*, 1993; Chen *et al.*, 2010a) (Yamazaki *et al.*, 1988; Kikuchi *et al.*, 1990).

4.1.2 Neuroanatomy of the Mouse Cerebellum and Brainstem

Since axonal dystrophy has previously been observed in the gracile and cuneate nuclei, as well as in the white matter of the cerebellum of other UCHL1 null mouse models, our neuropathological assessment of the UCHL1 mice mainly focused on those areas.

4.1.2.1 The Cerebellum

The primary function of the cerebellum is in the planning and execution of motor activity, in particular balance, walking and the co-ordination of fine or skilled movements (Ito, 2002). The cerebellum receives sensory input and communicates with the cerebral motor cortex, which controls muscle activity. Thus the cerebellum integrates the sensory and motor pathways, allowing body movements to be fine-tuned according to feedback from the sensory system. Interestingly, it has also been more recently established that the cerebellum is associated with cerebral networks involved in cognition and is involved in cognitive function (Buckner, 2013).

The overall structure of the mouse cerebellum is displayed in Figure 4.1A, using a Sagittal diagram of the cerebellum taken from Paxinos and Franklin's atlas, "The mouse brain" (Paxinos, 2001). The cerebellum can be divided into four developmentally relevant transverse zones: the anterior, central, posterior and nodular lobes, which are further divided into 10 lobules (I-X) (Larsell, 1952; Ozol *et al.*, 1999; Hawkes, 2001; Sgaier *et al.*, 2007). Each transverse zone can be further divided into a series of longitudinal 'stripes', which are defined by molecular markers expressed by Purkinje cells, the most characterised of these being Zebrin II (Brochu *et al.*, 1990).

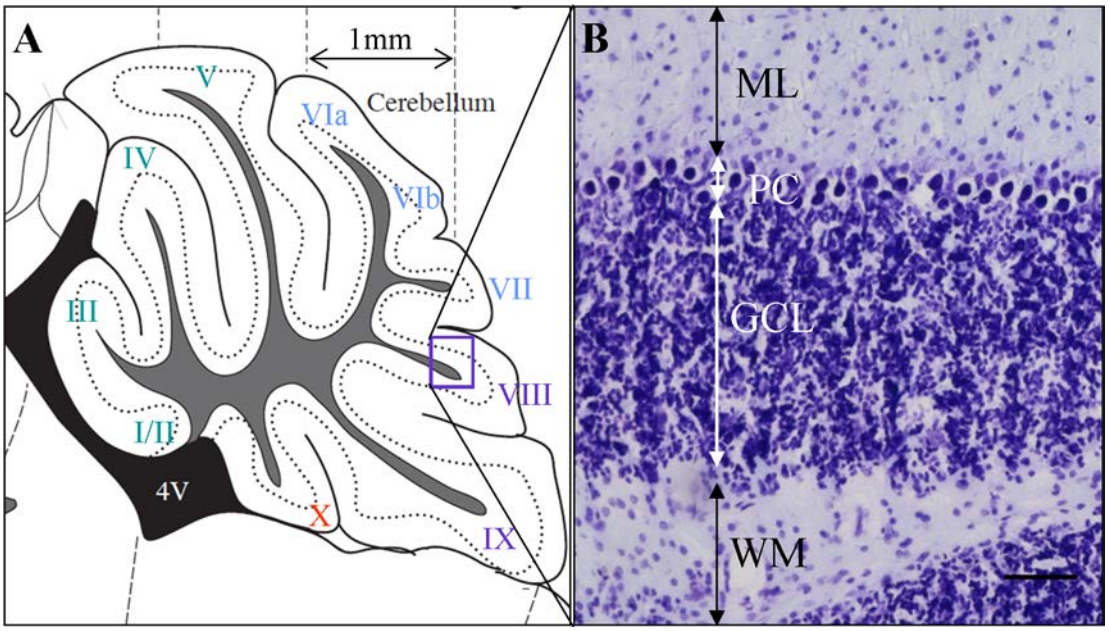

Figure 4.1: Structure and cytoarchitecture of the cerebellum.
A) Sagittal view of the mouse cerebellum in situ, above the Pons and Medulla, adapted from (Paxinos, 2001) pp 25, Scale bar = 1mm. Anterior Zone - lobules I-V (green), Central Zone – lobules VI-VII (blue), Posterior Zone - VIII and rostral IX (purple), Nodular Zone – caudal IX and X (red). B) Cresyl Fast Violet stain showing the cytoarchitecture of the cerebellum: Molecular Layer (ML), Purkinje Cell (PC) Layer, Granular Cell Layer (GC) and White Matter (WM) Scale bar = 50µm.

The cytoarchitecture of the cerebellum consists of three easily identifiable layers, surrounding the white matter and cerebellar nuclei; this is shown in Figure 4.1B, using a cresyl fast violet (CFV) stain to identify neuronal populations. In addition to efferent fibres from Purkinje cells, the white matter consists of mossy fibre afferents from the cuneocerebellar, dorsal spinocerebellar, pontocerebellar, and vestibulocerebellar tracts, and climbing fibres from the inferior olivary complex. Mossy fibres project into the granular layer, where they form glutamatergic synapses with granular cells, small excitatory neurons that are the most numerous cell type in the brain (Voogd and Glickstein, 1998). The granular cell layer (GCL) also contains Golgi cells, inhibitory interneurons which synapse with granule cell dendrites, providing feed-backward inhibition. Granule cells project their axons into the molecular layer, where they

bifurcate and run in parallel to the Purkinje cell layer (PCL), and are therefore known as parallel fibres. Parallel fibres terminate on the spiny branches of Purkinje cell dendritic trees or interneurons. The molecular layer (ML) also contains glial cell fibres, and two types of inhibitory interneurons, basket and stellate cells, which also synapse with Purkinje cells. Climbing fibres project through the GCL and PCL, and synapse with

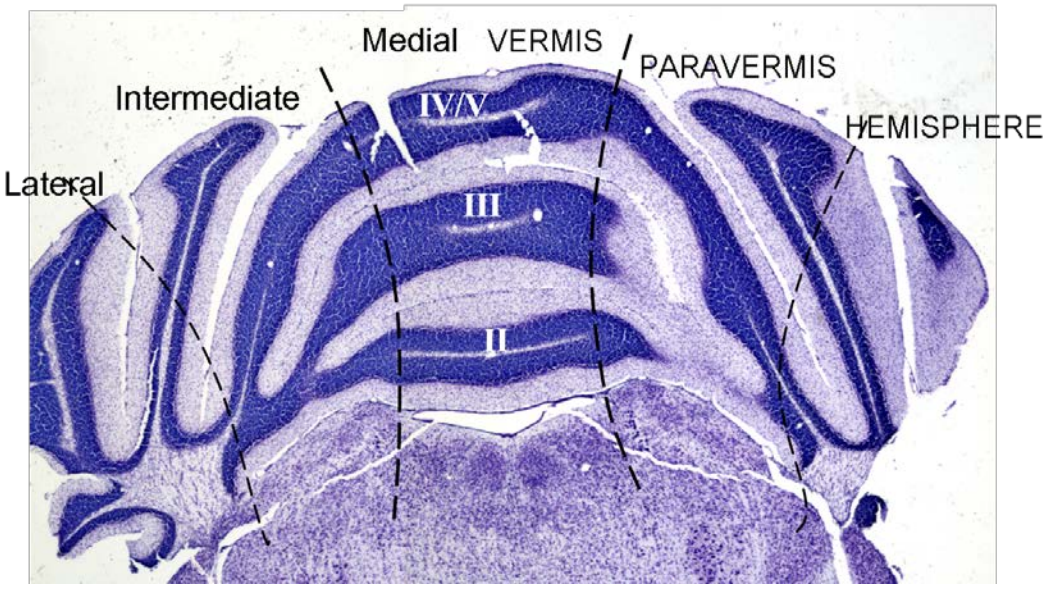

Figure 4.2: Longitudinal zones of the mouse cerebellum: Medial (Vermis), Intermediate (Paravermis) and lateral (Hemispheres).

Purkinje cells on the smooth lower branches of the dendritic tree. Purkinje cells are large GABAergic neurons, and their axons, which are the only output of the cerebellar cortex, target the deep cerebellar nuclei. Purkinje cells, therefore, integrate excitatory signals from granule cells or climbing fibres with feed-forward inhibition from stellate and basket interneurons, and granule cells integrate excitatory input from mossy fibres with inhibitory feed-backward inhibition from Golgi cells (Voogd and Glickstein, 1998). Figure 4.2 shows a coronal section of the mouse cerebellum, which can be compartmentalised into three longitudinal zones, the vermis (medial) and paravermis (intermediate), with hemispheres either side (lateral regions) (Apps and Hawkes, 2009). Although the mouse cerebellum is morphologically different to the human cerebellum, most mammalian cerebella are homologous in their organisation, and can be divided into lobules and longitudinal zones using the same terminology. It is useful to think of the cerebellum in terms of longitudinal zones when mapping the input from various white matter tracts.

4.1.2.2 Afferents to the Cerebellum

The dorsal spinocerebellar tract (which will be our focus) projects axons from the dorsal nucleus (Clarke's Column) at spinal cord levels L3 – C8, carrying sensory information

from the hind limbs and trunk. A recent study demonstrates that neurons from the cuneocerebellar tract (carrying information from forelimbs and trunk), and dorsal spinocerebellar tracts project to Purkinje cells in the medial and intermediate zones of the cerebellum (vermis and paravermis) in alternating 'stripes', (Gebre *et al.*, 2012), in the anterior and posterior zones (lobules I-V and VIII/IX).

Pontocerebellar fibres are projected from the pontine nuclei, enter the cerebellum via the middle cerebellar peduncle, and target symmetrical areas of the two hemispheres (lateral zones) of the cerebellum, in particular the paramedian lobule (PML) (Bukowska *et al.*, 2003). Olivocerebellar fibres (projections from the inferior olive) project to all longitudinal zones of the cerebellum (Apps and Hawkes, 2009), whereas the projections of the vestibulocerebellar system are restricted to the region historically known as the vestibulocerebellum, which maps to the nodular zone, lobules IX and X (Carleton and Carpenter, 1983).

4.1.2.3 Ascending Sensory Tracts

Since information on the ascending sensory tracts in mice is relatively sparse, and most mammals share a high level of homology with regards to the organisation of the spinal cord (Watson and Harrison, 2012b), I will start by describing the anatomy and function of relevant tracts in humans, and relate this, where possible, to mice.

4.1.2.4 The Spinocerebellar Tracts

There are two spinocerebellar tracts, dorsal and ventral, which carry proprioceptive and tactile information to the cerebellum, for unconscious proprioception (Craven, 2011). ***The dorsal spinocerebellar tract*** (DSCT) arises in the dorsal nucleus, also known as Clarke's column, which is present from around levels L2 or 3 to C8. Afferents from muscle spindles in the lower limbs and trunk, which have their cell bodies in the dorsal root ganglia, synapse with these neurons. Axons from the dorsal nucleus neurons then ascend in the dorsal spinocerebellar tract as large diameter myelinated fibres, and enter the cerebellum via the inferior cerebellar peduncle (ICP). The position of the dorsal spinocerebellar tract in the mouse spinal cord is illustrated in Figure 4.3.

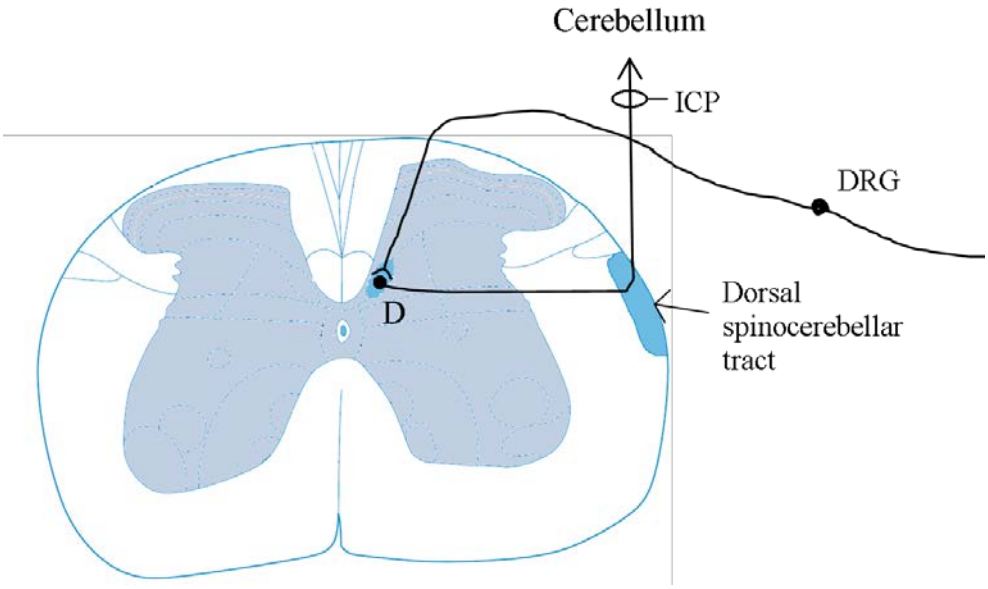

Figure 4.3: The Dorsal Spinocerebellar Tract at L3 of the Spinal Cord.
D=Dorsal Nucleus (Clarke's Column), DRG =Dorsal Root Ganglion, ICP = Inferior Cerebellar Peduncle. Adapted from **(Watson *et al.*, 2009b; Watson and Harrison, 2012a)**.

As Clarke's column does not ascend above C8 in the spinal cord, afferents from the upper limbs ascend the spinal cord in the cuneate fasciculus, and synapse in the external cuneate nucleus, as opposed to the dorsal nucleus. Cells of the external cuneate nucleus give rise to the ***cuneocerebellar tract*** (CCT) which also enters the cerebellum via the inferior cerebellar peduncle and terminates in the medial and intermediate zones of the anterior and posterior lobes (Gebre *et al.*, 2012). The cuneocerebellar tract is widely regarded as the functional equivalent of the dorsal spinocerebellar tract for the upper limbs. Like the dorsal spinocerebellar tract, the ***ventral spinocerebellar tract*** originates in the lumbar levels of the spinal cord, and carries information from the lower limbs, however it decussates in the lumbar spinal cord, and ascends as the ventral spinocerebellar tract, which is immediately ventral to the dorsal spinocerebellar tract. It ascends as far as the upper pontine level of the medulla, and then descends via the superior cerebellar peduncle to the cerebellum and terminates in the vermis of the anterior lobe. As opposed to the dorsal spinocerebellar tract, which conveys impulses from individual muscles for the fine-tuning of their individual movement, the ventral spinocerebellar tract conveys impulses from large receptive fields, often across different muscle groups, thereby allowing for the co-ordination of movement and position of the whole limb. The **spinothalamic tracts** transmit information regarding pain, temperature, light touch and pressure to the brain, terminating in the thalamus (Craven, 2011; Mancall, 2011).

4.1.2.5 The Dorsal Column

The dorsal funiculus of the spinal cord consists of two major ascending tracts; the gracile fasciculus and the cuneate fasciculus, which both carry myelinated fibres conveying information for conscious proprioception, discriminative touch and vibration.

Primary neurons of the dorsal column system, which are proprioreceptors or mechanoreceptors, have their cell bodies in the dorsal root ganglia, and project myelinated axons all the way to the gracile and cuneate nuclei before they synapse (Figure 4.4). Thus, those originating in the hind limbs are some of the longest axons in the body. Secondary neurons originating in the gracile and cuneate nuclei project to the ventral posterior nucleus of the thalamus, and finally sensory information is conveyed from the thalamus to the primary sensory cortex (Kiernan, 2013).

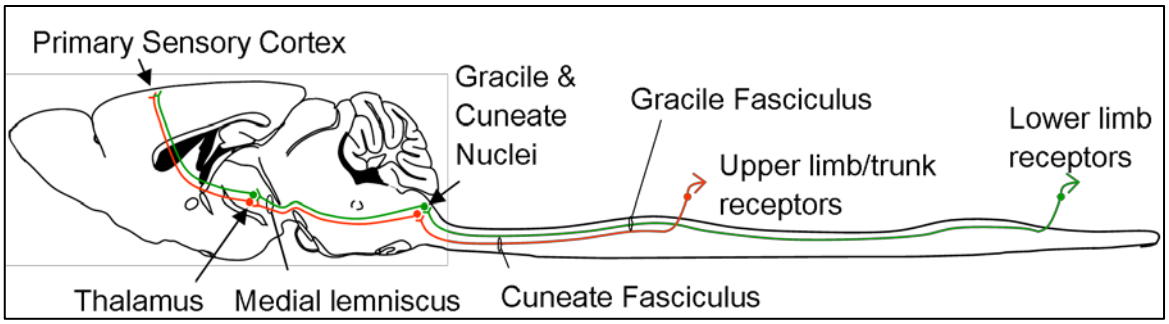

Figure 4.4: The Dorsal Column System.
Shows the path of the gracile and cuneate tracts to the primary sensory cortex via the gracile and cuneate nuclei, medial lemniscus and thalamus. Not to scale. Adapted from (Paxinos, 2001)

In a manner analogous to the organisation of dorsal spinocerebellar and cuneocerebellar tracts, axons entering the spinal cord below mid-thoracic levels ascend via the gracile fasciculus to the gracile nucleus, whereas axons entering above the mid-thoracic level belong to the cuneate tract and synapse at the cuneate nucleus. Therefore there is a functional distinction between the two tracts, with the gracile tract being responsible for lower limb/trunk proprioception and touch, and the cuneate tract conveying information from the trunk and upper limbs (Kiernan, 2013). Furthermore, axons that enter the spinal cord at caudal (sacral) levels are medial in the gracile fasciculus, whereas those entering more rostrally are more lateral, resulting in a medial-lateral somatotopic organisation across the gracile and cuneate fascicule (Watson *et al.*, 2009a). Interestingly, a more recent study has found that the dorsal column is primarily organised by modality (ie. mechanosensory afferents are more medial, whilst proprioceptive axons are more lateral), whilst retaining a somatotopic organisation (Niu *et al.*, 2013).

4.1.3 Aims of the Investigation

The aim of this chapter is to determine whether our UCHL1 knockout mice have a similar axonal dystrophy phenotype to the other UCHL1 null mouse models discussed in the literature, and to locate the main areas where neuropathology is evident. In addition, I aim to determine whether mitochondria in these regions are deficient in complexes I and IV of the mitochondrial respiratory chain, in order to complete investigations into the relationship between UCHL1 and mitochondria.

4.1.4 Methodological Approach and Optimisation of Methods

4.1.4.1 Dissection of Mouse Brains and Spinal Cords

The *gad* and UCHL1 mouse models display 'dying back' type axonal degeneration, whereby axonal degeneration starts distally, at presynaptic nerve terminals, and then spreads back towards the cell bodies. Denervation of hind limb muscles occurs progressively as axons projected from motor neurons retract from neuromuscular junctions (Chen *et al.,* 2010a). Previous neuropathology studies in UCHL1 knockout mice have revealed axonal swellings, or 'spheroids' in the gracile and cuneate tracts (Mukoyama *et al.,* 1989; Kikuchi *et al.,* 1990), and in the white matter of the cerebellum (Kikuchi *et al.,* 1990; Wu *et al.,* 1996).

Therefore, in order to locate and confirm this neuropathology in our UCHL1 knockout mice and then determine whether mitochondria are respiratory chain deficient here, I collected the brain, cerebellum, spinal cord and dorsal root ganglia from a total of 55 mice (Table 4.1; Appendix 2). These tissues were collected from mice at an early stage of pathology (9-12 weeks) and at and advanced stage of pathology (16 – 21 weeks), with the aim of establishing which pathological events occur first and elucidating the mechanism which axonal dystrophy occurs.

Frozen	**Early stage**	**Advanced stage**	*Fixed*	**Early stage**	**Advanced stage**
Wild Type	6	7	**Wild Type**	4	8
Knockout	4	10	**Knockout**	4	12

Table 4.1: Total numbers of mouse dissections.

4.1.4.2 Selection of Tissue for Western Blotting

In order to compare the levels of ubiquitin and ubiquitin-conjugated proteins in UCHL1 WT and KO mice, western blotting was carried out using homogenate from three WT and three KO mice, detailed in Table 4.2.

Wild Type				**Knockout**			
ID	*Sex*	*Age (Weeks)*	*Visual Score*	*ID*	*Sex*	*Age (Weeks)*	*Visual Score*
WT 9	♂	20.1	-	KO 10	♂	19.1	-
WT 32	♀	19.1	0	KO 30	♀	19.1	2
WT 33	♀	16.9	0	KO 31	♀	19.1	2

Table 4.2: Details of mice used to assess levels of ubiquitin by western blotting

4.1.4.3 Optimisation of Western Blotting

Initial protocols for electrophoresis and transfer of proteins onto a PVDF (Polyvinylfluoridine) membrane resulted in successful visualisation of the 'ubiquitin smear' (ubiquitin conjugates and conjugated proteins), but failed to resolve the ubiquitin monomer, or indeed any bands below approximately 40kDa, despite the use of an 8-16% gradient gel. Attempts were made to visualise the ubiquitin monomer on the same gel as the ubiquitin conjugates by decreasing transfer time, as ubiquitin is such a small protein that it could easily pass straight through the PVDF membrane under prolonged electrophoretic transfer. However this was not successful. It has previously been reported that including calcium chloride in transfer buffer improves the transfer of small proteins (McKeon and Lyman, 1991). The transfer buffer that I had been using contains 0.1% SDS (Sodium dodecyl sulphate), which binds to proteins, giving them a net negative charge. This is generally included in transfer buffer as it encourages proteins to leave the gel; this is especially important for the transfer of large proteins, which tend to stay on the gel. However, inclusion of the positive calcium ion encourages small proteins to be retained on PVDF membranes, whilst making it harder for large proteins to leave the gel. Therefore two protocols were developed with differing transfer conditions: a buffer containing 0.1% SDS was used for the transfer of large proteins, whilst a buffer containing 2mM Calcium Chloride (no SDS) was used for the transfer of small proteins, and for the successful visualisation of monomeric ubiquitin.

4.1.4.4 Selection of Tissue for Histology

In order to determine the areas of neuropathology in the UCHL1 null mouse, tissue sections from two wild type (WT) and two knockout (KO) mice, both 16 weeks, were stained histologically and immunohistochemically. Further analysis (densitometry, counting) was carried out on these four mice, as well as a further three WT and three KO mice, aged between 9 and 12 weeks (after the onset of pathology). Details of these mice are shown in Table 4.3.

Wild Type				**Knockout**			
ID	*Sex*	*Age (Weeks)*	*Visual Score*	*ID*	*Sex*	*Age (Weeks)*	*Visual Score*
WT 17	♀	11.6	0	KO 20	♂	9.3	1
WT 18	♀	11.6	0	KO19	♂	11.7	1.6
WT 23	♀	12.6	1	KO22	♀	12.7	2
WT 37	♂	16.1	0	KO39	♂	16.1	2
WT 38	♂	16.1	0	KO40	♂	16.1	2

Table 4.3: Details of mice used to assess neuropathology and mitochondrial function in UCHL1 mice. Visual score (based on Section 4.2.1) represents the mean score for each mouse.

4.1.4.5 *Optimisation of Immunohistochemistry*

In order to assess the location and distribution of neuropathology in UCHL1 knockout mice, and to assess the function of the mitochondrial respiratory chain, it was necessary to optimise immunohistochemistry protocols for a number of antibodies, detailed in Table 4.4.

Primary Antibody	**Target**	**Secondary Antibody**
Mitochondrial		
Complex I-20kDa (*NDUFB8)*	Antibody to subunit 20 of complex I of the mitochondrial respiratory chain (*NDUFB8*). To determine whether levels of complex I are reduced.	Goat α Mouse Biotinylated IgG1
Complex II-70kDa (*SDHA)*	Targets the SDHA subunit of mitochondrial RC complex II	Goat α Mouse Biotinylated IgG1
COX-1 (*MT-CO1)*	Targets Cytochrome C Oxidase; will allow us to detect reduced complex IV levels	Goat α Mouse Biotinylated IgG2a
Axonal		
SMI-31	Phosphorylated Neurofilament H, present in thick and thin axons, and some dendrites	Goat α Mouse Biotinylated IgG1
SMI-32	Non-phosphorylated Neurofilament H, present in neuronal cell bodies, dendrites and some thick axons	Goat α Mouse Biotinylated IgG1
MBP-4 (DAKO)	Myelin Basic Protein	Goat α Mouse Biotinylated IgG1
Other		
APP	Antibody to amyloid precursor protein, which is transported by fast axonal transport, and accumulates when axonal transport is defective.	Goat α Mouse Biotinylated IgG1
Synaptophysin	Synaptophysin, an integral membrane glycoprotein of small synaptic vesicles.	Goat α Mouse Biotinylated IgG1

Table 4.4: Details of antibodies used in immunohistochemistry

The overall process of immunohistochemistry is outlined in Figure 4.5. The two steps of the protocol which required the most extensive optimisation (antigen retrieval and adjustment of primary antibody dilution and incubation time) are highlighted in purple.

Formalin fixed, paraffin embedded (FFPE) tissue was used for immunohistochemistry and histological stains, as fixation with formalin ensures that good morphology is preserved; morphology of FFPE tissue sections is far better than frozen tissue sections. After deparaffinising and rehydrating tissue sections, antigen retrieval was performed (see section 4.1.4.6), and sections were subsequently incubated with 3% hydrogen peroxide in order to block endogenous peroxidase activity. An avidin biotin kit was then used to block endogenous biotin, biotin receptors and avidin binding sites, to allow use of an avidin/biotin complex for the amplification of signal later in the protocol (pale blue outline, Figure 4.5). A further blocking step was then carried out, using normal goat serum to bind any non-specific binding sites that exist within the tissue, thus preventing either primary or secondary antibodies binding non-specifically and reducing background. Since all antibodies used were raised in mouse hosts, it was also necessary to use a M.O.M (Mouse on Mouse) kit (italics, Figure 4.5) to reduce non-specific binding of the goat anti-mouse secondary antibodies to endogenous mouse immunoglobulins. The primary antibody was then applied at a carefully optimised dilution and incubation time (Section 4.1.4.7), before incubation with a secondary antibody, which binds to the mouse primary. All secondary antibodies were biotinylated, so that the signal could be amplified using an avidin/biotin complex which binds to the biotin motif on the secondary antibody, and also reacts with the DAB chromogen, causing it to form a brown precipitate.

For all antibodies, antigen retrieval conditions, and primary antibody dilution and incubation conditions were adjusted on the basis of previous IHC runs, in order to reduce non-specific staining whilst gaining the optimal staining intensity. ‘No primary antibody’ controls were included in each optimisation IHC run, to ensure that there was no non-specific binding of the secondary antibody or avidin biotin complex.

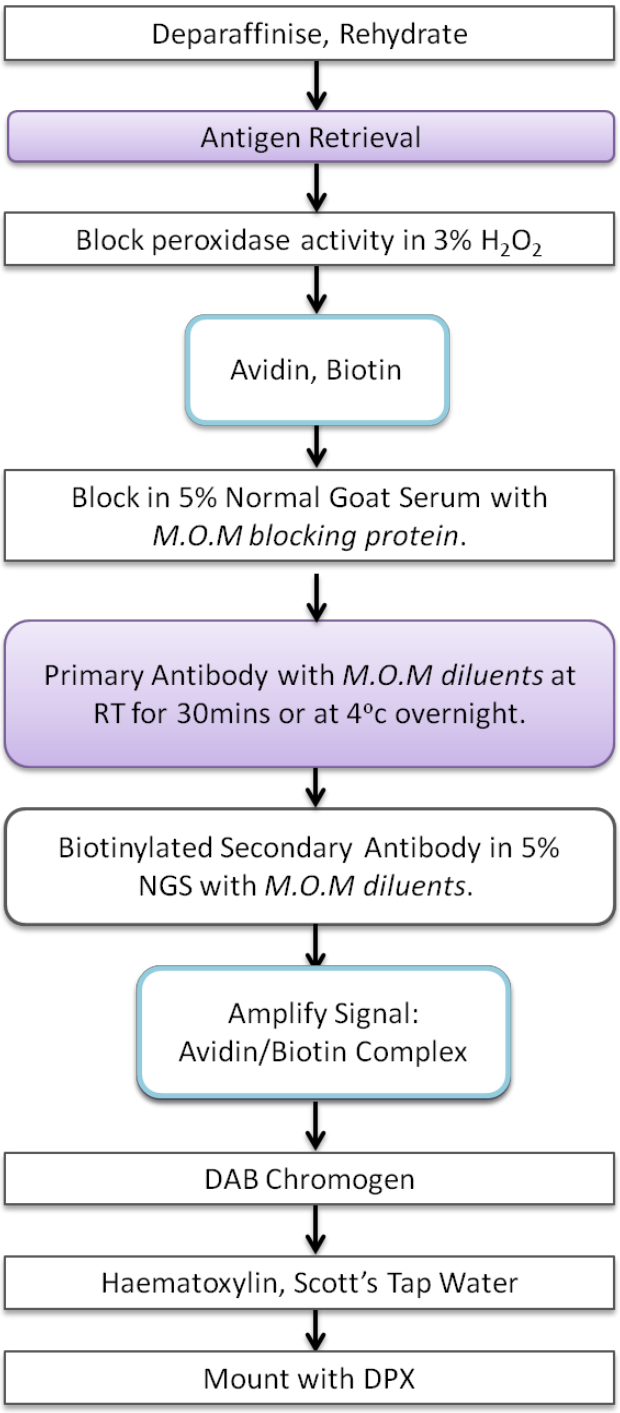

Figure 4.5: General Protocol for Immunohistochemistry.

4.1.4.6 Antigen Retrieval

The purpose of antigen retrieval is to allow the primary antibody access to the epitope. Fixation with formalin causes reversible cross-links between proteins, keeping them in their place and preventing autolysis and putrefaction. These cross-links can mask certain epitopes, and therefore antigen retrieval is required to break formalin cross-links and allow the antibody to bind to the antigen.

Antigen retrieval methods vary depending on the antigen which is to be accessed, for example, the SMI-31 antibody does not require antigen retrieval to allow access to the relevant epitope, and IHC to APP requires antigen retrieval in 10mM citrate heated in the microwave. The vast majority of antibodies used in this chapter required antigen retrieval in 1mM EDTA, pH8.

Initially antigen retrieval with EDTA was carried out using the MenaPath Access Retrieval Unit, which heats to 110^{o}c for 10 seconds, then increases the pressure to 124.5 psi. However, this unit became increasingly unreliable, and caused variability in staining between immunohistochemistry runs where all other factors were kept constant (Figure 4.6).

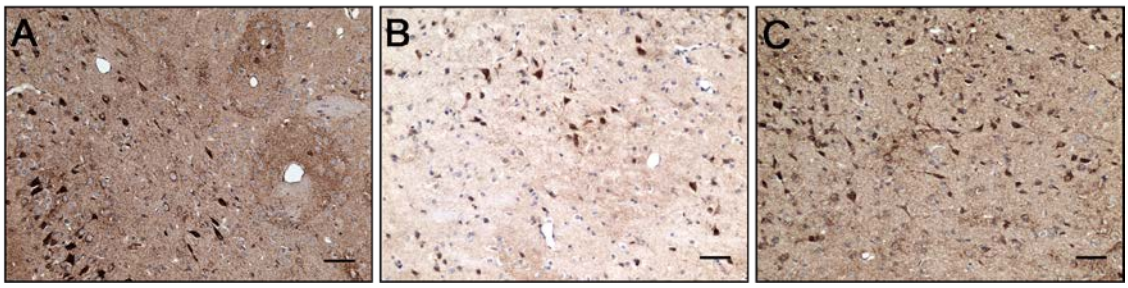

Figure 4.6: Variability in staining caused by the MenaPath Access Retrieval Unit.
5µm WT brain sections; Immunohistochemistry with the COX-1 antibody *(MTCO1)*, 1:400, antigen retrieval in the MenaPath Access Retrieval Unit with 10mM EDTA pH8

Therefore, alternative methods of antigen retrieval were trialled so that the IHC protocol would be reliable and replicable. These methods included a plastic pressure cooker that was placed inside the microwave; this method was successfully optimised for use with the mitochondrial antibodies and synaptophysin, however was then ruled out due to health and safety concerns. A different pressure cooker, which is heated on a hot plate was also trialled, however using this method staining was mainly non-specific.

A further antigen retrieval unit, the 2100 retriever, which had been successful in antigen retrieval for FFPE human brain sections, was also trialled. However, IHC to several mitochondrial antibodies (COX-1, CI-20, CII-70) appeared non-specific. Furthermore,

although staining seemed specific with SMI-32 and synaptophysin antibodies using this method of antigen retrieval, staining was variable across sections, and in all cases there was an unstained rim around the edge of this section.

Because of the non-specificity of staining and high background in areas where staining did look specific, it was suspected that the M.O.M kit was not functioning properly, therefore causing cross-reactivity of the secondary antibody with endogenous mouse IgGs. However, this possibility was ruled out by a series of immunohistochemistry runs where M.O.M blocking was increased, and a different M.O.M kit used. None of these modifications caused a difference to staining. A more thorough method was used to wash sections in-between application of the primary antibody, secondary antibody and ABC complex; however this did not improve staining specificity either.

Therefore, it was concluded that the antigen retrieval unit was the cause of the non-specific staining, which was perhaps due to antigen retrieval conditions being too harsh for the mouse tissue.

Since antigen retrieval in a simple plastic box in the microwave had worked well for other antibodies (APP, SMI-32), this method was trialled with the mitochondrial antibody CII-70, with 500ml EDTA pH8. This improved staining specificity, as compared to results from the antigen retrieval unit, and solved the problem of having an unstained rim around the edge of sections (Figure 4.7), although staining was of a higher intensity at the edge of the section. Staining appeared specific in the majority of the section, but still with a fairly high background, and in order to optimise staining specificity, various lengths of retrieval were trialled to find the optimal retrieval conditions (Figure 4.8). The optimal retrieval conditions were to microwave the buffer for 5 minutes, then add the sections for a further 5 minutes in the microwave and cool for 10 minutes. This highlights that often mouse brain tissue sections require much gentler antigen retrieval conditions than human brain tissue sections.

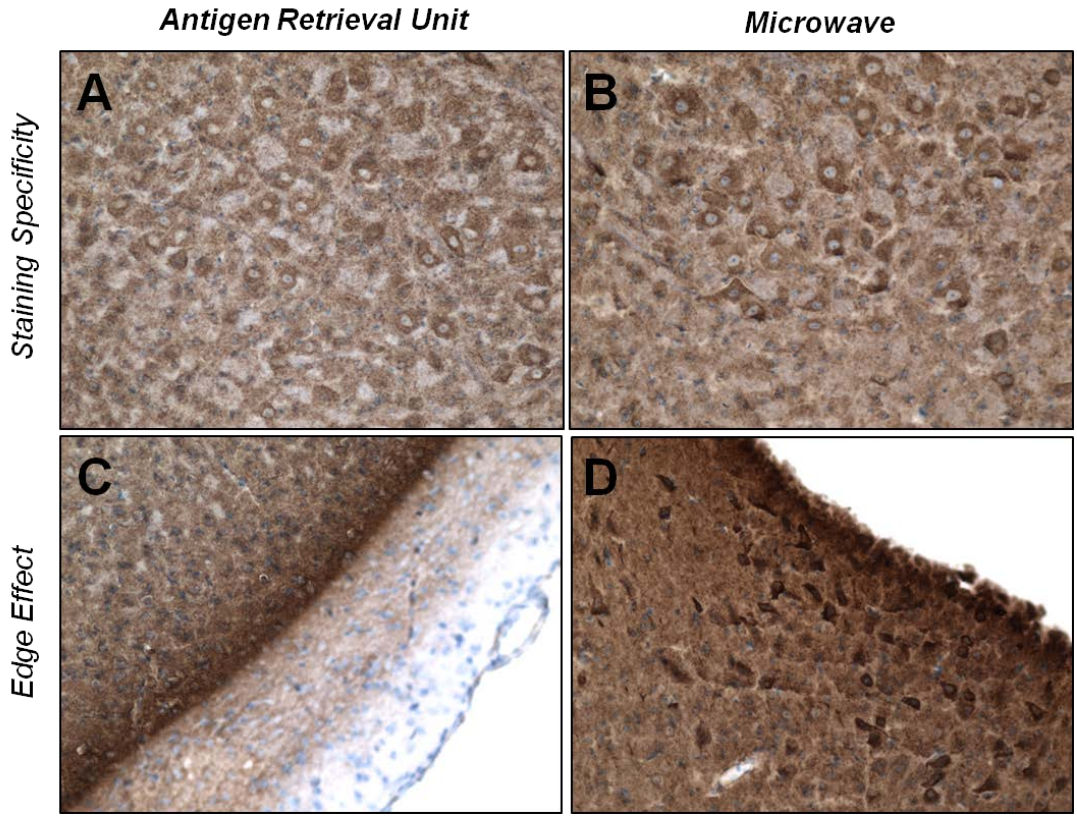

Figure 4.7: Comparison of IHC using the Antigen Retrieval Unit and Microwave.
All images show IHC with CII-70 1:200 in EDTA, pH8.

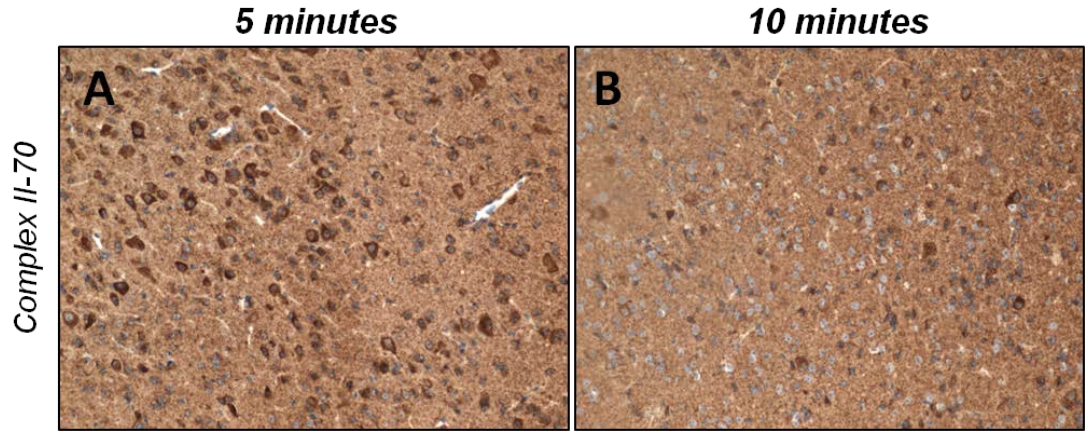

Figure 4.8: Adjustment of Antigen Retrieval Time.
500ml 1mM EDTA, pH8 was placed in the plastic box and microwaved at 70% power for 6 minutes. Tissue sections were then added and microwaved for either 5 (left) or 10 (right) minutes at 50% power. Sections were left to cool with the lid on for 10 minutes. A retrieval time of 5 minutes was determined to be optimal for Complex II-70 IHC.

4.1.4.7 Primary Antibody Dilution and Incubation Time

Starting dilutions of the primary antibodies were chosen based on values suggested in the manufacturer's data sheet, or on the previous experience of other members of the lab, however required adjusting for my particular tissue sections. Primary antibody dilution was adjusted so that staining was intense and specific, with little background. Additionally, I aimed to adjust the dilutions of the mitochondrial primary antibodies so that they were all of approximately the same intensity to allow for comparisons.

I will use MBP-4 as an example of how primary antibody dilution is adjusted to identify the optimal IHC conditions. A 1:1000 dilution of the MBP-4 antibody was considered to be too intense, whereas a 1:5000 dilution was too weak, as smaller myelinated fibres were very faint (Figure 4.9C). Therefore a 1:3000 dilution was chosen to be optimal, as myelinated fibres were easily visible, but staining was not too intense or non-specific (Figure 4.9B).

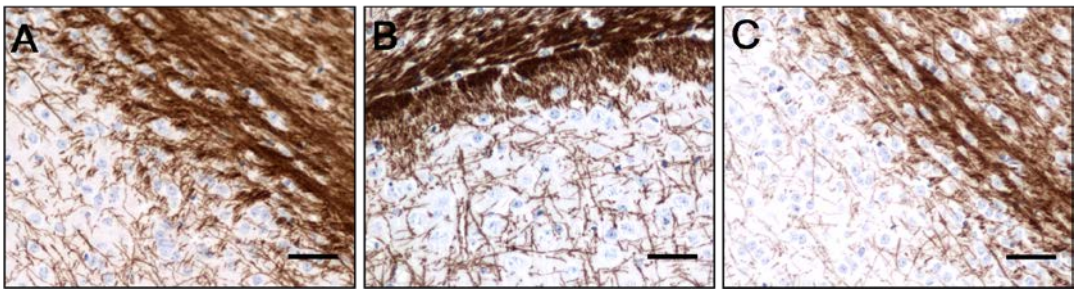

Figure 4.9: Adjustments to MBP-4 antibody dilution.
A) 1:1000, B) 1:3000, C) 1:5000. Scale Bars = 50μm.

Initially, many of the primary antibodies were applied to the sections for half an hour at room temperature, however applying the antibody at a lower temperature (4^{o}c) for more time (overnight) can slow the kinetics but allow the antibody more time to bind to the epitope. The Complex I-20 antibody for example, showed only very weak staining that was variable across the section, even at a dilution of 1:50. However, when it was applied overnight, its immunoreactivity was much greater.

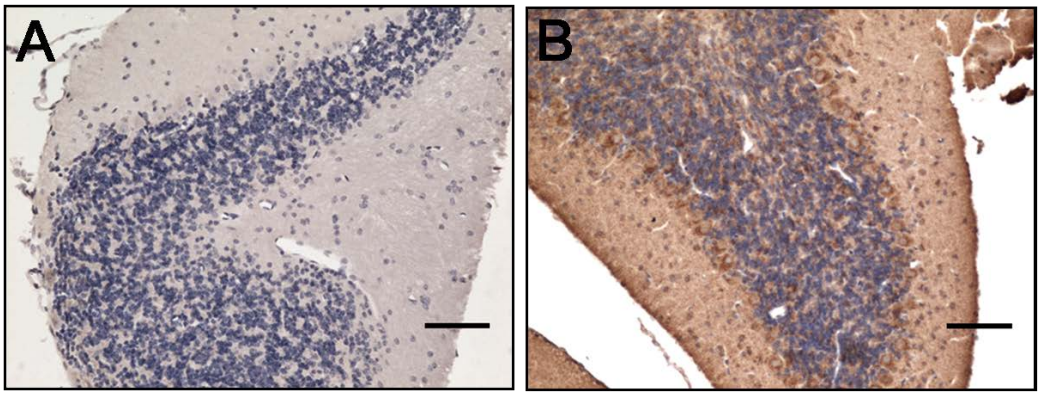

Figure 4.10: Antibody Incubation time and Temperature.
A) Tissue section incubated with CI-20 (1:50) for 30 minutes at room temperature, B) Tissue section incubated with CI-20 (1:50) at 4^{o}c for approximately 16 hours.

4.2 Results

4.2.1 Phenotypic Assessment of UCHL1 Knockout Mice

In order to quantify the phenotype of UCHL1 KO mice, I developed a visual scoring system (Figure 4.11) based on the hind limb splaying reflex action that occurs in healthy mice. Scoring was done on a blinded basis to prevent bias; mice were identified by cage number and ear notch position. 36 wild-type, 132 heterozyogous and 67 knockout mice were assessed on a weekly basis. These figures do not reflect the breeding ratio for these mice, since some mice were given away for different research projects. A total of 272 mice were born over 3 generations, with a breeding ratio of 1.0:2.4:1.3 (WT: Het: KO), roughly according to Mendel's ratios, in agreement with previous studies of UCHL1 null mice (Walters *et al.*, 2008)

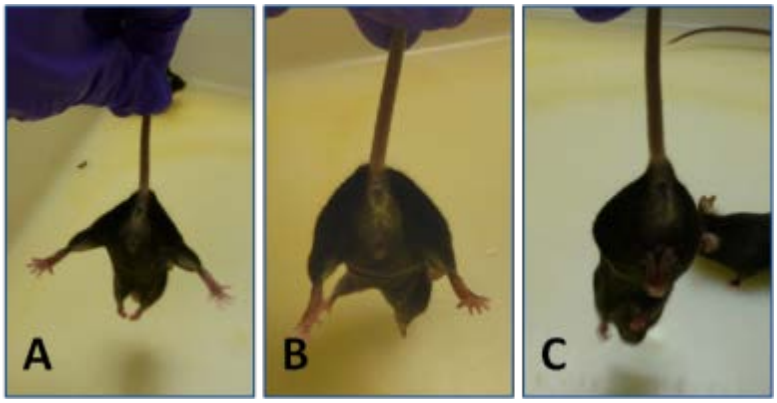

Figure 4.11: Visual Scoring method.
A) Hind limbs splayed indicating healthy reflexes and no hind limb impairment - score 0. B) Hind limbs are held hip width apart; moderate impairment of hind limb function- score 1. C) Hind limbs are clasped together or crossing over, showing severe hind limb impairment - score 2

UCHL1 knockout mice develop a hind limb impairment by 9 weeks of age (Figure 4.12A), which progressively worsens. The earliest hind limb impairment was observed at 7 weeks of age, with one KO mouse out of four showing a moderate impairment, determined by its inability to perform the hind limb splaying reflex. By 8 weeks, 50% of KO mice demonstrated a moderate impairment of hind limb function, whilst by 9 weeks only one KO mouse in five was unaffected, with three out of five mice showing a moderate impairment, and one demonstrating a severe impairment of hind limb function, shown by hind-limb clasping. Knockout mice become much less mobile than their wild type and heterozygous littermates as they develop this phenotype; their hind limbs fail to support them and are sometimes dragged underneath the body as they walk. UCHL1 KO mice also develop kyphosis and a tremor, and fail to put on weight, like their wild-type littermates (Figure 4.13). At 7-9 weeks UCHL1 KO mice are a normal weight, however once the hind-limb phenotype develops, they fail to gain any more weight,

perhaps due to their decreased ability to compete for food with WT littermates. The hind limb impairment is characterised by difficulty in performing the 'limb-splaying' reflex upon being picked up by the tail; as the impairment becomes more severe, knockout mice tend to clasp their hind limbs together or cross them over. Therefore the extent to which mice were able to carry out the limb-splaying reflex was chosen as the basis for my visual scoring method to assess the UCHL1 phenotype. This scale worked nicely as it demonstrates the progressive aspect of the UCHL1 KO phenotype (Figure 4.12A), however it sometimes proved difficult to distinguish a healthy limb splaying reflex from a slightly impaired reflex with legs held hip width apart. This resulted in some wild type and heterozygous mice receiving a score between 0 and 1 (Figure 4.12C) although WT mice and heterozygotes are unaffected. This figure also shows some UCHL1 knockout mice receiving a score of less than 1; this represents mice that were only assessed at 9 or less weeks of age, as they were then euthanized for collection of brain and spinal cord tissue.

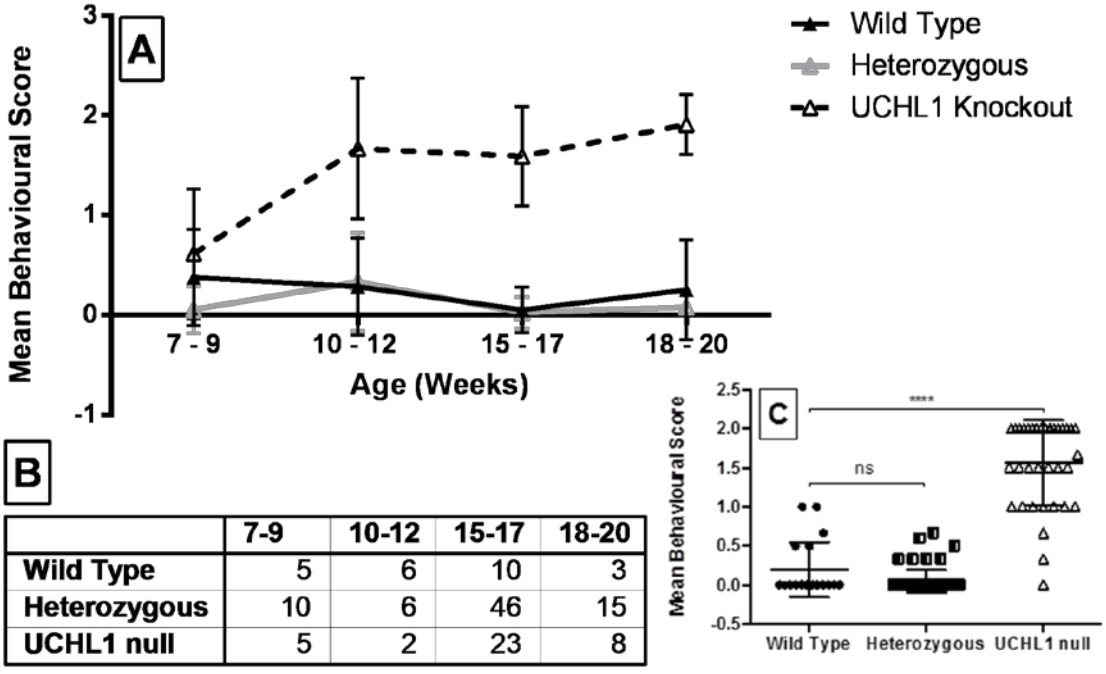

	7-9	10-12	15-17	18-20
Wild Type	5	6	10	3
Heterozygous	10	6	46	15
UCHL1 null	5	2	23	8

Figure 4.12: Assessment of hind limb function in UCHL1$^{-/-}$, UCHL1 $^{+/-}$ and WT mice.
Data points represent mean ± SEM of mice scored on a scale of 0-2. 0 = normal hind limb function, 1 = slight impairment, 2 = severe impairment of hind limb function. A) Severity of hind limb impairment increases with age in UCHL1 null mice; WT and heterozygous mice are unaffected. N = number of mice tested, values displayed in the table, panel B. Where mice were tested more than once in the 3 week time period, the average value was included. C) Population medians vary significantly between WT and UCHL1 null ($p < 0.0001$), but not between WT and heterozygous mice ($p > 0.05$), using a Kruskal-Wallis multiple comparisons test. Data points represent mean behavioural score for each mouse over 7 - 20 week time period. N=19 (Wild Type), N=67 (Heterozygous), N=36 (UCHL1 null).

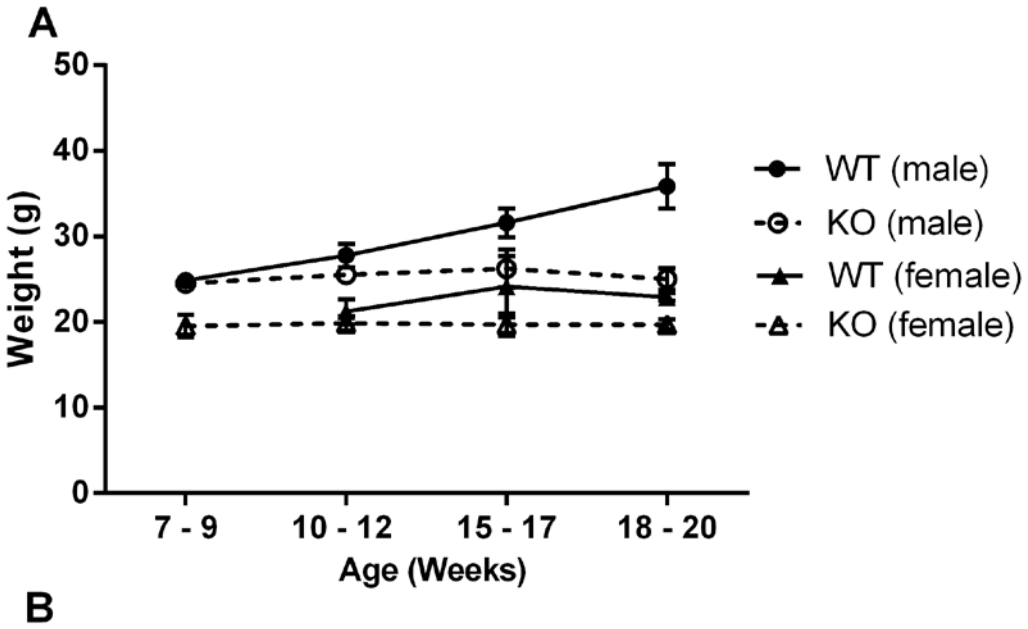

B

	WT (male)	KO (male)	WT (female)	KO (female)
7 - 9	1	2	0	2
10 - 12	2	1	7	3
15 - 17	5	8	5	4
18 - 20	2	2	3	8

Figure 4.13: UCHL1 KO Mice fail to gain weight after the hind limb impairment develops.
A) Weight (grams) of UCHL1 WT and KO mice, (split into male and female groups). Each data point represents mean ± SD. B) The number (n) of mice assessed for each data point is displayed in table B.

4.2.2 UCHL1 Knockout Mice have Reduced Monoubiquitin Levels

It is known that UCHL1 plays a crucial role in binding to and stabilising monomeric ubiquitin and levels of monomeric ubiquitin are decreased in mice that do not have functional UCHL1. Using western blots, I assessed levels of both monomeric ubiquitin and ubiquitin conjugates in UCHL1 knockout mice, as compared to wild type mice (Figure 4.14). We found that UCHL1 null mice have a significant decrease in levels of monomeric ubiquitin (Figure 4.14B, Figure 4.15A), p=0.0036, and that monomeric ubiquitin is decreased by around 50%. Levels of ubiquitin conjugates also appear slightly decreased in UCHL1 KO mice (Figure 4.14). However when levels of total ubiquitin conjugates are quantified and normalised to the loading control, the difference in ubiquitin conjugate levels between WT and KO UCHL1 mice is not significant (Figure 4.15B), p=0.0964, but is only decreased by trend. Furthermore, the optical density of each band on the ubiquitin ‘smear’ was quantified and normalised to the loading control. Results show that levels of ubiquitinated proteins of every molecular weight are consistently lower in knockout mice than wild type, however this difference is very slight and non-significant (Figure 4.15C).

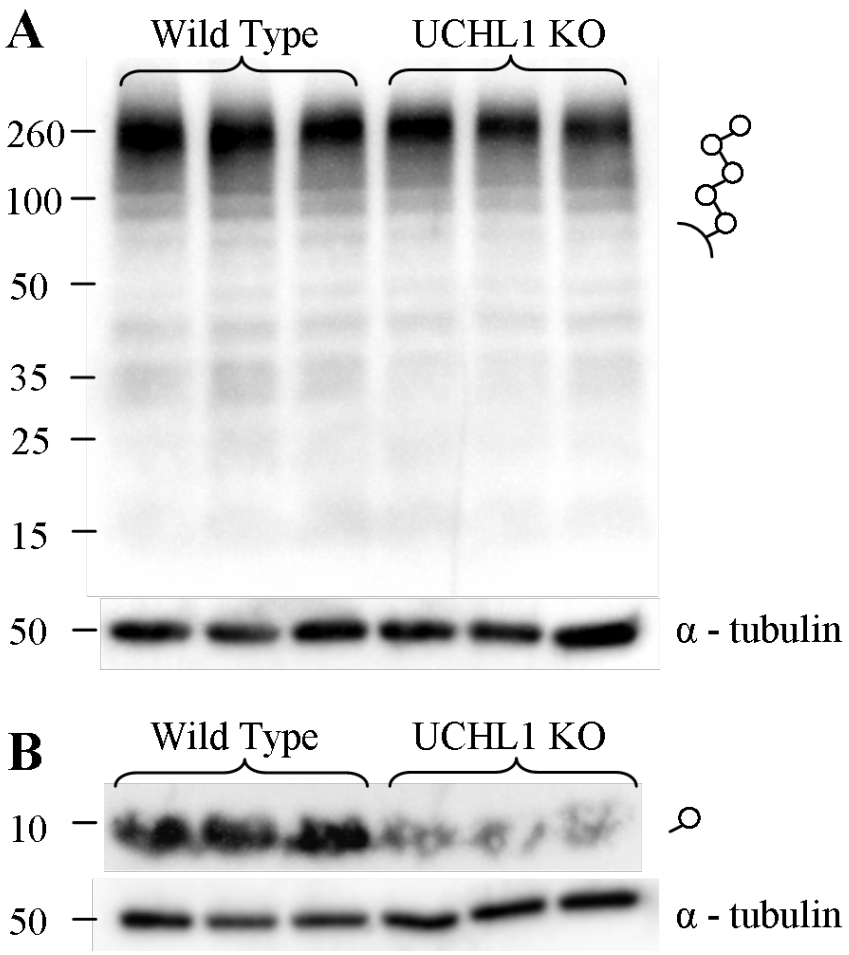

Figure 4.14: Reduced levels of ubiquitin conjugates and monoubiquitin in UCHL1 KO mice.
A) Western blot showing levels of ubiquitin conjugated proteins in Wild Type and UCHL1 KO mice. α – tubulin loading control (on the same blot) is shown underneath. B) Western blot showing decreased monoubiquitin in UCHL1 KO mice. (α – tubulin loading control also shown)

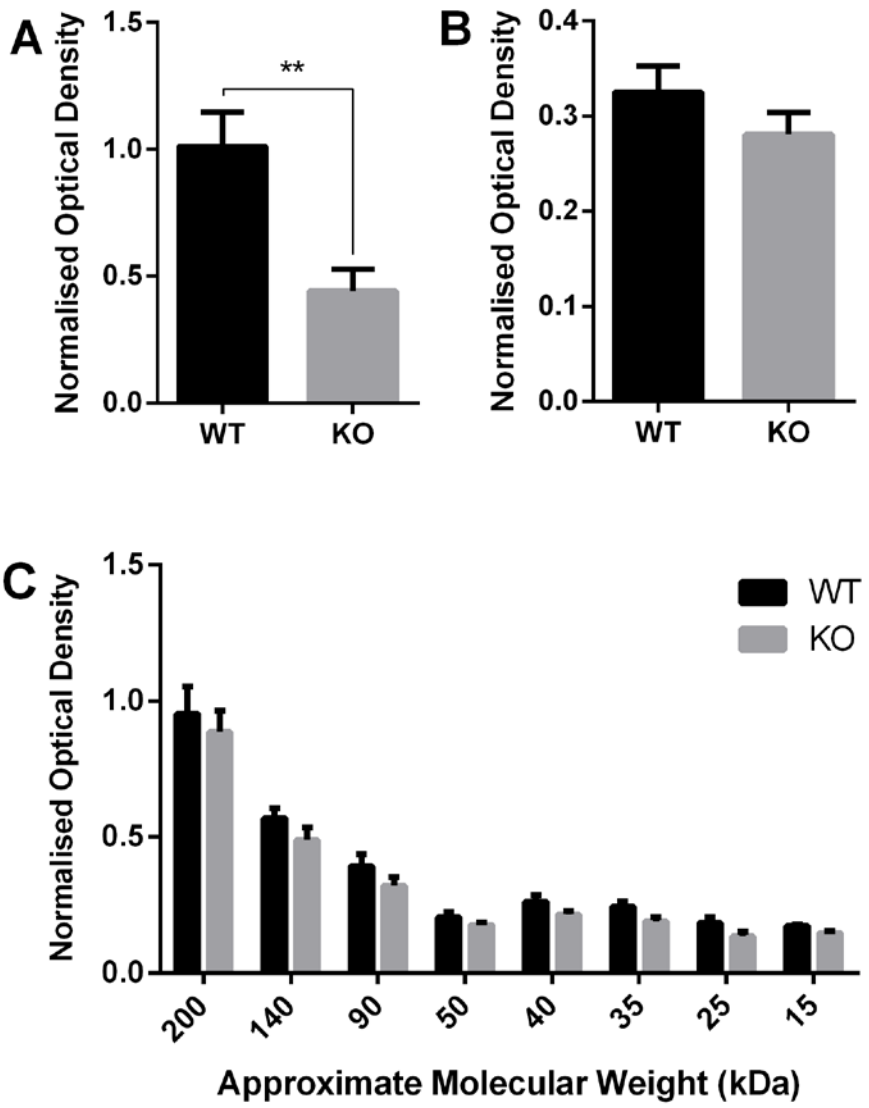

Figure 4.15: Densitometric quantification of monoubiquitin and ubiquitin conjugate levels in UCHL1 mice.
A) Monoubiquitin is significantly decreased in UCHL1 KO mice; p=0.0036, unpaired t test, n=3. B) Total ubiquitin conjugates are not significantly decreased in UCHL1 KO mice; p=0.0964, unpaired t-test, n=3). C) The normalised optical density of ubiquitin conjugate bands of all molecular weights are consistently but non-significantly decreased by trend (p=0.0442, p=0.0187, p=0.0311, p=0.3939, p=0.1491, p=0.1025, p=0.1398, p=0.4276), multiple t-tests with the Holm-Sidak correction, n=3, α=5%.

4.2.3 Neuropathological Assessment of UCHL1 Knockout Mice

4.2.3.1 COX/SDH Histochemistry

In order to test for the presence of a mitochondrial respiratory chain defect in the UCHL1 knockout mice, I performed COX/SDH dual histochemistry in sections taken from lumbar regions of WT and KO spinal cords. This well established assay reveals cytochrome *c* oxidase (COX, complex IV) deficient neurons as those which are positive for succinate dehydrogenase (SDH, Complex II) activity (blue), but negative for cytochrome *c* oxidase activity (brown) (Old and Johnson, 1989). However, no COX deficiency was observed in the spinal cord tissue from knockout mice, therefore we moved on to locate the neuropathology and look for complex I and complex IV deficiency in these areas, using immunohistochemistry.

4.2.3.2 Regions Assessed that do not Demonstrate Pathology

To assess whether any neuropathological changes that had not been previously reported were present in UCHL1 knockout mice, tissue sections were taken systematically from level Bregma -4.38 (Figure 4.16A, inset) through to the brainstem (Bregma -8.24) from the brains of two wild type and two UCHL1 knockout 16 week old mice. At regular intervals, sections were stained with CFV (stains neuronal cell bodies), Loyez Haematoxylin (myelin) and H&E (general morphological stain). In assessing whether any neuropathological changes had taken place, I paid particular attention to regions that are part of sensory-motor pathways, such as the medial lemniscus, middle cerebellar peduncle (Figure 4.16, blue arrows), and the pyramidal decussation. The medial lemniscus carries the axons of secondary neurons of the gracile tracts, whose cell bodies originate in the gracile nucleus of the medulla, and project axons to the thalamus, conveying sensory information. The middle cerebellar peduncle conveys axons of pontine grey neurons to the cerebellum (pontocerebellar tract), where they synapse with granule cells, forming part of the motor loop. The pyramidal decussation is the crossing of the bundles of the pyramidal tracts in the brainstem; the axons belonging to the tract at this point are those of upper motor neurons.

Tissue sections featuring the medial lemniscus and middle cerebellar peduncle, were stained with H&E, Loyez haematoxylin for myelin, and by immunohistochemistry to SMI-31 (phosphorylated neurofilaments). H&E staining appeared normal, and there were no eosinophilic axonal spheroids observed in the medial lemniscus or middle

cerebellar peduncle. There were no white matter lesions or loss of white matter apparent visible from Loyez haematoxylin staining, and no axonal loss visible from immunohistochemistry to phosphorylated neurofilaments.

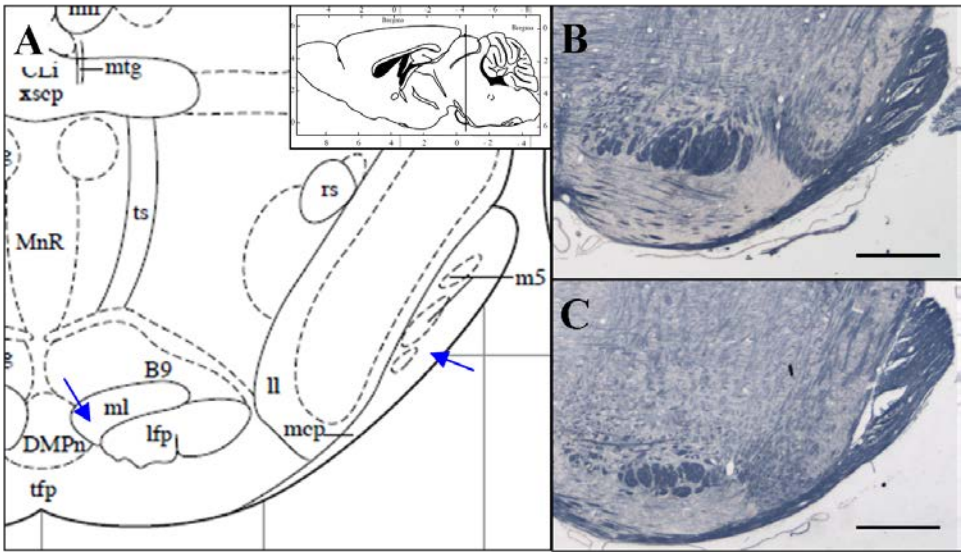

Figure 4.16: No pathological changes in the medial lemniscus or middle cerebellar peduncle.
A) Diagram of the brain region from which tissue sections were taken, adapted from (Paxinos, 2001). The medial lemniscus (ml) and middle cerebellar peduncle (mcp) are indicated by blue arrows. B) WT section showing Loyez staining in the ml and mcp. C) KO section showing staining in the ml and mcp. Scale bars = 50μm.

In order to assess whether there was any loss of myelin or axons in the middle cerebellar peduncle, high magnification images of SMI-31 immunohistochemistry and Loyez Haematoxylin staining in these regions were taken, and quantified densitometrically. There was no significant change in levels of phosphorylated neurofilaments or myelin (Figure 4.17), indicating that axons of pontine grey neurons are unaffected in UCHL1 knockout mice.

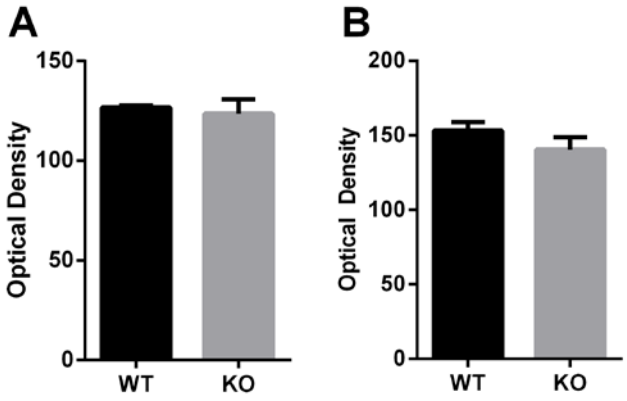

Figure 4.17: Densitometric quantification of phosphorylated neurofilament and myelin levels.
A) Optical density of SMI-31 immunohistochemistry in the middle cerebellar peduncle. No significant difference, unpaired t-test, p=0.5957, n=2. B) Optical Density of Loyez staining in the middle cerebellar peduncle. No significant difference, unpaired t-test, p=0.2167, n=2. Bars represent mean + SD

I also examined the pyramidal decussation using SMI-31 immunohistochemistry since this area contains upper motor neurons which carry motor information to all areas, including the hind limbs. It was previously found that the retraction of lower motor neurons from neuromuscular junctions in the hind limbs occurs progressively in UCHL1 null mice (Chen *et al.*, 2010a), therefore I wanted to assess whether the upper motor neurons, which synapse with these lower motor neurons were affected by axonal dystrophy. SMI-31 immunohistochemistry demonstrated that there was no evident loss of axonal density in this region, and there were no signs of axonal dystrophy or axonal spheroids.

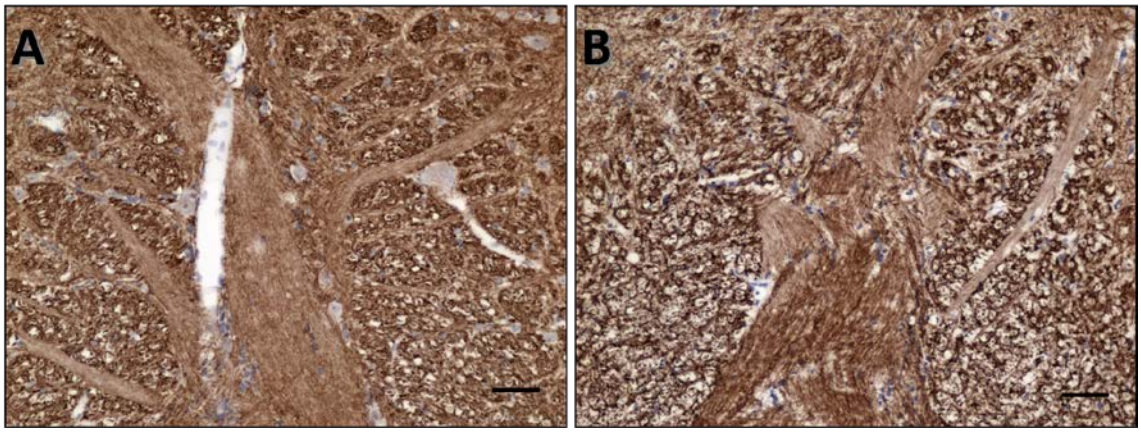

Figure 4.18: SMI-31 immunohistochemistry in UCHL1 KO mice.
No apparent axonal dystrophy or loss in the pyramidal decussation of UCHL1 KO mice. A) Wild Type; B) UCHL1 KO. Scale Bars = 50μm

Using H&E and CFV histological stains, I also examined the Purkinje cell layer in the cerebellum, as Purkinje cell loss is commonly observed in conditions such as mtDNA disease and cerebellar ataxia. I found that levels of Purkinje cells appeared normal, and there was no apparent cell loss. Using both Loyez haematoxylin staining and SMI-31 immunohistochemistry, I determined whether there was any myelin or axon loss in the white matter in the cerebellum of UCHL1 KO mice. At 16 weeks, there is clear axonal dystrophy, but no axon or myelin loss at detectable levels, and no lesions in the white matter. Subtle changes in axons, myelin and synapses would be difficult to identify in the cerebellum, as there is a lot of input from several axonal tracts in this area. Therefore, I went on to assess synapse levels in the gracile nucleus, an area in which axons from only one (affected) axonal tract synapse.

4.2.4 Axonal Spheroids: Location and Distribution in the Cerebellum

Axonal swellings (spheroids) are observed in the white matter of the cerebellum in knockout mice but not in wild type mice, and contain neurofilaments, synaptophysin, APP and mitochondria. Spheroids are present predominantly in the white matter of the cerebellum, close to (and occasionally in) the granular layer in the distal parts of the dystrophic axons, and are also observed in the inferior cerebellar peduncle (shown in Figure 4.19A), through which sensory neurons of the dorsal spinocerebellar tract pass into the cerebellum. Spheroids are seen predominantly in medial and intermediate regions of the cerebellum (Figure 4.19B,C); these are the regions of the cerebellum which are innervated by axons from the dorsal spinocerebellar and cuneocerebellar tracts (Gebre *et al.*, 2012). Axons from the olivocerebellar tract do also target these regions, however the distribution of axonal spheroids suggests that the neurons affected are either DSCT or CCT; if axons from the olivocerebellar or pontocerebellar tracts were affected, you would expect to see axonal spheroids in the more lateral regions of the cerebellum.

The cuneocerebellar tract consists of two neuronal populations. The first originates in the dorsal root ganglion above C8, and projects axons to the lateral cuneate nucleus, via the cuneate fasciculus. The neurons in the lateral cuneate nucleus then project into the cerebellum via the inferior cerebellar peduncle, synapsing with granular cells in the medial and lateral regions of the cerebellum. You would therefore expect axonal spheroids to be present in distal regions of axons projected from the DRG (in the cuneate fasciculus and nucleus), rather than in the cerebellar white matter. This further suggests that the axonal dystrophy seen in the medial and intermediate regions of the cerebellum is likely to affect the dorsal spinocerebellar tract, rather than the cuneocerebellar tract.

Spheroids are particularly prevalent in white matter innervating the anterior and posterior zones of the cerebellum (lobes I-V, VIII-IX), but not in the central and nodular zones (VI-VII, X) (Figure 4.19), further demonstrating that it is dorsal spinocerebellar tracts that are affected (Gebre *et al.*, 2012). Axonal spheroids are heterogeneous in size and appearance; the mean spheroid length is 15μm, however they range from 4μm diameter (around the same size as a nucleus), to a massive 76μm in length, far bigger than a Purkinje cell. Some spheroids appear roughly circular, whilst others are irregular or more elongated.

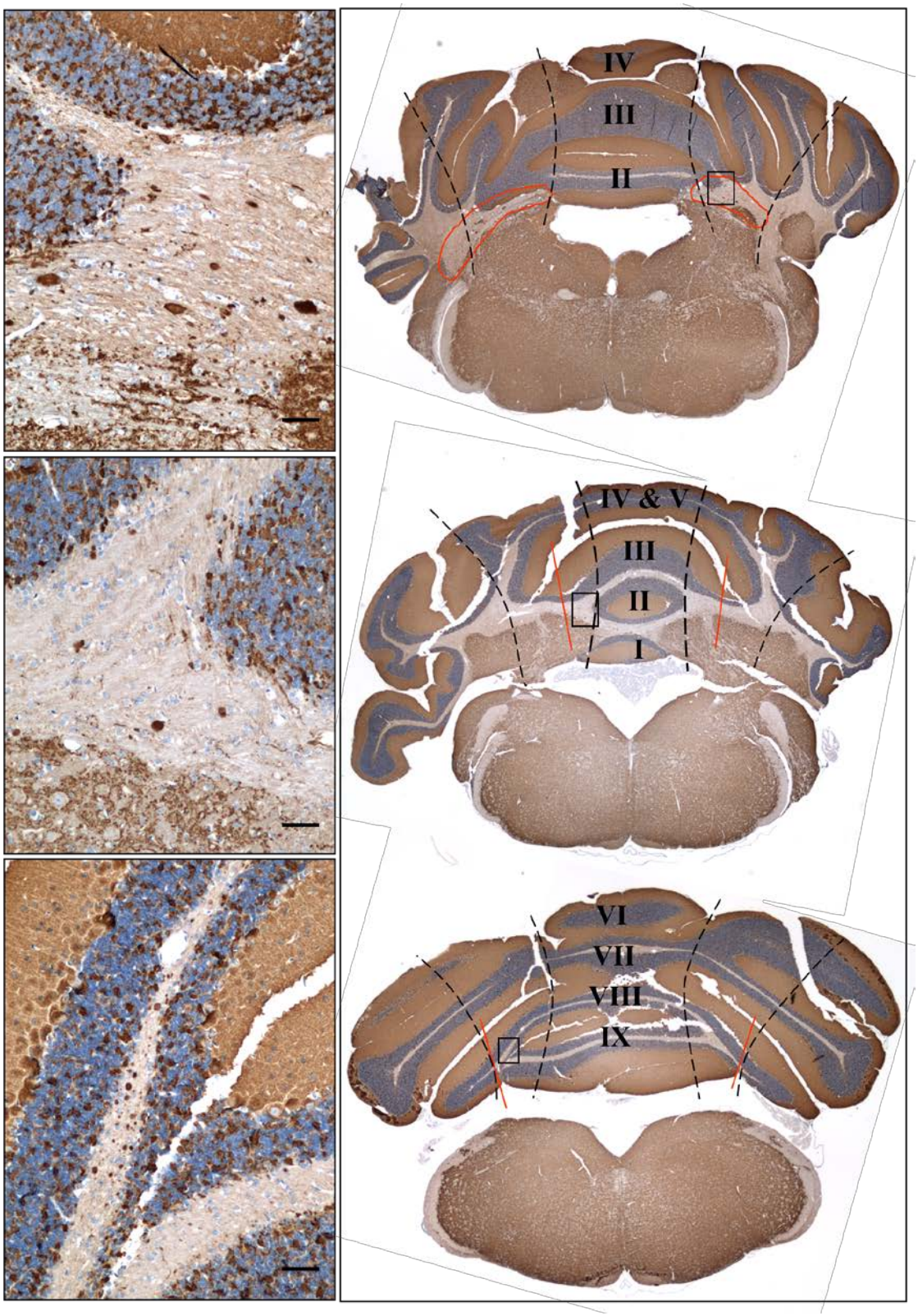

Figure 4.19: The distribution of axonal spheroids in the cerebellum.
Dashed lines indicate the vermis, paravermis and lateral hemispheres. Black boxes indicate position of high magnification images (left). Top) Axonal spheroids and dystrophic axons are seen in the inferior cerebellar peduncle as it enters the cerebellum (inside red circles) Middle) Spheroids are within the red lines, in white matter innervated lobules I-III of the cerebellum. Bottom) Spheroids are seen in the white matter of lobules VIII and IX, but not VII and VI.

4.2.5 Axonal Spheroids: Location and Distribution in the Brainstem

Axonal spheroids are abundant in the gracile nucleus and gracile fasciculus, and are also present in the cuneate nucleus, although less numerous. The gracile tract carries axons from sensory neurons with cell bodies in the dorsal root ganglia from thoracic level 6 downward. These axons synapse with neurons in the gracile nucleus, which then project to the thalamus. There are many axonal spheroids present in the gracile nucleus, with an average of 57 axonal spheroids per coronal cross section of the gracile nucleus in 16 week old UCHL1 knockout mice (counted using synaptophysin as a spheroid marker).

4.2.5.1 Synapse Loss in the Gracile Nucleus

Immunohistochemistry to synaptophysin, a marker of presynaptic vesicles, reveals the loss of synapses from the gracile nucleus of knockout mice (p=0.0364, Figure 4.20), but not from the cuneate nucleus (p=0.3195). The synapses lost are between the long sensory neurons of the gracile tract, which synapse with secondary neurons in the gracile nucleus, which project to the thalamus. The significant decrease in the density of synapses from the gracile nucleus, but not the cuneate nucleus demonstrates that the longest axons are most vulnerable to axonal dystrophy and synapse loss, since axons of neurons in the cuneate tract are shorter than those in the gracile tract, since they are projected only from the mid-thoracic level and above.

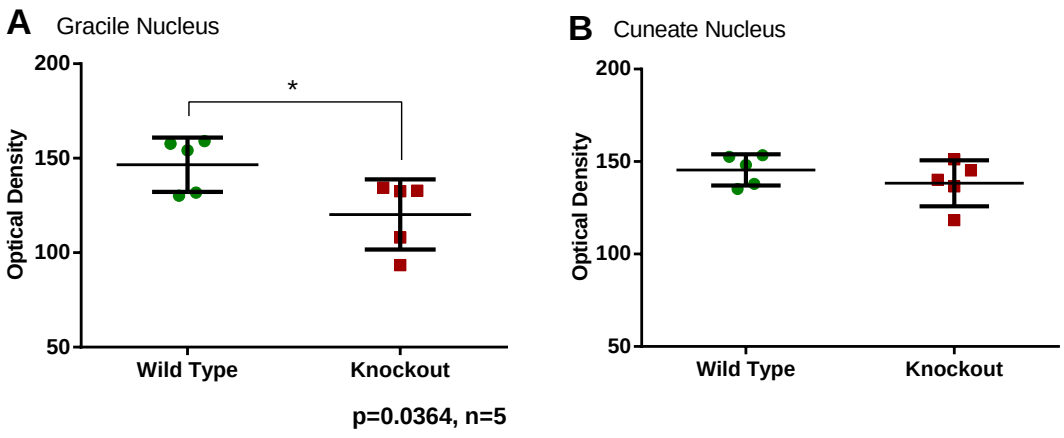

Figure 4.20: Loss of Synapses from the Gracile Nucleus.
Densitometric quantification of synaptophysin staining intensity, where optical density = 255- mean densitometric value. A) Gracile Nucleus (significant, p=0.0364, n=5), B) Cuneate Nucleus (not significant, p=0.3195, n=5). Calculated using an unpaired t test at 95% CI. Bars show mean ±SD.

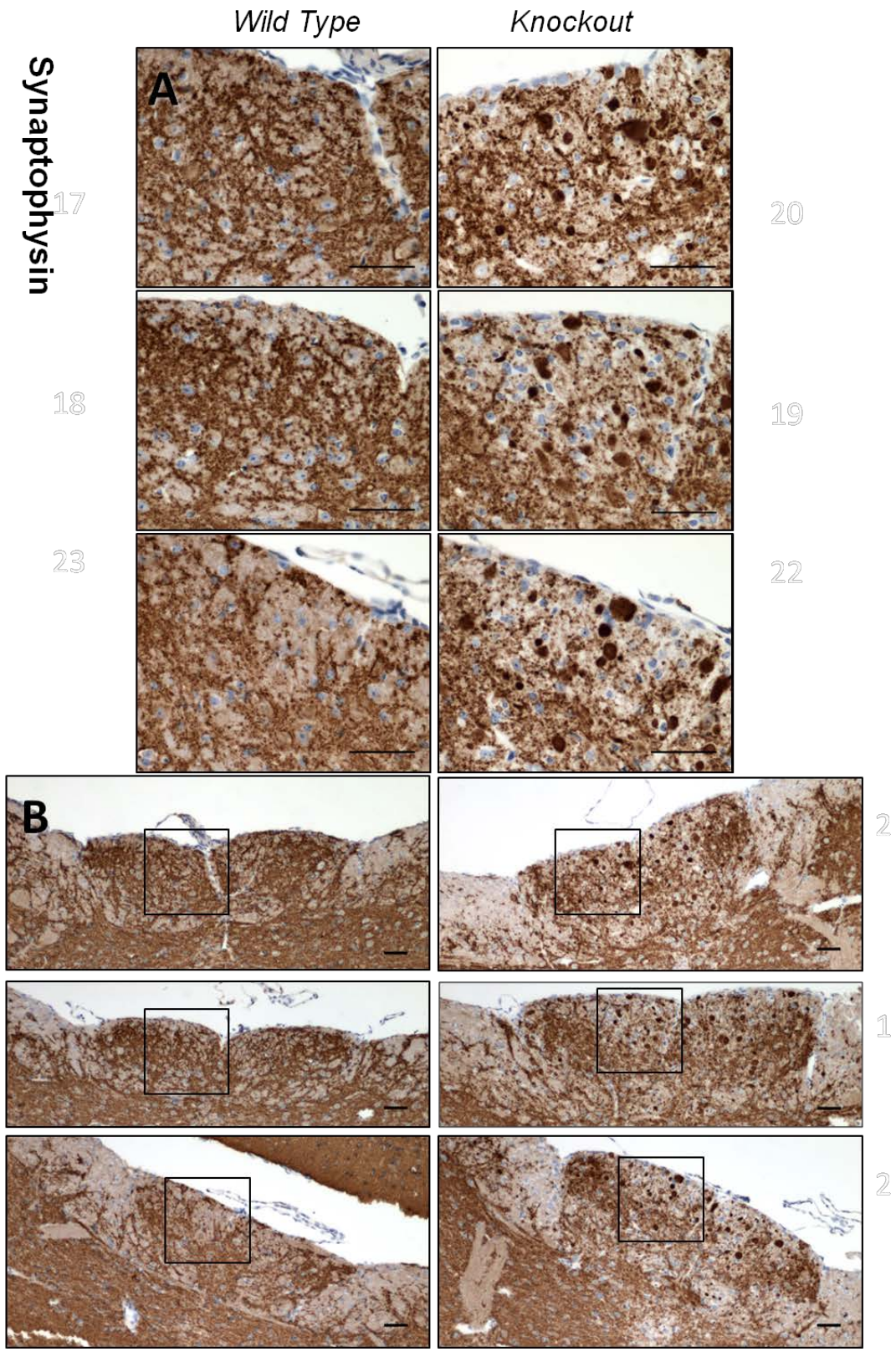

Figure 4.21: Images demonstrating loss of synapses from the gracile nucleus.
Images of 3 out of 5 WT (left) and KO (right), representative of those analysed in Figure 4.20. A) High magnification images of synaptophysin in the gracile nucleus, B) Low magnification images; black boxes indicate locations of high magnification images from panel B. Scale Bars = 50μm

In addition to showing the loss of synapses in the gracile nucleus, immunohistochemistry to synaptophysin also shows that it accumulates in axonal

spheroids as shown in Figure 4.22B, to the extent that the intense immunoreactivity to synaptophysin in spheroids is clearly distinguishable from surrounding synapses or white matter clearly.

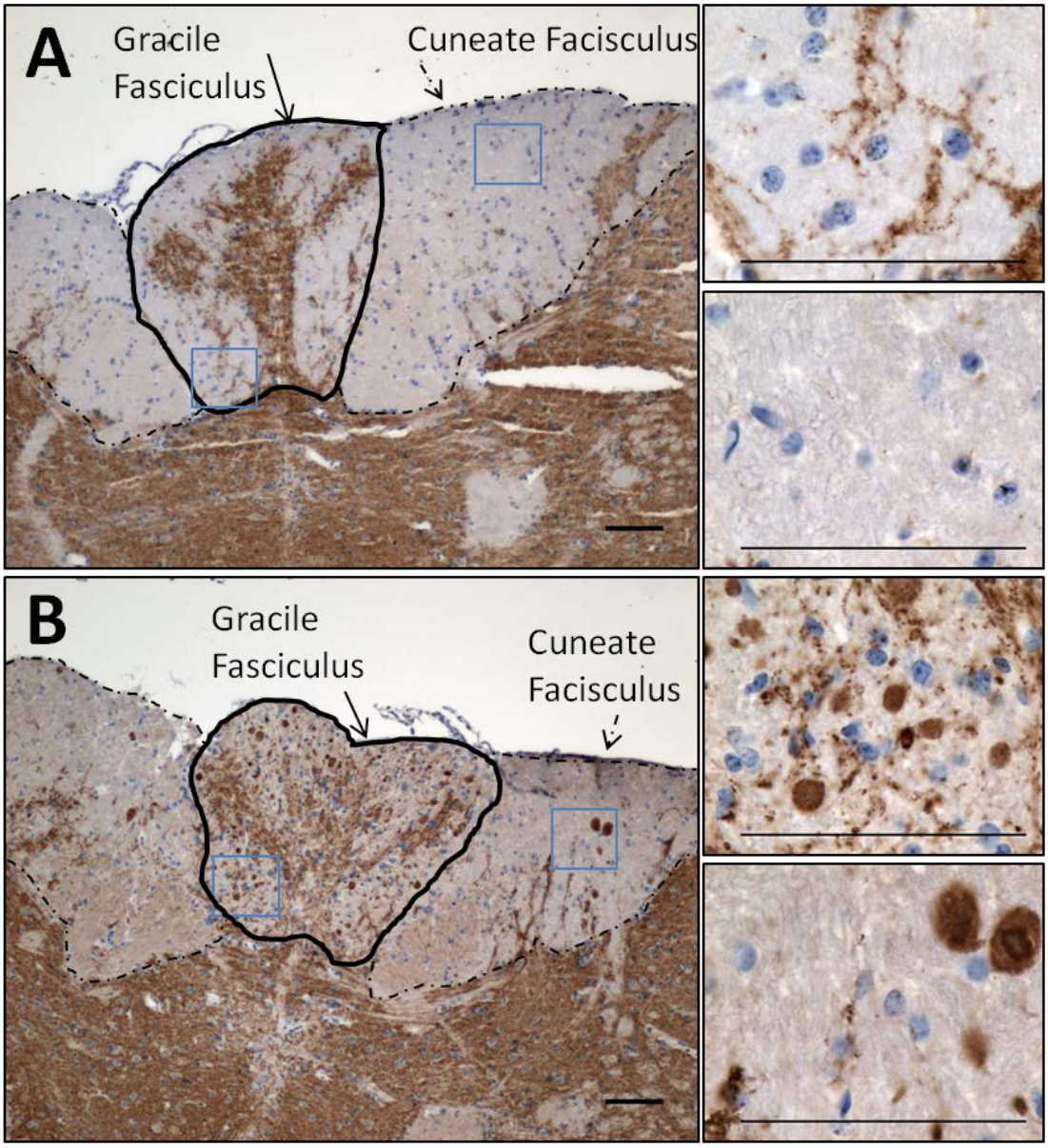

Figure 4.22: Synaptophysin accumulation in the Gracile and Cuneate Fasciculus.
Synaptophysin accumulates in axonal spheroids in the gracile (top right, panel A,B) and cuneate (bottom right, panel A,B) fasciculi of KO mice. A) Wt, B) KO.

4.2.5.1 Axonal Loss in the Gracile Tract

The antibody SMI-31, which binds to phosphorylated neurofilaments (heavy and medium subunits) was used as marker for axons, since axonal calibre is determined by the phosphorylation (and subsequent increase in diameter) of neurofilaments. High magnification images (x100) were taken of immunohistochemistry to SMI-31 from the gracile nucleus and gracile fasciculus from 5 wild type and 5 UCHL1 null mice. Quantification of SMI-31 immunohistochemistry by densitometry demonstrates a reduction in axonal density in the gracile fasciculus of the knockout mice, p=0.0037 (Figure 4.23). The loss of axons in the gracile tract is evident when comparing images of SMI-31 IHC from the same areas in WT and KO mice, as seen in Figure 4.24; in UCHL1 null mice, the distal ends of gracile tract axons are lost as early as 9 weeks. It is also evident from these images that neurofilaments accumulate in axonal spheroids, which are abundant in the gracile nucleus.

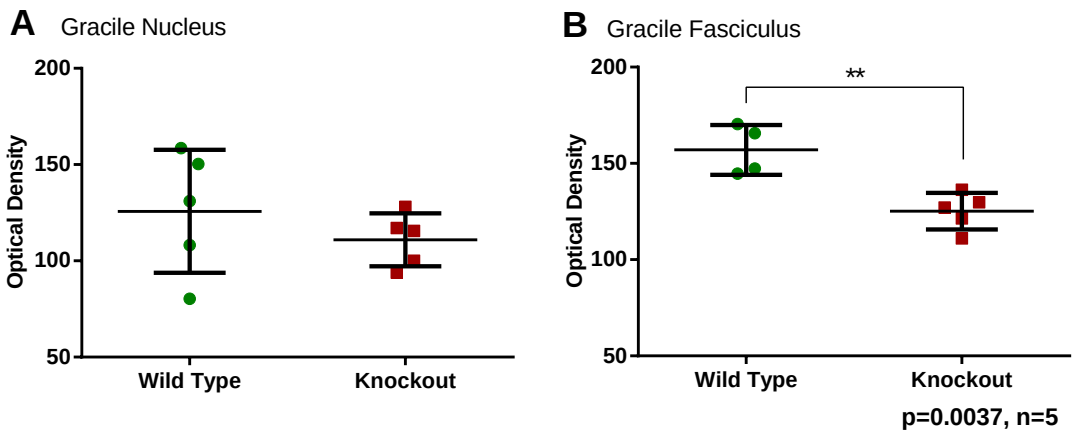

Figure 4.23: Axonal Loss in the Gracile Fasciculus.
A) Gracile Nucleus (Not significant, p=0.3829, n=5; unpaired t-test with Welch's correction). B) Gracile Fasciculus (Significant difference, p= 0.0037, n=5; unpaired t test.) Densitometric quantification of SMI-31 immunoreactivity, where 0= white and 255 = black. Bars show mean ±SD.

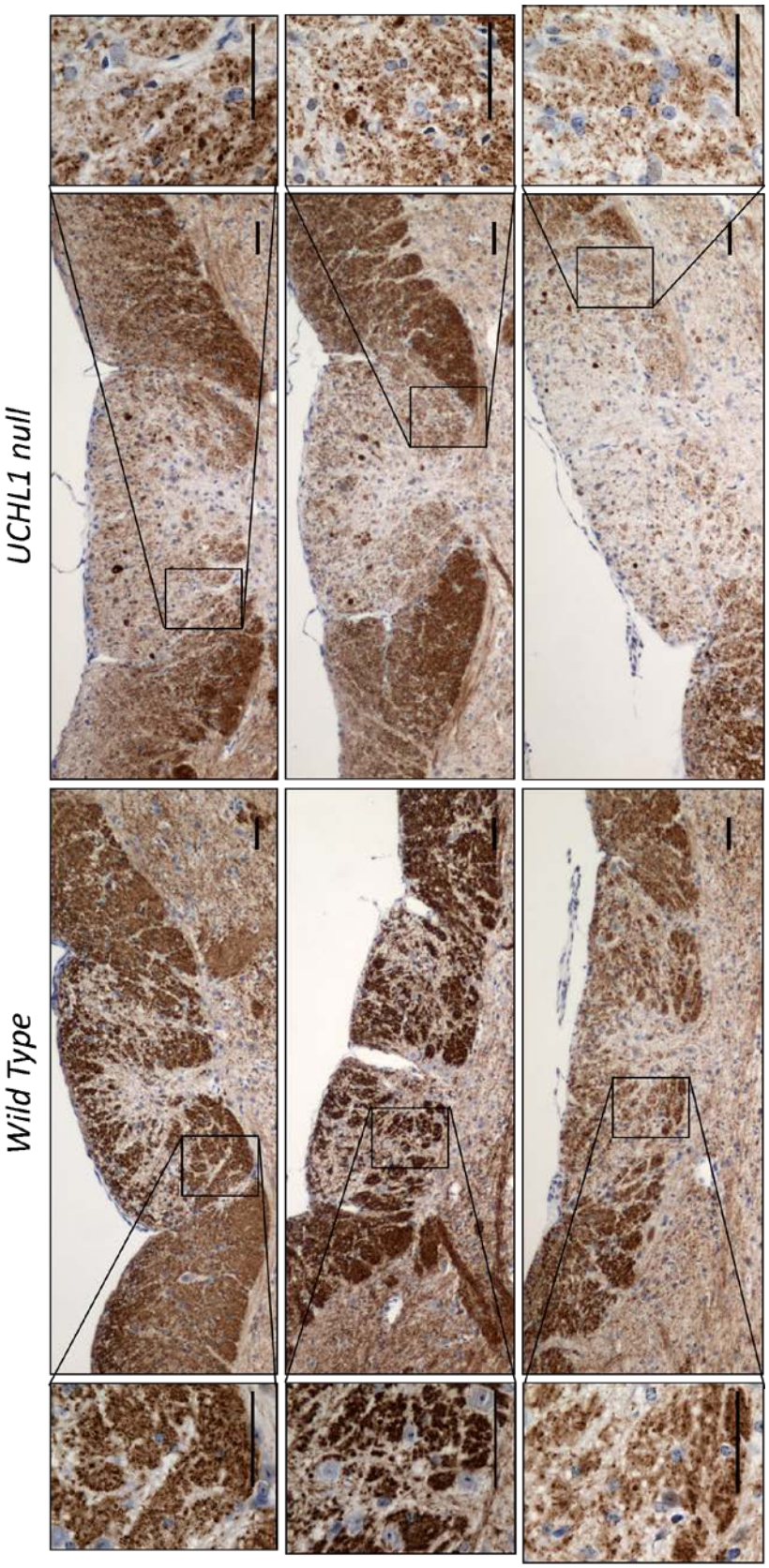

Figure 4.24: Axonal loss in the gracile tract.
Images are of immunohistochemistry using SMI-31, an antibody to phosphorylated neurofilaments, used as an axonal marker. Left hand side; images showing the gracile nucleus and fasciculus (and cuneate fasciculus) of 3 separate WT mice. Right hand side; equivalent images from 3 UCHL1 knockout mice. Outer-most images are high magnification images used for densitometry to assess axonal loss in the gracile fasciculus, in the regions indicated. Scale bars = 50μm.

4.2.5.2 Myelin Loss in the Gracile Tract

The possibility of axon demyelination or loss of myelinated axons in the gracile and cuneate nuclei and fasciculus were examined by assessing the immunoreactivity of MBP-4 (an antibody to myelin binding protein) in these areas. The comparison of images from equivalent brainstem areas suggests that there is a loss of myelin in the gracile fasciculus (Figure 4.25). Dark areas of DAB chromogen staining in the gracile fasciculus of WT mice (Figure 4.25A), appear much less intense in equivalent images from KO mice, due to a reduction in myelin levels. Quantification of high magnification images of MBP-4 immunohistochemistry in the gracile and cuneate tracts confirms that the loss of myelin from the gracile fasciculus in UCHL1 null mice is significant, $p=0.0159$ (Figure 4.26). However, myelin density in the gracile nucleus, cuneate nucleus and cuneate fasciculus of KO mice remain comparable to WT mice ($p=0.1262$, $p=0.8448$, $p=0.3968$, respectively).

The loss of myelin in the gracile fasciculus is due to the loss of myelinated axons from this area, rather than demyelination of intact axons. The areas in which a reduction of myelin is observed are the same as the areas in which axonal loss is also observed. As shown in Figure 4.23B, SMI-31 immunohistochemistry demonstrates that axons are lost from the gracile fasciculus in UCHL1 null mice, and the significant decrease in myelin density in the corresponding area shows that it is myelinated axons are lost.

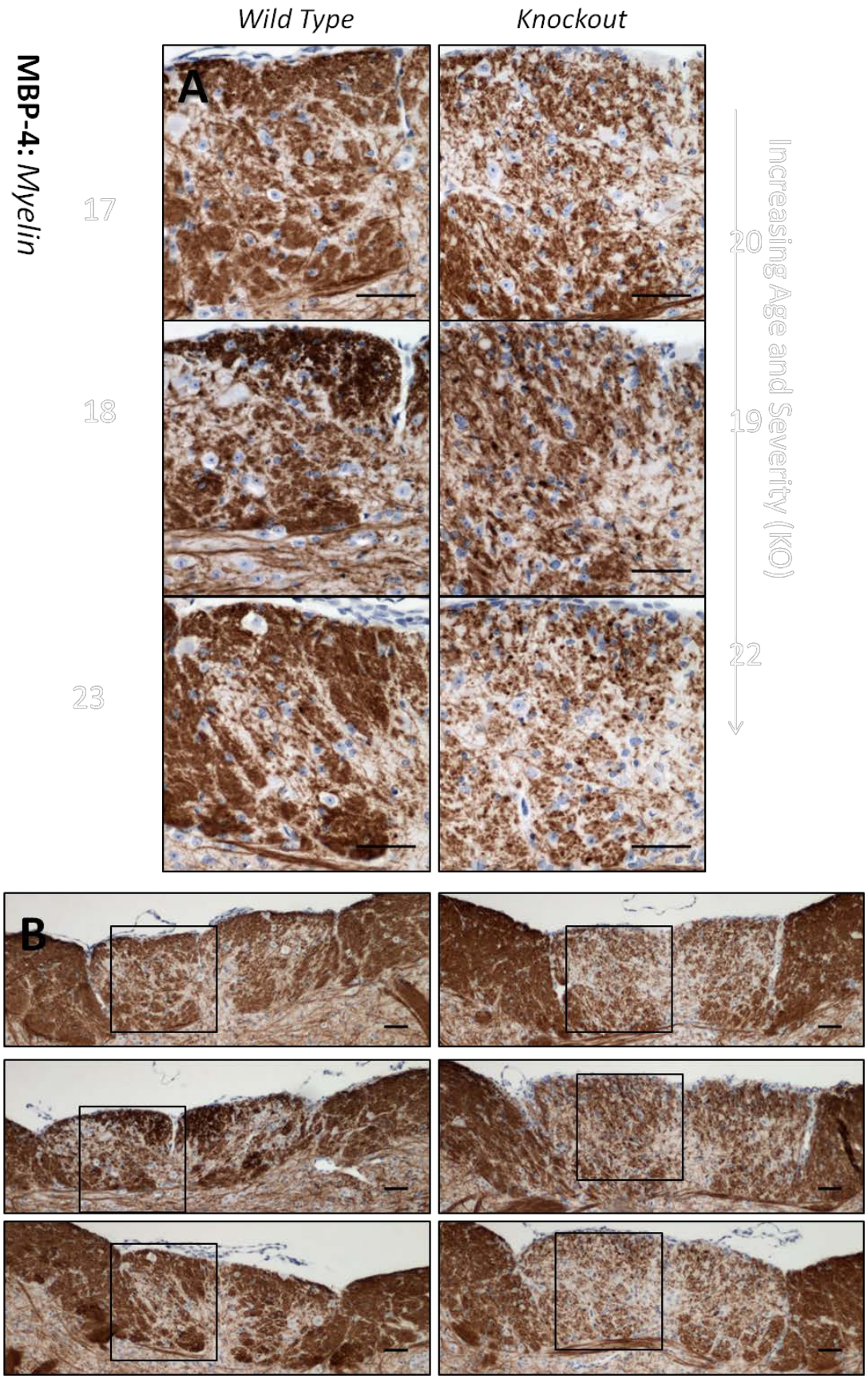

Figure 4.25: Images demonstrating loss of myelin loss in the gracile tract.
Images of 3 out of 5 WT (left) and KO (right), representative of those analysed in figure 4. A) High magnification images of myelin in the gracile nucleus and fasciculus, B) Low magnification images; black boxes indicate locations of high magnification images from panel B. Scale Bars = 50μm

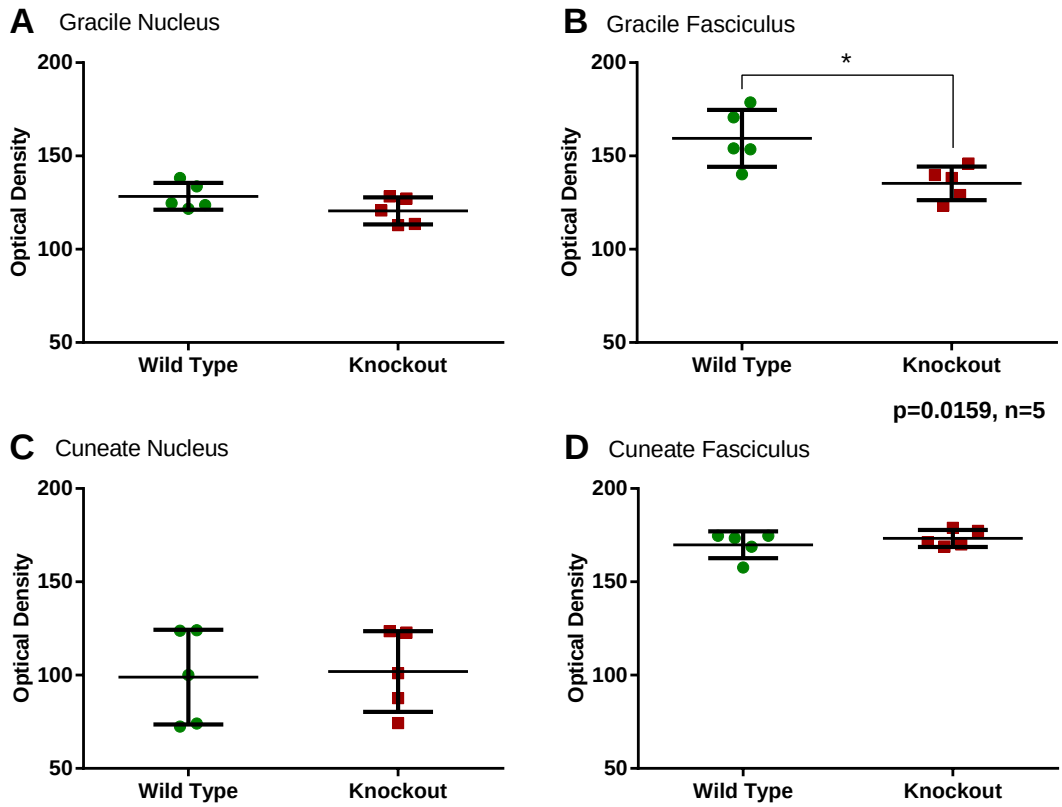

Figure 4.26: Myelin loss in the Gracile Fasciculus.
A) Gracile Nucleus (Not significant, p=0.1262, n=5; unpaired t-test). B) Gracile Fasciculus (Significant difference, p= 0.0159, n=5; unpaired t test.) C) Cuneate Nucleus (Not Significant, p= 0.8448, n=5, unpaired t test) D) Cuneate Fasciculus (Not Significant, p= 0.3968). Densitometric quantification of SMI-31 immunoreactivity, where 0= white and 255 = black. Bars show mean ±SD

4.2.5.3 APP Immunoreactivity in the Gracile Tract

APP (Amyloid Precursor Protein) is synthesised in neuronal cell bodies, and moved by fast axonal transport in a retrograde direction to the distal ends of axons. Therefore, antibodies to APP are widely used as indicators of axonal transport; blockages of axonal transport cause APP to accumulate in axons. Previous studies of the '*gad* mouse', which has no function UCHL1, have demonstrated an increase in the immunoreactivity of APP in the gracile nucleus, reflecting a possible decrease in axonal transport.

I have also examined the immunoreactivity of APP in the gracile nucleus, and I do observe a small but detectable increase in APP immunoreactivity in UCHL1 null mice, by eye (Figure 4.27). However, when quantified densitometrically, the increase in APP immunoreactivity is not significant (Figure 4.28). As demonstrated in Figure 4.27A, APP immunoreactivity is not as intense as would perhaps be expected in axonal spheroids, rather there seem to be small punctate accumulations of APP within axons.

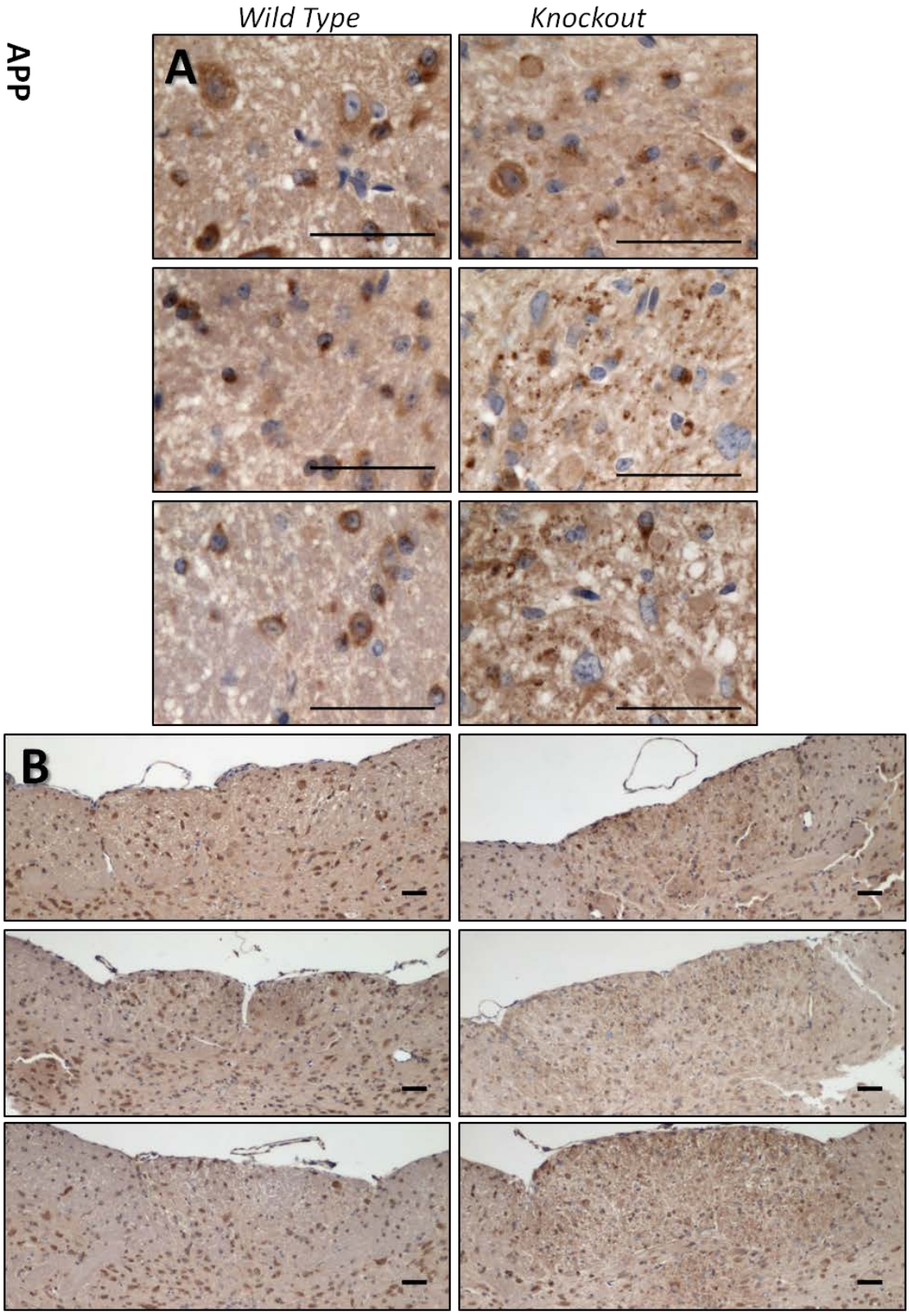

Figure 4.27: APP immunoreactivity in the gracile tract.
Images of 3 out of 5 WT (left) and KO (right), representative of those analysed in figure 4. A) High magnification images of APP in the gracile nucleus and fasciculus, demonstrating punctate APP accumulations B) Low magnification images of APP immunohistochemistry in the gracile tract and cuneate fasciculus. Scale Bars = 50μm

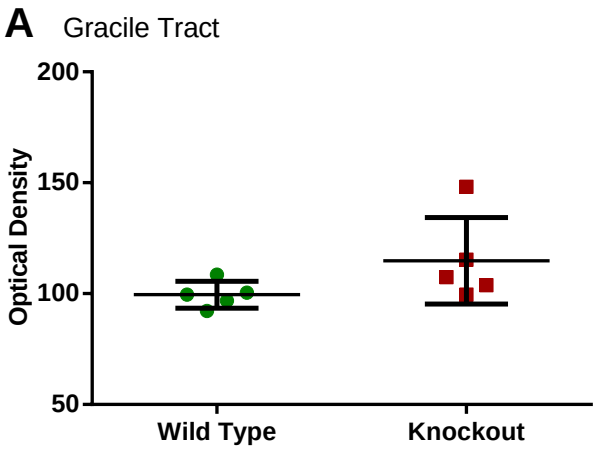

Figure 4.28: APP Immunoreactivity in the Gracile Tract.
Densitometric quantification indicates increased levels of APP in knockout mice by trend, however the difference is not significant (p=0.1567, n=5 mice, 95% CI unpaired t test with Welch's correction.) Optical density is a measure of image darkness, where 0= white and 255 = black. Bars show mean ±SD.

4.2.5.4 Neuronal Cell Bodies in the Gracile Nucleus

There does not appear to be a loss of neuronal cell bodies in the gracile nucleus, although this has not been quantified. The neurons in the gracile nucleus project axons to the thalamus via the medial lemniscus. No axonal spheroids have been observed in the medial lemniscus with H&E staining or SMI-31 immunohistochemistry and there is no axonal or myelin loss in this area (Section 4.2.3.2), therefore we can conclude that these neurons are unaffected by ubiquitin depletion.

4.2.5.5 Axon, Myelin and Synapse Loss in the cerebellum

Although axonal spheroids are abundant in the axonal tracts that synapse in the cerebellum, axon myelin and synapse loss is not obvious here. However there is a subtle reduction in SMI-31 (phosphorylated neurofilaments) and Loyez (myelin) staining in regions where there are many axonal spheroids, indicating that there may be some loss of axons and therefore myelin also.

There is no apparent loss of synaptophysin immunoreactivity in the granular layer of the cerebellum, although with the number of axonal spheroids present in the cerebellar white matter, and considering the synaptic loss observed in the gracile nucleus, you would expect that some synapses have been lost here. It is possible that the number of synapses lost is not enough to cause an observable reduction to synaptophysin immunoreactivity in the granular layer (Figure 4.32), due to the number of synapses in this region, and the number of different axonal tracts that project to the granular layer (detailed in section 4.2.4) Therefore, it is possible that due to the huge amount of input

into this region that even if a proportion of dorsal spinocerebellar tract synapse and axons are lost, it may not be obvious from immunohistochemically stained sections.

4.2.6 Characterization of Axonal Spheroids by Immunohistochemistry

4.2.6.1 Neurofilaments Accumulate in Axonal Spheroids

Axonal spheroids are positive for immunohistochemistry to SMI-31 and, to a lesser extent SMI-32 (Figure 4.29). This indicates the accumulation of phosphorylated (and sometimes non-phosphorylated) neurofilaments in axonal spheroids, revealing a breakdown in local cytoskeletal structure. Neurofilaments are an essential component of the cytoskeleton in axons, and phosphorylation of the medium and heavy chains of neurofilaments is a normal step leading to the increase of axon calibre.

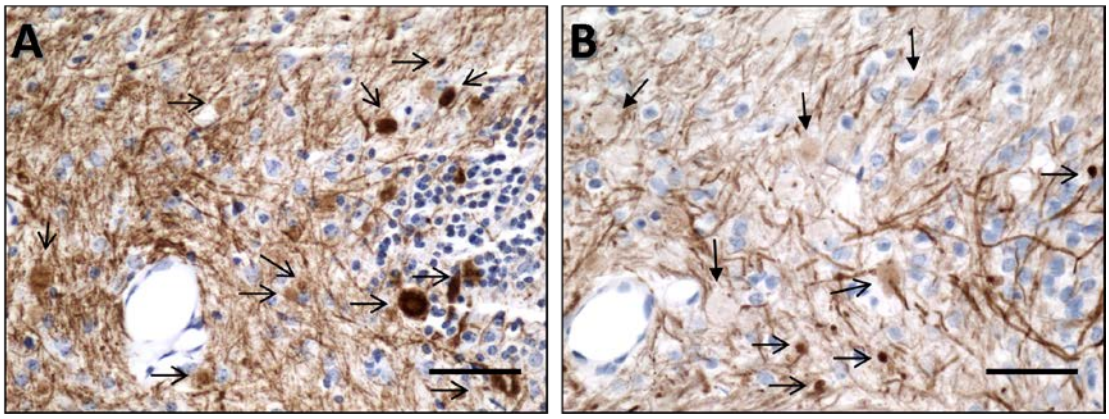

Figure 4.29 Neurofilaments accumulate in spheroids.
A) Accumulations of phosphorylated neurofilaments in axonal spheroids in axonal spheroids (red arrows) B) Some axonal spheroids contain accumulations of non-phosphorylated neurofilaments (red arrows), however there appear to be some axonal spheroids (areas with little or no staining) that do not contain non-phosphorylated neurofilaments (black arrows). Scale bars = 50μm.

4.2.6.2 Synaptophysin Marks Axonal Spheroids

In neurons, synaptophysin, an abundant integral membrane glycoprotein to synaptic vesicles, is synthesised in the cell body and inserted into membranes that originate from the endoplasmic reticulum. Synaptophysin is then transported on these membranes by retrograde fast axonal transport towards the synapses at distal regions of axons. Immunohistochemistry to synaptophysin strongly labels axonal spheroids in the cerebellum (Figure 4.30). Interestingly, there are some ‘spheroids’ that are very long and thin and some axons that stain faintly for synaptophysin. Therefore, since synaptophysin is synthesised in the cell body, its accumulation in axonal spheroids and dystrophic axons may indicate a blockage of fast axonal transport. Spheroids marked by synaptophysin immunohistochemistry are in stark contrast to the surrounding white matter, and are very easily identifiable, as opposed to SMI-31 immunohistochemistry, where it can be hard to distinguish whether an area of intense DAB chromogen is in fact a spheroid, or part of an axon. Therefore, synaptophysin is a very good antibody for use in unequivocally identifying axonal spheroids.

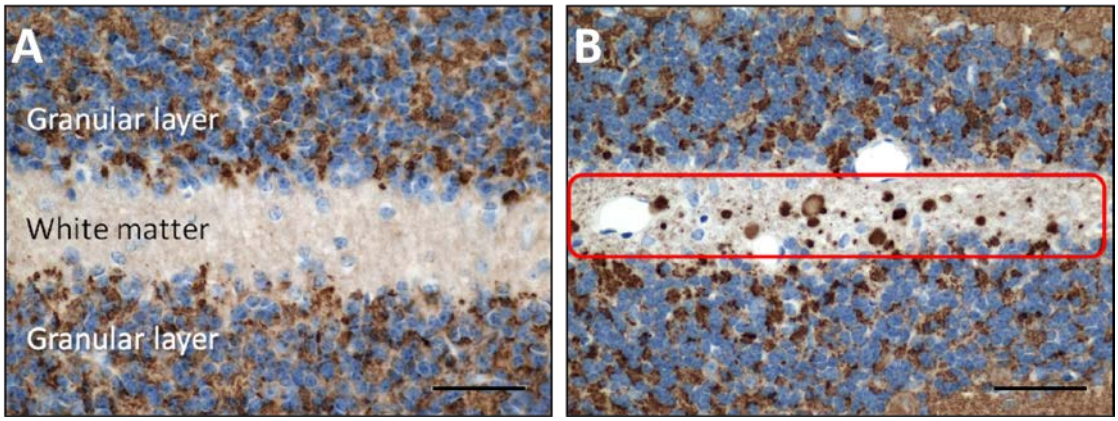

Figure 4.30: Synaptophysin marks axonal swellings in the cerebellum of knockout mice.
A) Wild Type, B) Knockout. Red rectangle denotes the area containing axonal spheroids (B). Images were taken from the same brain region in different mice. Scale Bars = 50μm

4.2.7 APP Accumulates in Axonal Spheroids

In knockout mice, APP accumulates in axonal spheroids and dystrophic axons in both the white matter of the cerebellum, and the inferior cerebellar peduncle, through which axonal tracts pass in order to reach the cerebellum (Figure 4.31). In tissue sections from the wild type mice, there is very little APP immunoreactivity; only faint staining in cell bodies, as expected in healthy axons.

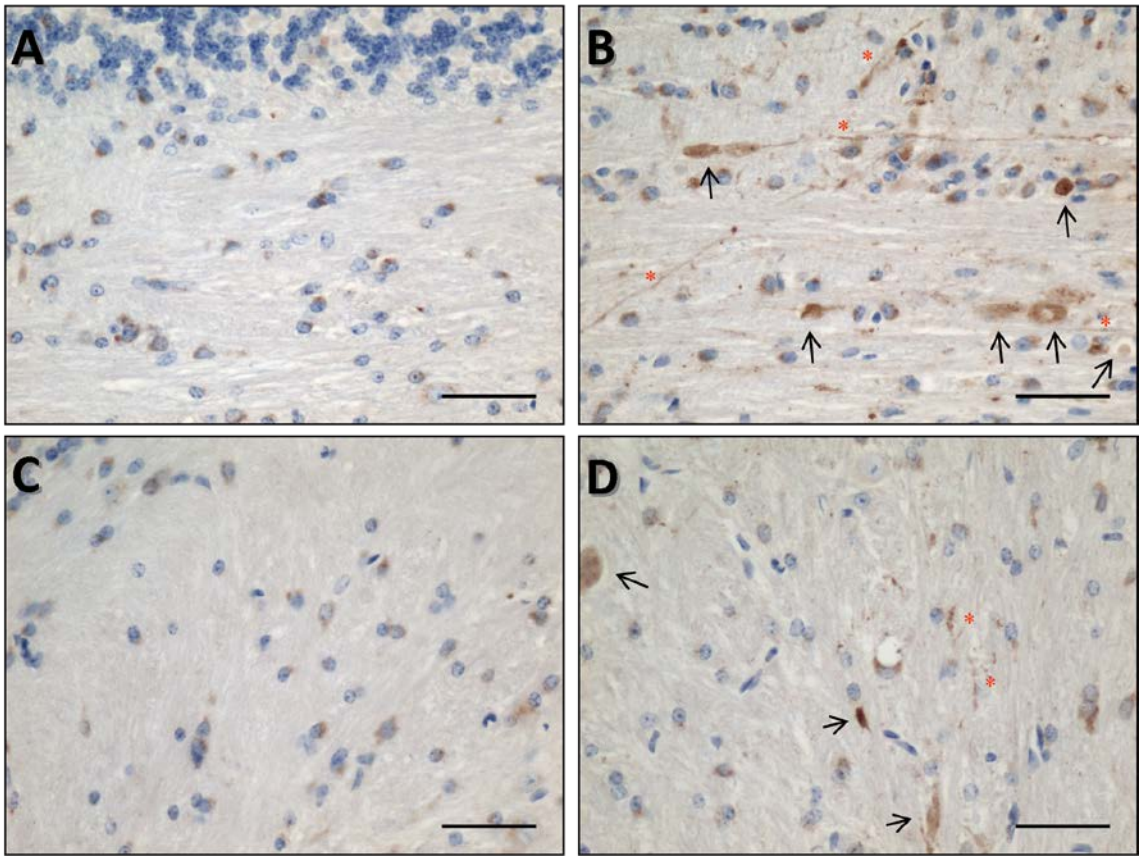

Figure 4.31: APP accumulation in dystrophic axons and spheroids.
APP builds up in dystrophic axons (red asterix) and spheroids (black arrows) in the cerebellar white matter (top) and inferior cerebellar peduncle (bottom) of knockout mice (B,D), but not wild type mice (A,C). Scale Bars = 50μm

Since APP is transported by fast axonal transport, the accumulation of APP in spheroids and dystrophic axons indicates that axonal transport is disrupted, and that a blockage of axonal transport may be part of the degenerative mechanism in these axons, however it is also noticeable that APP immunoreactivity in spheroids is far less than that of synaptophysin, and also the APP marks far fewer spheroids.

4.2.8 Mitochondria in Axonal Spheroids

I hypothesised that ubiquitin depletion in the distal regions of long axons would disrupt mitochondrial fission, fusion, motility and mitophagy, leading to the accumulation of damaged mitochondria. In order to test this hypothesis, I used markers to three mitochondrial respiratory chain complex subunits to assess respiratory chain deficiency and look at mitochondrial distribution.

Complex II of the mitochondrial respiratory chain is nuclear encoded, and therefore unaffected by damage to mtDNA. An antibody to the 70kDa subunit of complex II was used as a mitochondrial marker; results revealed accumulations of mitochondria in axonal spheroids in the cerebellum (Figure 4.32) and in the gracile tract. Measurements of the mitochondrial accumulations confirmed that they are the same size as axonal spheroids, and are distributed similarly in the white matter, indicating that mitochondria accumulate within axonal spheroids.

Axonal spheroids containing mitochondria are heterogeneous in size, shape and appearance. Most axonal spheroids are Complex II-70 positive, indicating that they are filled with mitochondria (Figure 4.32, top left). However, there are a small proportion of axonal spheroids that have little or no mitochondrial staining (Figure 4.32, bottom right), some of which seem to have a core containing mitochondria (Figure 4.32, bottom left).

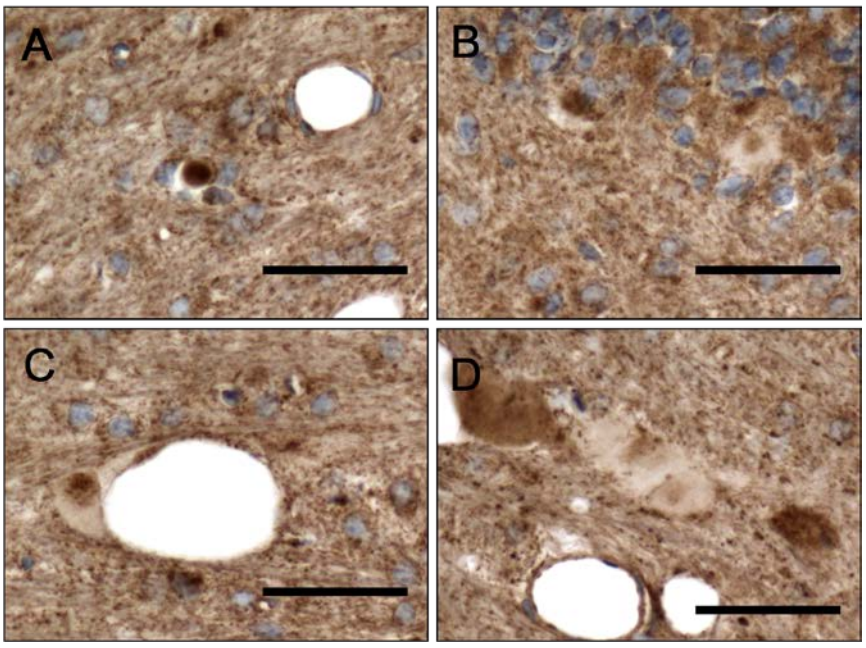

Figure 4.32: Axonal Spheroids containing mitochondria.
Spheroids can be filled with mitochondria (top left, contain a core of mitochondria (bottom left), or can appear to not contain mitochondria (bottom right) Images show immunohistochemistry to Complex II-70 in the white matter of the cerebellum, scale bars = 50μm.

To test for the presence of a respiratory chain deficiency, antibodies to complex I and complex IV subunits (*NDUFB8* and *MT-CO1)* were applied to a series of sections throughout the cerebellum and brainstem. Results do not indicate any mitochondrial respiratory chain deficiency.

There is no apparent decrease in the intensity of immunohistochemistry to Complex I and Complex IV in cerebellar white matter in UCHL1 null mice (Figure 4.33); neither is there any difference in Complex I and IV subunit immunohistochemistry in the granular layer or Purkinje cells.

Furthermore, immunohistochemistry to Complex I-20 and Complex IV-1 demonstrates that mitochondria in axonal spheroids are not deficient in either of those respiratory chain complexes, since they often have intense DAB chromogen staining, and certainly do not have less intense immunoreactivity than Complex II-70 (Figure 4.34). In order to quantify this, 100 axonal spheroids from sections stained using each of the three mitochondrial antibodies were classified according to their intensity and pattern of staining (Figure 4.35). These results show that there is no complex I or complex IV deficiency, as in this case you would expect to see a larger proportion of chromogen negative spheroids for CI-20 and COX-1 antibodies. However, this is not the case; results indicate that chromogen negative spheroids are in fact less common after immunohistochemistry to CI-20 and COX-1 (Figure 4.35).

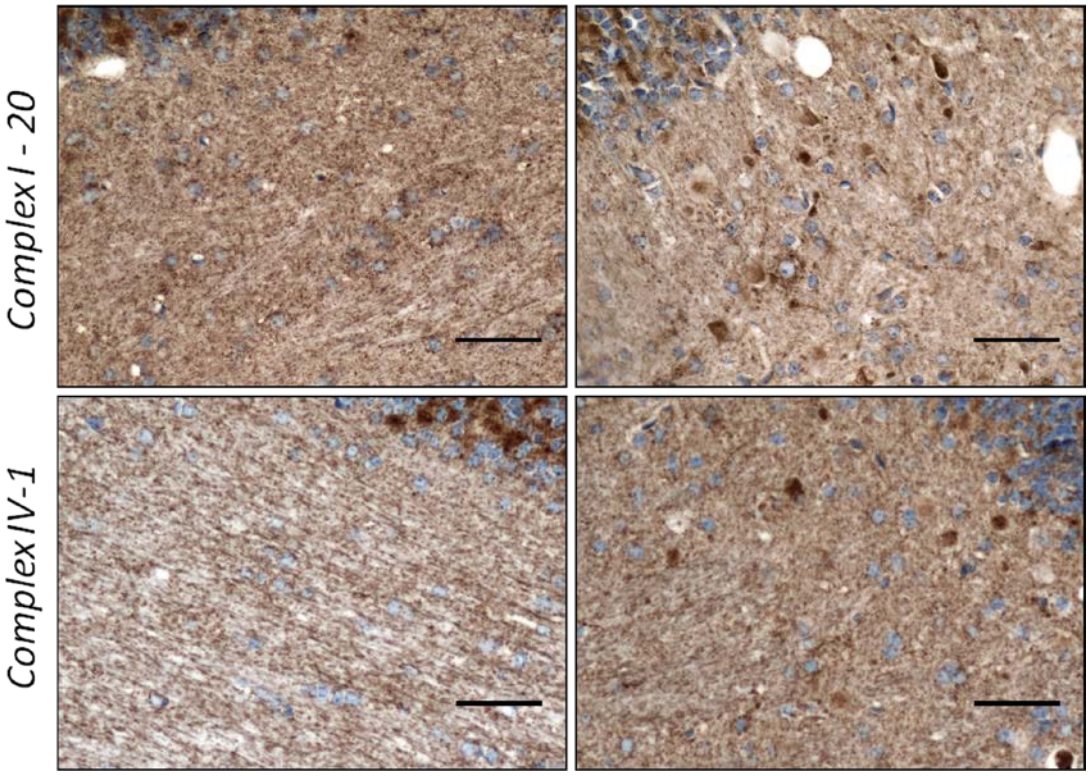

Figure 4.33: No evidence of Complex I or IV deficiency.
Immunoreactivity for Complex I-20 and Complex IV-1 is comparable between WT and KO mice. (Left, WT; Right, KO) Scale bars = 50μm

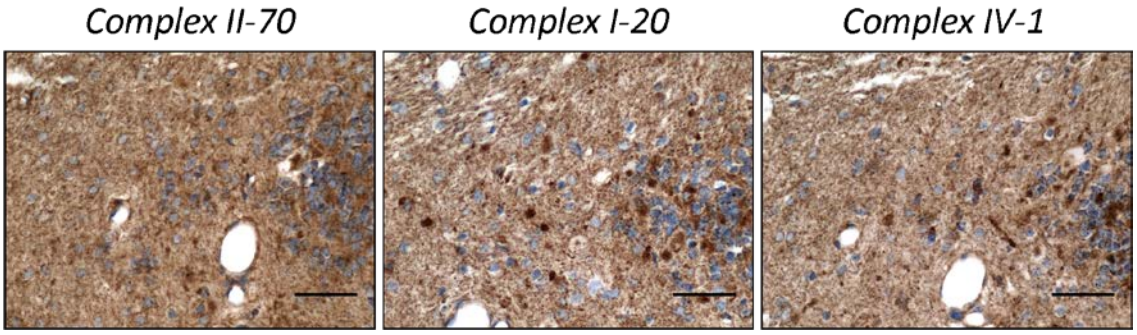

Figure 4.34: Immunohistochemistry to mtDNA encoded Complex I-20 and Complex IV-1 is comparable to nuclear encoded Complex II-70. Scale bars = 50 μm.

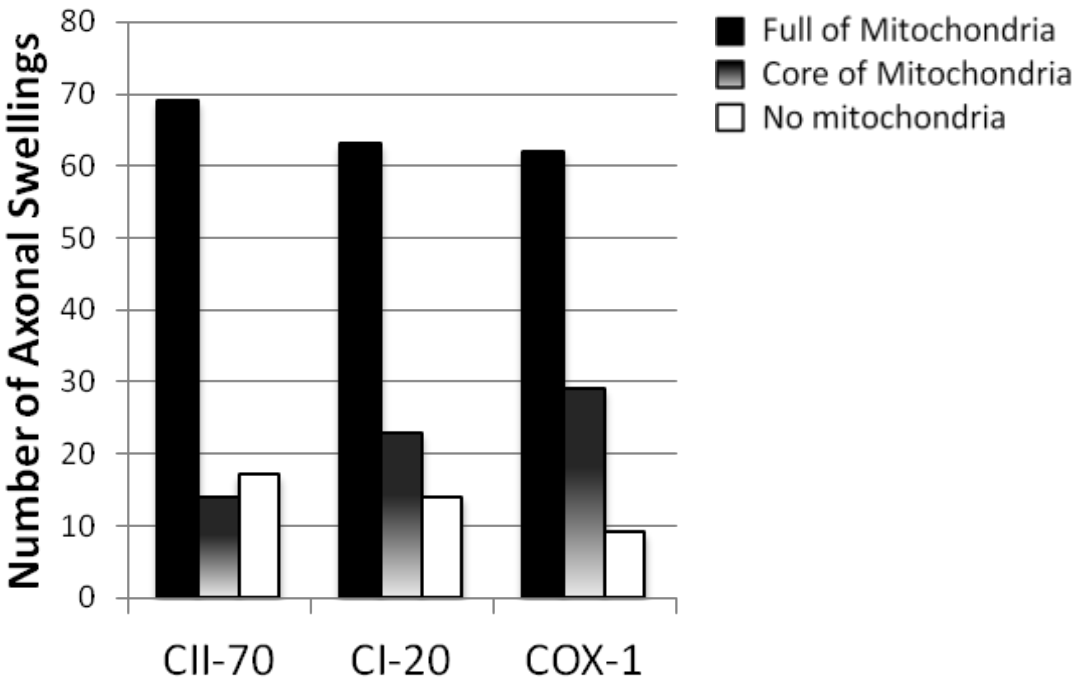

Figure 4.35: Classification of axonal spheroids according to intensity of mitochondrial respiratory chain subunit immunohistochemistry.
Proportions of spheroids without chromogen staining are similar for each marker. Counts from immunohistochemistry to CII-70, CI-20 and COX-1, n=100 for each marker.

4.3 Discussion

In this section I will discuss the results in the context of the literature and demonstrate the relevance of these findings.

4.3.1 Phenotype of UCHL1 Knockout Mice

Our UCHL1 knockout mice demonstrate the same phenotype as other UCHL1 null mouse models that have been described in the literature (Yamazaki *et al.*, 1988; Walters *et al.*, 2008; Chen *et al.*, 2010a); they display a tremor, kyphosis and experience progressive impairment of hind limb function. The onset of motor ataxia and hind-limb clasping behaviour in the UCHL1 knockout mice is around 9 weeks (63 days), which is two weeks earlier than the onset described in *gad* mice (Yamazaki *et al.*, 1988), but later than both UCHL1 null mice and the nm3419 mice, which experience the onset of motor ataxia at 7 weeks and 4 weeks respectively (Walters *et al.*, 2008; Chen *et al.*, 2010a). The slight differences in the onset of the hind-limb impairment may be due to the background of the mice; our UCHL1 knockout mice originated from a 129sv line and were backcrossed to C57BL/6J background (Coulombe *et al.*, 2014), whereas the *gad* mice resulted from an cross of CBA/Nga and RFM/Nga mice (Ichihara *et al.*, 1995). Both nm3419 mice and UCHL1 null mice were also maintained on the C57BL/6J background, however the knockout of the UCHL1 gene was generated in a different fashion (Walters *et al.*, 2008; Chen *et al.*, 2010a).

I found that UCHL1 KO mice fail to gain weight after 7 weeks of age; this has been confirmed by Doug Gray's group, who also observed morphological and functional abnormalities in the neurons that innervate the gut, and a decreased transit time of food through the gut (Coulombe *et al.*, 2014).

4.3.2 Decreased Monomeric Ubiquitin in UCHL1 Knockout Mice

The observation that UCHL1 knockout mice have decreased levels of monomeric ubiquitin is also in agreement with the literature on *gad* mice; it was firstly observed that ubiquitin accumulated in 'dot–like–structures' at swollen regions in axons, whereas ubiquitin immunoreactivity was faint or negative at the ends of dystrophic axons (Wu *et al.*, 1996), and subsequently shown that levels monomeric ubiquitin decrease by 20-30% in *gad* mice (Osaka *et al.*, 2003). I observed a slightly greater decrease in the monoubiquitin pool, to around 50% of WT levels; this could perhaps explain the slightly earlier onset of the hind limb impairment in our mice.

4.3.3 Neuropathological Characterisation of UCHL1 KO Mice

Our neuropathological characterisation of the UCHL1 knockout mice reveals pathology that is broadly similar to the *gad* mice. Axonal dystrophy and spheroids were predominantly observed in the gracile tract and in neurons from the dorsospinocerebellar tract in the cerebellum, in accordance with previous findings in *gad* mice (Yamazaki *et al.*, 1988; Kikuchi *et al.*, 1990).

4.3.3.1 Reduction in Synapse, Axon and Myelin Density

Immunohistochemistry to synaptophysin demonstrated a significant reduction in the density of synapses in the gracile nucleus of UCHL1 knockout mice, which has not previously been reported. Immunohistochemistry to SMI-31 (phosphorylated neurofilaments) and MBP-4 (Myelin Binding Protein 4) demonstrated a significant reduction in axonal density in the gracile fasciculus accompanied by a secondary loss of myelin. The loss of nerve fibres from the gracile fasciculus has been previously reported as an observation, but not densitometrically quantified (Mukoyama *et al.*, 1989), and our finding of significant secondary loss of myelin in the gracile fasciculus confirm findings from another UCHL1 knockout mouse, on a predominantly C57BL/6J background (Mi *et al.*, 2005). Interestingly, levels of myelin in the cuneate fasciculus of UCHL1 KO mice remain comparable to WT mice, although some axonal spheroid pathology is seen here. This further demonstrates the vulnerability of long axons to degeneration under conditions of ubiquitin depletion; the sensory neurons projected to gracile and cuneate nuclei are similar in all respects, except that cuneate neurons are only projected from thoracic level 6 of the spinal cord and above, therefore they are shorter than gracile neurons (see Figure 4.4).

4.3.3.2 APP Immunoreactivity in the Gracile Nucleus

An increase in the immunoreactivity of APP in the gracile nucleus of the *gad* mice was also reported (Ichihara *et al.*, 1995), however, whilst I observed a slightly increased level of APP immunoreactivity, this increase was not significant upon quantification. I have found for the first time that APP marks spheroids and dystrophic axons in the cerebellum, indicating that, to some extent, fast axonal transport is disrupted.

4.3.3.3 Characterisation of Axonal Spheroids

Electron microscopy studies of axonal spheroids in the *gad* mice have previously demonstrated that they contain neurofilaments, mitochondria and ‘tubulovesicular structures’ (Mukoyama *et al.*, 1989; Kikuchi *et al.*, 1990), and I have confirmed by immunohistochemistry that spheroids contain phosphorylated (and sometimes non-

phosphorylated) neurofilaments, and mitochondria in UCHL1 knockout mice. Furthermore, I found that synaptophysin, an internal membrane glycoprotein of synaptic vesicles, is a good marker for axonal spheroids in the cerebellum and the gracile nucleus; spheroids are usually strongly immunoreactive for synaptophysin, and IHC to synaptophysin clearly distinguishes axonal spheroids. IHC to synaptophysin has been done in the gracile nucleus of *gad* mice previously, however it was found to be "either faint or undetectable in spheroids" (Wang *et al.*, 2004). Since synaptophysin is synthesised in neuronal cell bodies, and transported on membranes by fast axonal transport in the retrograde direction towards synapses, the accumulation of synaptophysin in axonal spheroids may indicate that axonal spheroids form because of a blockage in fast axonal transport. Synaptophysin has previously been shown to accumulate on both proximal and distal sides of blockages to axonal transport in early nerve crush experiments (Li and Dahlström, 1997). This finding also explains the early observations that spheroids are packed with 'tubulovesicular structures' (Mukoyama *et al.*, 1989; Kikuchi *et al.*, 1990), these are likely to be the tubular membranes upon which synaptophysin is transported to axon terminals, as they have a diameter of approximately 50-80nm (Hannah et al., 1999), and are distinguishable from the smaller (40nm diameter), more spherical synaptic vesicles (Takamori *et al.*, 2006). Since APP is infrequently observed in spheroids at low levels but is also transported by fast axonal transport, this may indicate a specific disruption to the transport of the membranes on which synaptophysin is transported; APP and synaptophysin are transported on two distinct populations of vesicular membranes (Kaether *et al.*, 2000).

4.3.3.4 Assessment of Mitochondrial Respiratory Chain Complex Levels

In addition, I examined levels of mitochondrial respiratory chain complexes in UCHL1 mice. Initial findings suggested that mitochondria do not exhibit respiratory chain dysfunction; COX/SDH histochemistry did not reveal any COX (Cytochrome C Oxidase, Complex IV) deficiency in the spinal cord of UCHL1 KO mice. Since the catalytic subunits of Complex IV are encoded by mtDNA, COX deficiency is often observed in conditions where mtDNA deletions occur, such as mtDNA disease, ageing and age-related neurodegenerative diseases (Bender *et al.*, 2006; Dimauro *et al.*, 2012; Krishnan *et al.*, 2012). SDH (Succinate Dehydrogenase, Complex II) activity is unaffected by mtDNA damage as Complex II is entirely nuclear encoded. Furthermore, in order to confirm that mitochondria are not dysfunctional, I also located the regions of pathology and assessed levels of Complex I, II and IV in these areas

immunohistochemically, particularly assessing mitochondria that accumulated in axonal spheroids. I was particularly interested in assessing Complex I levels since Complex I deficiency is common in normal ageing and age-related neurodegenerative diseases (Smigrodzki *et al.*, 2004). I found that Complex I-20 and Complex IV-1 immunoreactivity in axonal spheroids is comparable to the immunoreactivity of Complex II-70, thereby showing that mitochondria are not deficient in levels of Complex I or IV of the mitochondrial respiratory chain. This finding, in addition to the results of Chapter 3, does not support my original hypothesis 'Ubiquitin depletion caused by UCHL1 inhibition or knockout will disrupt mitochondrial fission, fusion and trafficking, causing the accumulation of dysfunctional mitochondria'

4.3.4 Summary and Relevance of Results

In summary, this chapter demonstrates that the phenotype of UCHL1 knockout mice is comparable to *gad* mice, UCHL1 null mice and nm3419 mice. The UCHL1 knockout mouse neuropathology that I have characterised is in agreement with studies in *gad* mice, and I demonstrate a significant decrease in synaptic density and axonal density in the gracile nucleus.

Furthermore, I have demonstrated that synaptophysin is a good marker for axonal spheroids, and the reliable accumulation of synaptophysin in axonal spheroids probably explains earlier observations of spheroids being packed with tubulovesicular structures. This finding also supports the hypothesis that the formation of axonal spheroids is caused by a blockage to axonal transport. However the discrepancy between levels of synaptophysin and APP in spheroids is intriguing since both are transported by fast axonal transport, and raises the possibility that the defect may be more specific to the transport of precursors to synaptic vesicles, or a specific function of UCHL1 at synapses.

In addition, immunohistochemistry to Complexes I, II and IV of the mitochondrial respiratory chain shows that the mitochondria in axonal spheroids are not deficient in levels of these respiratory chain complexes. This finding suggests that the original hypothesis that 'Ubiquitin depletion caused by UCHL1 inhibition or knockout will disrupt mitochondrial fission, fusion and trafficking, causing the accumulation of dysfunctional mitochondria' is not true.

4.3.5 Future Work

Since the UCHL1 mouse displays neurodegenerative changes due to a decline in the function of the ubiquitin proteasome system, I have also examined how well UCHL1

KO mice model some of the pathological changes associated with human ageing in the subsequent chapter. This was done by comparing the UCHL1 KO gracile nucleus to the gracile nucleus of aged humans.

In order to build on this work and to elucidate the mechanism by which axonal spheroids form, further work was undertaken to characterise axonal spheroids in chapter 6. This was done in two ways; firstly by comparing the composition of axonal spheroids in UCHL1 KO mice at early and advanced stages of pathology, and secondly by using immunofluorescence to look at the three main components of axonal spheroids simultaneously; mitochondria, neurofilaments and synaptophysin.

Chapter 5.

The UCHL1 Mouse as a Model of Human Ageing

Chapter 5. **The UCHL1 Mouse as a Model of Human Ageing**

5.1 Introduction

UCHL1 knockout mice have a 50% reduction in levels of monomeric ubiquitin, as I have demonstrated in (Chapter 4, section 1.2.2). A similar reduction in monoubiquitin levels has been observed in *gad* mice (Osaka *et al.*, 2003). Ubiquitination is an essential step in the degradation of damaged proteins and in the normal turnover of proteins by the proteasome: a tag 4 or more ubiquitin moieties is sufficient to target protein substrates to the proteasome for degradation (Thrower *et al.*, 2000). Therefore a reduction in the pools of monomeric ubiquitin in neurons is expected to decrease the efficacy of the ubiquitin proteasome system, and other ubiquitin-mediated processes. Indeed, this has been previously demonstrated; *in vitro* inhibition of UCHL1 decreases the efficacy of the proteasomal degradation by around 50% (Cartier *et al.*, 2009).

The efficiency of the ubiquitin proteasome system declines with age (Dahlmann, 2007), and axonal spheroids have long been known to exist in ageing brains of many species, including humans (Brannon *et al.*, 1967; Zhang *et al.*, 1998; Jahns *et al.*, 2006).

Therefore I hypothesise that axonal dystrophy and spheroids, which are a feature of ageing in humans, are caused by the decline in the ubiquitin proteasome system, and that UCHL1 KO mice are a good model of human brain ageing.

5.1.1 Aim of the Investigation

The aim of this investigation is to determine whether UCHL1 knockout mice are a good model of human brain ageing. This will be done by comparing pathology in ageing human brains, specifically in the gracile nucleus, to the pathology that I have characterised in the gracile nucleus of UCHL1 knockout mice.

5.1.2 Methodological Approach

Immunohistochemistry using four markers to components of axonal spheroids (Synaptophysin, APP, CII-70, SMI-31) and to myelin (SMI-94) was carried out in sections from the gracile nucleus of four cases of normal human ageing, and in sections from the uncal cortex of one epilepsy case (2013-0823). These cases are detailed in Table 5.1. The source of this tissue is detailed in section 2.2.7.1.

Case ID	**Age**	**Sex**	**Post-Mortem delay (hours)**	**Fixation Time (days)**
2013-0823	68	Female	108	~90
2010-0195	86	Male	108	10
2007-0049	72	Female	27	9
2005-0053	69	Female	16	6
2008-0005	59	Female	19	11

Table 5.1: Details of human cases examined. Age given in years.

High power (x40) images were taken of each marker for each case using the Olympus BX51 light microscope. The number of axonal spheroids in one cross-section of the gracile nucleus was quantified for each marker of axonal spheroid components in each case, using Stereo Investigator (MBF Bioscience) software. Axonal spheroids were classified according to their intensity and staining pattern as follows:

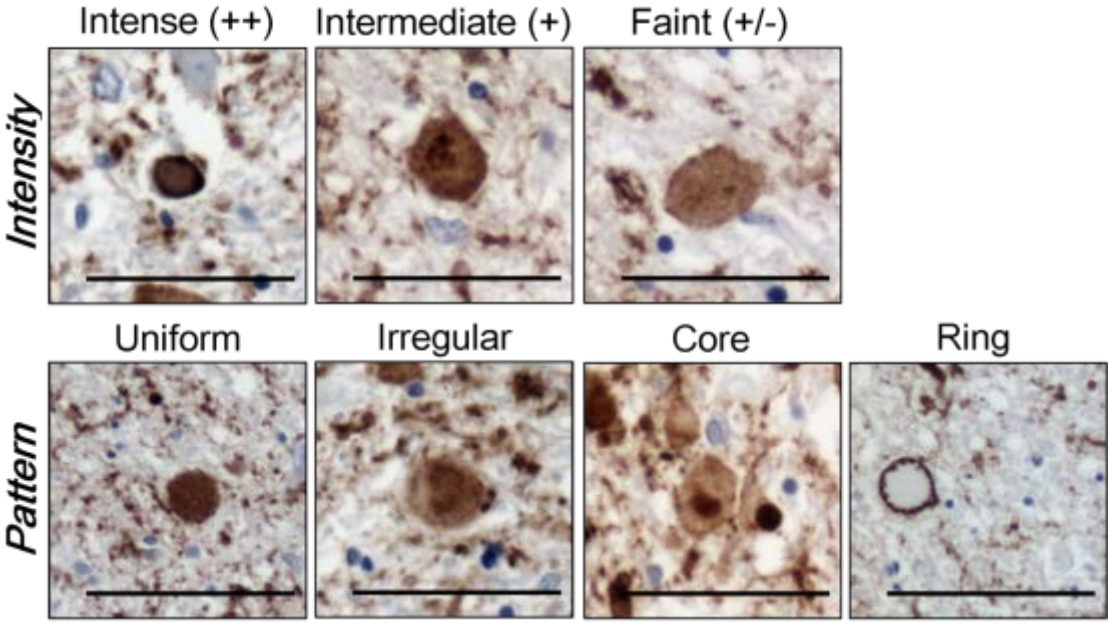

Figure 5.1: Classification system for axonal spheroids.
Classification according to intensity (Top, left to right: intense, intermediate, faint) and according to staining pattern (Bottom, left to right: uniform, irregular, core and ring). Scale Bars = 50μm.

In order to draw comparisons between the axonal dystrophy that occurs in normal human ageing, and in UCHL1 KO mice, axonal spheroids were quantified using Stereo Investigator and classified according to the system above. For each mouse, axonal spheroids from two cross-sections of the gracile nucleus were quantified, since the gracile nucleus in mice is far smaller than in humans. Details of the mice studied in this chapter are given in Table 5.2, including the behavioural score, used to quantify the severity of their hind limb impairment (0 = no impairment, 2 = severe).

Knockout			
ID	*Sex*	*Age (Weeks)*	*Behavioural Score*
KO 20	♂	9.3	1
KO19	♂	11.7	1.6
KO22	♀	12.7	2
KO39	♂	16.1	2
KO40	♂	16.1	2

Table 5.2: Details of mice studied

5.2 Results

5.2.1 UCHL1 Knockout Mice

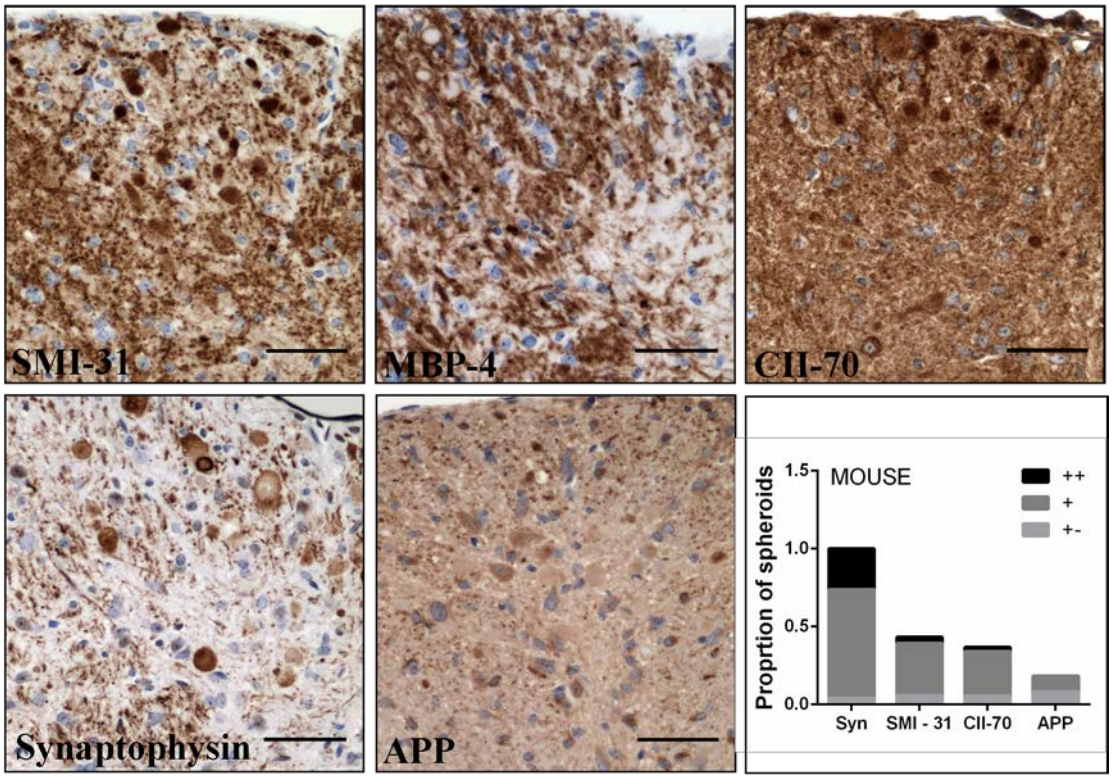

Figure 5.2: Gracile Nucleus of UCHL1 KO mice.
Immunohistochemistry to SMI-31, MBP-4, CII-70, Synaptophysin and APP, Scale Bars = 50μm. Bottom left: Proportions of axonal spheroids identified by each antibody marker, categorised according to their immunoreactivity (Intense (++), intermediate (+) or faint (+-)). Data shown is the summary of 5 mice, 2 cross-sections of the gracile nucleus were quantified for each mouse.

Figure 5.2 displays images of immunohistochemistry to four axonal spheroid markers and MBP-4 (Myelin Binding Protein) in the gracile nucleus of a UCHL1 knockout mouse, representative of a total of 5 mice. It is clear from these images that synaptophysin, SMI-31 and CII-70 are good markers for axonal spheroids, whilst APP only marks a small proportion (~20%) of spheroids (Figure 5.2), although APP immunoreactivity is generally high in the gracile nucleus, and there are small dots of APP immunoreactivity throughout the area. The graph in the bottom left of Figure 5.2 shows the proportion of axonal spheroids (relative to the number marked by synaptophysin) identified by each marker, and summarises data from 5 mice. Synaptophysin marks by far the highest number of axonal spheroids, whereas APP marks only a small proportion of this number. From this quantification, we can approximate that neurofilaments are present in nearly 50% of spheroids, whilst mitochondria are present in around 40%.

5.2.2 Case 2013-0823: Uncal Cortex

Unlike the other cases investigated in this chapter, case 823-13 is a patient with epilepsy, which displayed numerous axonal spheroids in the uncal cortex as a result of constant seizure activity. Sections from the uncal cortex were stained using antibodies to Synaptophysin, CII-70, APP, SMI-31 and SMI-94 (Figure 5.3), in order to determine whether the axonal spheroids displayed here are similar to those observed in the UCHL1 knockout mice.

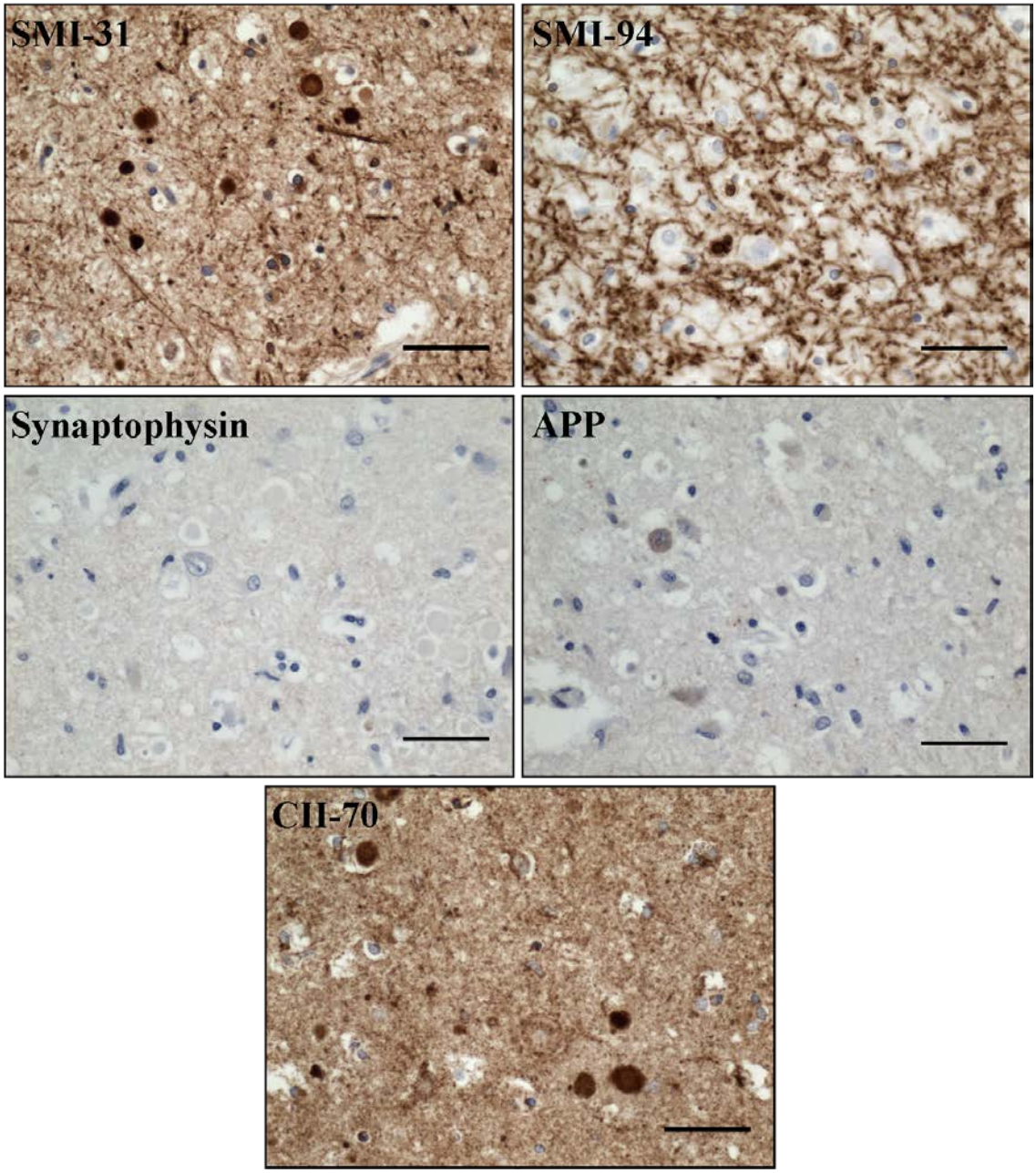

Figure 5.3: Case 823-13: Sections from the Uncal Cortex.
Immunohistochemistry to SMI-31 (Phosphorylated Neurofilaments), SMI-94 (Myelin Basic Protein), Synaptophysin, APP and CII-70. Scale bars = 50μm

Immunohistochemistry to sections from the uncal cortex of case 823-13 shows that axonal spheroids are homogenous, and mostly circular in shape with little variation in size. Immunohistochemistry to SMI-31 and the mitochondrial marker CII-70 demonstrates that phosphorylated neurofilaments and mitochondria accumulate in all axonal spheroids detected in this case

Synaptophysin immunohistochemistry was not successful on sections from tissue block 823-13 even at 1:50 dilution, despite giving good staining in tissue sections from a control case and case 195-10 in the same IHC run three times (Figure 5.4, Figure 5.5) This effect is most probably caused by the long fixation time; due to suspected CJD (Creutzfeldt - Jakob disease), the fixation time for this case was almost 3 months (Table 5.1). This may have had the effect of masking the synaptophysin epitope.

Immunohistochemistry to APP has worked in sections from this tissue block; there is some faint APP staining in neuronal cell bodies, as expected. However, there are very few spheroids that are immunoreactive to APP, indicating that axonal transport block is not central to the formation of these swellings.

It may have also been helpful to use immunohistochemistry to ubiquitin in this case, to determine whether damaged and ubiquitinated protein are present in these swellings.

From these results I can conclude that the axonal spheroids seen in this epilepsy case are different from those observed in UCHL1 knockout mice, due to differences in their composition, and their homogeneity in size and shape. However they are similar in composition to the torpedoes of axons proximal to purkinje cells in cases of mtDNA disease; SMI-31 is a reliable marker for these torpedoes, and they often contain mitochondria, but not APP (J. Phillips, personal communication).

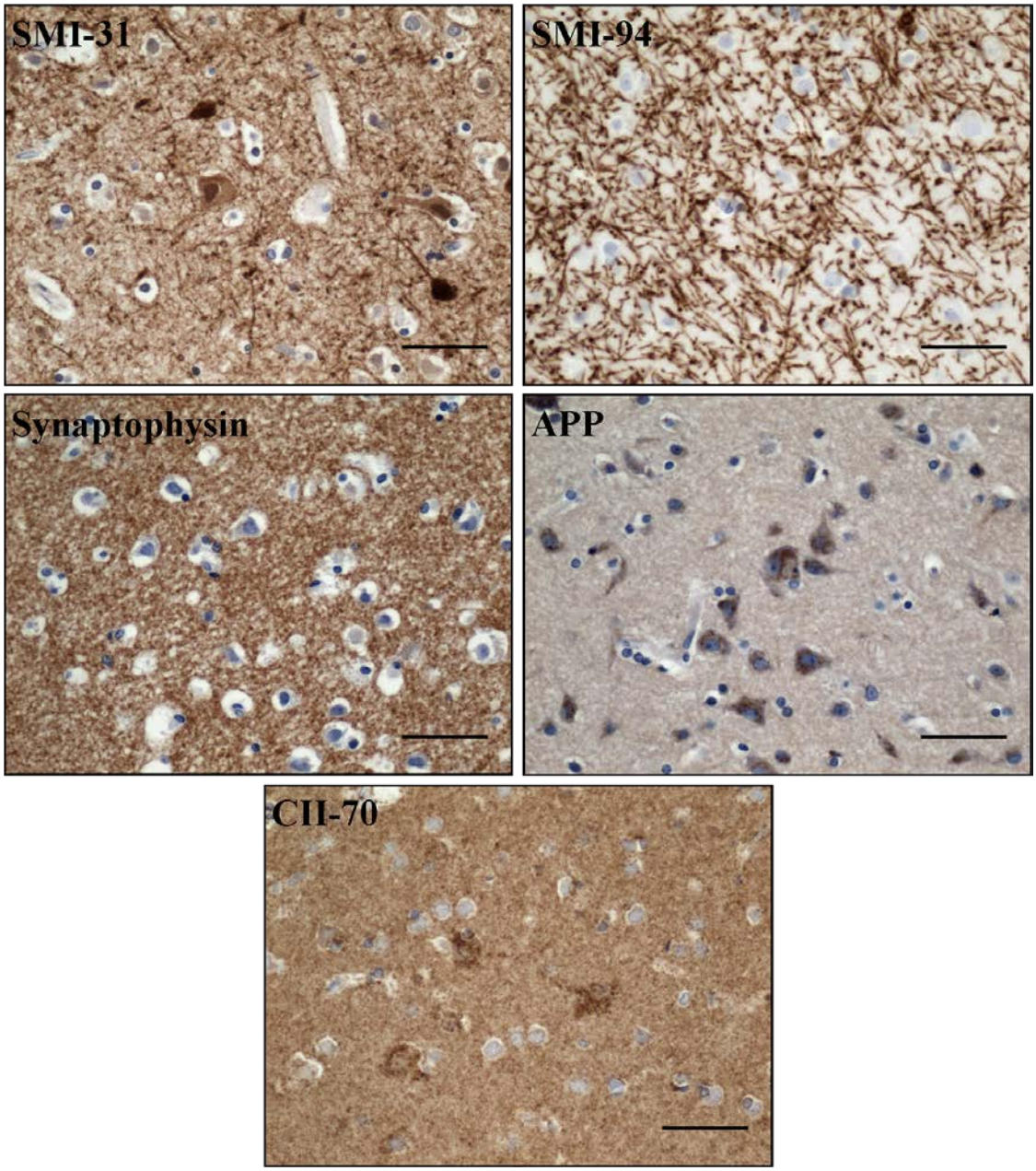

Figure 5.4: IHC Control Tissue Sections.
Immunohistochemistry to SMI-31 (Phosphorylated Neurofilaments), SMI-94 (Myelin Basic Protein), Synaptophysin, APP and CII-70, Scale bars = 50µm.

5.2.3 Case 195-10

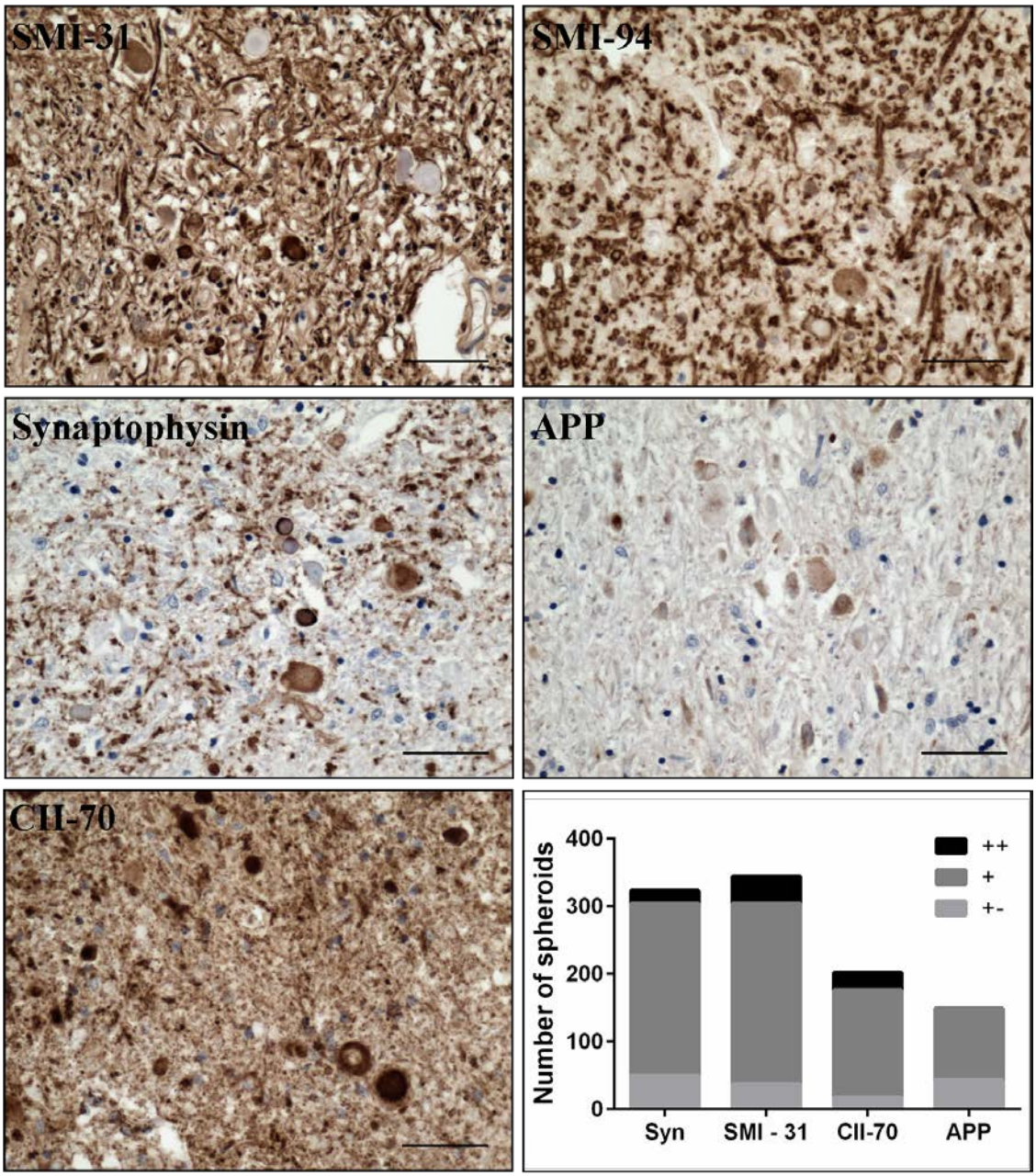

Figure 5.5: Case 195-10.
Immunohistochemistry to SMI-31 (Phosphorylated Neurofilaments), SMI-94 (Myelin Basic Protein), Synaptophysin, APP and CII-70, Scale bars = 50μm. Bottom left: graph showing quantification of spheroids in the gracile nucleus for each marker (Syn = Synaptophysin), classified according to staining intensity (++ = intense, + = intermediate, +- = faint.

Case 195-10 is an 86 year old male, with numerous axonal spheroids in the gracile nucleus. Case 195-10 is the oldest of the cases assessed in this chapter, and as expected for an age-related pathology, axonal spheroids are most abundant in this case, with over 300 spheroids present in one cross-section of the gracile nucleus.

Results show that SMI-31 and synaptophysin are the most reliable markers for axonal spheroids in this case (Figure 5.5). Although serial sections were stained for the purpose

of this analysis, it is not possible to guarantee that the exact same spheroids are present in both sections. Therefore the slight difference in the number of spheroids marked by these two antibodies may reflect that by chance, the SMI-31 section contains more spheroids, and it is probable that in this case, both phosphorylated neurofilaments and synaptophysin accumulate in all or most axonal spheroids.

IHC to CII-70 demonstrates the accumulation of mitochondria in axonal spheroids, but to a lesser extent than synaptophysin or neurofilaments. The antibody to APP marks the smallest number of spheroids, and has the largest proportion of spheroids classified as faintly immunoreactive (Figure 5.5), which is in concordance with observations with the UCHL1 mice. The proportions of spheroids marked by CII-70 and APP in case 195-10 is slightly higher than the proportions observed in UCHL1 knockout mice. There are some differences between axonal spheroids in aged humans and UCHL1 mice with regards to APP: in ageing, APP is specific to spheroids, whereas in UCHL1 mice, APP immunoreactivity is diffuse over the whole area of the gracile nucleus, marks few spheroids and is mainly visible as small dot-like aggregates.

A further difference between the gracile nucleus in aged humans and UCHL1 knockout mice is the presence of pale blue, spheroid-like objects in the human gracile nucleus, which appear empty with immunohistochemistry using SMI-31, APP and synaptophysin and CII-70 antibodies, apart from rings of intense immunoreactivity around the edge (Figure 5.6). These are relatively rare, comprising between 2-4% of the spheroid population when included in the count, but are consistently present in each cross-section of the gracile nucleus from every human case we have looked at. It is likely that these objects are corpora amylacea, so have been excluded from the analysis.

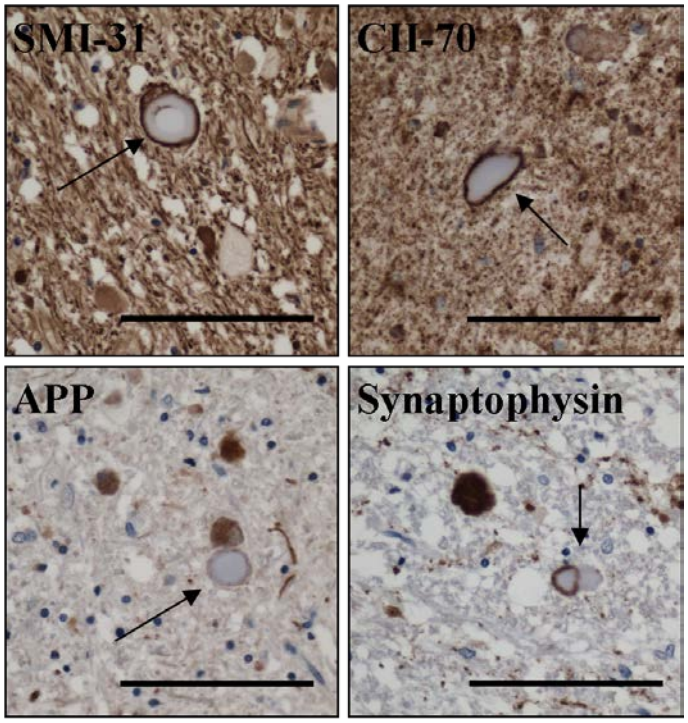

Figure 5.6: Empty, ‘blue’ spheroids with rings of immunoreactivity. Scale bars = 50μm

5.2.4 Case 49-07

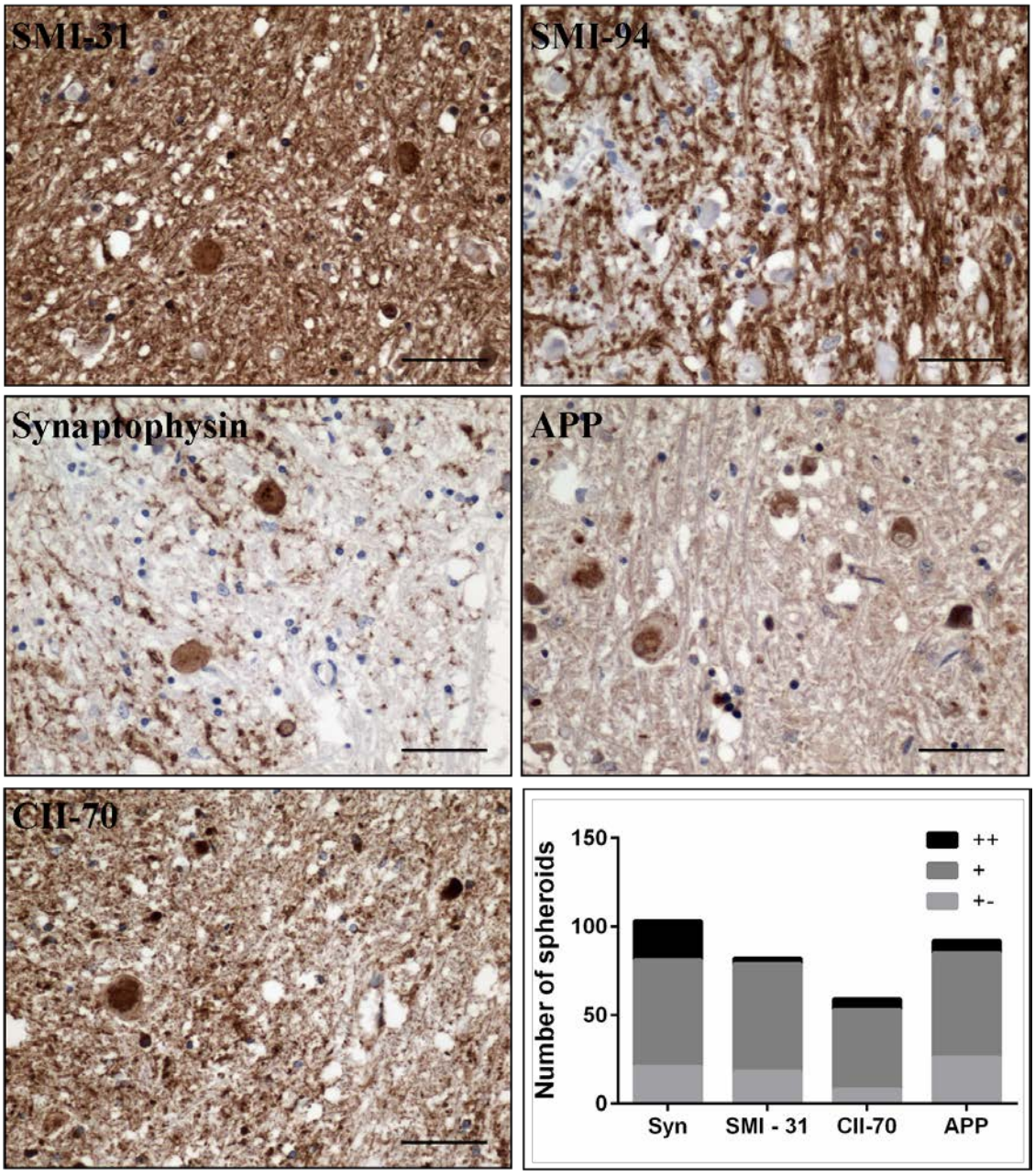

Figure 5.7: Case 49-07.
Immunohistochemistry to SMI-31 (Phosphorylated Neurofilaments), SMI-94 (Myelin Basic Protein), Synaptophysin, APP and CII-70, Scale bars = 50μm. Bottom left: graph showing quantification of spheroids in the gracile nucleus for each marker (Syn = Synaptophysin), classified according to staining intensity (++ = intense, + = intermediate, +- = faint).

Case 49-07 is a 72 year old female, and as the second oldest of the cases examined in this chapter, displays the second-most axonal spheroids; using synaptophysin as a marker for spheroids, there are over 100 in one cross-section of the gracile nucleus. The number of axonal spheroids quantified for each marker indicates that the composition of spheroids in this case is very similar to that in UCHL1 mice; synaptophysin accumulates in all axonal spheroids identified, whilst the majority accumulate neurofilaments and mitochondria. The main difference between axonal spheroids in this

case and in UCHL1 knockout mice is that there are a far greater proportion of spheroids that contain APP (approximately 90%); there are more spheroids that contain APP than mitochondria in this case and the majority of them have intermediate APP immunoreactivity. Some are even intensely immunoreactive for APP.

5.2.5 Case 53-05

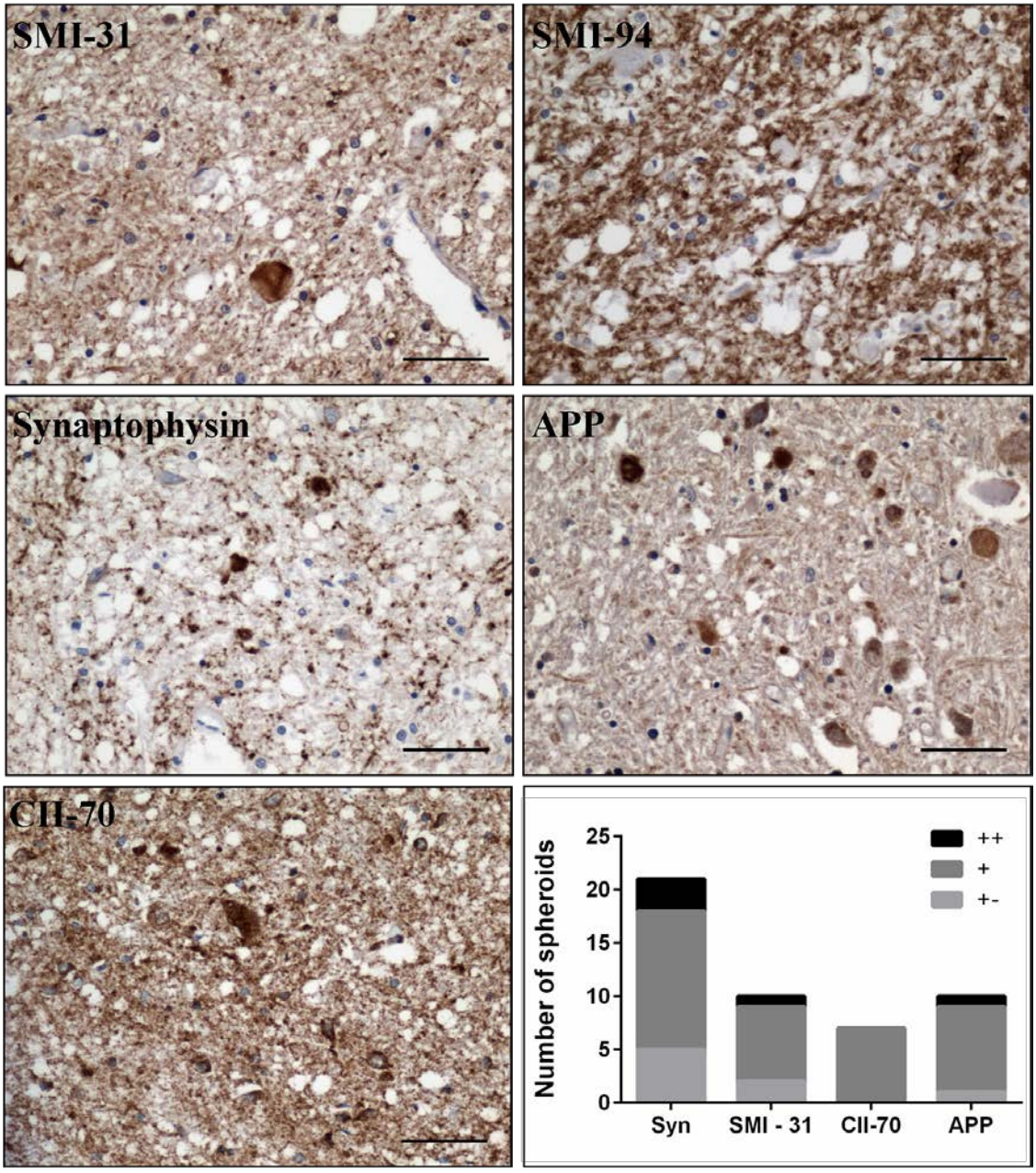

Figure 5.8: Case 53 – 05.
Immunohistochemistry to SMI-31 (Phosphorylated Neurofilaments), SMI-94 (Myelin Basic Protein), Synaptophysin, APP and CII-70, Scale bars = 50μm. Bottom left: graph showing quantification of spheroids in the gracile nucleus for each marker (Syn = Synaptophysin), classified according to staining intensity (++ = intense, + = intermediate, +- = faint).

Case 53-05 is 69 year old female, with few (less than 30) axonal spheroids throughout the gracile nucleus. Quantification of these spheroids demonstrates that their

composition is very similar to spheroids in UCHL1 knockout mice; synaptophysin is by far the best marker for axonal spheroids, indicating that the accumulation of synaptophysin is an essential step for axonal spheroid formation. Similarly to UCHL1 knockout mice, SMI-31 and CII-70 are the next best axonal spheroid markers. The distribution in this case is particularly similar to the mouse “KO40”, as is demonstrated in Figure 5.10.

5.2.6 Case 05-08

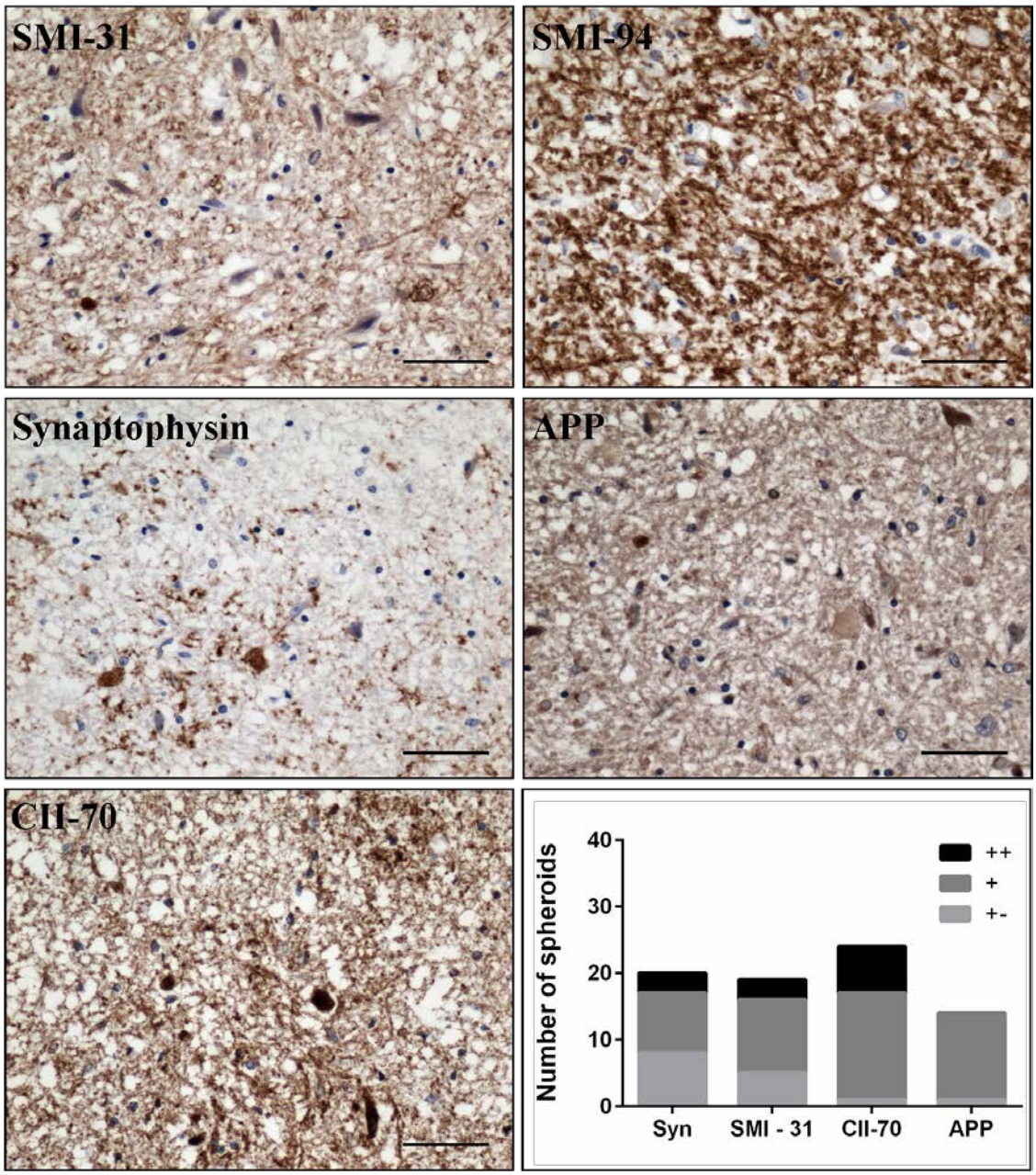

Figure 5.9: Case 05-08.
Immunohistochemistry to SMI-31 (Phosphorylated Neurofilaments), SMI-94 (Myelin Basic Protein), Synaptophysin, APP and CII-70, Scale bars = 50µm. Bottom left: graph showing quantification of spheroids in the gracile nucleus for each marker (Syn = Synaptophysin), classified according to staining intensity (++ = intense, + = intermediate, +- = faint.

Similarly to case 53-05, sections from the gracile nucleus of case 05-08 are also sparsely populated with axonal spheroids. Case 05-08 is a 59 year old female, the youngest of all of the cases. Unexpectedly, the most reliable spheroid marker here is CII-70, indicating that mitochondria accumulate in all axonal spheroids. The number and intensity of spheroids identified from SMI-31 and Synaptophysin IHC are comparable to each other, whilst APP is the least reliable marker of axonal spheroids. This distribution is different from the UCHL1 knockout mice, but also differs from other human aged gracile nucleus cases.

5.2.7 Comparison of Spheroids Identified by each Marker

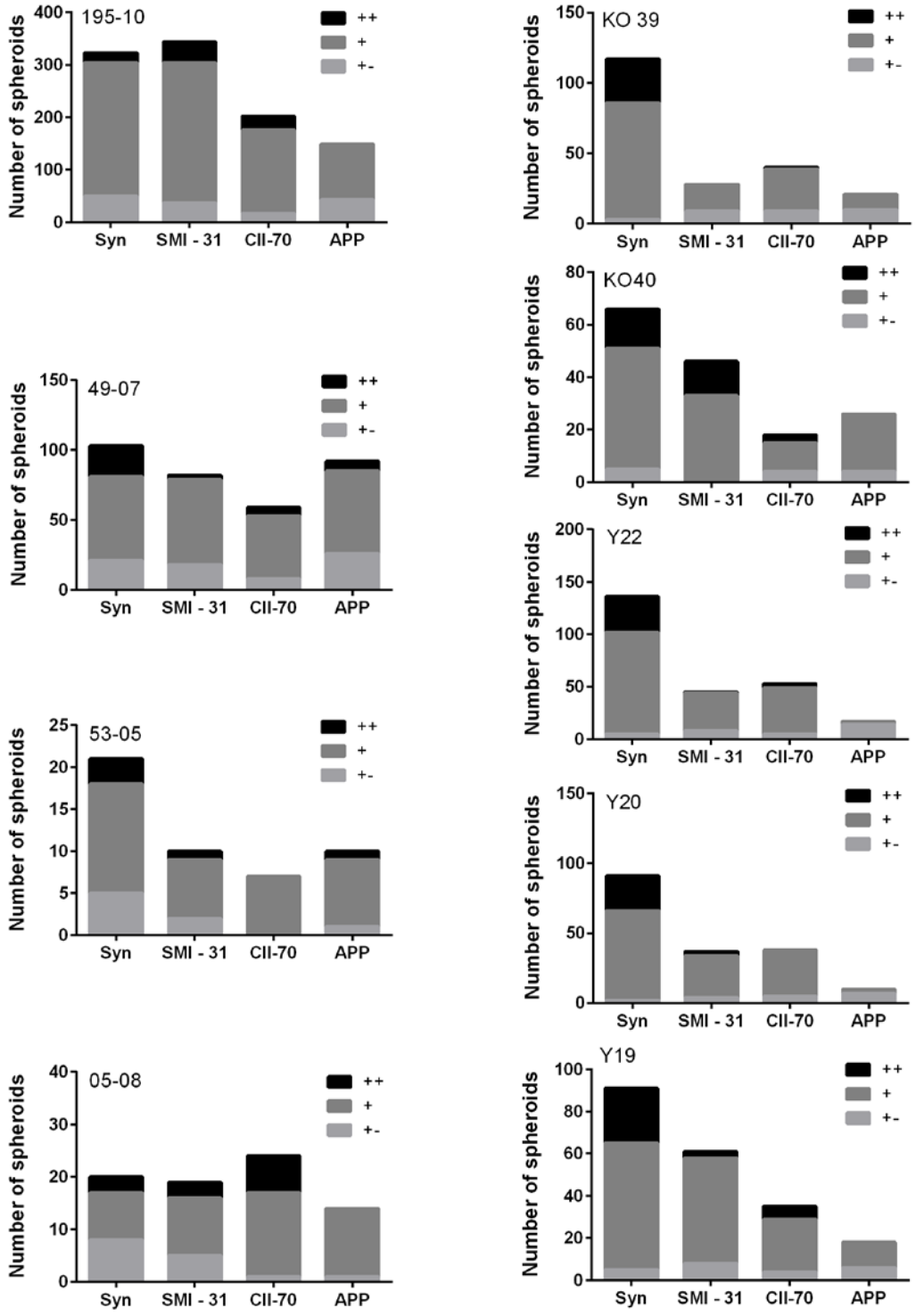

Figure 5.10: Intensity of immunoreactivity.
Number of spheroids marked by immunohistochemistry to synaptophysin, SMI-31, CII-70 and APP. Each spheroid is categorised as faint (+-), intermediate (+), or intense (++). Human cases are shown on the left hand side, and results from UCHL1 knockout mice are shown on the right.

Figure 5.10 shows a comparison between the quantification of axonal spheroids in the gracile nucleus of aged humans and of UCHL1 knockout mice. This data is summarised in Figure 5.11.

The first thing to observe is that in both aged humans and UCHL1 knockout mice, axonal spheroids are similar in composition; there are spheroids that contain synaptophysin, mitochondria, phosphorylated neurofilaments and APP. It is important to note that in other diseases and conditions, axonal swellings would not contain these elements, for example in mtDNA disease, the 'torpedoes' of Purkinje cell axons reliably contain phosphorylated neurofilaments and mitochondria, but do not accumulate synaptophysin or APP (J. Phillips, Personal Communication).

Secondly, there is variability in the numbers of axonal spheroids identified by each marker, particularly between human cases. There are human cases (particularly 49-07 and 53-05) which have similar profiles to mouse cases (KO40 and Y19), but also human cases which have quite different profiles (195-10, 05-08).

There are some clear differences in the numbers of spheroids identified by each marker for humans and mice. For UCHL1 knockout mice, it is clear that in every case, synaptophysin marks the greatest number of axonal spheroids, indicating that the accumulation of synaptophysin is an essential part of the mechanism by which axonal spheroids form. In the gracile nucleus of aged humans, however synaptophysin marks the greatest number of spheroids in 2 cases of 4; in the other 2 cases, the number of spheroids marked by synaptophysin is roughly equal to the number marked by SMI-31. This indicates that the accumulation of phosphorylated neurofilaments and synaptophysin may be equally important in the formation of spheroids in ageing. Furthermore, in UCHL1 knockout mice, the number of spheroids that contain APP is consistently low for each case, (approximately 20% of the number marked by synaptophysin) and the immunoreactivity of APP in spheroids is faint or intermediate, never intense. In human ageing, the proportion of spheroids marked by APP is generally higher than in UCHL1 knockout mice; Figure 5.11 indicates that in humans, APP marks approximately 50% of spheroids, around the same proportions as CII-70. In addition, the immunoreactivity of APP in spheroids is predominantly intermediate and sometimes intense. These results indicate that the accumulation of APP in spheroids, probably due to blocked axonal transport is of more importance to spheroid formation in human ageing than in UCHL1 knockout mice.

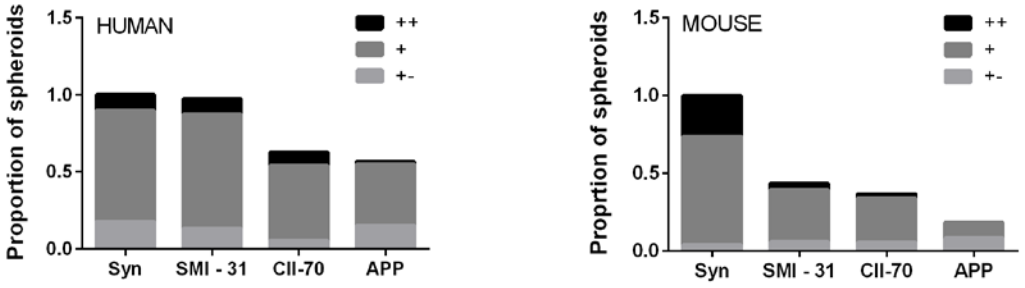

Figure 5.11: Comparison of the proportion of spheroids marked by each antibody in human ageing (left) and in UCHL1 mice (right).
Proportion calculated for each marker assuming that all spheroids have been identified by synaptophysin immunohistochemistry. Spheroids are categorised according to staining intensity: Intense (++), intermediate (+), faint (+-).

5.2.8 Comparison of the Immunoreactivity Pattern of Spheroid Markers

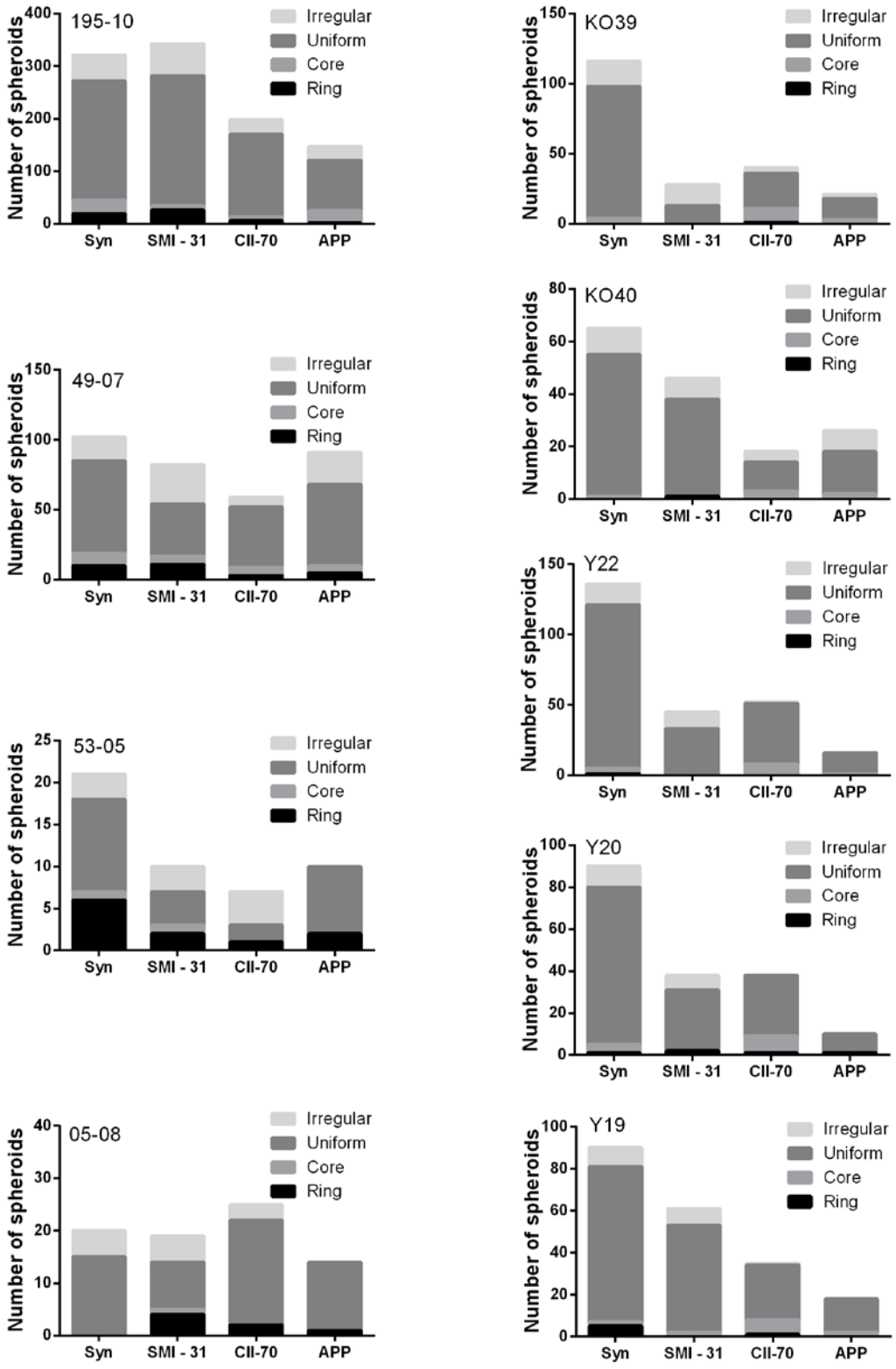

Figure 5.12: Number of spheroids marked by immunohistochemistry to Synaptophysin, SMI-31, CII-70 and APP. Spheroids are categorised according to the pattern of staining as irregular, uniform, core or ring. Cases of human ageing shown on the left, UCHL1 knockout mice shown on the right.

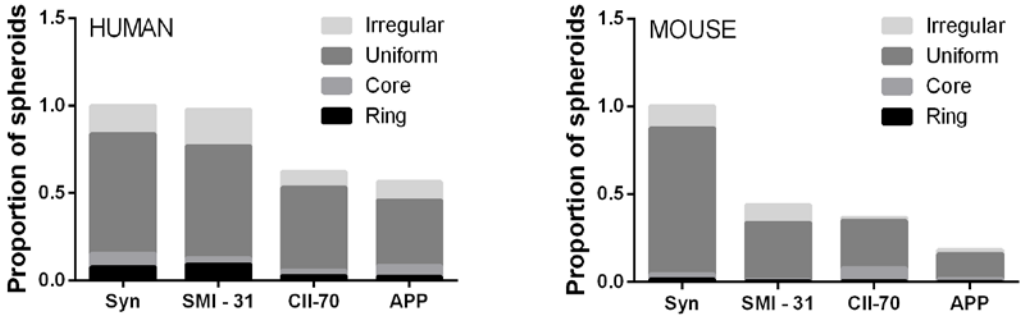

Figure 5.13: Comparison of the proportion of spheroids marked by each antibody according to the pattern of immunoreactivity.
Human ageing: left, UCHL1 KO mice: right. Proportion calculated for each marker assuming that all spheroids have been identified by synaptophysin immunohistochemistry. Spheroids are categorised as irregular, uniform, core, ring according to the pattern of staining intensity.

Figure 5.12 shows the number of spheroids identified by each spheroid marker (Synaptophysin, SMI-31, CII-70, APP), categorised according to the pattern of immunoreactivity. Images of axonal spheroids shown in Figure 5.2 to Figure 5.9 demonstrate that in both UCHL1 knockout mice and human ageing, axonal spheroids are heterogeneous in size and shape, and have both even and irregular staining patterns. This indicates that the spheroids in the gracile nucleus of UCHL1 knockout mice are similar in morphology to those that develop with age in humans.

Figure 5.12 and Figure 5.13 demonstrate that in both human ageing and in UCHL1 knockout mice, the majority of axonal spheroids have even immunoreactivity for all markers for, with some that have irregular patterns of immunoreactivity. In both human ageing and UCHL1 KO mice, there are axonal spheroids that have a core of immunoreactivity at the centre. In particular, in UCHL1 mice, there are a proportion of spheroids that have a core of mitochondria in their centre, whereas in human ageing there are small proportions of spheroids with cores of synaptophysin, neurofilaments, mitochondria and APP. The main difference in the patterns of immunoreactivity between human ageing and UCHL1 knockout mice is the presence of spheroids which have rings of immunoreactivity. In UCHL1 knockout mice, it is relatively rare to see an axonal spheroid which has a ring of immunoreactivity around the edge with a lighter centre, however this is occasionally occurs with each marker. However in every case of human ageing, there are a small proportion of spheroids that have a ring of immunoreactivity to synaptophysin, SMI-31, CII-70 and APP around the edge.

5.3 Discussion

5.3.1 Summary and relevance of results

In summary, this chapter has demonstrated that the axonal spheroids that occur in UCHL1 knockout mice do bear some similarities to the axonal spheroids that develop with ageing in the gracile nucleus of humans, and of other species. However, there are some important differences.

In both human ageing and in UCHL1 KO mice, there are axonal spheroids that contain synaptophysin, phosphorylated neurofilaments, mitochondria and APP. In human ageing, the number of spheroids marked by SMI-31 and synaptophysin are relatively similar, indicating that the accumulation of both of these components plays an important role in the formation of axonal spheroids. However, in UCHL1 knockout mice, synaptophysin is by far the best marker of axonal spheroids, indicating that synaptophysin accumulation is essential for axonal spheroid formation. This suggests that UCHL1 may have a more specific function in regulating the transport of synaptophysin, or in synaptic vesicle recycling. Furthermore, the proportion of spheroids that accumulate APP is higher in human ageing that in UCHL1 knockout mice. Since APP is normally only expressed at very low levels in neurons, it is probable that the accumulation of APP in these spheroids is due to an upregulation of APP expression combined with blocked axonal transport.

The size and shape of axonal spheroids in UCHL1 knockout mice is similar to those of human ageing. Additionally, most axonal spheroids in both human ageing and UCHL1 knockout mice have an even pattern of immunoreactivity, suggesting that the components of spheroids are evenly distributed across the whole spheroid. However, there are a subset of axonal spheroids with a ring of immunoreactivity around the edge that are present in human ageing, but are very rarely observed in UCHL1 knockout mice.

It is tempting to speculate that there may be multiple populations of spheroids present in ageing human brains; some caused by a decline in UPS, some caused by blockages in axonal transport, some caused by mitochondrial dysfunction, or a combination of these factors. This is likely since ageing is complex and involves the decline of multiple pathways. Therefore I can conclude that ageing in the human brain cannot be modelled accurately by a mouse model in which only one of these pathways is compromised. However the spheroids in the ageing human brain do share many of the same characteristics as those in UCHL1 knockout mice, indicating that the decline of the

ubiquitin proteasome system plays a significant role in axonal dystrophy and in the formation of axonal spheroids in ageing.

5.3.2 Limitations of this study

The major limitation of this study is that, using immunohistochemistry, it is only possible to view one marker per section. Therefore, it was necessary to use serial sections, each stained with immunohistochemistry to a different antibody which marks one component of axonal spheroids. The analysis assumes that since sections are close together (a maximum of 45μm) apart, the number of axonal spheroids in each serial section will remain relatively constant, therefore if one section has 100 spheroids, and the next has only 50, this implies that the second antibody has only marked 50% of spheroids. This method gives an estimate of the proportion of axonal spheroids that contain the four components, however it is not accurate, as there will be some variability between the number of spheroids on each section.

The further limitation is that immunohistochemistry for some antibodies used in this study marks not only axonal spheroids, but also the area around them. For example, the CII-70 antibody binds mitochondria in axonal spheroids, but also binds to mitochondria in the axons and cells surrounding the spheroids. This can make it difficult to identify spheroids that have similar levels of immunoreactivity to the surrounding area.

However further studies of the composition of axonal spheroids in UCHL1 KO mice have verified our observations using this method. Here I found that 37% of axonal spheroids marked by synaptophysin contain mitochondria, and using immunofluorescence (where mitochondria and synaptophysin in spheroids can be labelled simultaneously), I found that 38% contain more mitochondria than is normally present in axons, when the normal range is defined as the mean mitochondrial intensity in axons ± 2SD.

5.3.3 Future Work

This study has demonstrated that the axonal spheroids in UCHL1 knockout mice share some characteristics with the axonal spheroids that develop in normal human ageing. However, using immunohistochemistry as a method to compare the two has several limitations. Therefore, a better method to further examine the similarities and differences between spheroids in aged humans and UCHL1 KO mice is immunofluorescence; this way it would be possible to assess the levels of each component in a single axonal spheroid, and give a definitive answer to the proportion of

spheroids that each marker is present in. This would help to define how similar spheroids in UCHL1 knockout mice are to those seen in normal ageing, and to assess the intriguing possibility that there may be several types of axonal spheroid present in the ageing brain, caused by different factors. It would be interesting to compare the axonal spheroids in the gracile nucleus of aged humans with those in other diseases or disease models, for example mtDNA disease, amyotrophic lateral sclerosis (ALS), or multiple sclerosis (MS), for further insight into axonal dystrophy in ageing.

Chapter 6.

Mechanisms of Axonal Spheroid Formation

Chapter 6. **Mechanisms of Axonal Spheroid Formation**

6.1 Introduction

In neurodegenerative diseases, the loss of distal synapses and axons, due to “dying-back” type axonal degeneration (often accompanied by axonal swelling) can precede the loss of cell bodies by several months, thus “dying back”-type axon degeneration is a common early feature of neurodegeneration, occurring before the development of symptoms. Synapse and axon loss precedes neuronal loss in Parkinson’s disease (Braak *et al.*, 2003), Alzheimer’s disease (Adalbert *et al.*, 2009) and Huntington’s disease (Li and Conforti, 2013), amongst others. It is increasingly recognised that this is functionally important to disease progression, since attempts to protect axons and synapses have been more successful in slowing disease progress in some models than attempts to protect cell bodies (Saxena and Caroni, 2007). The loss of axons and synapses (preceding neuronal cell loss) is also seen in normal ageing (Pakkenberg and Gundersen, 1997), and is accompanied by the formation of axonal swellings, also known as spheroids (Brannon *et al.*, 1967), as is sometimes the case in neurodegenerative diseases including Parkinson’s Disease, Alzheimer’s Disease, HIV dementia, Huntington’s disease, multiple sclerosis and other myelin disorders, amyotrophic lateral sclerosis, hereditary spastic paraplegia, Creutzfeldt-Jakob disease, Niemann-Pick disease, stroke and traumatic brain injury (Mi *et al.*, 2005; Marangoni *et al.*, 2014). The reasons for axonal spheroid formation have not been well characterised, however associated axonal degeneration has been more extensively studied.

Several cellular processes are associated with axonal dystrophy and the formation of axonal spheroids, including protein aggregation, oxidative stress, axonal transport, and mitochondrial dysfunction. The inclusion bodies and axonal swellings associated with neurodegenerative diseases and aging often feature the accumulation of damaged and misfolded proteins, including components of the ubiquitin-proteasome system (Mori *et al.*, 1987; Lennox *et al.*, 1989; Lowe *et al.*, 1990; Ii *et al.*, 1997; Schlossmacher *et al.*, 2002; Choi *et al.*, 2004)., and therefore protein misfolding and aggregation is thought to be a core process involved in their formation. Oxidative stress is also associated with axonal swelling since many of the proteins that accumulate are oxidatively damaged. Furthermore, oxidative stress has also been shown to inhibit axonal transport (Fang *et al.*, 2012), another cellular process that is associated with the formation of axonal swelling and axon degeneration. Mutations in the kinesin-encoding gene *KHC* in drosophila causes the formation of axon swellings filled with organelles (Hurd and

Saxton, 1996). Mutations in the human orthologue *KIF5A* cause hereditary spastic paraplegia (Goizet *et al.*, 2009), a disease characterised by the dystrophy of long axons and causing spasticity and weakness of legs. Motor neuron disease, which also features axonal swelling, although usually in proximal regions of the axon, can be caused by mutations in the p150 subunit of dynactin, an adaptor protein for retrograde axonal transport (Münch *et al.*, 2004). Mitochondria and mitochondrial dysfunction are also associated with axonal swellings and degeneration, and mitochondria are commonly components of axonal swellings. A mutation affecting the mitochondrial AAA-ATPase paraplegin causes distal axonopathy, characterised by axon swelling and degeneration (Ferreirinha *et al.*, 2004). Furthermore, defects in mitochondrial motility have been implicated in axon degeneration in Huntington's disease and in Alzheimer's disease (Calkins and Reddy, 2011; Shirendeb *et al.*, 2011).

6.1.1 Wallerian-like Degeneration

The degeneration of an axon distal to a lesion (such as a transection or nerve-crush) was first described by Waller in 1850, and is thus termed Wallerian Degeneration (Waller, 1850). This term was classically used to describe the longer-term response to axon injury (24-72 hours post-lesion) in the PNS (Peripheral Nervous System). Interestingly, axon transection results in proximal-to-distal direction axon fragmentation and degeneration, whereas nerve crushing causes retrograde axonal degeneration (distal-to-proximal), which is of more relevance here (Beirowski *et al.*, 2005).

Recent research into the mechanism behind axon degeneration has been largely influenced by the discovery of the Wld^S (Wallerian Degeneration Slow) mouse, which is resistant to injury-induced axon degeneration. The Wld^S mutation results in the expression of a fusion protein between part of the E4 ubiquitin ligase UBE4B (Ubiquitination factor E4B), and NMNAT1, a nicotinamide mononucleotide adenine transferase involved in NAD^+ biosynthesis. Crosses of the Wld^S mouse with mouse models related to several diseases, and including the *gad* mouse, indicate that "dying back"-type degeneration shares, at least in part, a common mechanism with classical Wallerian degeneration, which has been more extensively characterised (Mi *et al.*, 2005; Conforti *et al.*, 2014). The Wld^S mutation confers some protection from axon degeneration and/or neuronal damage in models of Parkinson's disease, glaucoma, optic nerve injury, progressive motor neuropathy, Charcot Marie Tooth disease types 1A and 1B, hypoxic-ischaemic injury, global cerebral ischaemia, diabetes and tauopathy (Conforti *et al.*, 2014).

It is now thought that, rather than being a passive response to injury, axon degeneration is a tightly regulated process common to many conditions, analogous to but distinct from apoptosis (Whitmore *et al.*, 2003). Axon degeneration features microtubule depolymerisation, axon blebbing and axon fragmentation, followed by the degradation of neurofilaments and the removal of axon fragments and swellings by phagocytes (Lingor *et al.*, 2012). The molecular triggers of Wallerian-like degeneration are thought to feature the removal of NMNATs, which are essential for axon growth and survival, and the expression of pro-degenerative molecules SARM1 and PHR1 (Conforti *et al.*, 2014).

The offspring of a cross between Wld^S and *gad* mice displayed reduced axonal spheroid pathology, however their phenotype was no milder and synapse loss was not reduced (Mi *et al.*, 2005). Therefore UCHL1 loss triggers Wallerian-like degeneration, which is partly responsible for the pathological changes and phenotype observed in UCHL1 null mice. Therefore we aim to determine the factors resulting from UCHL1 loss that trigger axonal spheroid formation and Wallerian-like degeneration.

6.1.2 Axonal transport of APP and Synaptophysin

Of relevance to this chapter is the axonal transport of amyloid precursor protein (APP) and synaptophysin. The axonal transport of mitochondria has been previously described in the overall introduction (Section 1.8.3)

Synaptophysin is an integral membrane glycoprotein to synaptic vesicles, and is involved in various aspects of synaptic vesicle biogenesis, exocytosis and endocytosis (Valtorta et al., 2004). Synaptophysin is synthesised in neuronal cell bodies, and inserted into 50-80nm diameter tubular membranes originating from the Golgi apparatus, for retrograde-directed fast axonal transport to synapses (Hannah et al., 1999). Here membrane-mixing results in the formation of 50nm diameter synaptic vesicles containing synaptophysin, which is the second-most abundant synaptic vesicle protein. Interestingly, synaptophysin is proposed to be involved in sorting and recruiting other proteins to synaptic vesicles (Gordon and Cousin, 2014).

APP is synthesised in the ER in the neuronal soma, and passes through the Golgi network. It is then inserted into tubular post-Golgi vesicles and trafficked by fast axonal transport to presynaptic terminals (Haass *et al.*, 2012). Interestingly, the post-Golgi vesicles upon which APP is transported are distinct from the tubular membranes that synaptophysin is inserted into. APP-carrying post-Golgi vesicles move continuously

and extremely quickly (at an average of 4.5μm/second) along microtubules, whereas synaptophysin-containing tubular membranes move over shorter distances and at speeds of around 0.9μm/s (Kaether *et al.*, 2000). At the pre-synaptic terminal, post-Golgi vesicles fuse with the plasma membrane and are retrieved to form synaptic vesicles. A small amount of APP is present in synaptic vesicles; approximately 10% of synaptophysin-positive vesicles also contain APP (Groemer *et al.*, 2011).

6.1.3 Aims of this study

This investigation aims to further elucidate the mechanisms by which axonal spheroids form in UCHL1 knockout mice, by using immunofluorescence and by comparing mice at an early stage and a more advanced stage of pathology. By doing this, I hope to gain further insight into the mechanisms that can trigger axonal dystrophy and Wallerian-like axon degeneration, with relation to ageing and neurodegenerative diseases.

Previous characterisation of axonal spheroids by immunohistochemistry indicated that synaptophysin was the most common component of axonal spheroids in UCHL1 mice, whilst the presence of mitochondria, phosphorylated neurofilaments and APP in spheroids was less prominent. This chapter aims to confirm this using the more accurate method of immunofluorescence, allowing several components of each spheroid to be viewed simultaneously.

6.2 Immunohistochemistry in mice with early and advanced stage pathology

6.2.1 Methodology

6.2.1.1 Details of Mice Selected for this Study

In order to assess the mechanisms behind neurodegeneration in UCHL1 knockout mice, I compared pathology in the cerebellum and brainstem of three 9-12 week old mice (early stage of pathology) and two 16.1 weeks old UCHL1 knockout mice (advanced stage of pathology), along with their wild type controls. Details of these mice are shown in Table 6.1, including their mean behavioural score, which grades their hind-limb impairment on a scale of 0-2, where 2 represents severe hind-limb impairment.

	Wild Type				**Knockout**			
	ID	*Sex*	*Age (Weeks)*	*Behavioural Score (Mean)*	*ID*	*Sex*	*Age (Weeks)*	*Behavioural Score (Mean)*
Early Stage	WT 17	♀	11.6	0	KO 20	♂	9.3	1
	WT 18	♀	11.6	0	KO 19	♂	11.7	1.6
	WT 23	♀	12.6	1	KO 22	♀	12.7	2
Advanced	WT 37	♂	16.1	0	KO 39	♂	16.1	2
	WT 38	♂	16.1	0	KO 40	♂	16.1	2

Table 6.1: Details of mice from which tissue sections were taken for studies detailed in this chapter.

Figure 6.1 shows the behavioural scores of all mice assessed; the first black box shows the age of the 'early stage pathology' group, and demonstrates that they are in the progressive phase (between 9 and 12 weeks) where hind-limb function is becoming progressively worse. Mice in this group struggle to perform the limb-splaying reflex when picked up by the tail, this is characterised by holding hind-limbs only hip-width apart, or in the more severe cases, crossing or clasping limbs. The age of the 'advanced stage pathology' group is indicated by the second black box; in this group all mice have severely impaired hind-limb function, characterised by limb clasping. Heterozygous and WT mice have normal hind-limb function.

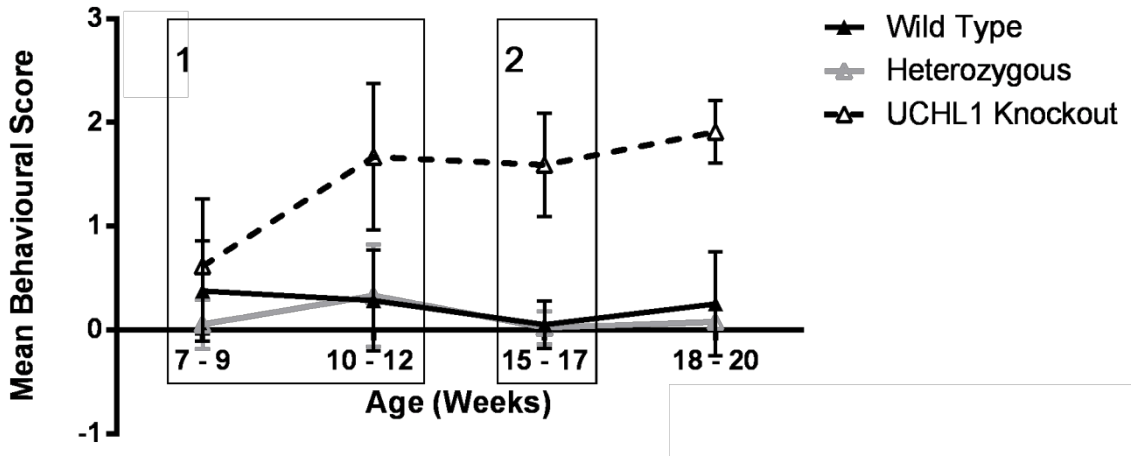

Figure 6.1: Mice grouped according to level of phenotype and pathology.
1) Indicates the mild phenotype of the early stage pathology group, age 9-12 weeks. 2) Indicates the more severe phenotype of the advanced stage pathology group, age 16 weeks. Graph taken from Chapter 4, Figure 12, showing hind limb function in UCHL1$^{-/-}$, UCHL1 $^{+/-}$ and WT mice. Data points represent mean ± SEM of mice scored on a scale of 0-2. 0 = normal hind limb function, 1 = slight impairment, 2 = severe impairment of hind limb function.

6.2.1.2 Microtomy

Each of the FFPE cerebellum blocks from were trimmed to Bregma – 5.68, the level at which pathology in the cerebellum can first be observed, so that the tissue sections being cut from each block are at roughly the same neuranatomical level of the cerebellum. Each batch of sections consisted of ten 5µm sections and one 20µm section. Sections continued to be taken until enough sections featuring the gracile nucleus and gracile tract in the brainstem had been obtained.

6.2.1.3 Selection of Tissue Sections for Immunohistochemistry

One section from each round of ten sections taken from the cerebellum, for all of the 6 'early stage' mice, were used for immunohistochemistry to synaptophysin, to identify pathology in the brains of the UCHL1 null mice. Sections from each mouse were then compared, and four levels of the cerebellum were chosen for further IHC studies, ensuring that sections were comparable in terms of neuroanatomy between the wild-type and knockout early stage mice, and between the early stage and advanced stage mice. One section from each round of sections taken from the brainstem were stained with H&E; these sections were then compared using light microscopy to pick four levels of the brainstem to examine with immunohistochemistry studies (ensuring WT and KO sections are at the same level neuroanatomically). The antibodies chosen for this study were SMI-31 (marker of phosphorylated neurofilaments), MBP-4 (Myelin binding protein), COX-1 and CII-70 (mitochondrial markers), APP (Amyloid precursor protein) and synaptophysin (marker of synapses and synaptic vesicles). The targets of these antibodies are outlined in Table 4.4. This selection of antibodies will allow me to

assess the loss of axons, synapses and myelin as neuroaxonal dystrophy progresses, and to observe the accumulation of mitochondria, neurofilaments, and proteins transported by fast axonal transport (APP and synaptophysin) within axonal spheroids.

6.2.2 Results

6.2.2.1 Comparison of Mice with Early and Advanced Stage Pathology

Figure 6.3 demonstrates axonal spheroids in the axons of the inferior and superior cerebellar peduncles, as they enter the cerebellum (Figure 6.2). The inferior cerebellar peduncle (icp) conveys both afferent and efferent axons, connecting the spinal cord and cerebellum, thus integrating sensory input with motor vestibular functions such as balance and posture. Amongst other axonal tracts, the inferior cerebellar peduncle carries the dorsal spinocerebellar tract and the cuneocerebellar tract, which both convey proprioceptive sensory information. As discussed in Chapter 4, it is unlikely that short cuneocerebellar tract axons that originate in the cuneate nucleus are damaged at this point; therefore we can infer that the spheroids and dystrophic axons seen in the icp are from the dorsal spinocerebellar tract. Interestingly, axonal spheroids are seen in the superior cerebellar peduncle of both young and old mice (Figure 6.3), which carries axons of the ventral spinocerebellar tract, originating in the dorsal horn (Clarke's column), to the cerebellum. These axons also carry proprioceptive sensory information.

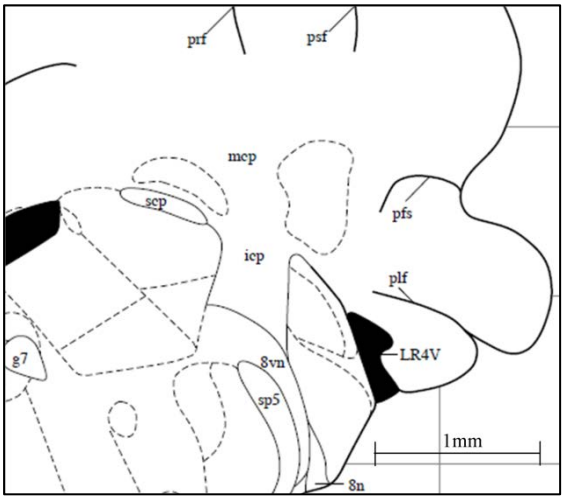

Figure 6.2: The inferior, middle and superior cerebellar peduncles ascending to the cerebellum.
Adapted from (Paxinos, 2001)

Figure 6.3 compares the pathology in the inferior and superior cerebellar peduncles in early stage (top row, 9-12 weeks) and advanced stage (bottom row, 16 weeks) mice. It demonstrates the worsening of pathology with increasing age, seen both by an increase in the number of axonal spheroids, varicosities and dystrophic axons, and also by the progression of pathology proximally in the inferior cerebellar peduncle. In Figure 6.3, image A (from a mouse dissected at 9.3 weeks), spheroids are relatively rare, and in the more distal regions of the axons. However, in Figure 6.3, images D and E, spheroids and dystrophic axons seem to be more common, particularly further down the inferior cerebellar peduncle, which is more proximal in the axon, since the axon projects into the cerebellum. These observations are in agreement with the 'dying back' mechanism of neurodegeneration, demonstrating the progression of pathology from distal to proximal. These images also show that axonal pathology is in the early stages at 9.3 weeks,

(presumably starting in the few weeks before), and that the number of dystrophic axons and spheroids increases between 9 and 16 weeks. This suggests that there should be informative differences between the ‘early stage’ (9-12 weeks) and ‘advanced stage’ (16.1 weeks) groups of mice.

In other areas of the cerebellum, there does not appear to be any difference between the abundance and size of axonal spheroids within the cerebellar white matter.

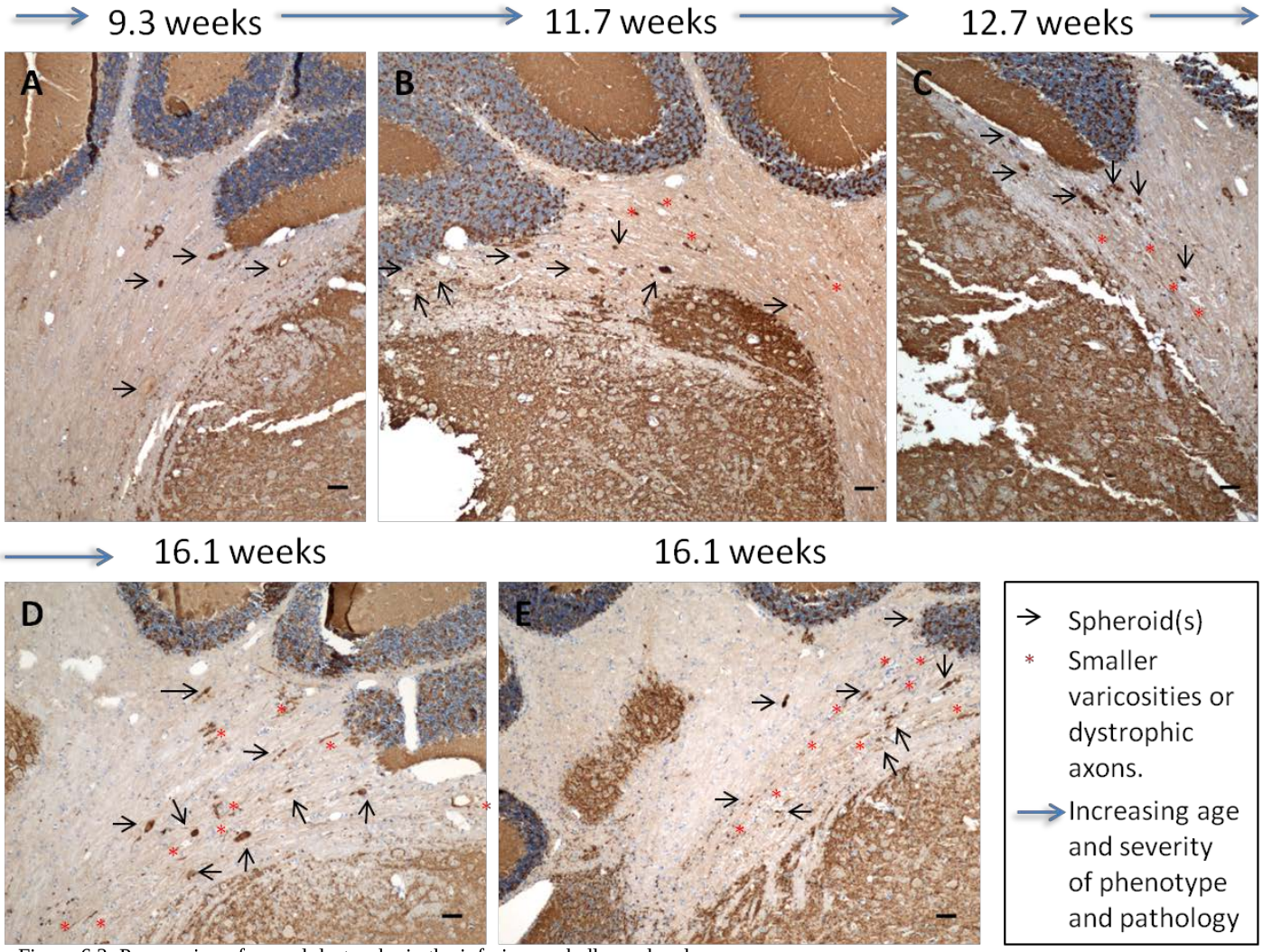

Figure 6.3: Progression of axonal dystrophy in the inferior cerebellar peduncle.
Low power images of IHC to synaptophysin taken of the inferior cerebellar peduncle in 5 mice, ranging from 9.3 weeks (A) to 16.1 weeks of age (D, E). Scale bars =50μm

6.2.2.2 Progression of Axon and Myelin Loss

Immunohistochemistry to SMI-31 (antibody to phosphorylated neurofilaments) demonstrates that the loss of distal parts of axons that innervate the gracile nucleus occurs early in the pathogenesis of UCHL1 KO mice. Axons are greatly reduced in density by 9.3 weeks, at a stage when mice still have a mild hind-limb phenotype. The density of axons continues to decrease up until around 12 weeks, and then does not appear to progress any further. The loss of the distal portions of axons very early in the pathogenesis of UCHL1 KO mice shows again that axonal die-back occurs in a distal to proximal direction.

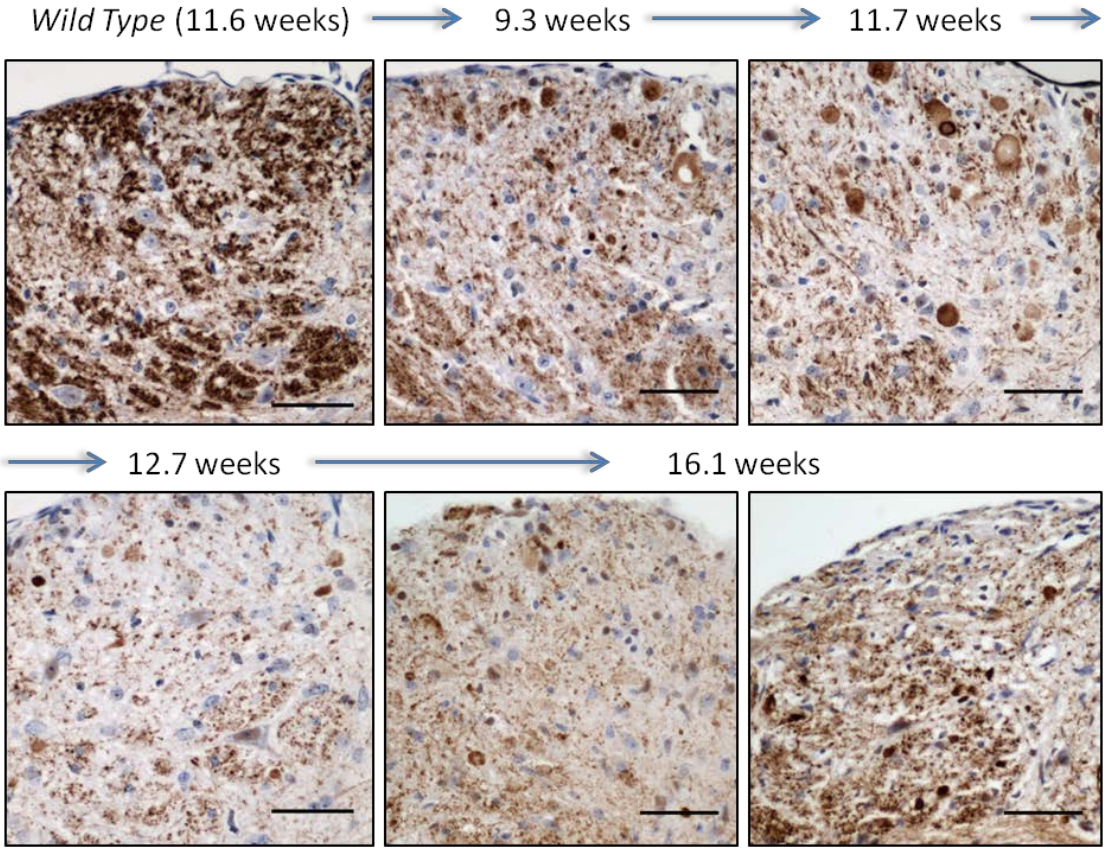

Figure 6.4: Progression of Axonal Loss in the Gracile Nucleus of UCHL1 KO mice.
Images of IHC to SMI-31(phosphorylated neurofilaments). Top left = equivalent region in WT mouse. The distal portions of the axons synapsing at the GrN are lost before 9 weeks; axonal loss becomes progressively worse up until around 12 weeks but does not appear to worsen any further. Some axonal spheroids accumulate phosphorylated neurofilaments. Scale bars =50μm

Similar to the observations of axonal loss, myelin density appears to be greatly reduced compared to WT mice by 9 weeks; the loss of distal myelinated axons is an early event in UCHL1 KO mice. Additionally, since the loss of myelin density is not more severe than the loss of axonal density, we can conclude that myelin loss is secondary to axonal loss. Similarly, the loss of myelin from the gracile nucleus of KO mice does not appear to worsen after 12.7 weeks of age.

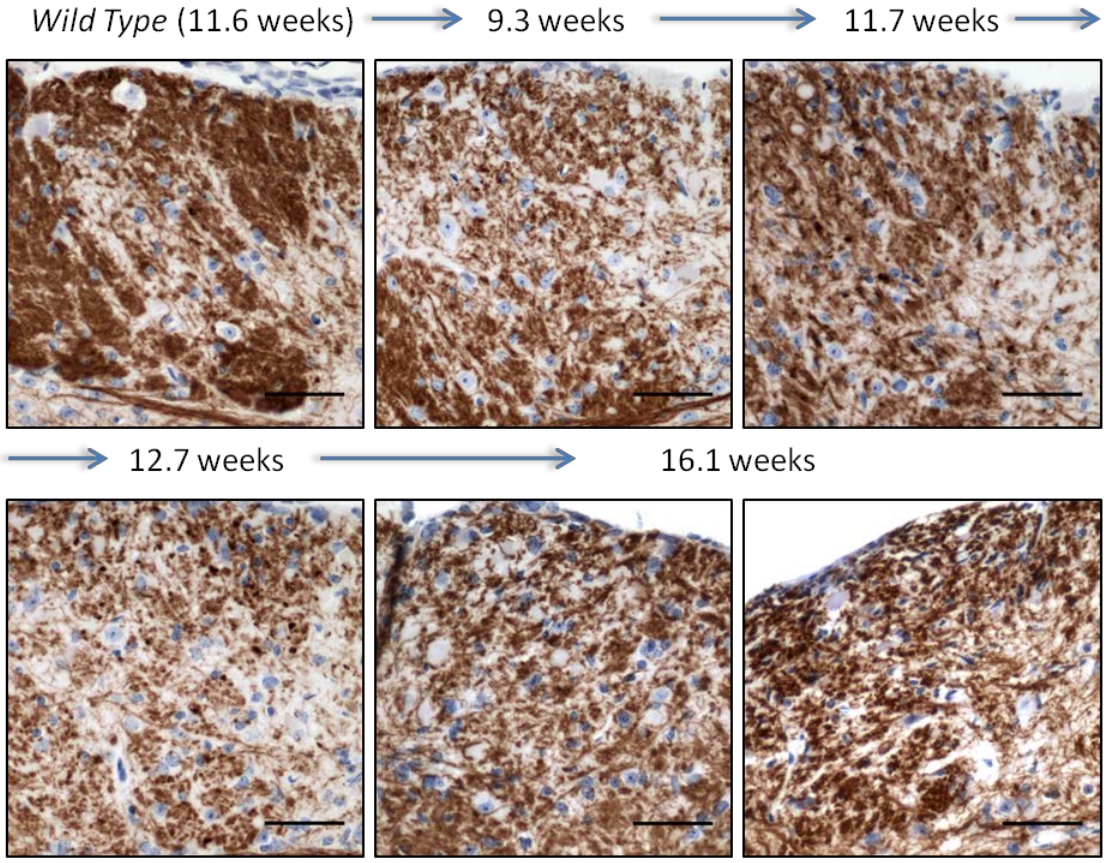

Figure 6.5: Myelin loss in the Gracile Nucleus of UCHL1 KO Mice.
Images are of immunohistochemistry to MBP-4 (Myelin Binding Protein). Top left image shows the equivalent region in a WT mouse. Myelin loss does not exceed axonal loss, and is therefore secondary. The density of myelinated axons decreases before mice reach 9 weeks, and appears to worsen only slightly after this stage. Scale bars =50µm

6.2.2.3 Progression of Synapse Loss and Spheroid Formation

As demonstrated in section 4.2.5.1, synapses are lost from the gracile nucleus of UCHL1 knockout mice, and synaptophysin accumulates in axonal spheroids. Figure 6.6 demonstrates that the loss of synapses occurs earlier than 9 weeks; therefore it may precede the onset of hind-limb impairment in UCHL1 knockout mice. Synapse loss is an early event in the pathogenesis of neuroaxonal dystrophy in UCHL1 knockout mice. Synapse loss progressively worsens week by week, and is more pronounced in 16 week old mice, with advanced stage pathology. Intense synaptophysin immunoreactivity is noticeable in axonal spheroids from as early as 9 weeks.

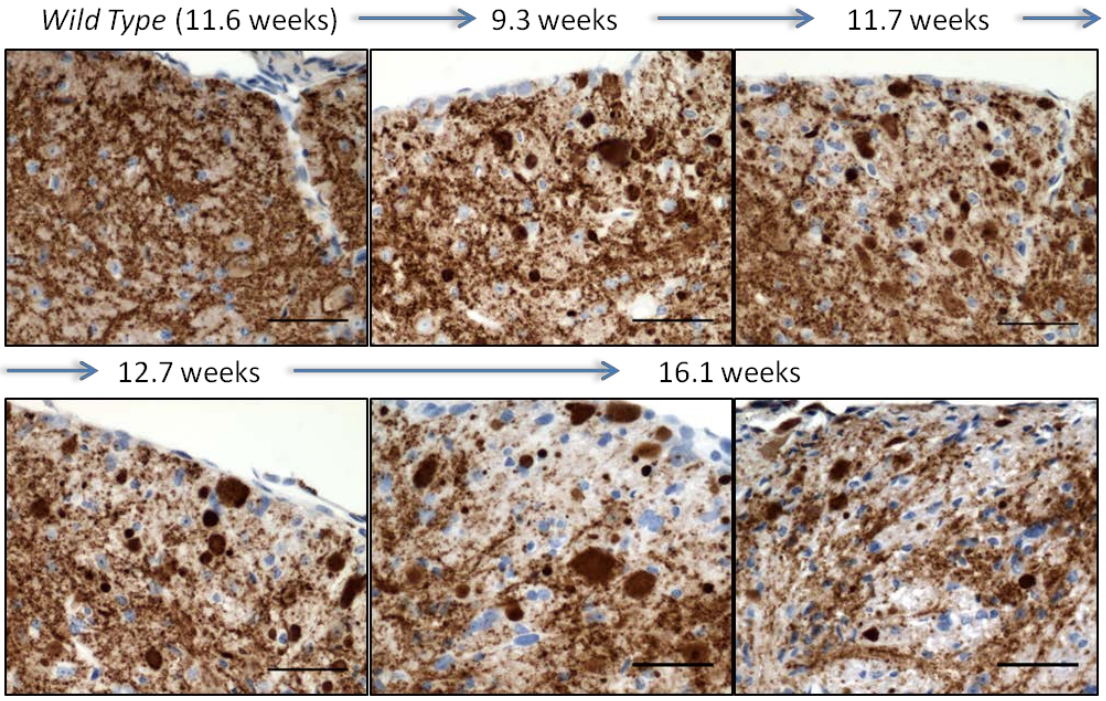

Figure 6.6: Progression of synapse loss and spheroid formation in the gracile nucleus of UCHL1 KO mice. Top left = equivalent region in WT mouse. Synapse loss and axonal spheroid formation starts before 9 weeks and gets progressively worse. Synapse loss is much more pronounced in 16.1 week old mice than in 9 week old mice. Scale bars =50µm

6.2.2.4 Progressive Accumulation of APP in the Gracile Fasciculi

Figure 6.7 demonstrates the progressive increase in APP immunoreactivity in the gracile fasciculi of UCHL1 knockout mice, between 9 and 16 weeks, compared to the gracile nucleus of a WT mouse (top left image). From 9 weeks of age, there are small dot-like accumulations of APP in the gracile fasciculi, and some axonal spheroids with faint APP immunoreactivity are present, but the level of APP in axons is comparable to WT mice. By 16 weeks the immunoreactivity of APP across the whole area of the gracile fasciculi has increased, and there are some spheroids which have accumulated APP.

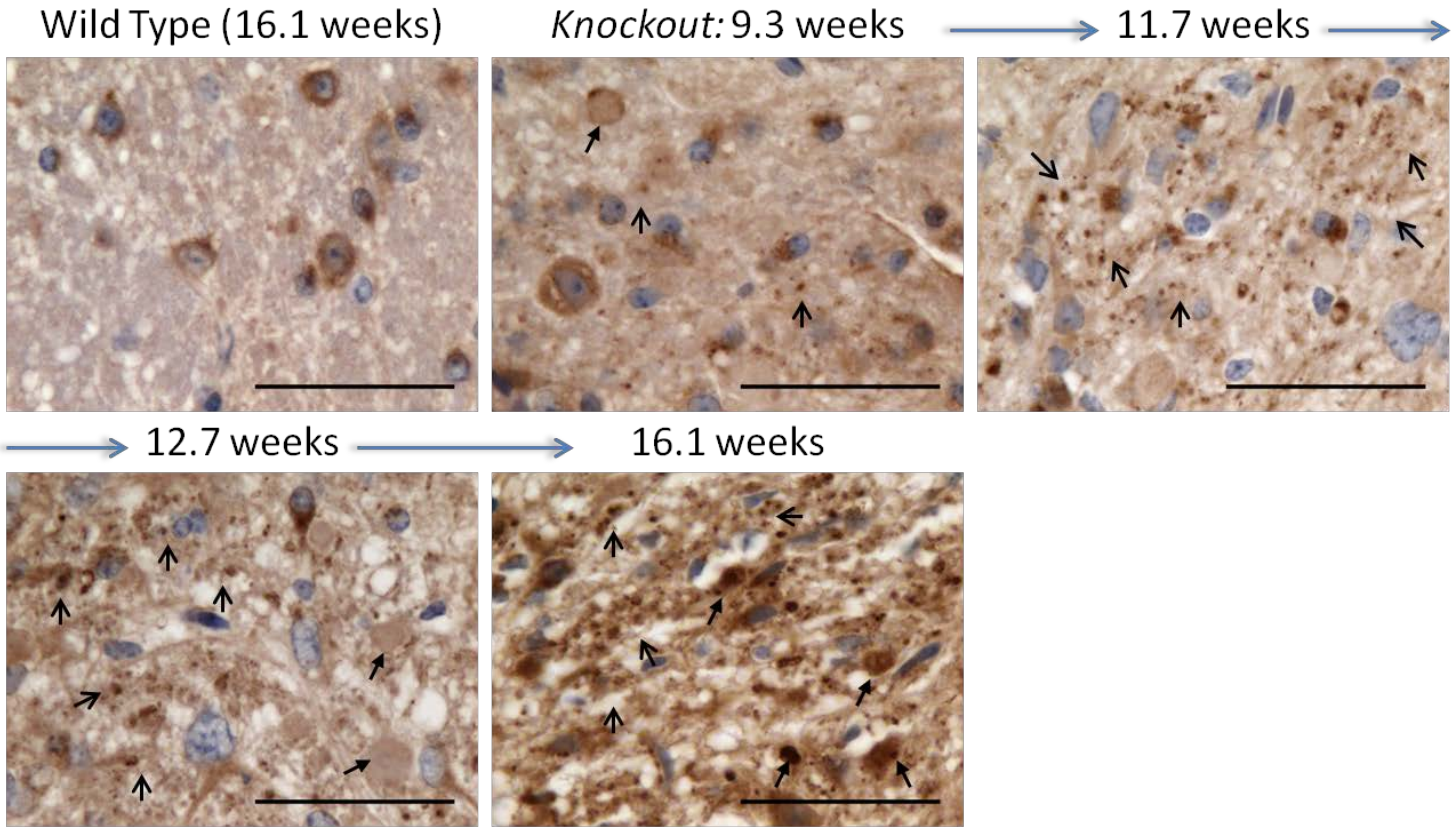

Figure 6.7: Build up of APP in the gracile fasciculi between 9 and 16 weeks.
Top left: equivalent region in WT mouse, for comparison. Open arrows indicate areas of small dot-like accumulations of APP, presumably in axons, closed arrows show axonal spheroids. Scale bars = 50μm

6.2.2.5 Mitochondria in Spheroids of Early and Advanced Stage Mice

The numbers of axonal spheroids that contain mitochondria in the gracile nucleus of early stage pathology (9-12 weeks) and advanced stage pathology (16 weeks) UCHL1 knockout mice were compared. Mitochondria are present in axonal spheroids at even the early stages of pathology. Figure 6.8 demonstrates that there is no appreciable difference between the number of axonal spheroids that contain mitochondria, or the level to which mitochondria accumulate in spheroids between knockout mice at an early stage of pathology, and those at a more advanced stage of pathology. Furthermore, levels of CII-70 and COX-1 immunoreactivity in axonal spheroids are comparable, showing that mitochondria in axonal spheroids are not COX (Cytochrome *c* oxidase, Complex IV) deficient in either early or late stages of pathology, as discussed in Section 4.2.8.

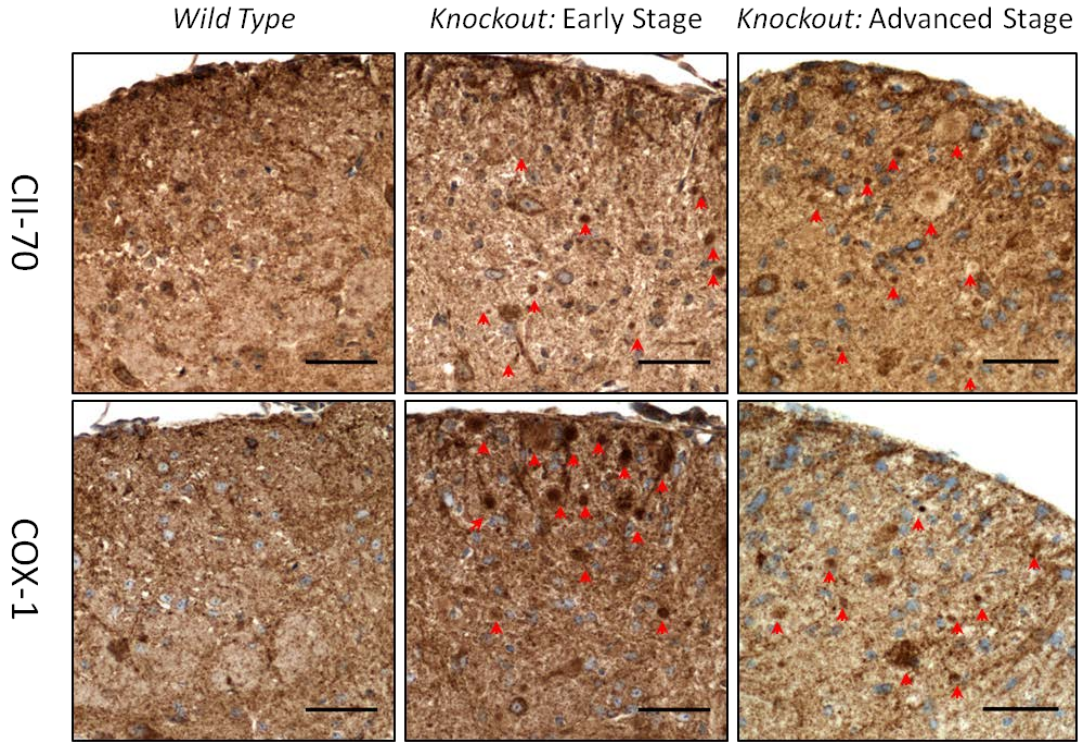

Figure 6.8: Accumulation of mitochondria in axonal spheroids in the gracile nucleus of UCHL1 knockout mice. Left: WT mice, Middle: UCHL1 knockout mice at an early stage of pathology, Right: UCHL1 knockout mice at an advanced stage of pathology. Top: Immunohistochemistry to CII-70, Bottom, Immunohistochemistry to COX-1. Scale bars =50μm

6.2.3 Components of Axonal Spheroids

I have previously observed that when serial sections of the gracile nucleus are stained by immunohistochemistry with antibodies to components of axonal spheroids, some antibodies are better spheroid markers than others (Section 5.2.1). In particular, SMI-31, CII-70 and APP antibodies only mark a proportion of the spheroids that can be identified by synaptophysin immunohistochemistry. Figure 6.9 and Figure 6.10 demonstrate that this principle is true in both early and advanced stages of pathology. Figure 6.9 shows axonal spheroids in the cerebellum of an 11.7 week old mouse (relatively early stage of pathology), stained by immunohistochemistry using synaptophysin, COX-1, APP, SMI-31 and CII-70 antibodies. Figure 6.10 shows the same for a 16.1 week old mouse (advanced stage of pathology). Figure 6.9F and Figure 6.10F show the proportion of axonal spheroids (defined by synaptophysin) marked by SMI-31, CII-70 and APP antibodies in mice at an early stage and advanced stage of pathology. Quantification was carried out as described in Section 5.1.2 for two cross-sections of the gracile nucleus for 3 early stage knockout mice (9-12 weeks) and 2 advanced stage (16 weeks) knockout mice. These results indicate that the composition of axonal spheroids is relatively similar in UCHL1 knockout mice at 9-12 weeks and at 16 weeks; synaptophysin reveals the most spheroids, around 50% of axonal spheroids contain phosphorylated neurofilaments, and a smaller proportion contain mitochondria and APP. There may be a small difference in the number of spheroids that contain mitochondria and APP, as these results indicate that there are less mitochondria-containing spheroids and more APP-containing spheroids in mice with advanced-stage pathology, compared to mice with early-stage pathology. However due to assumptions inherent in this methodology (such as there being a constant number of spheroids in all serial sections), it may not be possible to detect such small differences using this method.

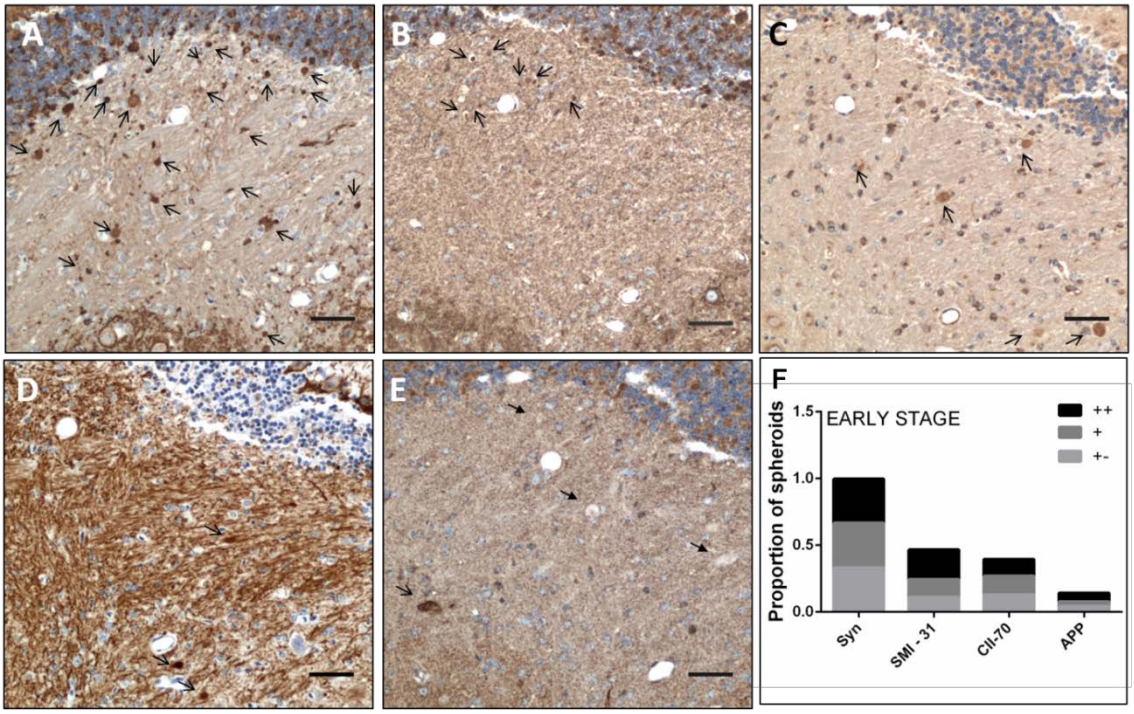

Figure 6.9: Early stage pathology in the cerebellum.
Axonal spheroids as shown by immunohistochemistry using the antibodies A) Synaptophysin, B) COX-1, C) APP, D) SMI-31, E) CII-70. Images from one 11.7 week old mouse, the same pattern is observed in two other mice aged 9.3 and 12.7 weeks. Scale bars = 50µm. F) Quantification of the number of spheroids marked by antibodies synaptophysin, SMI-31, CII-70 and APP, shown as a proportion of the number marked by synaptophysin. Stacked bars indicate the intensity of immunoreactivity: ++ intense, + intermediate, +- faint.

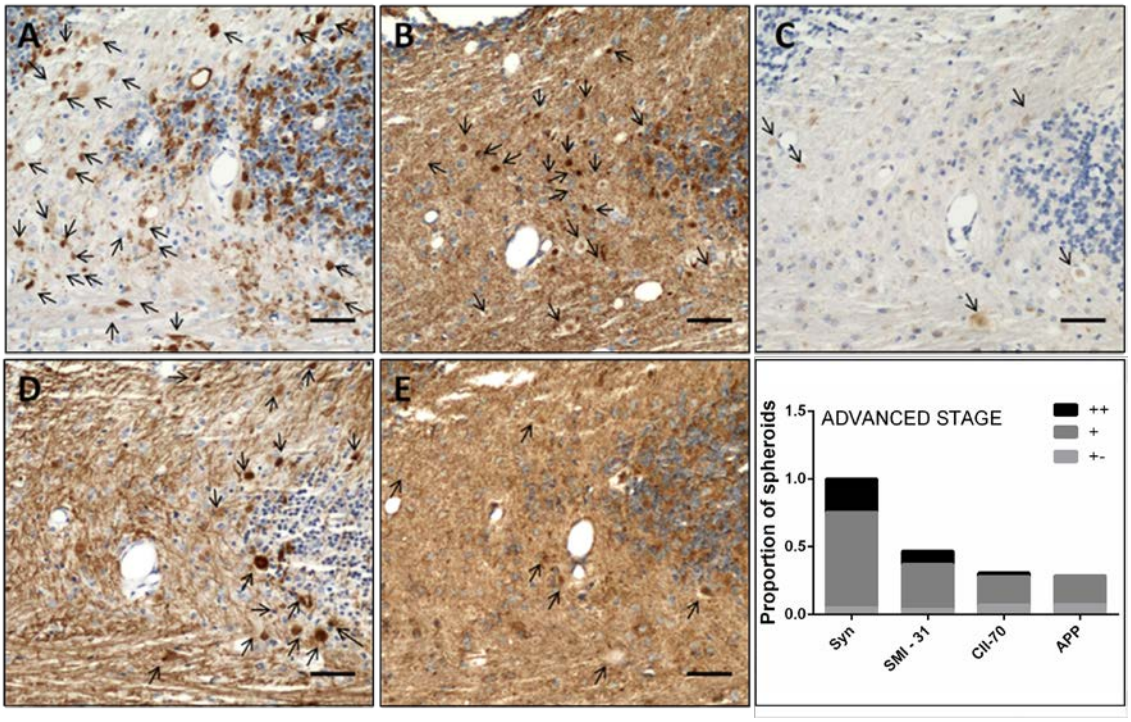

Figure 6.10: Advanced Stage Pathology in the Cerebellum.
Axonal spheroids shown by immunohistochemistry to: A) Synaptophysin, B) COX-1, C) APP, D) SMI-31, E) CII-70. Images from one 16.1 week old UCHL1 KO mouse, the same pattern is observed in its KO littermate. Scale bars = 50µm. F) Quantification of the number of spheroids marked by antibodies synaptophysin, SMI-31, CII-70 and APP, shown as a proportion of the number marked by synaptophysin. Stacked bars indicate the intensity of immunoreactivity: ++ intense, + intermediate, +- faint.

6.2.4 Discussion

The comparison of mice at an 'early stage' and advanced stage' of developing the UCHL1 phenotype reveals that there are some differences in the level of pathology between these two groups.

Results indicate that the loss of synapses, axons and myelin is an early event in the pathogenesis of neuroaxonal dystrophy in UCHL1 KO mice. At 9 weeks, synapse, axon and myelin density are reduced; the loss of synapses continues to progress, so that the 'advanced stage' group have more severe synapse loss than the 'early stage' group. However, there does not appear to be much further axon and myelin loss after around 12 weeks of age. APP accumulation in the gracile nucleus is noticeably increased in the 'advanced stage' group, compared to the 'early stage' group. The loss of synapses and accumulation of synaptophysin in spheroids seems to begin earlier and progress quicker than APP pathology; the difference between 9-12 week and 16 week-old mice is subtle when viewed with synaptophysin, but stark when looking at APP. It is also noticeable that axonal spheroids have already formed in the gracile nucleus by 9 weeks of age, and may even decrease in number with advancing age; this may be due to the dying back of axons and clearance of spheroids and fragmented axons by phagocytes. There are a similar number of axonal spheroids in the white matter of the cerebellum of both 'early stage' and 'advanced stage' mice.

Therefore we can conclude that the formation of axonal spheroids and the loss of synapses and the distal portions of axons is an early event in the pathogenesis of neuroaxonal dystrophy, whereas the accumulation of APP (a marker of fast axonal transport) is a consequence of axonal dystrophy rather than a cause. Interestingly, synaptophysin accumulation in axonal spheroids is an early event in neuroaxonal dystrophy, presumably caused by blocked fast axonal transport. It is possible that the preference for synaptophysin accumulation over APP could be due to a specific block in the movement of synaptophysin transport vesicles, since APP and synaptophysin are transported on two distinct populations of vesicles (Kaether *et al.*, 2000). However, the differences in the accumulation of these two factors may be more simply explained by their expression levels; synaptophysin, the second most common synaptic vesicle protein is highly expressed (Gordon and Cousin, 2014), whereas APP is only expressed at very low levels in neurons (Groemer *et al.*, 2011). Interestingly, it has been shown demonstrated that APP is upregulated in response to denervation (Turco *et al.*, 2014) and traumatic brain injury (Van Den Heuvel *et al.*, 1999; Van den Heuvel *et al.*, 2000).

Therefore it is probable that APP expression is only upregulated after axonal dystrophy in UCHL1 KO mice, and therefore APP accumulation in the gracile nucleus is a consequence of axonal dystrophy, rather than a cause. The relatively small amount of APP accumulation in axonal spheroids must reflect the low level of APP expression in normal axons before APP upregulation.

Immunohistochemistry using several antibodies to components of axonal spheroids shows that all axonal spheroids identifiable contain synaptophysin, whereas only around 50% contain phosphorylated neurofilaments, 40% contain mitochondria and only a small proportion contain APP. These results did not show any discernible difference between mice in the ‘early stage’ and ‘advanced stage’ groups.

6.3 Triple Immunofluorescence Study

6.3.1 Introduction

Immunohistochemistry using several antibodies to components of axonal spheroids shows that the abundance of spheroids is vastly different when looking at sections stained using different markers. The frequency with which different components accumulate in axonal spheroids may give an insight into the mechanism by which spheroids form, for example, IHC results indicate that the accumulation of synaptophysin is important in spheroid formation. Since it is difficult to accurately assess the contents of individual spheroids using IHC, triple immunofluorescence was used as a more accurate method to assess the composition of individual axonal spheroids, and also to characterise differences between 'early stage' and 'advanced stage' groups of mice, in order to give an insight into the progression of axonal spheroid formation.

6.3.2 Methodology

6.3.2.1 Experimental design

Several tissue sections from each mouse were stained with haematoxylin and eosin (H&E), and thus sections from two different regions of the cerebellum, approximately 1mm apart, were selected for each mouse, to ensure that results were directly comparable. Triple immunofluorescence staining with synaptophysin, COX-1 and Neurofilament-H antibodies, was carried on two tissue sections from each mouse detailed in Table 6.1 and Figure 6.1. These mice were split into four groups based on their age (early stage and advanced stage pathology) and genotype. Image acquisition, image analysis and data analysis was carried out on high resolution images of 15 spheroids or areas of white matter from each section. Differences were found between the groups with early stage and advanced stage pathology. Because these conclusions were based on a relatively small number of mice (3 early stage and 2 advanced stage), more mice were then included in this study; one mouse with early stage pathology (age 11.6 weeks) and four mice with advanced stage pathology (age 16-20 weeks), detailed in Table 6.2 and Figure 6.11. This extends the age-range of the 'advanced stage group', Figure 6.12, and ensures that conclusions are based on a greater number of animals. Image acquisition and analysis was undertaken using sections from these mice, stained using the same immunofluorescence protocol, and data from both immunofluorescent staining batches was analysed together, where appropriate.

	Wild Type				Knock Out			
	ID	*Sex*	*Age (Weeks)*	*Visual Score (mean)*	*ID*	*Sex*	*Age (Weeks)*	*Visual Score (mean)*
Early Stage	WT 16	♀	11.6	0	KO 21	♂	9.3	0.33
Advanced Stage	WT 47	♂	16.4	0	KO 48	♂	16.4	1.5
	WT 3	♀	20	-	KO 44	♂	19	1.5
	WT 45	♀	16.3	0	KO 4	♀	17.7	-
	WT 1	♀	17.7	-	KO 49	♀	18.5	2

Table 6.2: Details of additional mice included in the immunofluorescence study

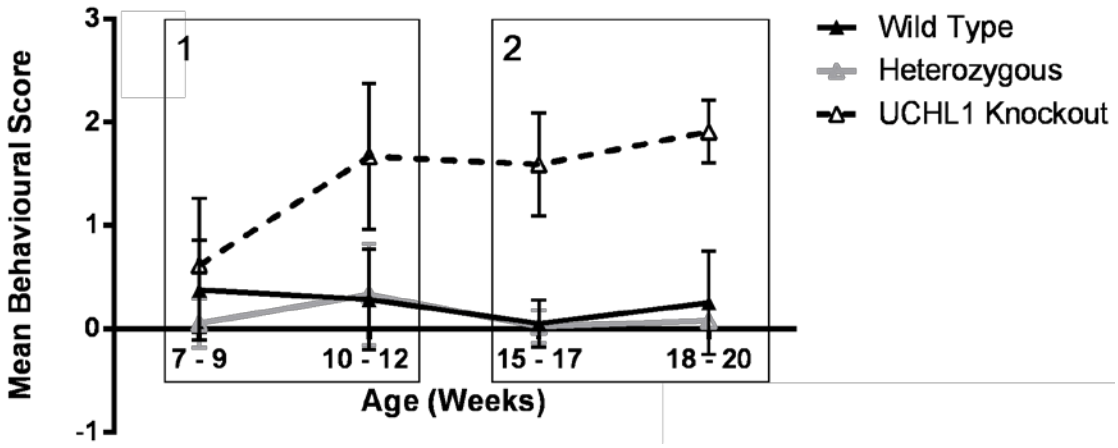

Figure 6.11: Mice used for immunofluorescence study grouped according to level of phenotype and pathology. 1) Indicates the mild phenotype of the early stage pathology group, age 9-12 weeks (Table 1 and 2). 2) Indicates the more severe phenotype of the advanced stage pathology group, age 16 - 19 weeks (Table 1 and 2). Graph taken from Chapter 4, Figure 12, showing hind limb function in UCHL1$^{-/-}$, UCHL1 $^{+/-}$ and WT mice. Data points represent mean ± SEM of mice scored on a scale of 0-2. 0 = normal hind limb function, 1 = slight impairment, 2 = severe impairment of hind limb function.

6.3.2.2 Microscopy

Microscopy was carried out using the Nikon A1R (invert) point scanning confocal microscope, due to its ability to capture high resolution images of immunofluorescent staining without photobleaching, enabling measurements of individual neurofilaments, mitochondria and spheroids.

Imaging settings (laser power, gain, offset, magnification) were kept constant when taking images of sections that were stained in the same batch. Laser power and gain were set up using a tissue section with a medial level of fluorescent signal so that fluorescent signal read at 2000-3000 units (out of a maximal 4095) to avoid overexposure. These settings were then tested on the brightest and dimmest sections to ensure that there was no overexposure in any section, and that the level of exposure was sufficient for the dimmest sections. Using a 'No Primary' control, the offset was adjusted to reduce background fluorescence to a minimal level. Settings for the 541 nm TRITC (tetramethylrhodamine isothiocyanate) and 488nm FITC (fluorescein isothiocyanate) channels were kept constant at all times during imaging, allowing absolute fluorescence intensities to be used for the analysis. However, at times it was necessary to adjust the 647nm laser intensity and gain (for detection of NF-H/ Cyanine 5 staining), so that visualisation of neurofilaments was optimal. This was accounted for by adjusting for background 647nm Cy5 (Cyanine 5) signal for each image at this wavelength for, when analysing neurofilament data. A second batch of tissue sections were stained using the same immunofluorescence protocol, however differences in the intensity of FITC and TRITC channels were observed. Therefore, laser power and gain settings were changed for these channels, so that there was no overexposure, and so that intensities of these channels were comparable to the first batch (Appendix C, Figure 8.4). Therefore, care should be taken when interpreting data based on fluorescence intensity from both batches grouped together. However it was feasible to take data on area and length from these sections, since these do not depend on fluorescence intensity, but on a manually applied threshold.

6.3.2.2.1 2D or 3D Image Acquisition

One of the main considerations when designing the image acquisition procedure for the triple immunofluorescence study was whether to take flat 2D images, or whether to build up a 3D picture of axonal spheroids and the surrounding axons, by taking several z-stack images. Both methods have advantages and disadvantages, so for several spheroids I took 2D and 3D images, and compared the outcome and feasibility of image

analysis. 2D ‘snapshot’ images are far quicker to take than 3D ‘z-stack images’, and therefore require far less microscope time, but are just as good in terms of resolution. Z-stack images build a more comprehensive view of axonal spheroids, however it is not possible to image a complete spheroid in most cases, since sections are only 5µm thick, and axonal spheroids can be up to 70µm diameter. In addition, taking detailed z-stack images can cause photobleaching; z-stack imaging is essentially taking multiple images of the same area of tissue, and with prolonged laser exposure, the flourophores are easily quenched. In fact, this is demonstrated in Figure 6.12, as the intensity of TRITC (Synaptophysin, red) is clearly diminished in the 3D images (Figure 6.12 B, C, D), as compared to the 2D image (Figure 6.12A). In addition to this, using z-stack images complicates image analysis unnecessarily. Figure 6.12A and B demonstrate the ease with which Volocity 6.0 (Perkin Elmer) selects neurofilaments and the mitochondria contained within them, in both 2D and 3D. However, the issue with 3D images arises when analysing axonal spheroids, as demonstrated in Figure 6.12C, selecting spheroids using a synaptophysin threshold is not effective for all spheroids, since not all are completely encircled by synaptophysin (white arrows). In addition, using a hand drawn region of interest (ROI) is inaccurate (Figure 6.12C), as the x-y plane area of the spheroid changes as you move through the z-plane, leading to regions outside of the spheroid being included in the analysis (white arrows). This is not an issue when analysing 2D images, and therefore it was determined that acquiring 2D images would be more efficient, accurate and comprehensive enough for this type of analysis. The image analysis protocol designed for analysing these images is detailed in section 6.3.2.3.

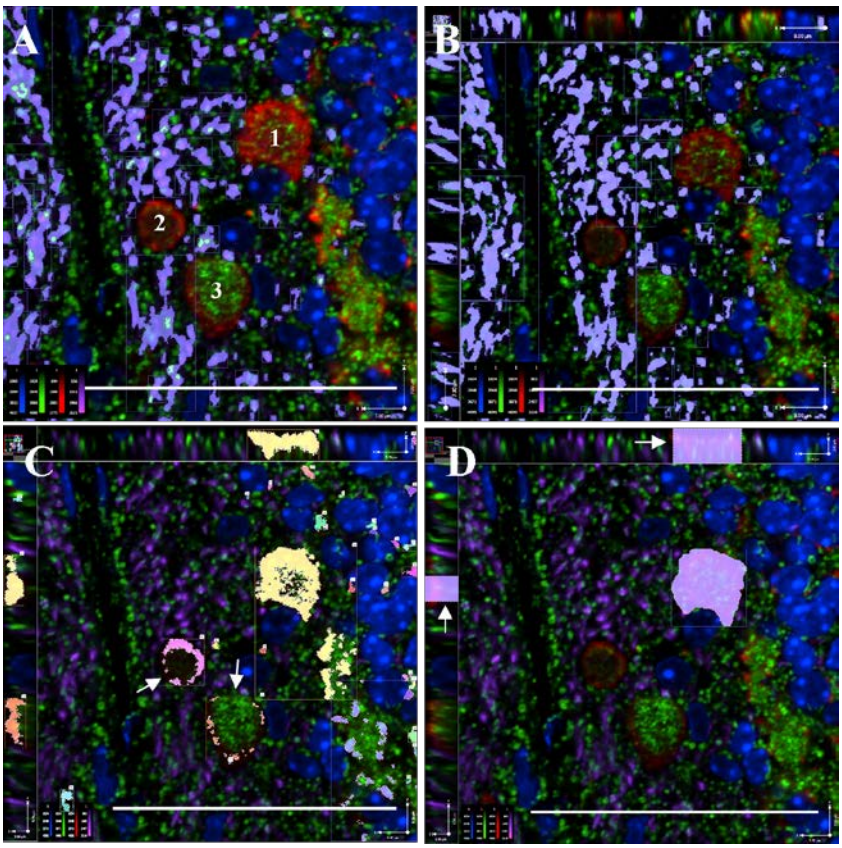

Figure 6.12: Image analysis of 2D and 3D images of spheroids.
A) 2D image of three axonal spheroids (labelled 1-3). Neurofilaments are highlighted (purple), showing measurement by Volocity 6.0 software of neurofilament area and intensity, and selection and measurement of mitochondria inside neurofilaments (2.8% of neurofilament area). B) 3D (z-stack) image of the same area, including y-z (left) and x-z (top) perspectives, showing measurement of neurofilaments and contained mitochondria (0.114% of neurofilament volume). C) 3D image demonstrating the difficulties of using synaptophysin as a marker for the automatic selection of spheroid volume by Volocity 6.0. Spheroid 1 is selected, however, spheroids 2 and 3 are not (white arrows), due to differences in intensities. D) 3D image showing the inaccuracy of using an ROI to select the 3D volume of a spheroid (white arrows)

6.3.2.3 Image Analysis

Using Volocity 6.0, I designed an image analysis protocol for the assessment of mitochondria, synaptophysin and neurofilament-H levels in both axons (as marked by neurofilament-H) and spheroids (marked by a combination of synaptophysin and by regions of interest (ROIs)). The identification of axons and spheroids is described in Figure 6.13.

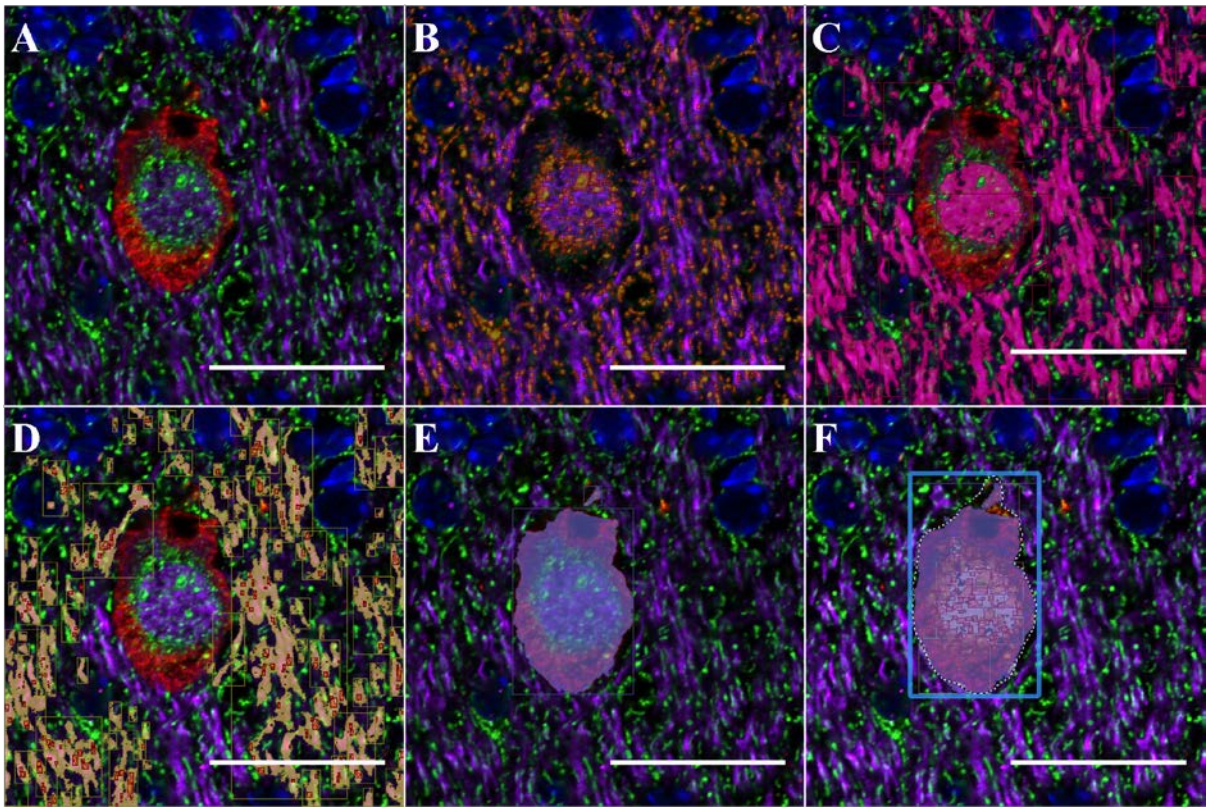

Figure 6.13: Image Analysis for Triple Immunofluorescence.
A) Original Image: Purple = Neurofilaments (Cy5), Green = Mitochondria (FITC), Red = Synaptophysin (TRITC), Blue = Nuclei (405nm). 1. Using Volocity 6.0, a threshold was applied so that all mitochondria were selected (B, orange), and a similar threshold was applied to select neurofilaments (C, pink). To obtain data on mitochondria and synaptophysin intensity, and mitochondrial area and number inside neurofilaments, 'Normal neurofilaments' (D, yellow) were selected by excluding neurofilaments touching spheroids, and mitochondria 'inside' neurofilaments were selected as contained items. A 'splitting' algorithm was applied to mitochondria. Volocity 6.0 then produced measurements of neurofilament, synaptophysin and mitochondrial intensity inside 'normal neurofilaments'. The 'splitting algorithm' was removed from mitochondria and their number and skeletal length was recorded. E) Axonal spheroids were selected by applying a threshold to synaptophysin, and excluding items touching the edge, and anything smaller than 10μm^2 to exclude analysis of synapses or incomplete spheroids. E) A 'limit to ROIs function' was introduced, and an ROI drawn around each spheroid (F), so that spheroids not filled with synaptophysin could be analysed. Mitochondria were defined according to the FITC threshold and as 'contained items', 'overlapping' spheroids, but inside ROIs, to ensure all mitochondria within spheroids were counted, even if the spheroid was not full of synaptophysin. Scale bars = 50μm.

6.3.3 Results

6.3.3.1 Mitochondria Form a Core within Spheroids

Using high resolution point scanning confocal microscopy, it is possible to view the structure of axonal spheroids, and the distribution of various spheroid components. Frequently, mitochondria form a core within the spheroid and are surrounded by synaptophysin Figure 6.14A, B, however mitochondria are occasionally dispersed throughout the spheroid, e.g. Figure 6.15A, Figure 6.16B. Where spheroids contain neurofilaments, it is also common for them to form a core, sometimes along with mitochondria, and become surrounded by synaptophysin (Figure 6.13, Figure 6.14B, Figure 6.16B).

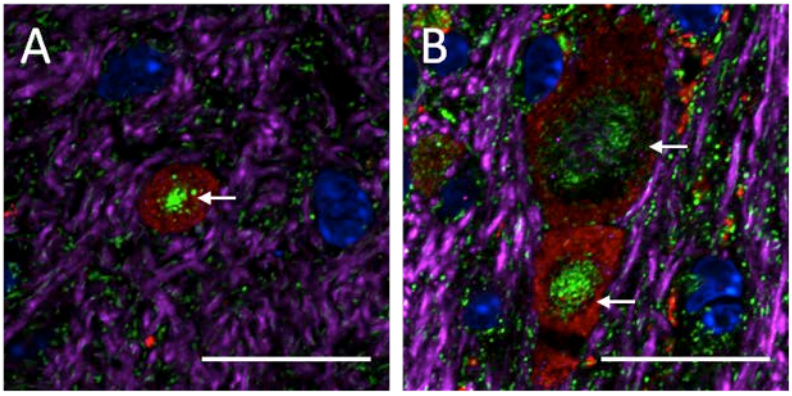

Figure 6.14: Mitochondria are frequently seen forming the core of axonal spheroids.
This is seen here in both transverse (A) and longitudinal (B) sections of two different spheroids. Blue = nuclei, Green = Mitochondria, Red = Synaptophysin, Purple = neurofilaments.

6.3.3.1.1 Axonal Spheroids can be End-Bulbs, En-Passant or Tandemly Repeated Swellings

In order to gain insight into the mechanism of axon degeneration in UCHL1 knockout mice, it is necessary to classify whether spheroids are end-bulbs or en-passant, that is, are they a swelling at the end of a parent axon, or are they part of a continuous axon? It is possible using immunofluorescent staining to identify both the parent axon (neurofilament-H antibody) and spheroid (synaptophysin antibody) simultaneously. My images indicate that whilst the majority of axonal spheroids are end-bulbs (Figure 6.15), some spheroids do seem to be swellings on a continuous axon, as it is possible to identify the axon coming into and leaving the spheroid. Figure 6.15C depicts an ‘end-bulb’ close-by to an en-passant spheroid on the same axon. These results indicate that axonal spheroids form prior to the fragmentation of the distal part of the axon; the blockage of axonal transport associated with spheroid formation then causes the distal part of the axon to degenerate.

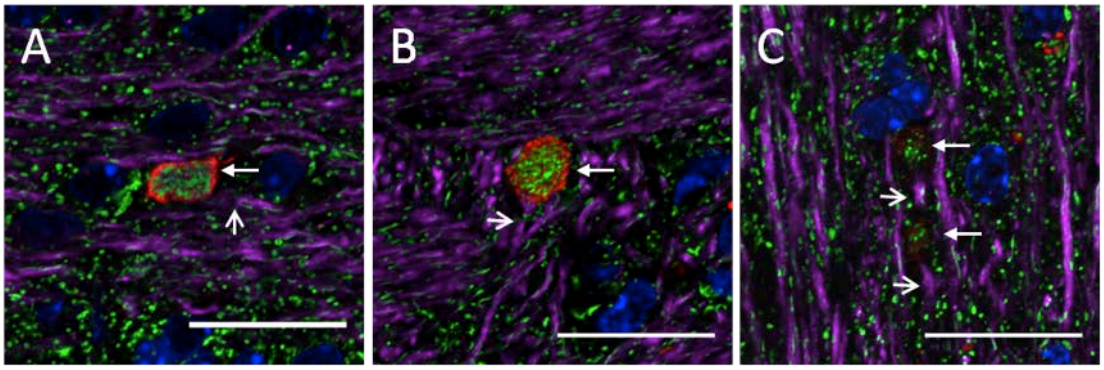

Figure 6.15: Spheroids could be end-bulbs or en-passant.
Figures A and B show axonal spheroids (filled arrowhead) with their parent axon (open arrowhead), and seem to be at the end of the axon. Figure C shows an axon that appears to be interrupted by two small axonal spheroids (filled arrows)

6.3.3.2 Multiple blockages of axonal transport

In addition to the observation of tandemly repeated swellings along a continuous axon, I have also observed that the shape of some axonal spheroids indicates that there are multiple blockages of axonal transport within one dystrophic axon (Figure 6.16). This can be seen in transverse sections of large axonal spheroids. I have indicated the probable site of axonal transport blockage with dashed white lines, Figure 6.16.

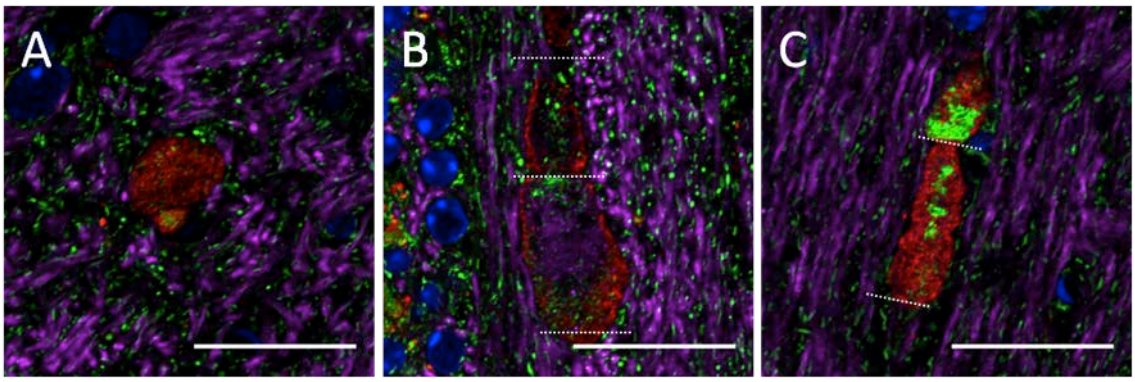

Figure 6.16: Multiple axonal transport blockages in axonal spheroids.
Dashed white line indicates potential site of axonal transport blockage.

6.3.3.3 Accumulation of Mitochondria and Synaptophysin in Axonal Spheroids

I have previously demonstrated using immunohistochemistry that synaptophysin, mitochondria and neurofilaments all accumulate in axonal spheroids (Chapter 4), to varying extents (Chapter 5). Quantification of the number of axonal spheroids in the gracile nucleus containing these three components indicated that synaptophysin marked all identifiable spheroids, whilst phosphorylated neurofilaments were present in 43% of this number and mitochondria were present in 37%. Since these results depend on the assumption that the number of spheroids remains constant in serial sections of the gracile nucleus, I have also used triple immunofluorescence to determine the

proportions of spheroids that contain each component as a comparison to their normal levels in axons, as this may give an insight into the mechanism by which axonal spheroids are formed.

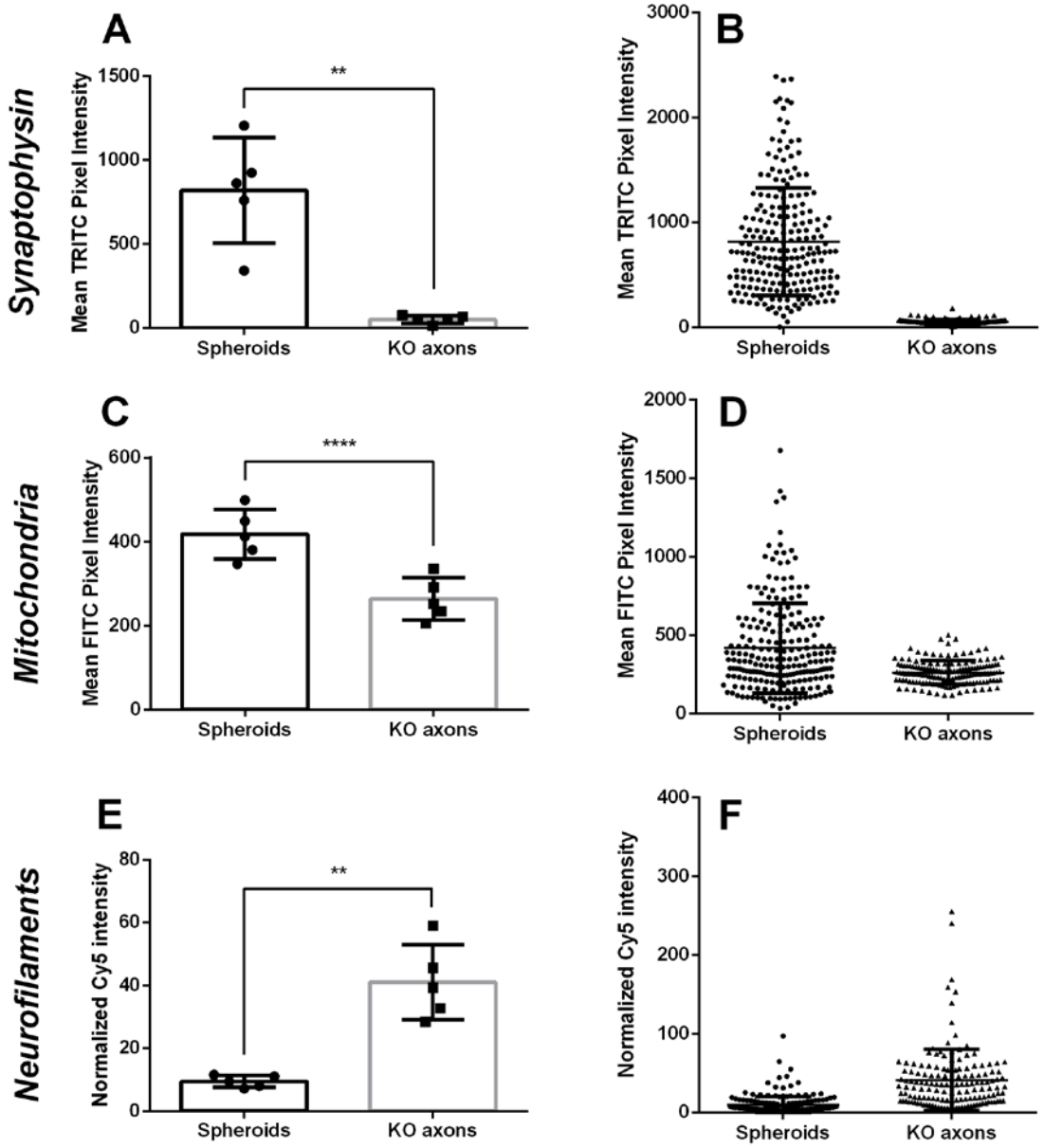

Figure 6.17: Synaptophysin, mitochondria and neurofilament levels in spheroids compared to nearby axons. A, B) Mean TRITC Intensity (marks synaptophysin) in Spheroids and KO axons. C, D) Mean FITC intensity (marks mitochondria) in spheroids and KO axons. E, F) Mean Cy5 intensity (marks NF-H) in spheroids and KO axons, normalized to background values. A, C, E) Data points represent the mean TRITC, FITC or Cy5 intensity for each mouse, bars show the mean ± SD. B, D, F) Each data point shows the mean TRITC, FITC or Cy5 intensity of one spheroid or area of axons, bars show mean ± SD. A) Difference is significant, p=0.0041, two-tailed paired t-test, n=5, CI=95%. C) Difference is significant, p<0.0001, two-tailed paired t-test, n=5, CI=95%. E) Difference is significant, p=0.0027, two-tailed paired t-test, n=5, CI=95%.

Results from detailed analysis of triple immunofluorescent staining show that levels of synaptophysin and mitochondria are significantly increased in axonal spheroids, compared to nearby normal axons (p=0.0041, p<0.0001), demonstrated in Figure 6.17A

and C. Figure 6.17B shows, as expected, that the amount of synaptophysin in normal axons is negligible, whilst synaptophysin is present at high levels in almost all axonal spheroids. The intensity of TRITC (which marks synaptophysin) is higher in spheroids than in surrounding axons in 99.5% of spheroids. This confirms the earlier assumption that synaptophysin accumulates in almost all axonal spheroids.

As we can see in Figure 6.17D, there is some FITC intensity (showing that mitochondria are present) in all axonal spheroids, however not all spheroids have higher FITC intensity than surrounding axons. Since the intensity of FITC in KO axons is normally distributed, we can assume that 95% of axons will have a FITC intensity which is within the mean ±2 standard deviations. Therefore, I have determined that the mean ±2 SD is a normal level of FITC intensity and used this as the range to compare the levels of mitochondria in spheroids to the level of mitochondria within axons. This method shows that 38% of spheroids accumulate mitochondria to a level which is higher than the normal range for axons. Interestingly, this figure is very similar to the number of spheroids identified with CII-70 immunohistochemistry, as a percentage of those identified by synaptophysin immunohistochemistry, verifying the methods of quantification used in Chapter 5. 54% of axonal spheroids have levels of mitochondria that are typical of surrounding axons (within mean ± 2 SD), whilst 9% of spheroids contain less mitochondria than is typical for axons. Around 65% of axonal spheroids contain higher levels of mitochondria than the axons immediately surrounding them.

Unexpectedly, this immunofluorescence data demonstrates that the levels of NF-H (Neurofilament Heavy chain) are significantly lower in axonal spheroids than in axons. This partially reflects that when analysing these images, axons are defined as regions marked by Neurofilament-H staining, whereas spheroids are a wider area. However when viewing images of axonal spheroids, it is clear that very few contain NF-H. The discrepancy between this observation and earlier immunohistochemistry studies may be due to the difference in antibodies used to identify neurofilaments. In immunohistochemistry studies, I used SMI-31, an antibody to phosphorylated NF-H and NF-M, whereas here I have used NF-H, an antibody to the phosphorylated heavy chain of neurofilaments. It may be that the breakdown of neurofilament structure that occurs when neurofilaments accumulate in spheroids may affect the epitopes that SMI-31 and NF-H bind to differently.

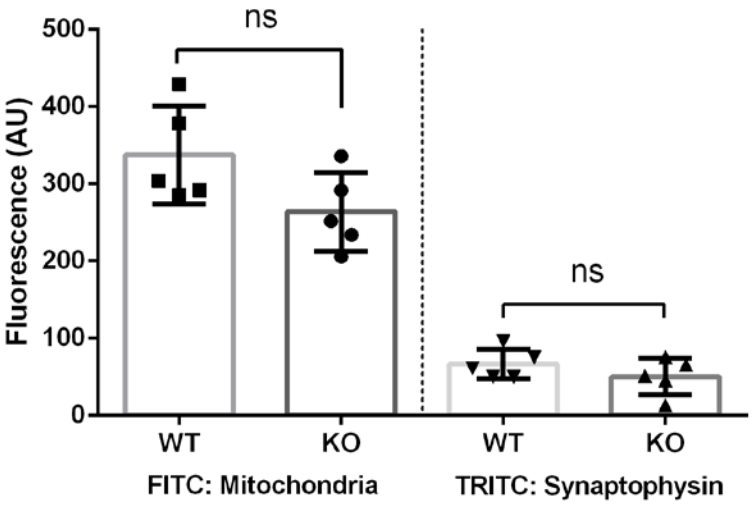

Figure 6.18: Levels of mitochondria and synaptophysin in axons or WT and UCHL1 KO mice.
No significant decrease in mitochondria, measured by FITC intensity in KO axons, p=0.0767, n=5, unpaired t-test.
No significant difference in synaptophysin levels in axons of UCHL1 KO mice, measured by TRITC intensity, p=0.2704, n=5, unpaired t-test.

In order to determine whether the accumulation of mitochondria and synaptophysin in axonal spheroids causes an increase or decrease in their levels in the axons of UCHL1 KO mice, I also quantified the intensity of FITC (mitochondria) and TRITC (synaptophysin) in WT mice. Results indicate that there is no difference in the levels of synaptophysin or mitochondria either in the axons of UCHL1 KO mice, as compared to WT mice (p=0.0767, p=0.2704, respectively), although mitochondrial levels are decreased by trend.

6.3.3.4 Number and Length of Mitochondria in Axons and Spheroids

Triple immunofluorescence staining was also used to determine the skeletal length of mitochondria in axons, and the average number of mitochondria per 100μm^2 axon area. The skeletal length of an object is found by reducing its width to 1 pixel, and recording the length. This is an accurate measurement of length of objects that are not uniform, as it takes into account their shape. Here, data from both batches of immunofluorescent staining (mice detailed in Table 6.1 and Table 6.2) were combined; length and number measurements will not be skewed by small differences in fluorescence intensity since they require a threshold to be applied. This was done to determine whether the accumulation of mitochondria in spheroids changes the number of mitochondria in nearby axons. This also serves a second purpose in re-examining our original hypothesis in vivo; the length of mitochondria can be indicative of a shift in mitochondrial dynamics towards fission or fusion. Therefore, assessment of the length of mitochondria

in UCHL1 KO axons will determine whether UCHL1 knockout and ubiquitin depletion in vivo disrupts mitochondrial fission and fusion dynamics.

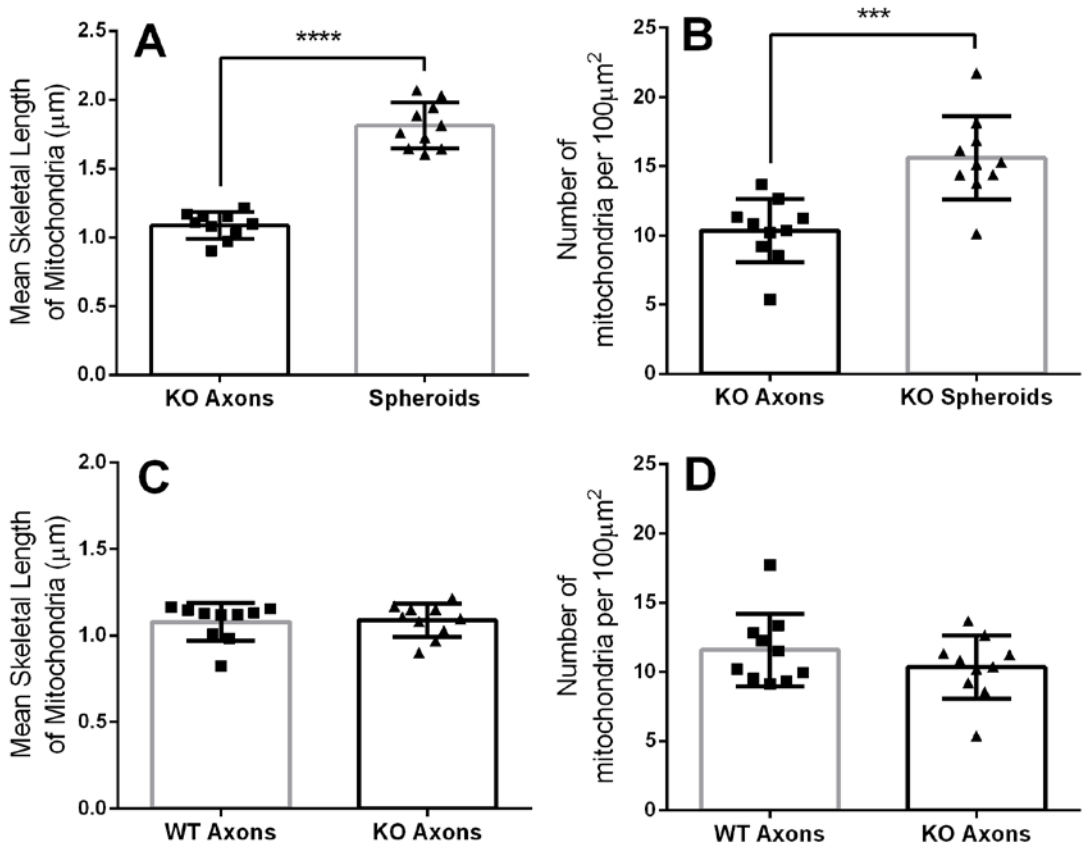

Figure 6.19: The number and length of mitochondria in axonal spheroids and in axons of WT and KO mice. A) The mean skeletal length of mitochondria in spheroids is significantly increased in spheroids ($p<0.0001$, n=10, paired t-test). B) The number of mitochondria per 100μm^2 area is significantly increased in spheroids compared to axons ($p=0.009$, n=10, unpaired t-test). C) No difference in the length of mitochondria between WT and KO axons ($p>0.999$, Mann-Whitney test, n=10). D) No difference in the number of mitochondria per 100μm^{2}between WT and KO axons ($p=0.5191$, Mann-Whitney test, n=10). Each data point represents the average of 30 spheroids or axons from 1 mouse, n=10 mice. Bars show mean ±SD.

Results show that there is a significant increase in the number of mitochondria in axonal spheroids, compared to both the level of mitochondria in WT axons and in KO axons ($p=0.0009$), Figure 6.19B, further demonstrating the accumulation of mitochondria in spheroids. However, the number of mitochondria in axons is not significantly different in UCHL1 knockout mice to WT mice ($p=0.5191$), Figure 6.19D, but is only decreased by trend, in the same way that the FITC intensity in KO axons is slightly decreased by trend.

The skeletal length of mitochondria in axonal spheroids is significantly increased compared to nearby KO axons, Figure 6.19A. By visually assessing the images from which this data is taken, it is clear that this is because mitochondria in spheroids are pushed together within a confined space, often creating large aggregates of

mitochondria, which have an increased skeletal length compared to normal mitochondria, so it is difficult to interpret the relevance or this result for mitochondria in spheroids. Furthermore, there is no difference between the skeletal length of mitochondria in WT axons and KO axons, Figure 6.19 C. This indicates that the balance between mitochondrial fission and fusion is not disrupted in UCHL1 knockout mice; if the balance shifted towards fission, you would see a decrease in the length of mitochondria, whereas if the balance shifted towards fusion, the length of mitochondria would increase. This further confirms my earlier conclusion that impairment of UCHL1 function and ubiquitin depletion does not affect mitochondrial dynamics, and validates the use of UCHL1 inhibitors in cell culture.

6.3.3.5 Categorising axonal spheroids

In order to determine whether there might be a difference between the composition of axonal spheroids in mice with early (9-12 weeks) and advanced (16 weeks) stage pathology to help elucidate mechanisms of axonal dystrophy, axonal spheroids were categorised according to what components they contained (Figure 6.20)

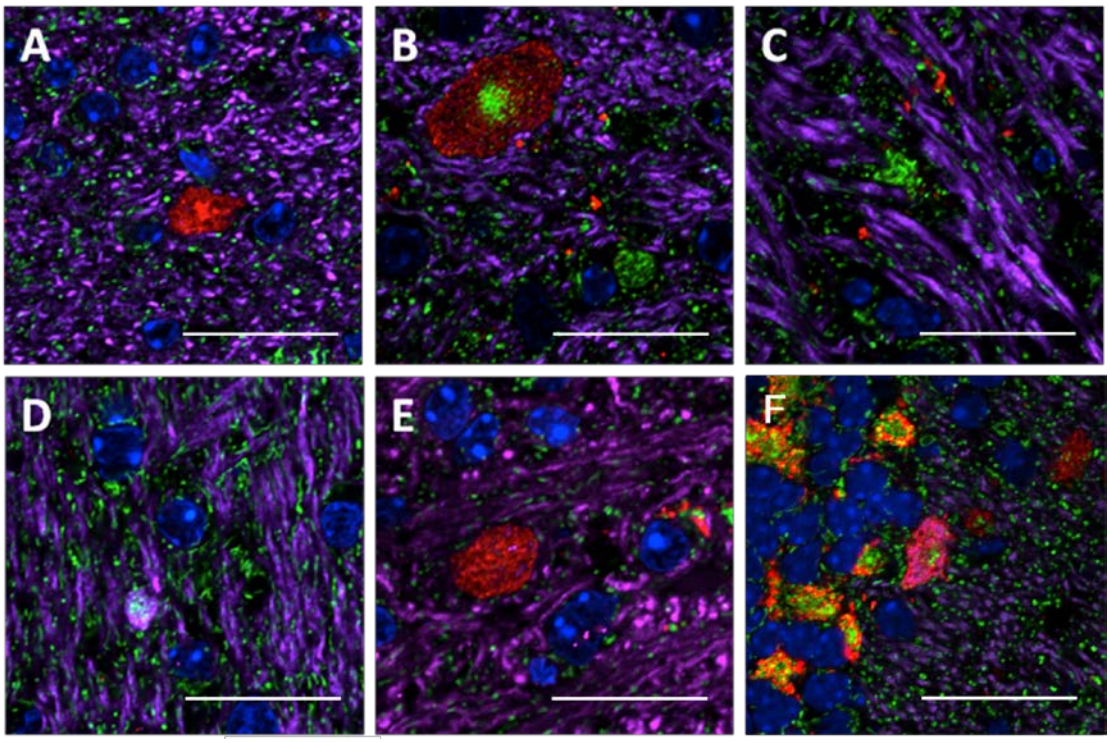

Figure 6.20: Categorising axonal spheroids according to their components.
Synaptophysin – Red, Mitochondria – Green, Neurofilaments – Purple, Nuclei – Blue. A) Spheroid containing only synaptophysin, B) Synaptophysin and Mitochondria, C) only mitochondria, D) Mitochondria and neurofilaments, E) Synaptophysin and Neurofilaments, F) Synaptophysin, Neurofilaments and Mitochondria. Scale Bars = 50μm.

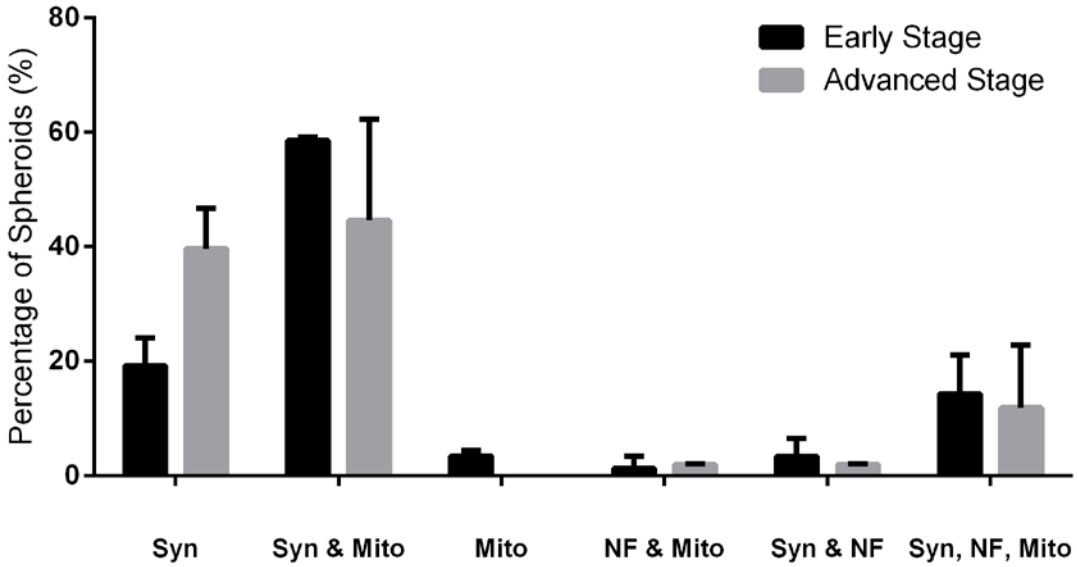

Figure 6.21: Axonal spheroids of mice with early and advanced stage pathology, categorised according to their components.
Expressed as a percentage of the total number of spheroids. Syn = Synaptophysin, Mito = Mitochondria, NF = Neurofilament-H. No significant differences: multiple t-tests with Holm-Sidak correction, α=5%, n=3, 2. p=0.0288, p=0.2320. p=0.0176, p=0.6994, p=0.5913, p=0.7713

Results demonstrated that axonal spheroids most commonly contain both synaptophysin and mitochondria (40-60% of spheroids contain these two components), and the second most common category of spheroids is those containing just synaptophysin (20-40%) of the total. Spheroids containing just mitochondria, or just neurofilaments and mitochondria (ie. those not containing synaptophysin) are very rare.

The composition of axonal spheroids in mice with early and advanced stage pathology was compared. Results indicated that that mice with advanced stage pathology may have more axonal spheroids that contain just synaptophysin, and less that contain synaptophysin and mitochondria together (Figure 6.21) perhaps suggesting that as spheroids develop, synaptic vesicles and synaptophysin continue to build up, whereas mitochondria are cleared or broken down. However, using multiple t-tests with the Holm-Sidak method for determining statistical significance, there were no significant differences between the composition of spheroids in mice with early and advanced stage pathology (p=0.0288, p=0.2320. p=0.0176, p=0.6994, p=0.5913, p=0.7713). Therefore, differences between mice at early and advanced stages of pathology were further examined using detailed image analysis of axonal spheroids, and by including more mice in the study.

6.3.3.6 Axonal Spheroids in Mice with Early and Advanced Stage Pathology

In order to determine whether levels of synaptophysin and mitochondria increase or decrease with advancing age in axonal spheroids, and to give an insight into spheroid development, I determined the intensity of synaptophysin and mitochondria immunofluorescent staining in 30 spheroids and surrounding areas of axons in each of 5 UCHL1 knockout mice (3 at an early stage of pathology, 2 at a more advanced stage of pathology). This initially indicated that the level by which mitochondria accumulates in axonal spheroids (relative to surrounding axons) decreases with age, whereas the extent to which synaptophysin accumulates increases with age, (Appendix C, Figure 8.3) perhaps suggesting that mitochondria are being cleared from axons. However, since this conclusion was based on a total of only 5 mice, several more mice were then included in this study, detailed in Table 6.2. Although some difference in the intensity of synaptophysin and COX-1 immunofluorescence was observed in the second batch of immunofluorescence, this was largely accounted for by adjusting the laser power and gain on the microscope (Appendix C, Figure 8.4). Data points resulting from the first batch of immunofluorescence are shown in green, and those from the second are shown in red (Figure 6.22).

Results show that there is no difference in the level of mitochondria in axons ($p=0.3524$) or spheroids ($p=0.6095$) between mice with early stage pathology (age 9 – 12 weeks) and mice with more advanced pathology (16-19 weeks), Figure 6.22A. The levels of mitochondria in axonal spheroids remains constant with increasing age and increasing severity of phenotype and pathology, indicating that there is no mechanism by which mitochondria are cleared from spheroids with time.

Furthermore, there is no difference in the intensity of synaptophysin immunofluorescence in axons ($p=0.5619$) or spheroids ($p=0.3333$) between mice with early and advanced stage pathology, Figure 6.22B. This indicates that once synaptophysin accumulates within an axon, forming a spheroid, either it does not continue to accumulate, or only continues to accumulate at the same rate by which the spheroid is growing; therefore the mean intensity of synaptophysin immunofluorescence in spheroids remains constant with advancing age, and increasing severity of phenotype and pathology.

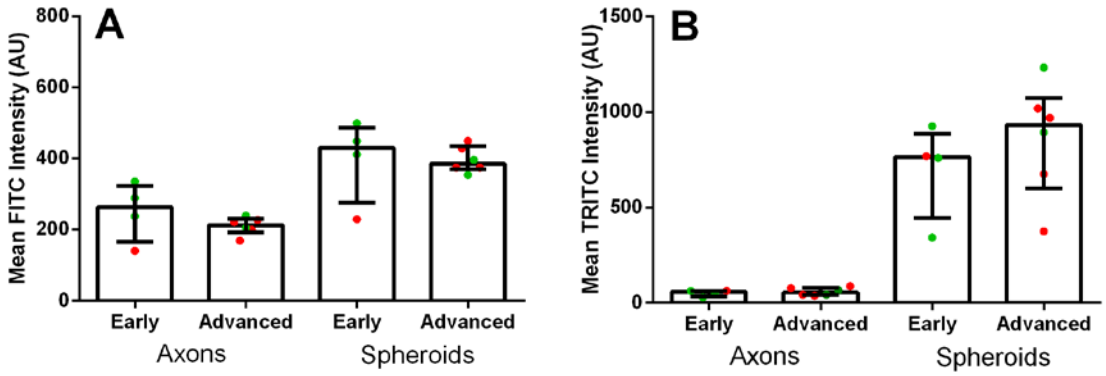

Figure 6.22: No difference in mitochondria or synaptophysin accumulation with age.
Comparison of mitochondria (A) and synaptophysin (B) levels between mice with early stage pathology (9-12 weeks), and advanced stage pathology (16-19 weeks). A) No difference in levels of mitochondria in axons (p=0.3524) or spheroids (p=0.6095) between mice with early and advanced stage pathology (Mann-Whitney tests, n=4,6) B) No difference in levels of synaptophysin in axons (p=0.5619) or spheroids (p=0.3333) between mice with early and advanced stage pathology (Mann-Whitney tests, n=4,6). Data points represent the mean FITC or TRITC intensity across 30 axon regions or spheroids for each mouse. Bars show the median and interquartile range. Green points indicate the first batch of staining, red points indicate the second.

6.3.4 Discussion

The analysis of high-resolution triple immunofluorescence images of axonal spheroids has given several insights into the formation of spheroids in UCHL1 null mice.

Firstly, I have found that axonal spheroids are usually present as 'end bulbs' (i.e. only one parent axon can be identified), but that there are spheroids that are en-passant, axons with tandemly repeated spheroids, and spheroids that appear to result from multiple blockages in axonal transport. This indicates that axon degeneration in this mouse model results from a focal swelling followed by dying-back degeneration of the distal portion of the axon, in a distal-proximal direction, in a manner similar to the response to nerve-crushing (Beirowski *et al.*, 2005).

My results indicate that the blockage of the fast axonal transport of synaptophysin transport vesicles is the primary event responsible for the formation of axonal spheroids, since synaptophysin is present in spheroids at higher levels than surrounding axons in the vast majority (99.5%) of cases. Synaptophysin immunoreactivity is generally spread across the whole of axonal spheroids whereas mitochondria and neurofilament accumulations are not as common, and generally form a core in the centre of spheroids. The mechanism leading from UCHL1 knockout to synaptophysin accumulation and spheroid formation is likely to feature the aggregation of misfolded proteins, since UCHL1 inhibition reduces the efficacy of the proteasome by around 50% (Cartier *et al.*, 2009), and UCHL1 null mice have a 50% decrease in monomeric ubiquitin, which is needed to target proteins to the 26S proteasome. My results suggest that it is also likely that UCHL1 has a specific function at synapses; synaptic loss is one of the earliest events in UCHL1 neuroaxonal dystrophy and the prevalence of synaptophysin accumulation in spheroids in UCHL1 mice is greater than in aged humans, who also have a less efficient ubiquitin proteasome system. This is consistent with other literature that suggests that UCHL1 functions at presynapses (Cartier *et al.*, 2009), and that UCHL1 colocalises with synaptophysin on synaptic vesicles (Liu *et al.*, 2002).

My results also demonstrate that the accumulation of mitochondria in axonal spheroids is a secondary consequence of spheroid formation, since the intensity of mitochondria in spheroids doesn't exceed the intensity in normal axons in all cases. 65% of spheroids contain more mitochondria than the immediately surrounding area of axons, whilst 38% contain more mitochondria than is normal for axons. This indicates that mitochondria

accumulate in spheroids as a consequence of blocked fast axonal transport, caused by protein aggregation and synaptophysin accumulation.

I also found that the number and skeletal length of mitochondria in spheroids is significantly increased compared to KO axons, but that there is no difference in the number or intensity of mitochondria between the axons of WT and KO mice. This shows that, although mitochondria do accumulate in spheroids, there is no depletion in the number of mitochondria in other regions of axons, such as those proximal to the spheroid. Finally, high resolution immunofluorescence images allowed me to calculate the length of mitochondria, and thus determine if there are any morphological indications of a defect in mitochondrial fission or fusion. My results demonstrated that the mitochondria in KO axons are of similar length to those in WT axons. This further demonstrates that mitochondrial fission and fusion occurs normally in the absence of UCHL1, and in conditions where monomeric ubiquitin is depleted, confirming the results of my live-cell imaging study in Chapter 3.

Chapter 7.

The Ubiquitin Proteasome System in Mitochondrial Disease

Chapter 7. **The Ubiquitin Proteasome System in Mitochondrial Disease**

7.1 Introduction

7.1.1 The m.3243A>G Mutation

The m.3243 A>G mutation is one of the most common pathogenic mtDNA mutations (Schaefer *et al.*, 2008), and is associated with several clinical phenotypes including Mitochondrial Encephalomyopathy with Lactic Acidosis and Stroke-like episodes (MELAS), Chronic Progressive External Ophthalmoplegia (CPEO) and Maternally Inherited Deafness and Diabetes (MIDD) (Nesbitt and McFarland, 2011). Notably, MELAS, a mitochondrial disease that was first described clinically in 1984 (Pavlakis *et al.*, 1984), is caused by the m.3243A>G mutation in around 80% of cases. m.3243 A>G is an A>G transition at position 3243 of the *MT-TL1* gene, which encodes $tRNA^{Leu(URR)}$ (Goto *et al.*, 1990; Goto *et al.*, 1992) . A variety of mechanisms have been put forward to explain the pathogenic effect of the m.3243A>G mutation, including defects in transcription termination, tRNA processing and protein synthesis (Koga *et al.*, 2012). The replacement of the highly conserved A residue with G leads to structural alterations of the tRNA, including the absence of a taurine modification at the U 'wobble base' of the $tRNA^{Leu(URR)}$, causing errors in the recognition of UUA and UUG codons (Kirino *et al.*, 2004). This results in the misincorporation of amino acids during mitochondrial protein synthesis, particularly in the polypeptides CO III, CO II and ATP6; this disrupts the assembly of RC complexes I, IV and V (Sasarman *et al.*, 2008).

Clinically, MELAS features stroke-like episodes before age 40, encephalopathy (seizures, dementia or both), and ragged red fibres or lactic acidosis, which characteristically presents as nausea, vomiting and exercise intolerance (Hirano *et al.*, 1992). The age of onset is often during childhood (age 4-15 years), but cases with much later onset have been documented. MELAS features multiple infarct-like lesions in the occipital, parietal and temporal lobes of the cerebral cortex and in the cerebellar cortex (Tanahashi *et al.*, 2000), and Purkinje-cell loss in the cerebellum (Betts *et al.*, 2004). The high level of COX deficiency in the walls of blood vessels indicates a mitochondrial vascular involvement in the development of these lesions (Betts *et al.*, 2006; Lax *et al.*, 2012).

7.1.2 The m.8344A>G Mutation

The m.8344 A>G mutation results in a progressive and severe mitochondrial disease, usually beginning in childhood, but the age of onset varies even within the same family (Fukuhara, 1995). The m.8344 A>G mutation was first described in myoclonic epilepsy with ragged red fibres (MERRF), and indeed accounts for around 80% of MERRF cases, although there is some heterogeneity in the phenotype associated with this mutation (Mancuso *et al.*, 2013; Blakely *et al.*, 2014). The most common clinical presentation of disease associated with m.8344A>G is myoclonus however symptoms are heterogeneous and can be both neurological and non-neurological. Neurological characteristics include ataxia, generalised seizures, hearing loss, cognitive impairment, neuropathy, ptosis, opthalmoparesis, optic atrophy, tremor and migraine. Non-neurological symptoms include muscle weakness, multiple lipomatosis, exercise intolerance, cardiomyopathy, muscle wasting, respiratory impairment, diabetes and muscle pain (Mancuso *et al.*, 2013).

The m.8344 A>G mutation falls within the *MT-TK* gene, which encodes $tRNA^{Lys}$, and is associated with defects in OXPHOS complexes I and IV (Shoffner *et al.*, 1990). This mutation causes a change in position 55 of the TψC loop of $tRNA^{Lys}$, resulting in the absence of a taurine modification in the anticodon loop. This disrupts interactions of the $tRNA^{Lys}$ anticodon with codons (Yasukawa *et al.*, 2001), causing it to lose translational activity for both of its cognate codons (Yasukawa *et al.*, 2002).

The histological hallmark of m.8344A>G mutation is the ragged red fibres evident in muscle. In addition to this, COX-negative fibres are also present in the majority of cases (Mancuso *et al.*, 2013). In terms of neuropathology, m.8344A>G cases often display neuronal loss accompanied by astrogliosis in the dentate nucleus and regions of the cerebellar cortex. Neuronal loss is also observed in ascending sensory tracts of the spinal cord: in the DRG, Clarke's column, and in gracile and cuneate nuclei. Secondary demyelination is also observed in the superior cerebellar peduncle and posterior spinal column (Sparaco *et al.*, 1993). Furthermore, neurons of the dentate nucleus and inferior olivary nucleus demonstrate COXII depletion (Sparaco *et al.*, 1995). More recently, extensive neuronal loss has been demonstrated in olivary-cerebellum areas, accompanied by neuronal respiratory chain deficiencies, particularly of complex I. Furthermore, greater levels of respiratory chain deficiencies were observed in areas with more extensive cell loss (Lax *et al.*, 2012).

7.1.3 POLG mutations

As discussed in the introduction (section 1.62) the mitochondrial DNA Polymerase ɣ (POLɣ) carries out the replication of mtDNA, in association with the mitochondrial DNA helicase TWINKLE and mtSSB. In addition to ensuring the faithful replication of mtDNA, as the only mitochondrial DNA polymerase, POLɣ is also central to all forms of mtDNA damage repair (Longley *et al.*, 1998; Graziewicz *et al.*, 2006). Considering the central roles of POLɣ in mtDNA replication and repair, it is not surprising that mutations in the nuclear-encoded *POLG* gene result in changes in the copy number of mtDNA and secondary mtDNA mutations or deletions, resulting in a variety of mitochondrial disorders. The many mutations in the human *POLG* gene are outlined in Figure 7.1, and grouped according to their clinical presentation.

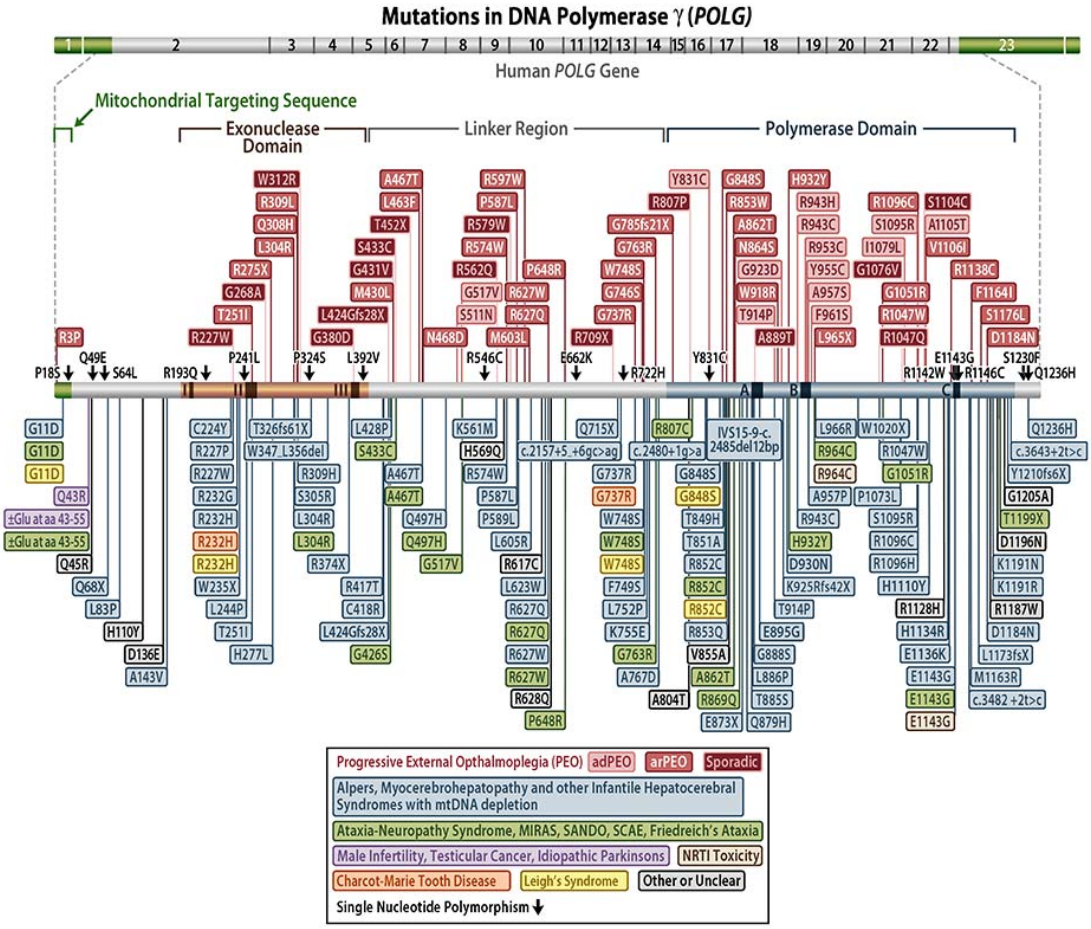

Figure 7.1: Mutations in *POLG*.
A comprehensive overview of the mutations in the human mitochondrial POLG gene, colour-coded according to their clinical presentations. Taken from http://tools.niehs.nih.gov/polg/

The major mitochondrial disorder resulting from *POLG* mutations is PEO (Progressive External Opthalmoplegia). PEO is usually transmitted in an autosomal dominant fashion,

although it can also be autosomal recessive or sporadic. Patients with autosomal dominant PEO were shown to have multiple large-scale deletions of mtDNA (Zeviani *et al.*, 1989); this observation led to the hypothesis that a nuclear gene was responsible for this mtDNA instability, which was later demonstrated to be *POLG.* The onset of PEO is relatively late for a mitochondrial disorder (18-40 years of age), and it is characterized by bilateral ptosis, blepharoptosis, opthalmoparesis and exercise intolerance (Graziewicz *et al.*, 2006).

Other mitochondrial disorders associated with *POLG* mutations include the early onset disease Alpers Syndrome, mitochondrial neurogastrointestinal encephalomyopathy (MNGIE), sensory ataxic neuropathy, dysarthria and opthalmoparesis (SANDO) and, interestingly, Parkinsonism (Graziewicz *et al.*, 2006).

7.1.4 Disruption of the UPS by Mitochondrial Dysfunction

A wide variety of neurological symptoms are well recognised in patients with mitochondrial disease (Hirano *et al.*, 1992; Graziewicz *et al.*, 2006; Mancuso *et al.*, 2013), and neurodegenerative changes are observed in the brains of mitochondrial disease patients (Sparaco *et al.*, 1993; Tanahashi *et al.*, 2000; Betts *et al.*, 2006; Lax *et al.*, 2012). However the pathological cascade leading from mtDNA mutations to neurodegeneration is not well characterised. Since disruption to the ubiquitin proteasome system is observed in many neurodegenerative disorders that also feature mitochondrial dysfunction, including Parkinson's and Alzheimer's diseases (Schapira, 2008; Cook and Petrucelli, 2009) (Moreira *et al.*, 2006; Ihara *et al.*, 2012), it is important to consider the role UPS impairment could play in mitochondrial disease.

Several studies have demonstrated a decline in the function of the UPS in response to mitochondrial respiratory chain dysfunction (Alemi *et al.*, 2007; Domingues *et al.*, 2008; Martins-Branco *et al.*, 2012). In both ρ0 cells (which have no mtDNA), and ρ+ cells treated with the Complex I inhibitor MPP^+ , a decrease of the chymotrypsin-like and PGPH –like activities of the 20S proteasome was observed, accompanied by an increase in ubiquitin conjugated proteins (Domingues *et al.*, 2008). A further study by this group also reported an increase in ubiquitinated protein content in *ndufa2* knockdown cells (indicating reduced UPS function), however this was accompanied by an increase in chymotrypsin-like activity of the 20S proteasome (Martins-Branco *et al.*, 2012). Another group showed that in patient cell lines and cybrids with 4.9kb or 7.5kb mtDNA deletions, the chymotrypsin activity of the 20S proteasome was decreased. Additionally,

in cells from KSS (Kearns-Sayre Syndrome) and CPEO (Chronic Progressive External Opthalmoplegia) patients, which harboured mtDNA deletions, there was a prominent inhibition of transcripts encoding ubiquitin-mediated proteasome activity (Alemi *et al.*, 2007). In addition, a more recent study has used a novel approach to demonstrate the stabilisation of a proteasome substrate upon RNAi depletion of components of the mitochondrial respiratory chain, and inhibition of mitochondrial fission and the mitochondrial unfolded protein response (Segref *et al.*, 2014). They also demonstrate reduced proteasome substrate degradation in cybrids from patients with a defect in COX1, and in cells derived from patients with isovaleric academia (IVA) (Segref *et al.*, 2014) (a metabolic disorder arising from a defect in a nuclear-encoded enzyme which acts in the mitochondrial matrix (Vockley and Ensenauer, 2006)), thus linking mitochondrial dysfunction to UPS activity in humans.

These studies together, hypothesize that mitochondrial respiratory dysfunction may cause a decline in the function of the ubiquitin proteasome system in the following ways. Firstly that increased levels of reactive oxygen species associated with mitochondrial dysfunction may inhibit the 20S proteasome (Domingues *et al.*, 2008), secondly that ATP deficiency resulting from OXPHOS defects would directly inhibit proteasome activity, since ATP is required for the assembly and function of the 26S proteasome (Martins-Branco *et al.*, 2012), and thirdly that the deletion of mitochondrial tRNA genes would decrease the rate of mitochondrial translation and increase protein misfolding and oxidative damage, which would increase levels of damaged, ubiquitinated proteins and inhibit proteasome function (Alemi *et al.*, 2007).

Although the studies above indicate that mitochondrial dysfunction may disrupt proteasomal degradation, this is yet to be demonstrated in tissue from patients with mitochondrial disease, and it is not clear how important UPS dysfunction is to the pathogenesis of mitochondrial disorders.

Adult onset neurodegenerative disorders invariably feature some form of protein aggregation, and often display inclusions containing ubiquitinated proteins or components of the UPS (Lowe *et al.*, 1990; Schlossmacher *et al.*, 2002; Huang and Figueiredo-Pereira, 2010). It is therefore striking that mitochondrial diseases do not feature protein aggregates or inclusions containing ubiquitinated proteins, despite their neurological involvement. Common neuropathological features of mitochondrial

disease include neuronal loss, necrosis, gliosis, demyelination and spongiform degeneration (Betts *et al.*, 2004), but not protein aggregation.

7.1.5 Aims of this Study

The aim of this chapter is to determine the effect of mitochondrial dysfunction on the ubiquitin proteasome system, by comparing levels of ubiquitin conjugated proteins and the function of the 20S proteasome in tissue homogenates from patients harbouring m.8344A>G, and m.3243A>G point mutations and *POLG* mutations, as compared to age-matched and aged controls. I hypothesize that proteasome function is impaired in patients with mitochondrial disease, causing an increase in ubiquitinated protein levels. This may be caused by the increase in levels of misfolded and oxidatively damaged proteins associated with translational errors that occur in mtDNA disease (Yasukawa *et al.*, 2002; Sasarman *et al.*, 2008), which are known to cause proteasome inhibition (Friguet and Szweda, 1997), or by ATP depletion caused by respiratory deficiencies in mitochondrial disease (Betts *et al.*, 2006; Lax *et al.*, 2012), since ATP is essential for the activation of ubiquitin and for the assembly and function of the 26S proteasome (Lam *et al.*, 2002; Bacik *et al.*, 2010; Kim *et al.*, 2013).

7.1.6 Methodological Approach

In order to assess whether ubiquitinated-conjugated proteins accumulate in mitochondrial disease, as a result of a declining ubiquitin proteasome system, frozen tissue samples were requested from cases with *POLG* mutations or mtDNA disease (m.8344 A>G and m.3243 A>G) along with age-matched controls and aged controls. Tissue samples were homogenized, and western blots were performed, to assess levels of ubiquitin, ubiquitin conjugates and to ascertain respiratory chain deficiency using mitochondrial complex I and porin, as described in Section 2.2.10.

Additionally, I have carried out a preliminary assay to measure the chymotrypsin-like, trypsin-like and PGPH/caspase-like activities of the 20S proteasome in each of these samples.

The 26S proteasome is responsible for the ATP-dependent degradation of ubiquitin-conjugated proteins, and this represents the major pathway for the normal turnover of proteins. However, assessment of the activities of the 26S proteasome requires addition of ATP, in order to allow the 19S regulatory particle to function (Powell *et al.*, 2007). Since I am assessing the effect of mitochondrial respiratory chain deficiency on proteasome function, it was not appropriate to add ATP, as this would confound results; therefore, I assessed the activity of the 20S proteasome.

The 20S core particle exists as a proteasome in its own right, but when flanked by two 19S regulatory particles, it is the central subunit of the 26S proteasome, in which proteolysis takes place. Proteolysis by the 20S proteasome is ATP-independent, and it is widely accepted that the 20S proteasome is responsible for the proteolysis of damaged and oxidised proteins (Grune *et al.*, 2004; Jung and Grune, 2008). The catalytic centre of the 20S proteasome is made up of two inner β rings, each of which has three catalytic subunits: β1, β2, β5. These subunits possess post-glutamyl peptide hydrolyzing (PGPH)/caspase-like, trypsin-like and chymotrypsin-like activity, respectively.

In order to directly assess the three catalytic activities of the 20S proteasome in mtDNA disease samples and controls, I utilised fluorogenic peptides, which are directed to each of the three catalytic subunits of the 20S proteasome. Each of these peptides is conjugated to AMC (7-amino-4-methylcoumarin), which becomes strongly fluorescent when cleaved from the peptide by the proteasome.

In order to distinguish the activity of the proteasome from background fluorescence, and cleavage of the fluorogenic peptides by other peptidases present, each sample was also incubated with a proteasome inhibitor, either MG132 or lactacystin.

7.1.6.1 Details of Samples

The details of the cases that were initially assessed by western blotting are displayed in Table 7.1. All tissue was taken from the grey matter of the occipito-parietal cortex, as this region of the brain is frequently involved in mtDNA disease (Tanahashi *et al.*, 2000). This tissue was obtained from the Newcastle Brain Tissue Resource (NBTR), as stated in section 2.2.7.2.

Case ID	**Condition**	**Age (years)**	**Sex**	**Post-Mortem delay (hours)**
1983-0347	Control	50	Male	7
1990-0172	Control	40	Female	3
1995-0147	Control	47	Male	15
2006-0082	m.8344A>G	42	Female	59
2011-0065	m.8344A>G	58	Male	66
2011-0224	POLG	55	Male	112
2011-E648	Aged Control	89	Female	98
2011-1131	Aged Control	86	Female	45
2012-0269	Aged Control	87	Female	77

Table 7.1: Details of cases initially assessed by western blotting.
NB: case 2011-0224 – p. Trp748Ser, p. Arg1096Cys.

Due to equivocal results from the samples in Table 7.1, further POLG, mtDNA disease and control samples were requested from the NBTR. The details of these cases are given in Table 7.2. These samples were also taken from the grey matter of the occipito-parietal cortex.

Case ID	Condition	Age (years)	Sex	Post-Mortem delay (hours)
1983-0305	Control	56	Female	36
1996-0152	Control	51	Male	16
1997-0039	Control	53	Male	19
2006-0081	Control	58	Female	39
2008-0005	Control	59	Female	19
2009-0118	Control	55	Male	41
2004-0067	m.3243A>G	59	Female	10
2003-0144	m.3243A>G	36	Female	42
2008-0038	m.3243A>G	30	Male	69
2009-0061	m.3243A>G	20	Female	187
2005-0110	POLG	59	Male	67
2001-0017	POLG	24	Female	83

Table 7.2: Details of MtDNA disease and POLG cases and controls.
NB: Case 2005-0110 – p.Gly848Ser, p.Ser1104Cys, Case 2001-0017 – p.Ala467Thr, Trp748Ser.

7.2 Results

7.2.1 Validation of Western Blotting Assay

In order to assess the validity of western blotting for detecting changes in protein levels, sequentially increasing amounts of protein were loaded on to gels, and membranes were blotted using ubiquitin, α-tubulin, Porin and CI-20 antibodies. Figures 1 and 2 demonstrate the sensitivity of the assay for assessing changes in ubiquitin conjugates, mitochondrial mass (Porin), Complex I and monomeric ubiquitin. They also demonstrate that the α-tubulin loading control reflects the amount of protein loaded on the gel. Figure 7.2 also demonstrates that although Porin is closer in molecular weight to the ubiquitin monomer, α-tubulin is a more suitable loading control for these transfer conditions.

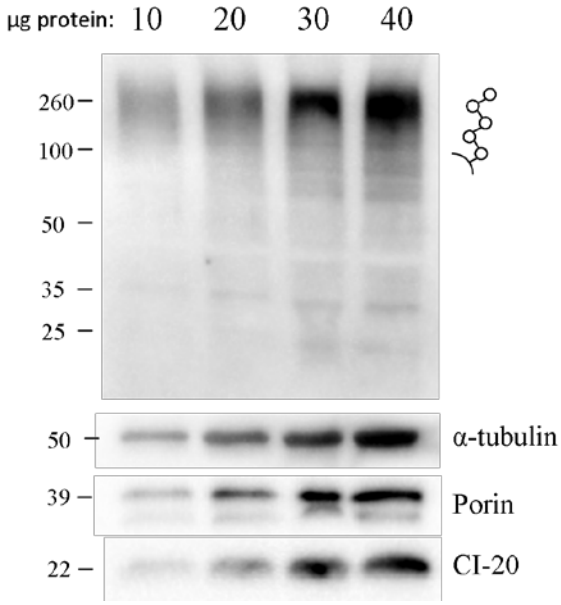

Figure 7.3: Western Blot demonstrating the sensitivity of the assay to changes in levels of ubiquitinated proteins, porin and Complex I-20. Each lane contains 10, 20, 30 and 40µg total protein, respectively.

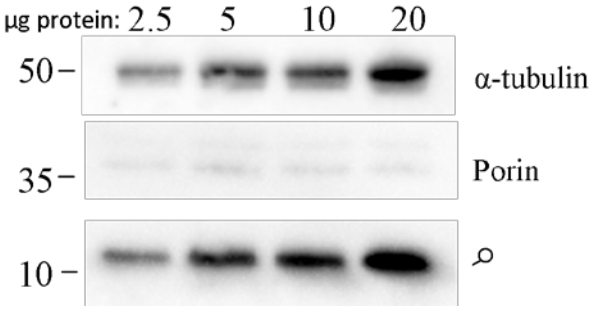

Figure 7.2: Western Blot demonstrating changes in ubiquitin band intensity according to the level of protein loaded in each lane. α - tubulin is a suitable loading control, whereas the porin antibody is not sensitive enough for these levels of protein.

7.2.2 mtDNA disease, Age-Matched and Aged Controls

Three repeats of western blots were carried out to compare levels of monoubiquitin, ubiquitin conjugates and to assess levels of mitochondrial Complex I in relation to Porin, in control and mtDNA disease samples (Figure 7.4). Samples were loaded onto the gel in the order that they are listed in Table 7.1 .

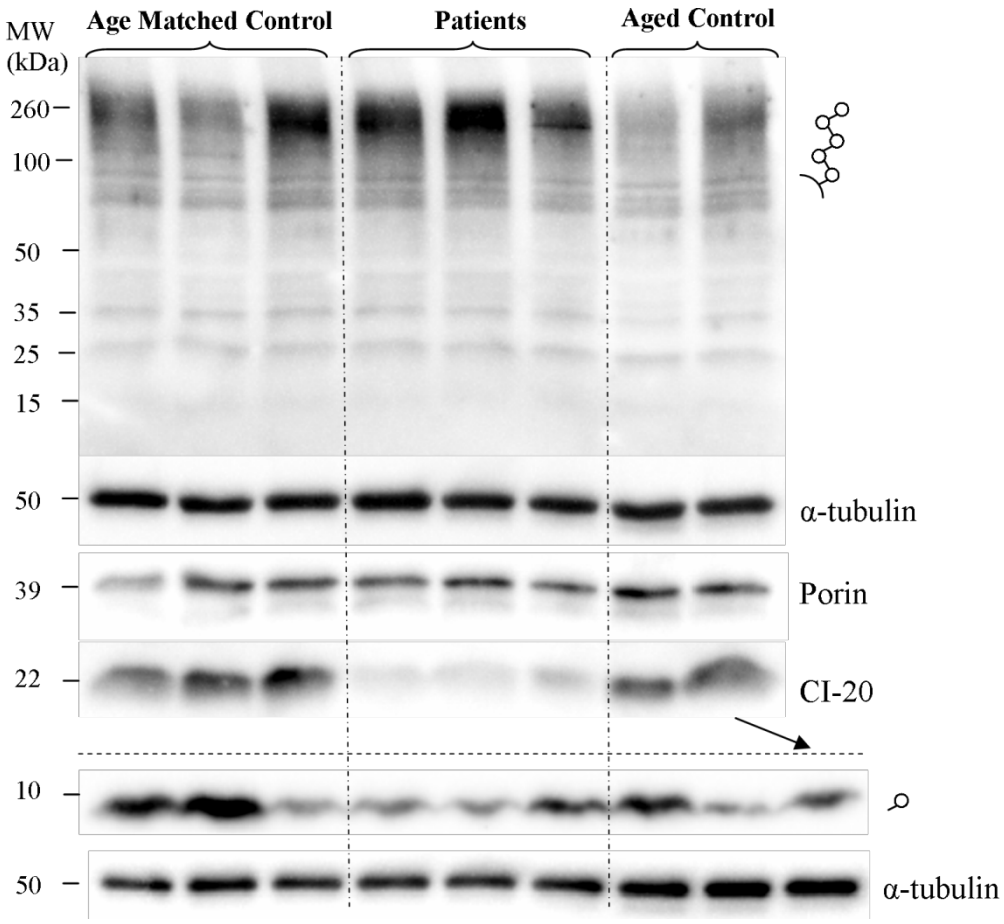

Figure 7.4: Western Blots of ubiquitin conjugates and mitochondrial proteins (top), and ubiquitin monomer (bottom). Top blot: Lanes 1-3: Aged matched controls (age 50, 40, 47); Lane 4-5: m.8344 A>G (age 42, 58); Lane 6: POLG, age 55; Lane 7-8: Aged controls (age 89, 87). Bottom blot: Lane 9 corresponds to lane 8 of the top blot (indicated by arrow), and lane 8 is another aged control, age 86. This blot is representative of three repeats.

7.2.2.1 Levels of Ubiquitin in mtDNA Disease and Control Samples

From these western blots, it is difficult to determine whether patients with mtDNA disease experience an increase in the levels of ubiquitin conjugates. In two of the mtDNA disease cases (lanes 4&5, both m.8344A>G MERRF, there are high levels of ubiquitin conjugates, but low levels of ubiquitin monomer. This could perhaps indicate decreased proteasome efficiency leading to a build up of ubiquitinated proteins, and therefore depletion of monomeric ubiquitin, which would fit with my hypothesis. However, this is also seen (almost identically) in one of the control cases (lane 3, age

47). Interestingly, in samples where there are high levels of ubiquitin conjugated proteins, monoubiquitin levels are low, and vice versa.

Compared to the controls in lanes 1 and 2, the POLG case (lane 6), could be considered to have a slight increase in ubiquitinated protein conjugates and a slight decrease in monomeric ubiquitin, but this is not true when comparing to the control in lane 3.

Furthermore, the aged controls (which were expected to show an increase in ubiquitinated protein conjugates) have similar levels of monoubiquitin and ubiquitinated proteins as the controls in lanes 1 and 2. This is in disagreement with literature showing increased levels of ubiquitin conjugates with age (Ohtsuka *et al.*, 1995; Gray *et al.*, 2003). Quantification of levels of monoubiquitin and ubiquitin conjugates for each sample over three repeats is shown in Figure 7.5A. Results are reflective of Figure 7.4, indicating that results for western blotting were consistent over three repeats, but do not show the increases in ubiquitin conjugates expected in mtDNA disease and ageing. Figure 7.5B and C show these results summarised for each group: control, mtDNA disease and aged. These results demonstrate that there is no significant difference in levels of monoubiquitin or ubiquitin conjugates between groups ($p=0.4258$, $p=0.2461$, respectively)

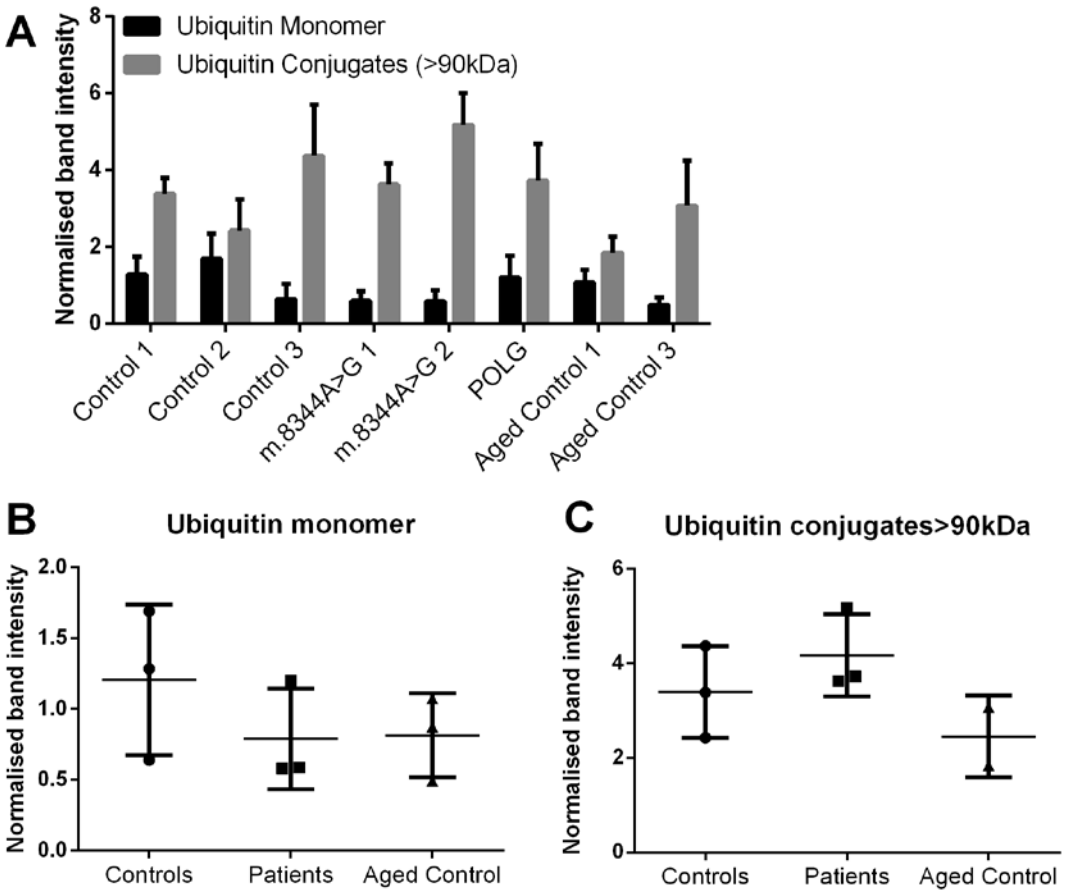

Figure 7.5: Quantification of band intensity.
A) Intensity of ubiquitin monomer band and ubiquitin conjugates larger than 90kDa, normalised to α-tubulin loading control. Bars represent mean + SD of three repeats. B, C) Data points represent the mean band intensity, normalised to α-tubulin (loading control) band intensity for three repeats of western blots. Bars show the mean and standard deviation of 3 samples (2 samples for the aged control in C). B) No significant differences in monoubiquitin levels between age- matched controls and patient or aged control samples; ordinary one way ANOVA with Dunnett's multiple comparisons, p=0.4258. C) No significant differences between levels of ubiquitin conjugates more than 90kDa between age- matched controls and patient or aged control samples; ordinary one way ANOVA with Dunnett's multiple comparisons, p=0.2461

7.2.2.2 Complex I Deficiency in mtDNA Disease

Figure 7.4 clearly demonstrates that Complex I levels are greatly decreased in m.8344 A>G and POLG samples, as compared to both age-matched and aged controls. It is clear that mitochondria are Complex I deficient, since levels of the mitochondrial mass marker, porin, remain normal and are comparable to both sets of controls. This has been quantified for all three repeats using Image J (NIH), and results are shown in Figure 7.6. Figure 7.6A demonstrates that results are relatively consistent across all repeats (apart from Control 1), and the reduction in CI-20 relative to Porin is repeated in all three repeats for the three mtDNA disease samples. Since no reduction in Complex I relative to Porin was demonstrated in the aged controls, Figure 7.6B groups age-matched and aged controls. An unpaired t-test shows that the reduction in Complex I-20 relative to Porin is significant for POLG and m.8344 A>G samples compared to all controls

(p=0.0008, n=5, 3). Figure 7.6 demonstrates that this decrease is also significant when compared just to the age-matched controls (p=0.0031).

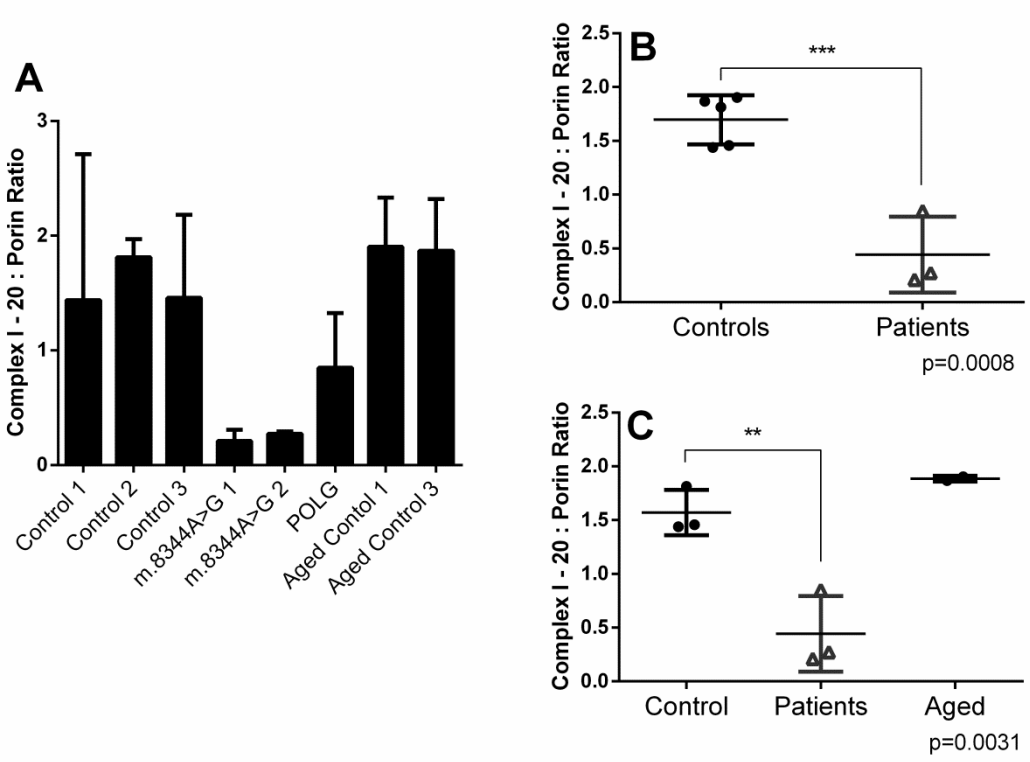

Figure 7.6: Complex I deficiency in m.8344 A>G and POLG tissue homogenates.
A) Ratio of Complex I-20 and Porin Band intensities for each sample. Bars represent mean + SD. B) Significant decrease in Complex1-20: Porin ratio between all controls and mtDNA disease samples (unpaired t-test, p=0.0008, n=5,3, α=5%). C) Significant decrease in Complex I-20: Porin Ratio in MtDNA disease samples compared to age-matched controls. Ordinary One Way ANOVA, p=0.0031 with Dunnett's multiple comparisons test: Control vs. mtDNA disease, significant (**), Control vs. Aged Control, not significant.

7.2.3 POLG and Age Matched Controls

Since initial findings on the levels of monoubiquitin and ubiquitin conjugates in mtDNA diseases samples were ambiguous, samples were requested from further mtDNA disease cases and age-matched controls. Since findings were quite different for m.8344 A>G and POLG cases, POLG and m.3243 A>G cases were requested and assessed separately, in case levels of ubiquitination were affected differently in these two conditions. Unfortunately, there were no further m.8344 A>G cases available.

Figure 7.7 shows a western blot of three POLG samples, and controls that were as closely age matched as possible. Samples (detailed in Table 7.1 and Table 7.2) were loaded onto the gel in the following order (lanes 1-6): 1990-0172, 1983-0305, 1997-0039, 2011-0224, 2005-0110, 2001-0017.

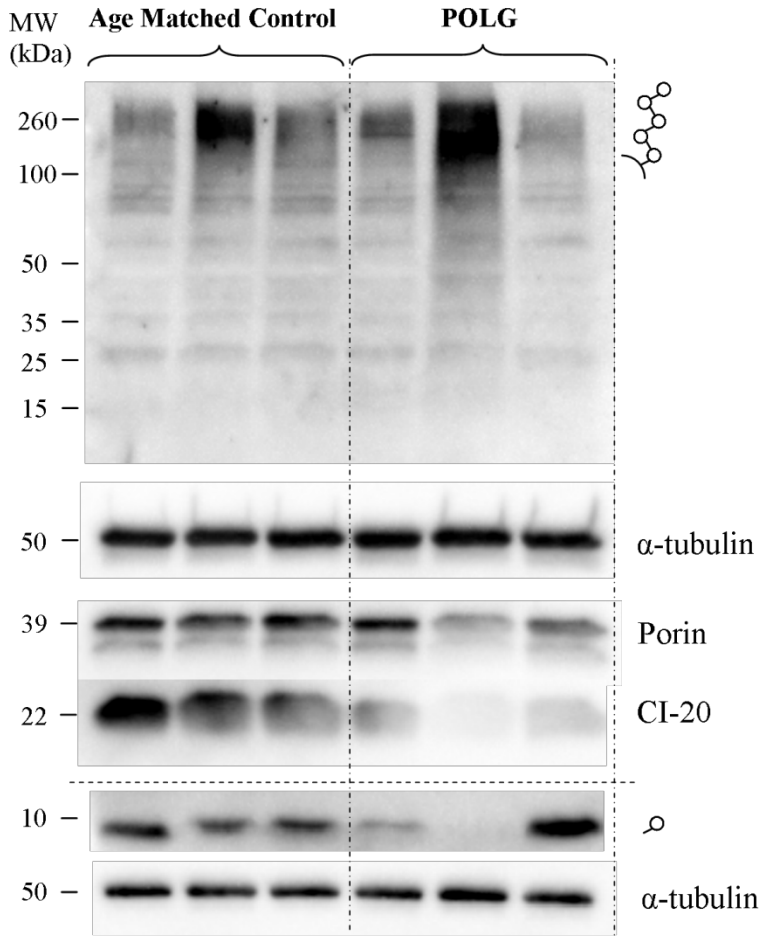

Figure 7.7: Western Blots of ubiquitin conjugates and mitochondrial proteins and the ubiquitin monomer. Top, representative of 2 repeats; bottom, representative of 3 repeats. Lanes 1-3: Aged matched controls (age 50, 56, 53); Lane 4-6: POLG, age 55, 59, 24.

Figure 7.7 does not demonstrate a consistent increase in levels of ubiquitin conjugates in patients with a POLG mutation, compared to controls. Results show that whilst one POLG patient has high levels of ubiquitin conjugates and decreased monomeric ubiquitin, this is also true of one of the control samples. Therefore I am not able to conclude whether POLG patients have increased levels of ubiquitin conjugated protein. Results do, however, show that POLG samples have consistently decreased levels of CI-20 compared to controls. Mitochondrial mass remains relatively constant for POLG samples (apart from a slight reduction in the penultimate lane), therefore we can conclude that POLG patients have Complex I deficient mitochondria.

7.2.4 m.3243 A>G and Age Matched Control Samples

Since no further m.8344 A>G cases were available, I requested frozen tissue samples from four m.3243 A>G cases, and controls that were age-matched as closely as possible. These were run along with case 1990-0172 (Table 7.1), which was kept constant for all three western blots. All other cases are detailed in Table 7.2, and were loaded in the following order (lanes 2-10): 1996-0152, 2006-0081, 2008-0005, 2009-0118, 2004-0067, 2003-0144, 2008-0038, 2009-0061.

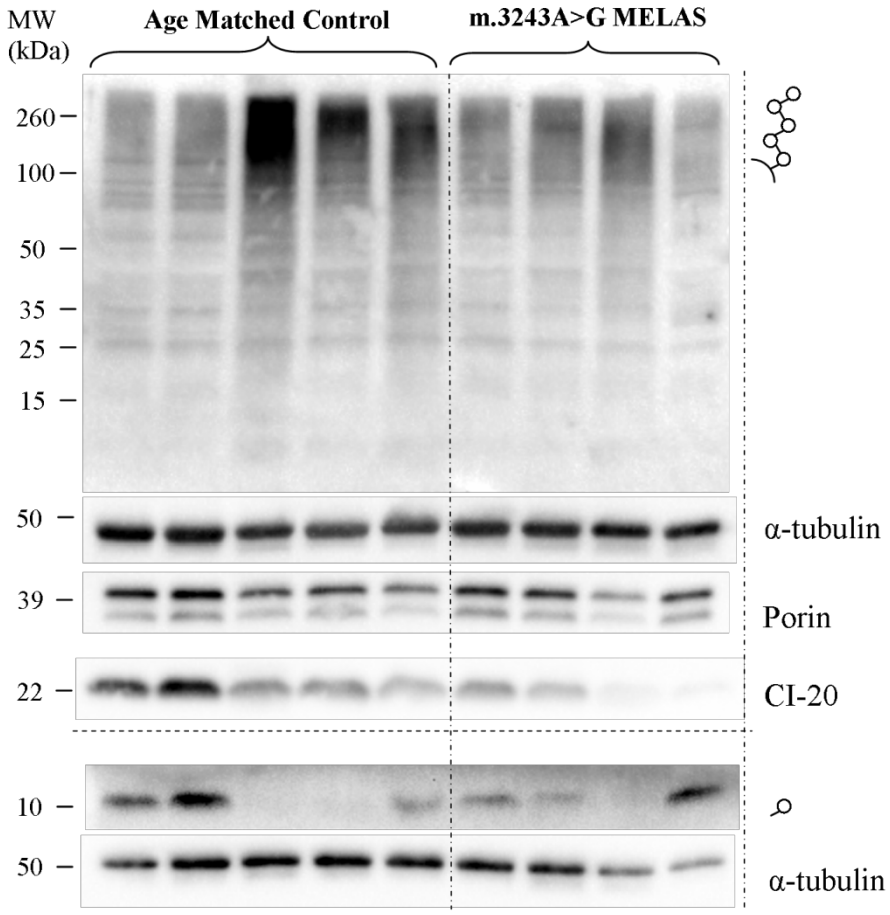

Figure 7.8: Western Blots of ubiquitin conjugates and mitochondrial proteins and ubiquitin monomer.
Top, representative of 3 repeats; bottom, representative of 2 repeats. Lanes 1-3: Aged matched controls (age 40, 51, 58, 59, 55); Lane 4-6: M.3243 A>G cases (age 59, 36, 30, 59).

The ubiquitin conjugates blot in Figure 7.8 does not give any indication that ubiquitin conjugated proteins accumulate in m.3243 A>G samples. High molecular weight ubiquitin conjugate bands are not as intense as several of the controls. In general, those samples with high levels of ubiquitin conjugated proteins have very little monomeric ubiquitin (lanes 3-5, 9). However, there is no consistent relationship between the severity of Complex I deficiency and levels of ubiquitin conjugated proteins. Therefore, it is not possible to draw any conclusions as to the effect of mtDNA disease on the function of the ubiquitin proteasome system from these results, due to the variability

that was seen amongst controls for unknown reasons, which I will address in the discussion.

Figure 7.8 does however demonstrate Complex I deficiency in m.3243 A>G samples; levels of CI-20 bands have noticeably reduced intensity, whilst Porin bands remain constant. It may also be noted that the controls in lanes 3, 4 and 5 have decreased levels of ComplexI-20. Complex I deficiency has previously been observed in these control cases using an alternative method (Dr N. Lax, personal communication), therefore it can be considered genuine, however the reason for this is unknown.

7.2.5 Assay for 20S Proteasome Activity: Optimisation

My protocol for the assessment of the three catalytic activities of the 20S proteasome relies on the experience of the literature (Powell *et al.*, 2007; Domingues *et al.*, 2008; Lima and Rattan, 2010; Martins-Branco *et al.*, 2012), however I determined the ideal concentrations of the fluorogenic substrates, type of proteasome inhibitor and amount of sample for each assay experimentally. Since the availability of human tissue for optimisation work is limited, and human samples for this experiment were limited in terms of protein concentration, this assay was initially optimised using frozen mouse brain tissue, homogenised using the same buffer as the human samples.

7.2.5.1 Chymotrypsin-like Activity: Suc-LLVY-AMC

In order to assess the chymotrypsin-like activity of the proteasome, the fluorogenic substrate Suc-LLVY-AMC was used. Suc-LLVY-AMC is specifically broken down by the chymotrypsin-like activity of the 20S proteasome, producing free AMC, which is strongly fluorescent, with 380nm excitation and 460nm emission wavelengths. In order to determine a suitable concentration of Suc-LLVY-AMC for this assay, three concentrations were trialled, based on concentrations previously used in the literature (Alemi *et al.*, 2007; Martins-Branco *et al.*, 2012). 10μM lactacystin was used to inhibit the chymotrypsin-like activity of the 20S proteasome; this has previously been shown to be effective (Andersson *et al.*, 1999). This assay was carried out using 10, 30 and 50μg total protein in order to determine the amount of protein required to effectively assess chymotrypsin-like activity. Results are displayed in Figure 7.9. From these results, 50μM was taken to be a sufficient concentration of Suc-LLVY-AMC. Results also indicate that 30μg total protein is required to give a good indication of the chymotrypsin-like activity of the proteasome.

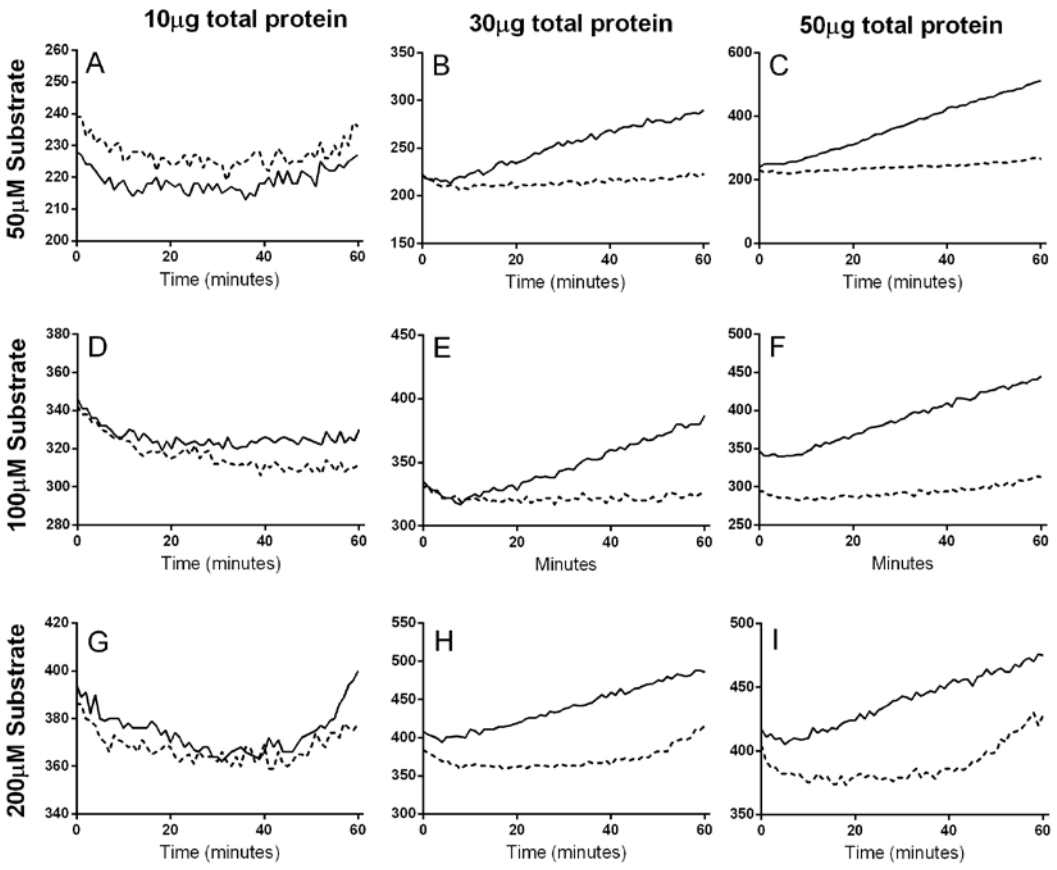

Figure 7.9: Optimisation of Chymotrypsin Assay.
Concentration of 20S substrate Suc-LLVY-AMC (μM), indicated by row titles. Amount of total protein (μg) indicated by column titles. Dashed lines indicate wells to which 10μM lactacystin has been added. The Y axis indicates fluorescence (AU).

7.2.5.2 Trypsin – like activity: Boc-LRR-AMC

The trypsin-like activity of the 20S proteasome was measured using the fluorogenic peptide Boc-LRR-AMC, which is broken down specifically by the β2 trypsin-like catalytic subunit to produce the strongly fluorescent molecule AMC. Since early experiments indicated that 10μg total protein is sufficient to breakdown Boc-LRR-AMC, causing a linear increase in fluorescence, assays using 10μg total protein were used to determine a suitable concentration of Boc-LRR-AMC, and to select the best inhibitor of β2 catalytic activity. Whilst lactacystin inhibits the chymotrypsin-like activity of the 20S β5 subunit sufficiently, it is not effective for the inhibition of the trypsin-like activity of the β2 catalytic subunit (Andersson *et al.*, 1999). Therefore, I also ran the assay using MG132, a peptide aldehyde inhibitor which potently inhibits the 20S core at 35μM (Lima and Rattan, 2010). Results demonstrate that 35μM MG132 is a more effective inhibitor or 20S trypsin-like activity than 10μM lactacystin, and that 50μM Boc-LRR-AMC is sufficient (Figure 7.10A).

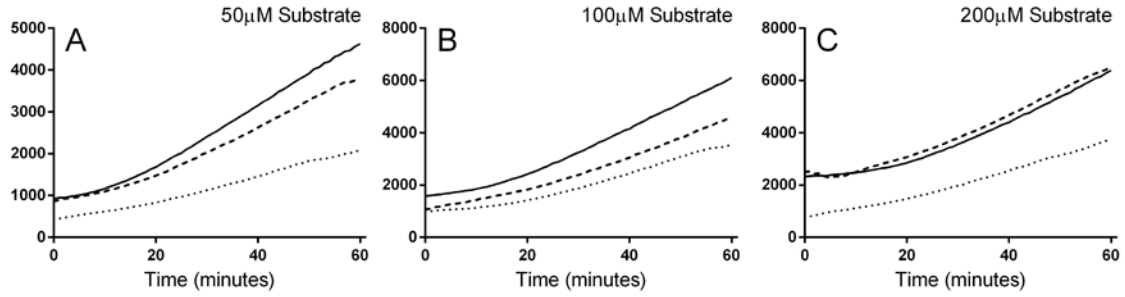

Figure 7.10: Optimisation of the Trypsin-like activity assay.
Each assay uses 10μg total protein from a mouse brain sample. Concentration of 20S substrate Boc-LRR-AMC (μM), indicated in the top right of each graph. Dashed lines indicate wells to which 10μM lactacystin has been added, dotted lines indicate wells with 35μM MG132. The Y axis indicates fluorescence (AU).

7.2.5.3 PGPH activity: Z-LLE-AMC

The fluorogenic peptide Z-LLE-AMC was used to assay the PGPH activity of the 20S proteasome, which is catalysed by the β1 subunit. Similarly to the trypsin-like assay, lactacystin is not effective at inhibiting the activity of the β1 subunit, therefore I tested both lactacystin and 35μM MG132 as proteasome inhibitors. Results demonstrate that lactacystin does not inhibit the PGPH activity of the proteasome, but that 35μM MG132 is an effective proteasome inhibitor (Figure 7.11). From these results, I also determined that the optimal concentration of Z-LLE-AMC for this assay is 100μM, and that 30μg protein is sufficient to measure the PGPH activity for the 20S proteasome.

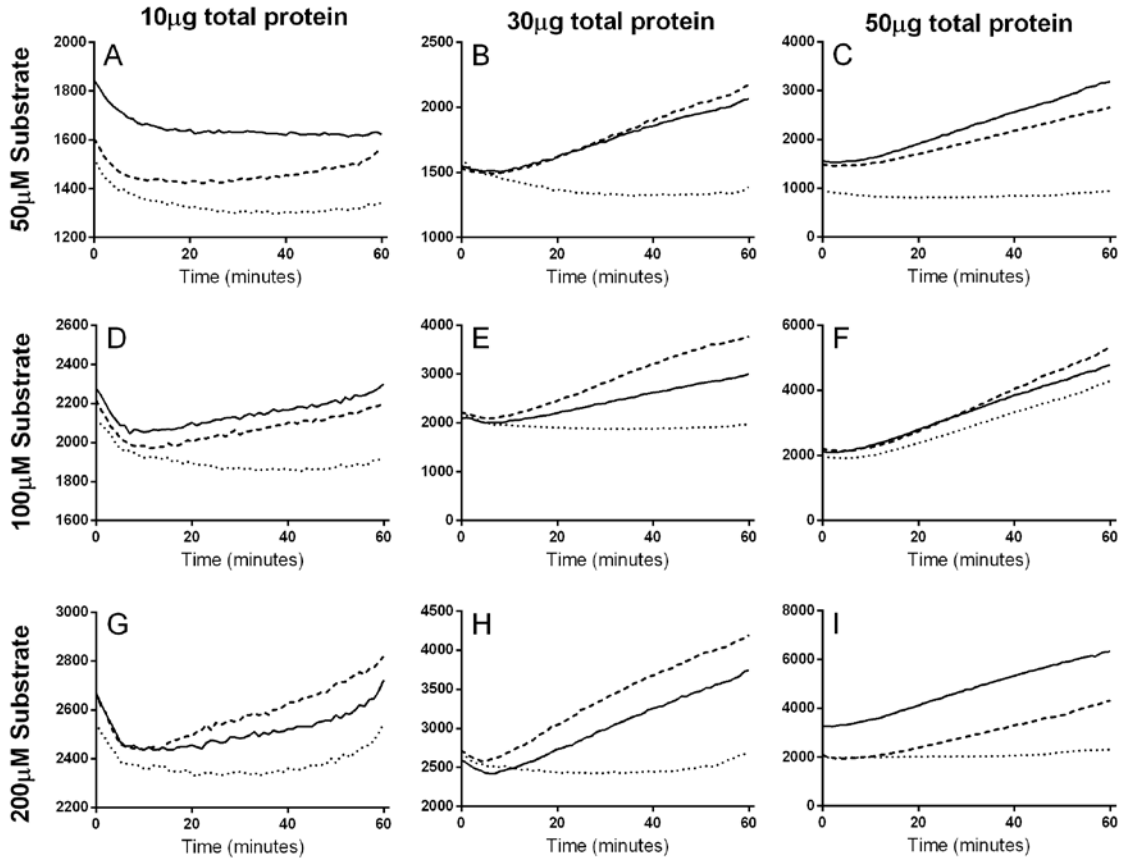

Figure 7.11: Optimisation of PGPH activity assay.
Concentration of 20S substrate Z-LLE-AMC (μM), indicated by row titles. Amount of total protein (μg) indicated by column titles. Dashed lines indicate wells to which 10μM lactacystin has been added, dotted lines indicate wells with 35μM MG132. The Y axis indicates fluorescence (AU).

7.2.6 Preliminary Results: 20S Chymotrypsin-like Activity

Assays for the three catalytic activities of the 20S proteasome were carried out as described in the methods section, for all of the samples detailed in Table 7.1 and Table 7.2, apart from the aged controls. Results of the Bradford assay indicated that the protein concentration of samples 2006-0082 and 2011-0065 (both M.8344 A>G) were not high enough to perform this assay, and that the protein concentration of sample 2008-0005 (Control) was not high enough for assays of PGPH and chymotrypsin-like activities, since they require 30μg protein/well, therefore these samples were not included.

The chymotrypsin -like activity of the 20S proteasome was successfully measured in 5 Control samples and 3 POLG samples (shown in Figure 7.12A-H). In these assays, fluorescence increases in a linear fashion, and samples which have been incubated with lactacystin do not demonstrate an increase in fluorescence with time. The rate at which the proteasome breaks down the fluorogenic substrate was calculated by subtracting the background activity (fluorescence/time with lactacystin) was from the total activity (fluorescence/time without lactacystin). This data is summarised in Figure 7.12I, and demonstrates that there is no difference in the chymotrypsin-like activity of the proteasome between samples from controls, and samples from patients with *POLG* mutations (p=0.8774).

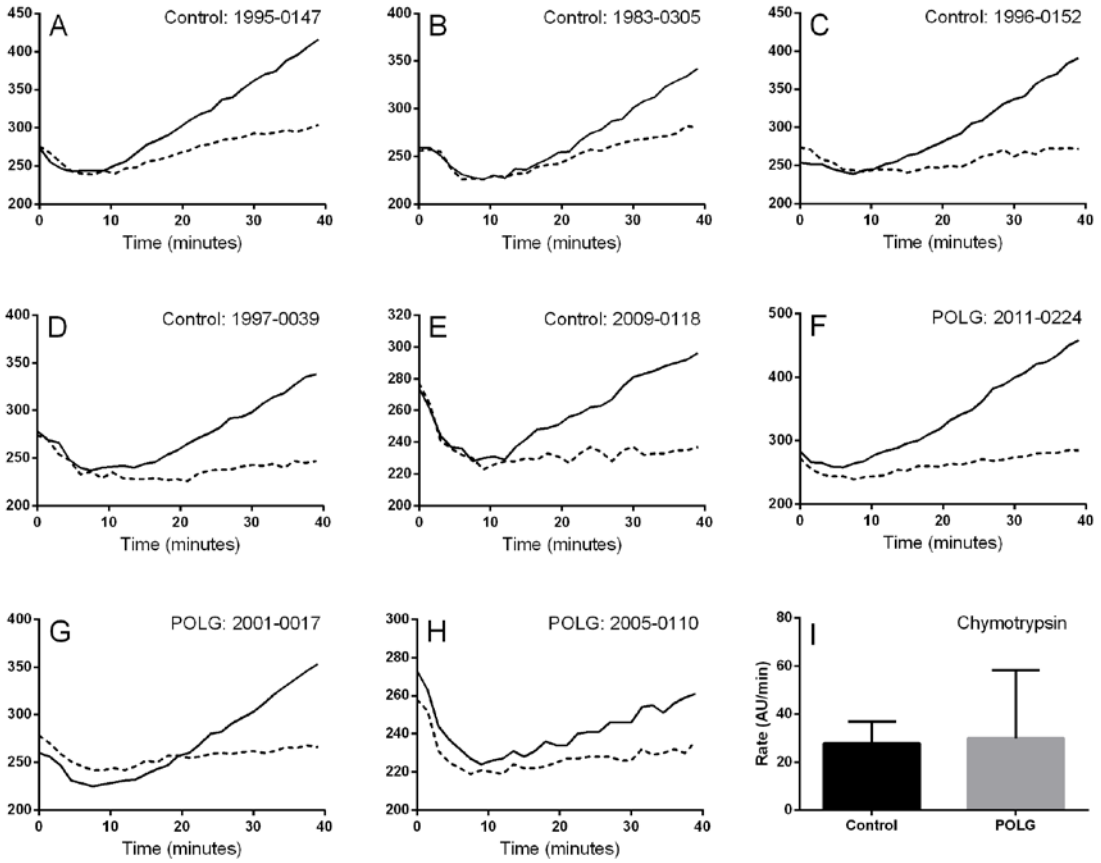

Figure 7.12: Chymotrypsin Activity of the 20S proteasome.
A-H) Graphs showing the increase of fluorescence intensity (Y axis, AU), with time (minutes) produced by chymotrypsin-like proteasomal degradation of the substrate Suc-LLVY-AMC in 5 control (A-E) and 3 POLG (F-H) samples. Dashed lines indicate wells containing 10μM lactacystin. I) Chymotrypsin-like proteasome activity (between 10 and 40 minutes) is calculated as activity measured without lactacystin (Fluorescence (AU)/min) – activity measured with lactacystin (Fluorescence (AU)/min). Bars represent the mean and standard deviation of 5 control and 3 POLG samples. No significant difference between means, unpaired t-test, p=0.8774, n=5 (Control), n=3 (POLG)

Assays for chymotrypsin activity in the remaining samples indicated that protein concentrations were not sufficient for accurate measurements of proteasomal activity; when fluorescence intensity is plotted against time, lines are jagged, and levels of fluorescence in the wells with lactacystin are often not distinguishable from those without. These graphs show a lot of similarities to Figure 7.9A, D and E. These graphs display optimisation runs in which only 10μg total protein was added to each well. Therefore, I can conclude that the 20S proteasome is less active in grey matter from the occipito-parietal region of the human brain than it is in mouse brain, which was used to optimise these assays. For these samples, therefore, 30μg total protein is not sufficient to reliably measure the chymotrypsin-like activity of the 20S proteasome.

7.2.7 Preliminary Results: 20S Trypsin-like and PGPH Activity

Similarly to the assay for 20S chymotrypsin-like activity, several samples did not have sufficient protein levels to accurately measure trypsin-like and PGPH-like activities of the 20S proteasome. The trypsin-like activity of the 20S proteasome was, however successfully measured in two control samples, two samples from patients with *POLG* mutations, and one from a m.3243 A>G patient. These preliminary results indicate that there is no difference in the trypsin activity of the 20S proteasome between Control and Patient samples (p=0.9670, unpaired t-test). The PGPH activity of the 20S proteasome was successfully measured in four samples (Figure 7.13), however since these were all control samples, it is not possible to comment on PGPH activity in mtDNA disease or POLG patients.

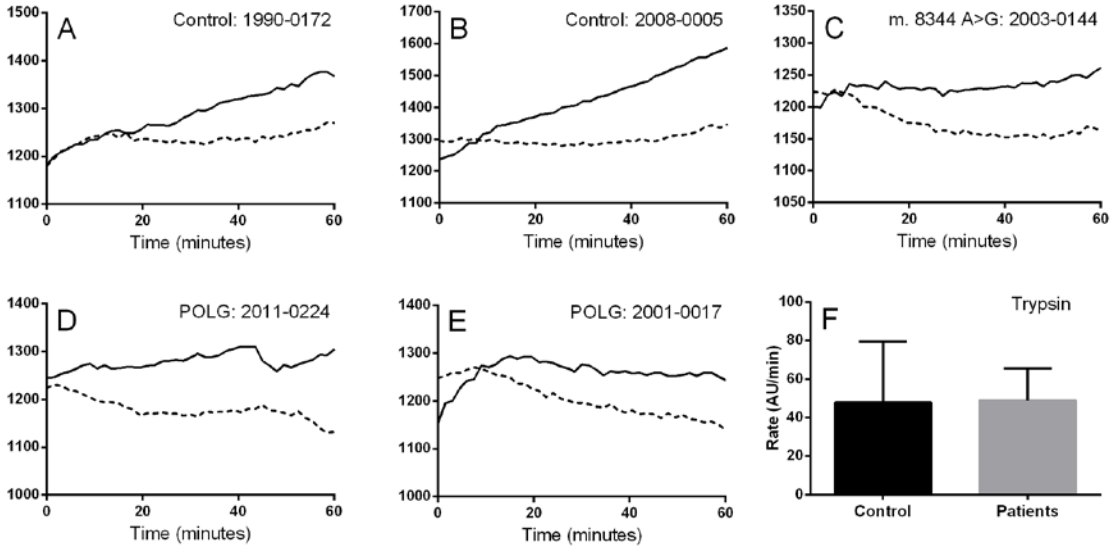

Figure 7.13: Trypsin-like activity of the 20S Proteasome.
A-E) Degradation of the substrate Boc-LRR-AMC by the trypsin-like activity of the 20S proteasome, Y-axis shows fluorescence intensity (AU). Dashed lines indicate wells containing 35μM MG132. F) Trypsin-like proteasome activity is calculated as activity measured without MG132 (Fluorescence (AU)/min) – activity measured with MG132 (Fluorescence (AU)/min). No significant difference in means: unpaired t-test, p=0.9670, n=2 (Control), n=3 (Patients). Bars represent the mean and SD.

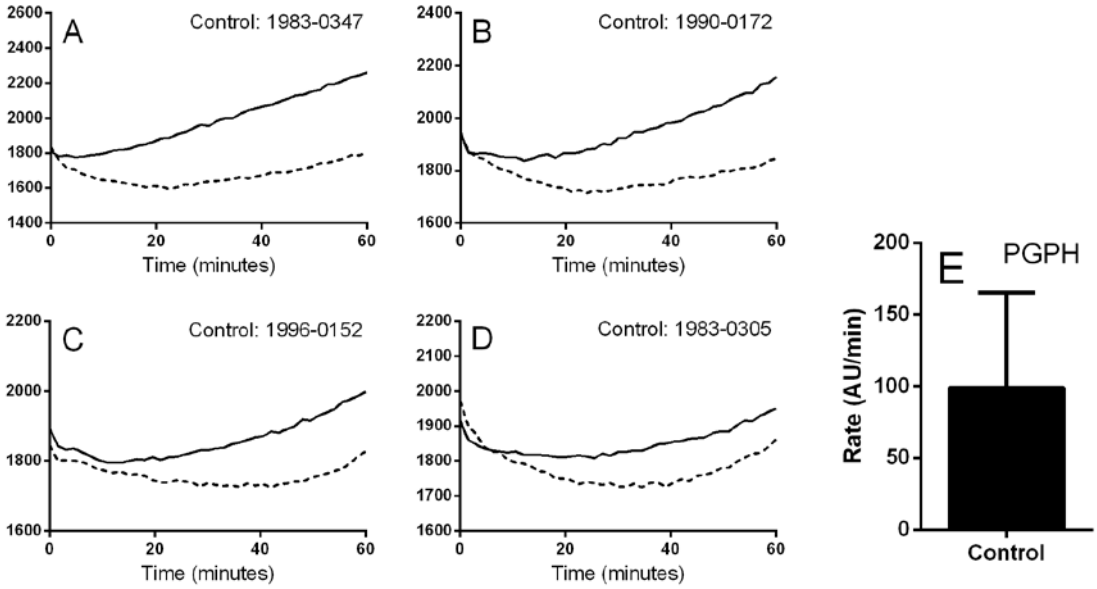

Figure 7.14: PGPH activity of the 20S Proteasome.
A-D) Degradation of the substrate Z-LLE-AMC by the PGPH activity of the 20S proteasome, Y-axis shows fluorescence intensity (AU). Dashed lines indicate wells containing 35μM MG132. E) PGPH proteasome activity is calculated as activity measured without MG132 (Fluorescence (AU)/min) – activity measured with MG132 (Fluorescence (AU)/min). Bars represent the mean and SD for 4 control cases.

7.3 Discussion

7.3.1 Ubiquitin-conjugated proteins

With the number of mtDNA disease patients and controls available to me, and the variability in levels of ubiquitin conjugates seen, it is not possible to draw conclusions as to the effect of mitochondrial disease and associated respiratory chain deficiency on the ubiquitin proteasome system. The variations in the levels of monomeric ubiquitin and ubiquitin conjugates amongst controls and mitochondrial disease samples alike may be due to a variety of factors, such as age, length of the post-mortem delay, cause of death, and inherent differences between unrelated cases.

The same method was also used to assay levels of monomeric ubiquitin and polyubiquitin conjugates in UCHL1 knockout mice (Section 4.2.2). In that case, ubiquitin profiles were very consistent between several wild type mice and between several knockout mice. In that case, mice were littermates from a homogenous genetic background, whereas here the relationship between cases is not known, however they are likely to be from a broad heterogeneous genetic background. The successful use of this assay previously (Section 4.2.2) demonstrates that the methods used are reliable, and may indicate that there may be inherent differences between unrelated cases. However, several studies have successfully assessed ubiquitin and ubiquitin conjugate levels by western blot in human post mortem samples with consistent results (Ali-Khan *et al.*, 1992; Fraile *et al.*, 1996; Rabuel *et al.*, 2010), therefore this variability was not to be anticipated.

It is possible that such wide variations in the state of ubiquitin conjugation amongst samples may occur because of the way the tissue is processed after death; mouse tissue, which gave consistent results, was always frozen over liquid nitrogen immediately after dissection, however this is not true for human samples, and there was frequently a delay of several hours before the post-mortem took place. In this time delay, it is possible that autolysis was taking place, causing ubiquitin conjugates and ubiquitin conjugated proteins to be broken down; however we do not observe any correlation between the length of post-mortem delay and the proportion of ubiquitin present as a monomer. The age for each of our samples is known, and there is no apparent correlation with ubiquitin conjugate levels.

Western blots successfully detected complex I deficiency in mitochondrial disease samples; in general, Complex I-20 was depleted, whilst Porin levels were normal.

Results demonstrated that in cases where monoubiquitin pools were depleted, levels of ubiquitin conjugated proteins were high and vice versa. The pools of ubiquitin in cells shift from being maintained as monoubiquitin, to being conjugated to proteins or in polyubiquitin chains (high MW).

7.3.2 20S Proteasome Activity Assay

Preliminary results from the assay of the activity of the 20S proteasome indicate that there is no difference in chymotrypsin activity of the 20S proteasome between control and POLG patients and no difference in the trypsin activity of the proteasome between control and POLG and m.3243 A>G patients.

Whilst this finding conflicts with recent studies linking mitochondrial dysfunction to proteasome activity (Alemi *et al.*, 2007; Domingues *et al.*, 2008; Segref *et al.*, 2014), it is perhaps not surprising that mitochondrial disease patients appear to have normally functioning 20S proteasomes. As mentioned earlier, mitochondrial diseases are distinctive amongst neurological disorders for not featuring inclusions containing ubiquitinated and damaged proteins (Betts *et al.*, 2004; Huang and Figueiredo-Pereira, 2010). Therefore, these findings indicate that the ubiquitin proteasome system does not have a prominent role in the pathogenesis of mitochondrial diseases.

7.3.3 Future Work

Due to the limited availability of human tissue for the optimisation of the 20S proteasome assay, a homogenised mouse brain was used to optimise the assay, and determined that total protein concentrations of 30µg, 10µg and 30µg would be sufficient to accurately measure chymotrypsin-like, trypsin-like and PGPH activities of the 20S proteasome, respectively. However, results of the assay in human brain samples indicated that the activity of the 20S proteasome is lower in these samples than in mouse, and therefore in some of the samples, it was not possible to accurately measure the activity of the proteasome. Therefore it would be beneficial to repeat this assay in the cases described above using at least 50µg total protein from each sample; due to the limited size of samples it was not possible to do this in the time remaining.

Chapter 8.

General Discussion and Conclusions

Chapter 8. **General Discussion and Conclusions**

8.1 Discussion and Conclusions

The initial aim of this thesis was to test the following hypothesis: 'Ubiquitin depletion caused by UCHL1 inhibition or knockout will disrupt mitochondrial trafficking, fission and fusion and cause the accumulation of dysfunctional mitochondria'.

By monitoring the movement, fission and fusion of mitochondria by live cell imaging, I demonstrated that inhibiting of a broad range of deubiquitinase enzymes and therefore effectively disabling the ubiquitin proteasome system prevents mitochondrial trafficking, fission and fusion, and distorts mitochondrial morphology. However, mitochondrial dynamics were not disrupted by either the inhibition of UCHL1 hydrolase activity or UCHL1-mediated monoubiquitin stabilisation. Furthermore, in UCHL1 knockout mice, the mitochondria that accumulate in axonal spheroids do not appear to be dysfunctional, since they have normal levels of respiratory chain complexes I and IV, which are commonly depleted in response to mtDNA defects. Mitochondria do not become elongated or shortened in UCHL1 null mice, confirming that there is no fission or fusion defect, and the number of mitochondria in axons of KO mice is similar to that in WT mice, which again indicates that there is no defect in mitochondrial motility or distribution. These results allow me to refute my original hypothesis. They also indicate that the loss of UCHL1 hydrolase activity caused by oxidative modification of UCHL1 or in the UCHL1^{I93M} mutation (Leroy *et al.*, 1998; Nishikawa *et al.*, 2003) does not disrupt mitochondrial dynamics in Parkinson's disease. Furthermore, although we see here that the UPS is required for mitochondrial dynamics, my results indicate that the level by which UPS efficiency declines in ageing and age-related neurodegenerative diseases is not sufficient to disrupt mitochondrial dynamics and function. There has been much recent interest in the link between the UPS and mitochondrial dynamics, and although defects in particular UPS proteins (for example mitochondrial-localised E3 ubiquitin ligases) can disrupt mitochondrial dynamics and/or quality control, these results show that mitochondria are not so heavily dependent on the UPS that a generic UPS decline could disrupt this process.

I also aimed to characterise the phenotype and neuropathology of UCHL1 knockout mice, and found that the UCHL1 KO phenotype is characterised by motor ataxia, which begins at around 9 weeks of age, accompanied by tremor and kyphosis. The neuropathological hallmark of UCHL1 KO mice is axonal spheroids, which occur in the

gracile and cuneate nuclei and in the white matter of the cerebellum, and contain synaptophysin, phosphorylated neurofilaments, mitochondria and sometimes low levels of APP. UCHL1 KO mice display dying-back type axonal dystrophy, and I found that synapses are lost from the gracile nucleus, and that axon and myelin density are significantly reduced in the gracile fasciculi. Axonal dystrophy occurs at the distal portions of the long axons of the dorsal spinocerebellar tract and dorsal column. These findings are in agreement with studies of *gad* mice, and other types of UCHL1 null mice (Yamazaki *et al.*, 1988; Walters *et al.*, 2008; Chen *et al.*, 2010a).

I have also demonstrated that the axonal spheroids in the gracile nucleus of UCHL1 knockout mice show some similarities to the spheroids that occur in the gracile nucleus of ageing humans, indicating the decline of the UPS with age is a large factor driving axon-related pathology in the brain, although it is clear that ageing involves the decline of many cellular systems, including mitochondria. A larger proportion of spheroids in UCHL1 KO mice contain synaptophysin than in aged human brains, this could indicate that UCHL1 has a particular function at synapses or at synaptic vesicles, a theory that is supported by other literature (Liu *et al.*, 2002; Cartier *et al.*, 2009).

Triple immunofluorescent staining confirmed that synaptophysin accumulates in the vast majority of axonal spheroids (99.5%), further implicating blocked axonal transport, or a specific role for UCHL1 at synapses in the formation of axonal spheroids. Mitochondria were another common component of axonal spheroids, however since they are not complex I or IV deficient, and there is no evidence of fission, fusion or motility defects (mitochondria are of a normal length and at normal levels in KO axons), I can conclude that the accumulation of mitochondria in spheroids is a secondary consequence of axonal transport blockage. Comparisons between UCHL1 mice with ‘early stage’ and ‘advanced stage’ phenotypes indicated that the loss of synapses, axons and myelin is an early event in UCHL1 null mice, occurring at or before 9 weeks of age, however APP upregulation is a delayed response to axonal damage.

Based on this data, my model for the formation of axonal spheroids and axon degeneration in UCHL1 null mice is that UCHL1 is required for the stabilisation and recycling of monomeric ubiquitin in particular at synaptic vesicles and synapses (which are furthest away from the site of ubiquitin biogenesis in the soma). The depletion of ubiquitin in these areas may lead to axonal transport disruption via the aggregation of damaged proteins, or by specifically disrupting processes such as synaptophysin

transport vesicle trafficking. This blockage of axonal transport then leads to the accumulation of further components such as mitochondria in spheroids, and triggers Wallerian-like degeneration of the axon distal to the swelling, in a distal-proximal direction, in the same manner as a nerve-crush experiment would (Beirowski *et al.*, 2005).

I have also assessed the impact of mitochondrial dysfunction on the UPS, using tissue from mitochondrial disease patients. There was no indication that mitochondrial dysfunction causes a decline in UPS efficiency and an associated increase in ubiquitin-conjugated proteins. This data is in line with neuropathological observations of mitochondrial disease patients, who do not have accumulations of aggregated proteins (Betts *et al.*, 2004), however further studies should be undertaken before this hypothesis can be discounted.

In summary, this study suggests that the decline of the ubiquitin proteasome system with ageing and in age-related neurodegenerative disorders does not cause mitochondrial dysfunction to decline; the decline of mitochondrial function with age is probably caused by a ubiquitin-independent mechanism, such as the incidence and clonal expansion of mtDNA mutations (Elson *et al.*, 2001). The decline of the UPS is more likely to cause functional deficits with age by the build-up of damaged proteins that the proteasome is not able to break down, and this could lead to disruptions in axonal transport that induce axonal dystrophy and degeneration. These results indicate that the links between UPS function and mitochondria may not be as tight as previously thought.

8.2 Further Work

In chapter 3, I found that inhibition of UCHL1 hydrolase activity and monoubiquitin stabilisation does not affect mitochondrial dynamics or morphology, although the ubiquitin system is required for mitochondrial dynamics to occur. It would be beneficial to carry out further experiments to confirm these results.

Firstly, although the inhibitors LDN 57444 and LDN 91946 have been characterised by other groups (Liu *et al.*, 2003; Mermerian *et al.*, 2007; Tan *et al.*, 2008; Altun *et al.*, 2011), it is important to characterise these inhibitors in primary neurons, since inhibitors may behave differently depending on the cell type. Carrying out cytotoxicity assays and creating dose-response curves would improve the reliability and validity of the results in chapter 3. It would also be beneficial to confirm these results in a different experimental

system. For example, if neurons were cultured from UCHL1 KO mice, it would be possible to compare mitochondrial dynamics in neurons not expressing UCHL1 to neurons from WT mice. It would then be interesting to transfect UCHL1 KO neurons with the UCHL1^{C90S} and UCHL1^{D30K} mutant forms, which lack hydrolase and ubiquitin binding activity, respectively (Osaka *et al.*, 2003), and assess mitochondrial dynamics in these neurons. Alternatively, this hypothesis could be approached by impairing the function of the UPS in another way. For example, siRNA (small interfering RNA) could be utilised to knockdown certain subunits of the 20S proteasome, to mimic the decrease of proteasome activity in aging.

In chapter 4, I did not find any evidence for mitochondrial respiratory chain deficiency in UCHL1 KO mice; levels of mitochondrial respiratory chain complexes I and IV appeared normal. In order to back up the conclusion that ubiquitin depletion does not cause mitochondrial dysfunction, further assessment of mitochondrial function could be carried out by biochemically assessing the activity of each mitochondrial respiratory chain complex using frozen tissue samples from UCHL1 KO and WT mice.

Appendix A. These experiments, in addition to those suggested in section 7.3.3, would help to confirm and validate the findings of

this thesis. Interaction of LDN-57444 with MitoRFP and Mitotracker Green

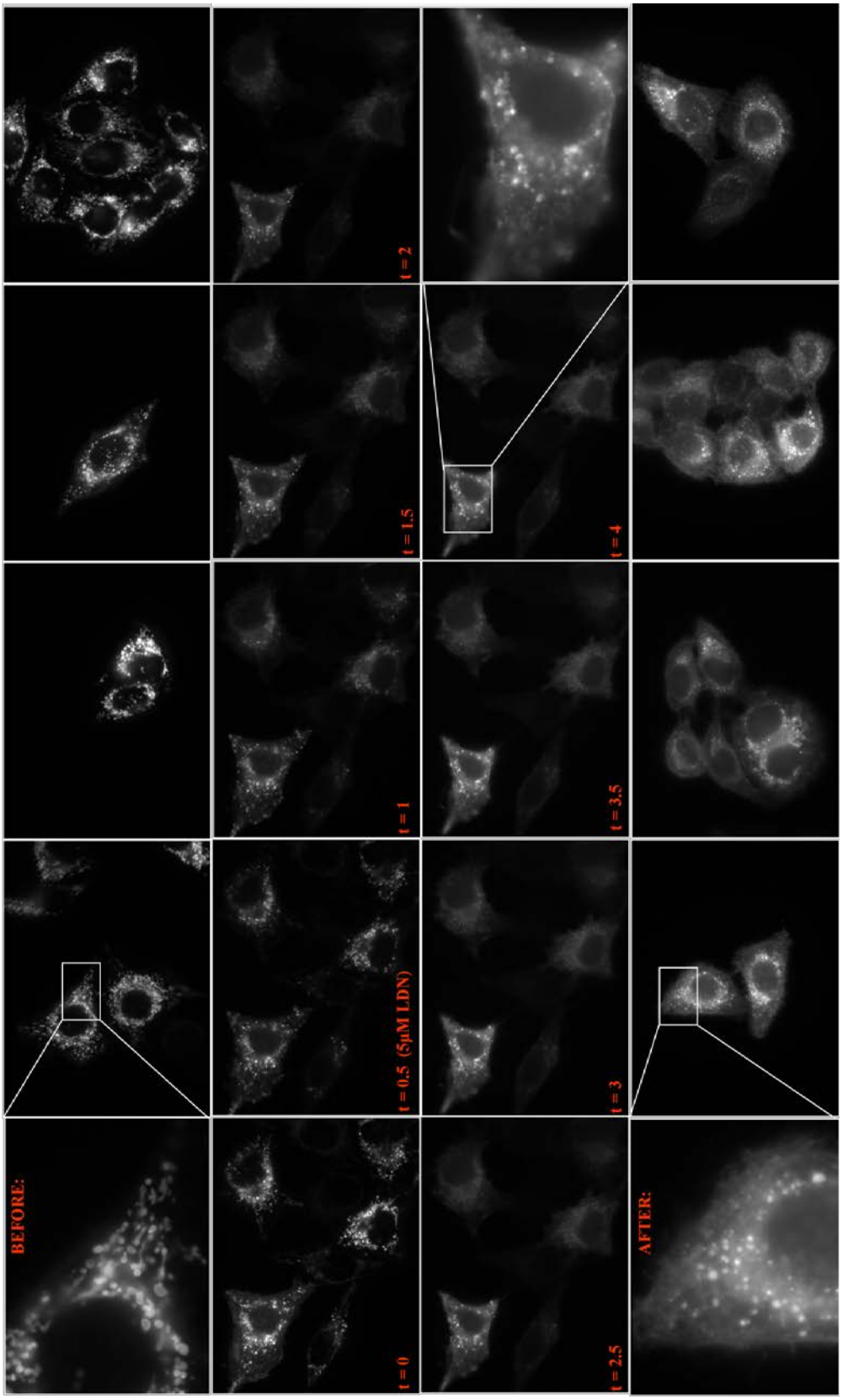

Figure 8.1: Unknown interaction of LDN-57444 with MitoRFP.
Top row: images of mitochondria in several cells immediately before addition of 5μM LDN-57444. Rows 2&3: Images of mitochondria immediately before addition of LDN-57444 (t=0) and every 30 seconds afterwards. Bottom row: Images of mitochondria at least 4 minutes after addition of LDN-57444

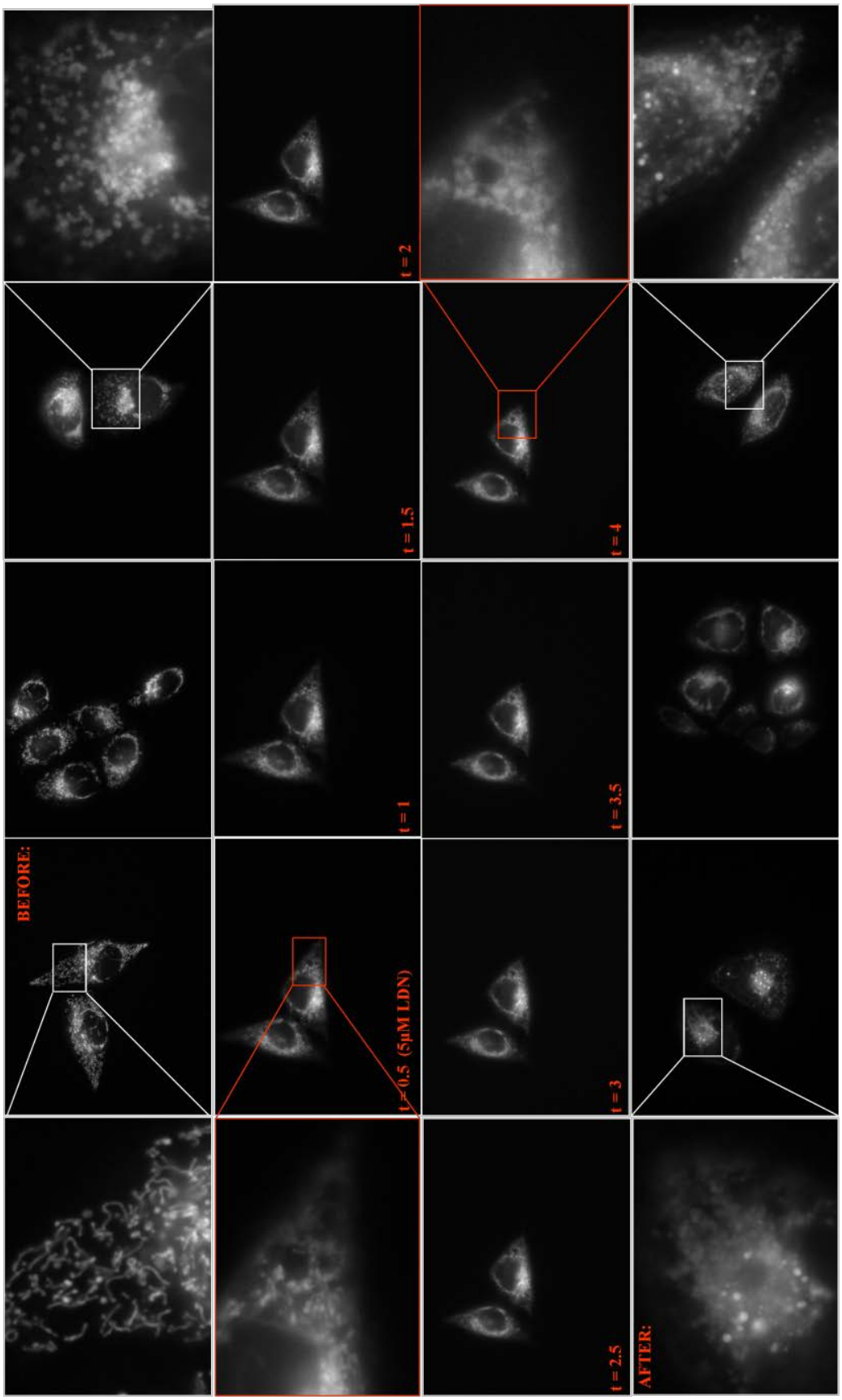

Figure 8.2: Unknown interaction of LDN-57444 with Mitotracker Green.
Top row: images of mitochondria stained with mitotracker green immediately before addition of 5μM LDN-57444. Middle two rows: mitochondria imaged 30 seconds (t=0.5) to 4 minutes (t=4) after addition of LDN-57444. Bottom row: Images of mitochondria at least 4 minutes after addition of LDN-57444.

Appendix B. Details of Mouse Dissections

New ID	Sex	Cage number	Cage ID	Weight (g)	Gen	Date of Birth	Date Dissected	Age (Weeks)	Fixation
1	F	G3759	2	29.92	WT	26/01/12	29/05/12	17w 5d	Fixed
4	F	G3759	1	18.8	KO	26/01/12	29/05/12	17w 5d	Fixed
5	M	G3758	3	25	KO	26/01/12	29/05/12	17w 5d	Fixed
2	M	G3582	1	37.7	WT	10/01/12	29/05/12	20w	Fixed
3	F	G3581	1	23.1	WT	10/01/12	29/05/12	20w	Fixed
6	F	G3581	2	19.6	KO	10/01/12	29/05/12	20w	Fixed
10	M	G3582	2	25.9	KO	10/01/12	30/05/12	19w 2d	Frozen
11	F	G3583	3	19.1	KO	16/01/12	30/05/12	19w 2d	Frozen
7	F	G3585	3	19.35	KO	16/01/12	30/05/12	19w2d	Fixed
8	F	G3585	1	22.4	WT	16/01/12	30/05/12	19w2d	Frozen
9	M	G3582	3	34	WT	10/01/12	30/05/12	20w 1d	Frozen
12	F	G4971	1	20.3	WT	07/04/12	22/06/12	10w 6d	Frozen
13	F	G4971	3	20.7	WT	07/04/12	22/06/12	10w 6d	Frozen
14	F	G4971	4	20.2	KO	07/04/12	22/06/12	10w6d	Frozen
15	F	G4971	7	20.4	KO	07/04/12	22/06/12	10w6d	Frozen
16	F	G4973	5	21.1	WT	13/04/12	03/07/12	11w4d	Fixed
17	F	G4973	6	22	WT	13/04/12	03/07/12	11w4d	Fixed
18	F	G4973	1	20.4	WT	13/04/12	03/07/12	11w4d	Fixed
19	M	G4972	1	25.5	KO	13/04/12	04/07/12	11w 5d	Fixed
20	F	G4971	5	18.9	KO	07/04/12	04/07/12	12w4d	Fixed
21	F	G4971	6	24.2	WT	07/04/12	04/07/12	12w4d	Fixed
22	M	G5081	1	24.4	KO	30/04/12	04/07/12	9w2d	Fixed
23	M	G5081	3	24.6	KO	30/04/12	04/07/12	9w2d	Fixed
24	F	G5082	1	20.42	KO	30/04/12	05/07/12	9w 3d	Frozen
25	F	G5082	2	18.62	KO	30/04/12	05/07/12	9w3d	Frozen
26	M	G5081	2	24.85	WT	30/04/12	05/07/12	9w3d	Frozen
27	M	G4972	3	26.8	WT	13/04/12	06/07/12	12w	Frozen
28	F	G4971	2	19.8	WT	07/04/12	06/07/12	12w 6d	Frozen
29	M	G4970	1	28.7	WT	07/04/12	06/07/12	12w 6d	Frozen
30	F	G4261	1	20.2	KO	23/02/12	06/07/12	19w1d	Frozen
31	F	G4261	3	20.3	KO	23/02/12	06/07/12	19w1d	Frozen
32	F	G4261	4	23.2	WT	23/02/12	06/07/12	19w1d	Frozen
33	F	G4620	1	23.04	WT	17/03/12	13/07/12	16w 6d	Frozen
34	M	G4619	1	27.64	KO	17/03/12	13/07/12	16w 6d	Frozen
35	F	G4263	5	20.73	KO	20/02/12	13/07/12	21w 1d	Frozen
36	F	G4263	6	19.05	KO	20/02/12	13/07/12	21w 1d	Frozen
37	M	G4837	1	31.4	WT	02/04/12	17/07/12	16w 1d	Fixed
38	M	G4837	2	29	WT	02/04/12	17/07/12	16w 1d	Fixed
39	M	G4837	4	27.4	KO	02/04/12	17/07/12	16w 1d	Fixed
40	M	G4837	5	25.8	KO	02/04/12	17/07/12	16w 1d	Fixed
41	M	G4837	6	23	KO	02/04/12	17/07/12	16w 1d	Fixed
42	F	G4836	1	20.4	WT	02/04/12	17/07/12	16w 1d	Fixed
43	F	G4836	3	18.3	KO	02/04/12	17/07/12	16w 1d	Fixed

45	F	G4836	4	24.6	WT	02/04/12	18/07/12	16w 2d	Fixed
46	F	G4836	6	20.76	KO	02/04/12	18/07/12	16w 2d	Fixed
47	M	G4835	9	32.56	WT	01/04/12	18/07/12	16w 3d	Fixed
48	M	G4835	2	27.77	KO	01/04/12	18/07/12	16w 3d	Fixed
49	F	G4403	2	19.33	KO	09/03/12	18/07/12	18w5d	Fixed
50	M	G4839	5	31.5	WT	01/04/12	20/07/12	16w 5d	Frozen
51	M	G4839	3	33.5	WT	01/04/12	20/07/12	16w 5d	Frozen
52	M	G4839	4	23.8	KO	01/04/12	20/07/12	16w 5d	Frozen
53	M	G4839	7	29.4	KO	01/04/12	20/07/12	16w 5d	Frozen
54	F	G4834	6	22.7	WT	01/04/12	20/07/12	16w 5d	Frozen
55	F	G4834	5	20.9	KO	01/04/12	20/07/12	16w 5d	Frozen

Table 8.1: Details of mouse dissections

Appendix C. Triple Immunofluorescence

Initial results indicated that the extent of mitochondrial accumulation on axonal spheroids decreases with age (Figure 8.3A, p=0.0190), whilst the extent of synaptophysin accumulation increases with age (Figure 8.3B, p=0.0229).

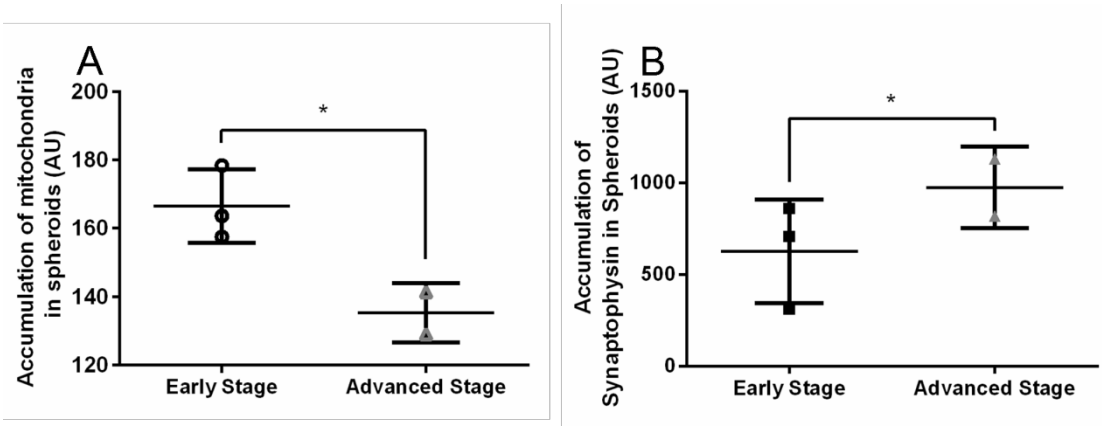

Figure 8.3: Changes in extent of mitochondria and synaptophysin accumulation in mice with early and advanced stage pathology.
A) Accumulation of mitochondria in spheroids (AU) is defined as FITC intensity in spheroids – FITC intensity in surrounding axons. Each data point represents the mean of 30 spheroids for one mouse, n=3, 2. Bars show the mean ±SD. P=0.0190, unpaired t-test. B) Accumulation of synaptophysin in spheroids (AU) is defined as TRITC intensity in spheroids – TRITC intensity in surrounding axons. Each data point represents the mean of 30 spheroids for one mouse, n=3, 2. Bars show the mean ±SD. P=0.0229, unpaired t-test

Serial sections from a positive control were included in both batches of immunofluorescence, in order to adjust for changes in immunofluorescence intensity. Since FITC intensity was brighter, and TRITC intensity was dimmer in the second batch of sections, it was necessary to adjust laser power and gain in the 488nm and 541nm channels, to avoid overexposure in the 488nm channel and ensure that fluorescence intensities were comparable between the two batches, Figure 8.4.

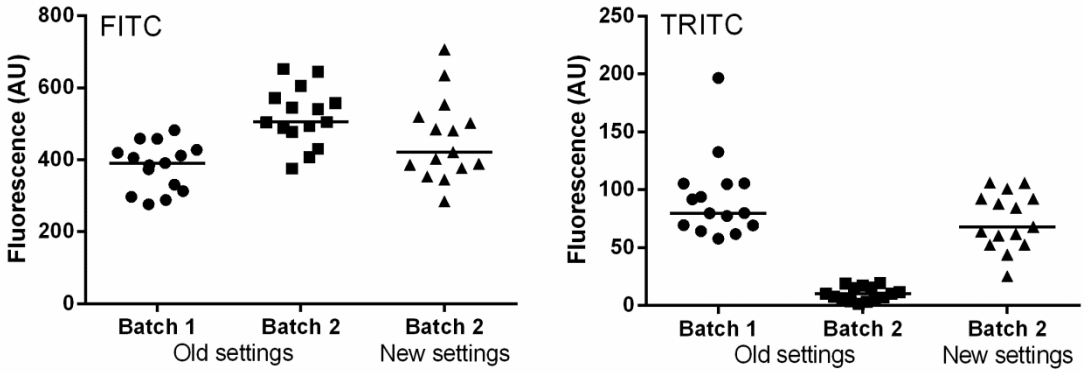

Figure 8.4: Adjustment of microscope settings.
Each point represents the mean FITC or TRITC intensity in one area of neurofilaments. Data is from serial sections of a positive control included in both batches of immunofluorescence staining, and imaged with both old microscope settings, and new settings resulting from adjustment of the laser power intensity and gain.

Bibliography

(!!! INVALID CITATION !!!).

Abd El Mohsen, M.M., Iravani, M.M., Spencer, J.P.E., Rose, S., Fahim, A.T., Motawi, T.M.K., Ismail, N.A.F. and Jenner, P. (2005) 'Age-associated changes in protein oxidation and proteasome activities in rat brain: Modulation by antioxidants', *Biochemical and Biophysical Research Communications*, 336(2), pp. 386-391.

Adalbert, R., Nogradi, A., Babetto, E., Janeckova, L., Walker, S.A., Kerschensteiner, M., Misgeld, T. and Coleman, M.P. (2009) 'Severely dystrophic axons at amyloid plaques remain continuous and connected to viable cell bodies', *Brain*, 132(2), pp. 402-416.

Adam-Vizi, V. and Chinopoulos, C. (2006) 'Bioenergetics and the formation of mitochondrial reactive oxygen species', *Trends in Pharmacological Sciences*, 27(12), pp. 639-645.

Ahlberg, J. and Glaumann, H. (1985) 'Uptake - microautophagy - and degradation of exogenous proteins by isolated rat liver lysosomes. Effects of pH, ATP, and inhibitors of proteolysis', *Experimental and Molecular Pathology*, 42(1), pp. 78-88.

Alemi, M., Prigione, A., Wong, A., Schoenfeld, R., DiMauro, S., Hirano, M., Taroni, F. and Cortopassi, G. (2007) 'Mitochondrial DNA deletions inhibit proteasomal activity and stimulate an autophagic transcript', *Free Radical Biology and Medicine*, 42(1), pp. 32-43.

Ali-Khan, Z., Normand, J., Alizadeh-Khiavi, K., Robitaille, Y. and Chronopoulos, S. (1992) 'Ubiquitin profile and amyloid enhancing factor activity in Alzheimer and 'normal' human brain extracts', *Neuroscience Letters*, 139(1), pp. 24-28.

Altun, M., Kramer, H.B., Willems, L.I., McDermott, J.L., Leach, C.A., Goldenberg, S.J., Kumar, K.G.S., Konietzny, R., Fischer, R., Kogan, E., MacKeen, M.M., McGouran, J., Khoronenkova, S.V., Parsons, J.L., Dianov, G.L., Nicholson, B. and Kessler, B.M. (2011) 'Activity-based chemical proteomics accelerates inhibitor development for deubiquitylating enzymes', *Chemistry and Biology*, 18(11), pp. 1401-1412.

Anand, R., Wai, T., Baker, M.J., Kladt, N., Schauss, A.C., Rugarli, E. and Langer, T. (2014) 'The i-AAA protease YME1L and OMA1 cleave OPA1 to balance mitochondrial fusion and fission', *Journal of Cell Biology*, 204(6), pp. 919-929.

Anderson, S., Bankier, A.T., Barrell, B.G., de Bruijn, M.H.L., Coulson, A.R., Drouin, J., Eperon, I.C., Nierlich, D.P., Roe, B.A., Sanger, F., Schreier, P.H., Smith, A.J.H., Staden, R. and Young, I.G. (1981) 'Sequence and organization of the human mitochondrial genome', *Nature*, 290(5806), pp. 457-465.

Andersson, F.I., Werrell, E.F., McMorran, L., Crone, W.J.K., Das, C., Hsu, S.T.D. and Jackson, S.E. (2011) 'The effect of Parkinson's-disease-associated mutations on the deubiquitinating enzyme UCH-L1', *Journal of Molecular Biology*, 407(2), pp. 261-272.

Andersson, M., SjÖStrand, J. and Karlsson, J.-O. (1999) 'Differential Inhibition of Three Peptidase Activities of the Proteasome in Human Lens Epithelium by Heat and Oxidation', *Experimental Eye Research*, 69(1), pp. 129-138.

Andersson, V., Hanzén, S., Liu, B., Molin, M. and Nyström, T. (2013) 'Enhancing protein disaggregation restores proteasome activity in aged cells', *Aging*, 5(11), pp. 802-812.

Andrews, R.M., Kubacka, I., Chinnery, P.F., Lightowlers, R.N., Turnbull, D.M. and Howell, N. (1999) 'Reanalysis and revision of the Cambridge reference sequence for human mitochondrial DNA', *Nat Genet*, 23(2), pp. 147-147.

Anton, F., Dittmar, G., Langer, T. and Escobar-Henriques, M. (2013) 'Two Deubiquitylases Act on Mitofusin and Regulate Mitochondrial Fusion along Independent Pathways', *Molecular Cell*, 49(3), pp. 487-498.

Apps, R. and Hawkes, R. (2009) 'Cerebellar cortical organization: a one-map hypothesis', *Nat Rev Neurosci*, 10(9), pp. 670-681.

Bacik, J.P., Walker, J.R., Ali, M., Schimmer, A.D. and Dhe-Paganon, S. (2010) 'Crystal structure of the human ubiquitin-activating enzyme 5 (UBA5) bound to ATP: Mechanistic insights into a minimalistic E1 enzyme', *Journal of Biological Chemistry*, 285(26), pp. 20273-20280.

Barrachina, M., Castaño, E., Dalfó, E., Maes, T., Buesa, C. and Ferrer, I. (2006) 'Reduced ubiquitin C-terminal hydrolase-1 expression levels in dementia with Lewy bodies', *Neurobiology of Disease*, 22(2), pp. 265-273.

Barrell, B.G., Anderson, S., Bankier, A.T., de Bruijn, M.H., Chen, E., Coulson, A.R., Drouin, J., Eperon, I.C., Nierlich, D.P., Roe, B.A., Sanger, F., Schreier, P.H., Smith, A.J., Staden, R. and Young, I.G. (1980) 'Different pattern of codon recognition by mammalian mitochondrial tRNAs', *Proceedings of the National Academy of Sciences*, 77(6), pp. 3164-3166.

Baugh, J.M., Viktorova, E.G. and Pilipenko, E.V. (2009) 'Proteasomes Can Degrade a Significant Proportion of Cellular Proteins Independent of Ubiquitination', *Journal of Molecular Biology*, 386(3), pp. 814-827.

Behrends, C., Sowa, M.E., Gygi, S.P. and Harper, J.W. (2010) 'Network organization of the human autophagy system', *Nature*, 466(7302), pp. 68-76.

Beirowski, B., Adalbert, R., Wagner, D., Grumme, D.S., Addicks, K., Ribchester, R.R. and Coleman, M.P. (2005) 'The progressive nature of Wallerian degeneration in wild-type and slow Wallerian degeneration (WldS) nerves', *BMC Neuroscience*, 6.

Bence, N.F., Sampat, R.M. and Kopito, R.R. (2001) 'Impairment of the ubiquitin-proteasome system by protein aggregation', *Science*, 292(5521), pp. 1552-1555.

Bender, A., Krishnan, K.J., Morris, C.M., Taylor, G.A., Reeve, A.K., Perry, R.H., Jaros, E., Hersheson, J.S., Betts, J., Klopstock, T., Taylor, R.W. and Turnbull, D.M. (2006) 'High levels of mitochondrial DNA deletions in substantia nigra neurons in aging and Parkinson disease', *Nature Genetics*, 38(5), pp. 515-517.

Beregi, E., Regius, O., Huttl, T. and Gobl, Z. (1988) 'Age-related changes in the skeletal muscle cells', *Zeitschrift fur Gerontologie*, 21(2), pp. 83-86.

Bernales, S., Morales Soto, M.A. and McCullagh, E. (2012) 'Unfolded protein stress in the endoplasmic reticulum and mitochondria: a role in neurodegeneration', *Frontiers in Aging Neuroscience*, 4.

Bestwick, M.L. and Shadel, G.S. (2013) 'Accessorizing the human mitochondrial transcription machinery', *Trends in Biochemical Sciences*, 38(6), pp. 283-291.

Betts, J., Jaros, E., Perry, R.H., Schaefer, A.M., Taylor, R.W., Abdel-All, Z., Lightowlers, R.N. and Turnbull, D.M. (2006) 'Molecular neuropathology of MELAS: level of heteroplasmy in individual neurones and evidence of extensive vascular involvement', *Neuropathology and Applied Neurobiology*, 32(4), pp. 359-373.

Betts, J., Lightowlers, R.N. and Turnbull, D.M. (2004) 'Neuropathological Aspects of Mitochondrial DNA Disease', *Neurochemical Research*, 29(3), pp. 505-511.

Bilguvar, K., Tyagi, N.K., Ozkara, C., Tuysuz, B., Bakircioglu, M., Choi, M., Delil, S., Caglayan, A.O., Baranoski, J.F., Erturk, O., Yalcinkaya, C., Karacorlu, M., Dincer, A., Johnson, M.H., Mane, S., Chandra, S.S., Louvi, A., Boggon, T.J., Lifton, R.P., Horwich, A.L. and Gunel, M. (2013) 'Recessive loss of function of the neuronal ubiquitin hydrolase UCHL1 leads to early-onset progressive neurodegeneration', *Proceedings of the National Academy of Sciences of the United States of America*, 110(9), pp. 3489-3494.

Bingol, B., Tea, J.S., Phu, L., Reichelt, M., Bakalarski, C.E., Song, Q., Foreman, O., Kirkpatrick, D.S. and Sheng, M. (2014) 'The mitochondrial deubiquitinase USP30 opposes parkin-mediated mitophagy', *Nature*, 510(7505), pp. 370-375.

Birsa, N., Norkett, R., Higgs, N., Lopez-Domenech, G. and Kittler, J.T. (2013) 'Mitochondrial trafficking in neurons and the role of the Miro family of GTPase proteins', *Biochemical Society Transactions*, 41(6), pp. 1525-1531.

Blakely, E.L., Alston, C.L., Lecky, B., Chakrabarti, B., Falkous, G., Turnbull, D.M., Taylor, R.W. and Gorman, G.S. (2014) 'Distal weakness with respiratory insufficiency caused by the m.8344A > G “MERRF” mutation', *Neuromuscular Disorders*, 24(6), pp. 533-536.

Bogenhagen, D.F. (2012) 'Mitochondrial DNA nucleoid structure', *Biochimica et Biophysica Acta (BBA) - Gene Regulatory Mechanisms*, 1819(9–10), pp. 914-920.

Boveris, A., Cadenas, E. and Stoppani, A.O.M. (1976) 'Role of ubiquinone in the mitochondrial generation of hydrogen peroxide', *Biochemical Journal*, 156(2), pp. 435-444.

Braak, H., Tredici, K.D., Rüb, U., de Vos, R.A.I., Jansen Steur, E.N.H. and Braak, E. (2003) 'Staging of brain pathology related to sporadic Parkinson's disease', *Neurobiology of Aging*, 24(2), pp. 197-211.

Brannon, W., McCormick, W. and Lampert, P. (1967) 'Axonal dystrophy in the gracile nucleus of man', *Acta Neuropathologica*, 9(1), pp. 1-6.

Bremm, A. and Komander, D. (2011) 'Emerging roles for Lys11-linked polyubiquitin in cellular regulation', *Trends in Biochemical Sciences*, 36(7), pp. 355-363.

Brickley, K., Smith, M.J., Beck, M. and Stephenson, F.A. (2005) 'GRIF-1 and OIP106, members of a novel gene family of coiled-coil domain proteins: Association in vivo and in vitro with kinesin', *Journal of Biological Chemistry*, 280(15), pp. 14723-14732.

Brochu, G., Maler, L. and Hawkes, R. (1990) 'Zebrin II: a polypeptide antigen expressed selectively by Purkinje cells reveals compartments in rat and fish cerebellum', *Journal of Comparative Neurology*, 291(4), pp. 538-552.

Brown, W.M., George, M. and Wilson, A.C. (1979) 'Rapid evolution of animal mitochondrial DNA', *Proceedings of the National Academy of Sciences*, 76(4), pp. 1967-1971.

Buckner, R.L. (2013) 'The cerebellum and cognitive function: 25 years of insight from anatomy and neuroimaging', *Neuron*, 80(3), pp. 807-815.

Bukowska, D., Zguczyński, L. and Mierzejewska-Krzyzowska, B. (2003) 'Pontocerebellar projection to the rabbit paramedian lobule by means of axonal collaterals: Evidence for intralobular connections', *Acta Neurobiologiae Experimentalis*, 63(4), pp. 295-308.

Bulteau, A.-L., Szweda, L.I. and Friguet, B. (2002) 'Age-Dependent Declines in Proteasome Activity in the Heart', *Archives of Biochemistry and Biophysics*, 397(2), pp. 298-304.

Bulteau, A.L., Petropoulos, I. and Friguet, B. (2000) 'Age-related alterations of proteasome structure and function in aging epidermis', *Experimental Gerontology*, 35(6-7), pp. 767-777.

Butterfield, D.A., Gnjec, A., Poon, H.F., Castegna, A., Pierce, W.M., Klein, J.B. and Martins, R.N. (2006) 'Redox proteomics identification of oxidatively modified brain proteins in inherited Alzheimer's disease: An initial assessment', *Journal of Alzheimer's Disease*, 10(4), pp. 391-397.

Calkins, M.J. and Reddy, P.H. (2011) 'Amyloid beta impairs mitochondrial anterograde transport and degenerates synapses in Alzheimer's disease neurons', *Biochimica et Biophysica Acta - Molecular Basis of Disease*, 1812(4), pp. 507-513.

Campello, S., Strappazzon, F. and Cecconi, F. (2014) 'Mitochondrial dismissal in mammals, from protein degradation to mitophagy', *Biochimica et Biophysica Acta - Bioenergetics*, 1837(4), pp. 451-460.

Canevari, L., Clark, J.B. and Bates, T.E. (1999) 'β-Amyloid fragment 25-35 selectively decreases complex IV activity in isolated mitochondria', *FEBS Letters*, 457(1), pp. 131-134.

Carleton, S.C. and Carpenter, M.B. (1983) 'Afferent and efferent connections of the medial, inferior and lateral vestibular nuclei in the cat and monkey', *Brain Research*, 278(1-2), pp. 29-51.

Carrard, G., Bulteau, A.-L., Petropoulos, I. and Friguet, B. (2002) 'Impairment of proteasome structure and function in aging', *The International Journal of Biochemistry & Cell Biology*, 34(11), pp. 1461-1474.

Cartier, A.E., Djakovic, S.N., Salehi, A., Wilson, S.M., Masliah, E. and Patrick, G.N. (2009) 'Regulation of synaptic structure by ubiquitin C-terminal hydrolase L1', *Journal of Neuroscience*, 29(24), pp. 7857-7868.

Castegna, A., Aksenov, M., Aksenova, M., Thongboonkerd, V., Klein, J.B., Pierce, W.M., Booze, R., Markesbery, W.R. and Butterfield, D.A. (2002) 'Proteomic identification of oxidatively modified proteins in Alzheimer's disease brain. Part I: Creatine kinase BB, glutamine synthase, and ubiquitin carboxy-terminal hydrolase L-1', *Free Radical Biology and Medicine*, 33(4), pp. 562-571.

Chan, N.C., Salazar, A.M., Pham, A.H., Sweredoski, M.J., Kolawa, N.J., Graham, R.L., Hess, S. and Chan, D.C. (2011) 'Broad activation of the ubiquitin-proteasome system by Parkin is critical for mitophagy', *Human Molecular Genetics*, 20(9), pp. 1726-1737.

Chau, V., Tobias, J.W., Bachmair, A., Marriott, D., Ecker, D.J., Gonda, D.K. and Varshavsky, A. (1989) 'A multiubiquitin chain is confined to specific lysine in a targeted short-lived protein', *Science*, 243(4898), pp. 1576-1583.

Chen, F., Sugiura, Y., Myers, K.G., Liu, Y. and Lin, W. (2010a) 'Ubiquitin carboxyl-terminal hydrolase L1 is required for maintaining the structure and function of the neuromuscular junction', *Proceedings of the National Academy of Sciences of the United States of America*, 107(4), pp. 1636-1641.

Chen, H., Chomyn, A. and Chan, D.C. (2005) 'Disruption of fusion results in mitochondrial heterogeneity and dysfunction', *Journal of Biological Chemistry*, 280(28), pp. 26185-26192.

Chen, H., Detmer, S.A., Ewald, A.J., Griffin, E.E., Fraser, S.E. and Chan, D.C. (2003) 'Mitofusins Mfn1 and Mfn2 coordinately regulate mitochondrial fusion and are essential for embryonic development', *Journal of Cell Biology*, 160(2), pp. 189-200.

Chen, H., Vermulst, M., Wang, Y.E., Chomyn, A., Prolla, T.A., McCaffery, J.M. and Chan, D.C. (2010b) 'Mitochondrial fusion is required for mtdna stability in skeletal muscle and tolerance of mtDNA mutations', *Cell*, 141(2), pp. 280-289.

Choi, J., Levey, A.I., Weintraub, S.T., Rees, H.D., Gearing, M., Chin, L.S. and Li, L. (2004) 'Oxidative Modifications and Down-regulation of Ubiquitin Carboxyl-terminal Hydrolase L1 Associated with Idiopathic Parkinson's and Alzheimer's Diseases', *Journal of Biological Chemistry*, 279(13), pp. 13256-13264.

Chondrogianni, N., Stratford, F.L.L., Trougakos, I.P., Friguet, B., Rivett, A.J. and Gonos, E.S. (2003) 'Central role of the proteasome in senescence and survival of human fibroblasts. Induction of a senescence-like phenotype upon its inhibition and resistance to stress upon its activation', *Journal of Biological Chemistry*, 278(30), pp. 28026-28037.

Christian, B.E. and Spremulli, L.L. (2012) 'Mechanism of protein biosynthesis in mammalian mitochondria', *Biochimica et Biophysica Acta - Gene Regulatory Mechanisms*, 1819(9-10), pp. 1035-1054.

Ciechanover, A. and Stanhill, A. (2014) 'The complexity of recognition of ubiquitinated substrates by the 26S proteasome', *Biochimica et Biophysica Acta - Molecular Cell Research*, 1843(1), pp. 86-96.

Clague, M.J., Coulson, J.M. and Urbé, S. (2012) 'Cellular functions of the DUBs', *Journal of Cell Science*, 125(2), pp. 277-286.

Clayton, D.A. (2000) 'Transcription and replication of mitochondrial DNA', *Human Reproduction*, 15(SUPPL. 2), pp. 11-17.

Conconi, M., Szweda, L.I., Levine, R.L., Stadtman, E.R. and Friguet, B. (1996) 'Age-Related Decline of Rat Liver Multicatalytic Proteinase Activity and Protection from Oxidative Inactivation by Heat-Shock Protein 90', *Archives of Biochemistry and Biophysics*, 331(2), pp. 232-240.

Conforti, L., Gilley, J. and Coleman, M.P. (2014) 'Wallerian degeneration: An emerging axon death pathway linking injury and disease', *Nature Reviews Neuroscience*, 15(6), pp. 394-409.

Cook, C. and Petrucelli, L. (2009) 'A critical evaluation of the ubiquitin-proteasome system in Parkinson's disease', *Biochimica et Biophysica Acta - Molecular Basis of Disease*, 1792(7), pp. 664-675.

Cooper, E.M., Cutcliffe, C., Kristiansen, T.Z., Pandey, A., Pickart, C.M. and Cohen, R.E. (2009) 'K63-specific deubiquitination by two JAMM/MPN+ complexes: BRISC-associated Brcc36 and proteasomal Poh1', *EMBO Journal*, 28(6), pp. 621-631.

Coulombe, J., Gamage, P., Gray, M., Zhang, M., Tang, M., Woulfe, J., Saffrey, M.J. and Gray, D. (2014) 'Loss of UCHL1 promotes age-related degenerative changes in the enteric nervous system', *Frontiers in Aging Neuroscience*, 6.

Craven, J. (2011) 'Major ascending and descending tracts in the spinal cord', *Anaesthesia and Intensive Care Medicine*, 12(1), pp. 26-27.

Crick, F.H.C. (1966) 'Codon—anticodon pairing: The wobble hypothesis', *Journal of Molecular Biology*, 19(2), pp. 548-555.

Cuervo, A.M. (2010) 'Chaperone-mediated autophagy: Selectivity pays off', *Trends in Endocrinology and Metabolism*, 21(3), pp. 142-150.

Cuervo, A.M., Bergamini, E., Brunk, U.T., Dröge, W., Ffrench, M. and Terman, A. (2005) 'Autophagy and aging: the importance of maintaining "clean" cells', *Autophagy*, 1(3), pp. 131-140.

Cuervo, A.M. and Dice, J.F. (2000) 'Age-related decline in chaperone-mediated autophagy', *Journal of Biological Chemistry*, 275(40), pp. 31505-31513.

Cummins, J.M. and Vogelstein, B. (2004) 'HAUSP is Required for p53 Destabilization', *Cell Cycle*, 3(6), pp. 687-690.

Dahlmann, B. (2007) 'Role of proteasomes in disease', *BMC Biochemistry*, 8(SUPPL. 1).

Das, C., Hoang, Q.Q., Kreinbring, C.A., Luchansky, S.J., Meray, R.K., Ray, S.S., Lansbury, P.T., Ringe, D. and Petsko, G.A. (2006) 'Structural basis for conformational plasticity of the Parkinson's disease-associated ubiquitin hydrolase UCH-L1', *Proceedings of the National Academy of Sciences of the United States of America*, 103(12), pp. 4675-4680.

Davies, K.J.A. (2001) 'Degradation of oxidized proteins by the 20S proteasome', *Biochimie*, 83(3-4), pp. 301-310.

De Grey, A.D.N.J. (1997) 'A proposed refinement of the mitochondrial free radical theory of aging', *BioEssays*, 19(2), pp. 161-166.

De Vos, K.J. and Sheetz, M.P. (2007) 'Visualization and Quantification of Mitochondrial Dynamics in Living Animal Cells', in Liza, A.P. and Eric, A.S. (eds.) *Methods in Cell Biology*. Academic Press, pp. 627-682.

Deretic, V. (2009) 'Links between autophagy, innate immunity, inflammation and Crohn's disease', *Digestive Diseases*, 27(3), pp. 246-251.

Dice, J.F. (1990) 'Peptide sequences that target cytosolic proteins for lysosomal proteolysis', *Trends in Biochemical Sciences*, 15(8), pp. 305-309.

DiMauro, S. and Schon, E.A. (2003) 'Mitochondrial respiratory-chain diseases', *New England Journal of Medicine*, 348(26), pp. 2656-2668.

Dimauro, S., Tanji, K. and Schon, E.A. 748 (2012) 'The many clinical faces of cytochrome c oxidase deficiency' *Advances in Experimental Medicine and Biology*. pp.

341-357. Available at: http://www.scopus.com/inward/record.url?eid=2-s2.0-84863746788&partnerID=40&md5=874ca7d33f5a17469170e7f272ebd4e3.

Djuranovic, S., Hartmann, M.D., Habeck, M., Ursinus, A., Zwickl, P., Martin, J., Lupas, A.N. and Zeth, K. (2009) 'Structure and Activity of the N-Terminal Substrate Recognition Domains in Proteasomal ATPases', *Molecular Cell*, 34(5), pp. 580-590.

Domingues, A.F., Arduíno, D.M., Esteves, A.R., Swerdlow, R.H., Oliveira, C.R. and Cardoso, S.M. (2008) 'Mitochondria and ubiquitin-proteasomal system interplay: Relevance to Parkinson's disease', *Free Radical Biology and Medicine*, 45(6), pp. 820-825.

Dynek, J.N., Goncharov, T., Dueber, E.C., Fedorova, A.V., Izrael-Tomasevic, A., Phu, L., Helgason, E., Fairbrother, W.J., Deshayes, K., Kirkpatrick, D.S. and Vucic, D. (2010) 'C-IAP1 and UbcH5 promote K11-linked polyubiquitination of RIP1 in TNF signalling', *EMBO Journal*, 29(24), pp. 4198-4209.

Ehlinger, A. and Walters, K.J. (2013) 'Structural insights into proteasome activation by the 19S regulatory particle', *Biochemistry*, 52(21), pp. 3618-3628.

Eletr, Z.M. and Wilkinson, K.D. (2014) 'Regulation of proteolysis by human deubiquitinating enzymes', *Biochimica et Biophysica Acta - Molecular Cell Research*, 1843(1), pp. 114-128.

Elgass, K., Pakay, J., Ryan, M.T. and Palmer, C.S. (2013) 'Recent advances into the understanding of mitochondrial fission', *Biochimica et Biophysica Acta (BBA) - Molecular Cell Research*, 1833(1), pp. 150-161.

Elson, J.L., Samuels, D.C., Turnbull, D.M. and Chinnery, P.F. (2001) 'Random intracellular drift explains the clonal expansion of mitochondrial DNA mutations with age', *American Journal of Human Genetics*, 68(3), pp. 802-806.

Escobar-Henriques, M. and Anton, F. (2013) 'Mechanistic perspective of mitochondrial fusion: Tubulation vs. fragmentation', *Biochimica et Biophysica Acta (BBA) - Molecular Cell Research*, 1833(1), pp. 162-175.

Escobar‐Henriques, M. and Langer, T. (2014) *Dynamic survey of mitochondria by ubiquitin*.

Falkenberg, M., Gaspari, M., Rantanen, A., Trifunovic, A., Larsson, N.G. and Gustafsson, C.M. (2002) 'Mitochondrial transcription factors B1 and B2 activate transcription of human mtDNA', *Nature Genetics*, 31(3), pp. 289-294.

Falkenberg, M., Larsson, N.-G. and Gustafsson, C.M. (2007) 'DNA Replication and Transcription in Mammalian Mitochondria', *Annual Review of Biochemistry*, 76(1), pp. 679-699.

Fang, C., Bourdette, D. and Banker, G. (2012) 'Oxidative stress inhibits axonal transport: Implications for neurodegenerative diseases', *Molecular Neurodegeneration*, 7(1).

Fang, Y., Fu, D. and Shen, X.Z. (2010) 'The potential role of ubiquitin c-terminal hydrolases in oncogenesis', *Biochimica et Biophysica Acta - Reviews on Cancer*, 1806(1), pp. 1-6.

Ferreirinha, F., Quattrini, A., Pirozzi, M., Valsecchi, V., Dina, G., Broccoli, V., Auricchio, A., Piemonte, F., Tozzi, G., Gaeta, L., Casari, G., Ballabio, A. and Rugarli, E.I. (2004) 'Axonal degeneration in paraplegin-deficient mice is associated with abnormal mitochondria and impairment of axonal transport', *The Journal of Clinical Investigation*, 113(2), pp. 231-242.

Fleming, J.E., Miquel, J., Cottrell, S.F., Yengoyan, L.S. and Economos, A.C. (1982) 'Is Cell Aging Caused by Respiration-Dependent Injury to the Mitochondrial Genome?', *Gerontology*, 28(1), pp. 44-53.

Fornai, F., Schlüter, O.M., Lenzi, P., Gesi, M., Ruffoli, R., Ferrucci, M., Lazzeri, G., Busceti, C.L., Pontarelli, F., Battaglia, G., Pellegrini, A., Nicoletti, F., Ruggieri, S., Paparelli, A. and Südhof, T.C. (2005) 'Parkinson-like syndrome induced by continuous MPTP infusion: Convergent roles of the ubiquitin-proteasome system and α-synuclein', *Proceedings of the National Academy of Sciences of the United States of America*, 102(9), pp. 3413-3418.

Förster, A., Whitby, F.G. and Hill, C.P. (2003) 'The pore of activated 20S proteasomes has an ordered 7-fold symmetric conformation', *EMBO Journal*, 22(17), pp. 4356-4364.

Fraile, B., Martin, R., De Miguel, M.P., Arenas, M.I., Bethencourt, F.R., Peinado, F., Paniagua, R. and Santamaria, L. (1996) 'Light and electron microscopic immunohistochemical localization of protein gene product 9.5 and ubiquitin

immunoreactivities in the human epididymis and vas deferens', *Biology of Reproduction*, 55(2), pp. 291-297.

Fransson, Å., Ruusala, A. and Aspenström, P. (2003) 'Atypical Rho GTPases have roles in mitochondrial homeostasis and apoptosis', *Journal of Biological Chemistry*, 278(8), pp. 6495-6502.

Fransson, Å., Ruusala, A. and Aspenström, P. (2006) 'The atypical Rho GTPases Miro-1 and Miro-2 have essential roles in mitochondrial trafficking', *Biochemical and Biophysical Research Communications*, 344(2), pp. 500-510.

Frey, T.G. and Mannella, C.A. (2000) 'The internal structure of mitochondria', *Trends in Biochemical Sciences*, 25(7), pp. 319-324.

Fridlender, B., Fry, M., Bolden, A. and Weissbach, A. (1972) 'A new synthetic RNA-dependent DNA polymerase from human tissue culture cells (HeLa-fibroblast-synthetic oligonucleotides-template-purified enzymes)', *Proceedings of the National Academy of Sciences of the United States of America*, 69(2), pp. 452-455.

Friedman, J.R., Lackner, L.L., West, M., DiBenedetto, J.R., Nunnari, J. and Voeltz, G.K. (2011) 'ER Tubules Mark Sites of Mitochondrial Division', *Science*.

Friguet, B. and Szweda, L.I. (1997) 'Inhibition of the multicatalytic proteinase (proteasome) by 4-hydroxy-2-nonenal cross-linked protein', *FEBS Letters*, 405(1), pp. 21-25.

Fu, M., St-Pierre, P., Shankar, J., Wang, P.T.C., Joshi, B. and Nabi, I.R. (2013) 'Regulation of mitophagy by the Gp78 E3 ubiquitin ligase', *Molecular Biology of the Cell*, 24(8), pp. 1153-1162.

Fukuhara, N. (1995) 'Clinicopathological features of MERRF', *Muscle and Nerve*, 18(SUPPL. 3), pp. S90-S94.

Furukawa, Y., Vigouroux, S., Wong, H., Guttman, M., Rajput, A.H., Ang, L., Briand, M., Kish, S.J. and Briand, Y. (2002) 'Brain proteasomal function in sporadic Parkinson's disease and related disorders', *Annals of Neurology*, 51(6), pp. 779-782.

Gabuzda, D., Busciglio, J., Chen, L.B., Matsudaira, P. and Yankner, B.A. (1994) 'Inhibition of energy metabolism alters the processing of amyloid precursor protein and

induces a potentially amyloidogenic derivative', *Journal of Biological Chemistry*, 269(18), pp. 13623-13628.

Gaspari, M., Falkenberg, M., Larsson, N.G. and Gustafsson, C.M. (2004) 'The mitochondrial RNA polymerase contributes critically to promoter specificity in mammalian cells', *EMBO Journal*, 23(23), pp. 4606-4614.

Gasparini, L., Racchi, M., Benussi, L., Curti, D., Binetti, G., Bianchetti, A., Trabucchi, M. and Govoni, S. (1997) 'Effect of energy shortage and oxidative stress on amyloid precursor protein metabolism in COS cells', *Neuroscience Letters*, 231(2), pp. 113-117.

Gavilán, M.P., Pintado, C., Gavilán, E., García-Cuervo, L.M., Castaño, A., Ríos, R.M. and Ruano, D. (2012) 'Age-related differences in the dynamics of hippocampal proteasome recovery', *Journal of Neurochemistry*, 123(4), pp. 635-644.

Gebre, S., Reeber, S. and Sillitoe, R. (2012) 'Parasagittal compartmentation of cerebellar mossy fibers as revealed by the patterned expression of vesicular glutamate transporters VGLUT1 and VGLUT2', *Brain Structure and Function*, 217(2), pp. 165-180.

Gegg, M.E., Cooper, J.M., Chau, K.Y., Rojo, M., Schapira, A.H.V. and Taanman, J.W. (2010) 'Mitofusin 1 and mitofusin 2 are ubiquitinated in a PINK1/parkin-dependent manner upon induction of mitophagy', *Human Molecular Genetics*, 19(24), pp. 4861-4870.

Geisler, S., Holmström, K.M., Skujat, D., Fiesel, F.C., Rothfuss, O.C., Kahle, P.J. and Springer, W. (2010) 'PINK1/Parkin-mediated mitophagy is dependent on VDAC1 and p62/SQSTM1', *Nature Cell Biology*, 12(2), pp. 119-131.

Gerencser, A.A., Doczi, J., Töröcsik, B., Bossy-Wetzel, E. and Adam-Vizi, V. (2008) 'Mitochondrial Swelling Measurement In Situ by Optimized Spatial Filtering: Astrocyte-Neuron Differences', *Biophysical Journal*, 95(5), pp. 2583-2598.

Gieche, J., Mehlhase, J., Licht, A., Zacke, T., Sitte, N. and Grune, T. (2001) 'Protein oxidation and proteolysis in RAW264.7 macrophages: Effects of PMA activation', *Biochimica et Biophysica Acta - Molecular Cell Research*, 1538(2-3), pp. 321-328.

Giles, R.E., Blanc, H., Cann, H.M. and Wallace aD, C. (1980) 'Maternal inheritance of human mitochondrial DNA', *Proceedings of the National Academy of Sciences of the United States of America*, 77(11 I), pp. 6715-6719.

Gilkerson, R.W., Schon, E.A., Hernandez, E. and Davidson, M.M. (2008) 'Mitochondrial nucleoids maintain genetic autonomy but allow for functional complementation', *Journal of Cell Biology*, 181(7), pp. 1117-1128.

Glater, E.E., Megeath, L.J., Stowers, R.S. and Schwarz, T.L. (2006) 'Axonal transport of mitochondria requires milton to recruit kinesin heavy chain and is light chain independent', *Journal of Cell Biology*, 173(4), pp. 545-557.

Goizet, C., Boukhris, A., Mundwiller, E., Tallaksen, C., Forlani, S., Toutain, A., Carriere, N., Paquis, V., Depienne, C., Durr, A., Stevanin, G. and Brice, A. (2009) 'Complicated forms of autosomal dominant hereditary spastic paraplegia are frequent in SPG10', *Human Mutation*, 30(2), pp. E376-E385.

Gong, B., Cao, Z., Zheng, P., Vitolo, O.V., Liu, S., Staniszewski, A., Moolman, D., Zhang, H., Shelanski, M. and Arancio, O. (2006) 'Ubiquitin Hydrolase Uch-L1 Rescues β-Amyloid-Induced Decreases in Synaptic Function and Contextual Memory', *Cell*, 126(4), pp. 775-788.

Gordon, S.L. and Cousin, M.A. (2014) 'The Sybtraps: Control of Synaptobrevin Traffic by Synaptophysin, α-Synuclein and AP-180', *Traffic*, 15(3), pp. 245-254.

Goto, A., Wang, Y.L., Kabuta, T., Setsuie, R., Osaka, H., Sawa, A., Ishiura, S. and Wada, K. (2009) 'Proteomic and histochemical analysis of proteins involved in the dying-back-type of axonal degeneration in the gracile axonal dystrophy (gad) mouse', *Neurochemistry International*, 54(5-6), pp. 330-338.

Goto, Y., Horai, S., Matsuoka, T., Koga, Y., Nihei, K., Kobayashi, M. and Nonaka, I. (1992) 'Mitochondrial myopathy, encephalopathy, lactic acidosis, and stroke-like episodes (MELAS): A correlative study of the clinical features and mitochondrial DNA mutation', *Neurology*, 42(3), pp. 545-550.

Goto, Y.I., Nonaka, I. and Horai, S. (1990) 'A mutation in the tRNALeu(UUR) gene associated with the MELAS subgroup of mitochondrial encephalomyopathies', *Nature*, 348(6302), pp. 651-653.

Gray, D.A., Tsirigotis, M. and Woulfe, J. (2003) 'Ubiquitin, proteasomes, and the aging brain', *Science of aging knowledge environment [electronic resource] : SAGE KE*, 2003(34).

Graziewicz, M.A., Longley, M.J. and Copeland, W.C. (2006) 'DNA polymerase γ in mitochondrial DNA replication and repair', *Chemical Reviews*, 106(2), pp. 383-405.

Groemer, T.W., Thiel, C.S., Holt, M., Riedel, D., Hua, Y., Hüve, J., Wilhelm, B.G. and Klingauf, J. (2011) 'Amyloid precursor protein is trafficked and secreted via synaptic vesicles', *PLoS ONE*, 6(4).

Groll, M., Ditzel, L., Löwe, J., Stock, D., Bochtler, M., Bartunik, H.D. and Huber, R. (1997) 'Structure of 20S proteasome from yeast at 2.4 Å resolution', *Nature*, 386(6624), pp. 463-471.

Grune, T., Jung, T., Merker, K. and Davies, K.J.A. (2004) 'Decreased proteolysis caused by protein aggregates, inclusion bodies, plaques, lipofuscin, ceroid, and 'aggresomes' during oxidative stress, aging, and disease', *The International Journal of Biochemistry & Cell Biology*, 36(12), pp. 2519-2530.

Guliaeva, N.A., Kuznetsova, E.A. and Gaziev, A.I. (2006) 'Proteins associated with mitochondrial DNA protect it against the action of X-rays and hydrogen peroxide', *Biofizika.*, 51(4), pp. 692-697.

Haas, A.L., Warms, J.V., Hershko, A. and Rose, I.A. (1982) 'Ubiquitin-activating enzyme. Mechanism and role in protein-ubiquitin conjugation', *Journal of Biological Chemistry*, 257(5), pp. 2543-2548.

Haass, C., Kaether, C., Thinakaran, G. and Sisodia, S. (2012) 'Trafficking and proteolytic processing of APP', *Cold Spring Harbor Perspectives in Medicine*, 2(5).

Hannah, M.J., Schmidt, A.A. and Huttner, W.B. 15 (1999) 'Synaptic vesicle biogenesis'. pp. 733-798. Available at: http://www.scopus.com/inward/record.url?eid=2-s2.0-0033281065&partnerID=40&md5=86b0a9d5262d2750b923e0e45c7d5751.

Harman, D. (1956) 'Aging: a theory based on free radical and radiation chemistry', *Journal of gerontology*, 11(3), pp. 298-300.

Harman, D. (1972) 'The biologic clock: the mitochondria?', *Journal of the American Geriatric Society*, 20, pp. 145-147.

Hawkes, R. (2001) 'Cerebellum: Anatomy and Organisation', in *eLS*. John Wiley & Sons, Ltd.

Hay-Koren, A., Caspi, M., Zilberberg, A. and Rosin-Arbesfeld, R. (2011) 'The EDD E3 ubiquitin ligase ubiquitinates and up-regulates β-catenin', *Molecular Biology of the Cell*, 22(3), pp. 399-411.

Hershko, A. and Ciechanover, A. 67 (1998) 'The ubiquitin system'. pp. 425-479. Available at: http://www.scopus.com/inward/record.url?eid=2-s2.0-0031657807&partnerID=40&md5=459b4f8647dc5c042245f5b56958dcda.

Hirano, M., Ricci, E., Richard Koenigsberger, M., Defendini, R., Pavlakis, S.G., DeVivo, D.C., DiMauro, S. and Rowland, L.P. (1992) 'MELAS: An original case and clinical criteria for diagnosis', *Neuromuscular Disorders*, 2(2), pp. 125-135.

Hochstrasser, M. (2000) 'Evolution and function of ubiquitin-like protein-conjugation systems', *Nature Cell Biology*, 2(8), pp. E153-E157.

Hochstrasser, M. (2006) 'Lingering mysteries of ubiquitin-chain assembly', *Cell*, 124(1), pp. 27-34.

Holloszy, J.O. and Booth, F.W. (1976) 'Biochemical Adaptations to Endurance Exercise in Muscle', *Annual Review of Physiology*, 38(1), pp. 273-291.

Holt, I.J. and Reyes, A. (2012) 'Human mitochondrial DNA replication', *Cold Spring Harbor Perspectives in Biology*, 4(12).

Horibe, T. and Hoogenraad, N.J. (2007) 'The <italic>Chop</italic> Gene Contains an Element for the Positive Regulation of the Mitochondrial Unfolded Protein Response', *PLoS ONE*, 2(9), p. e835.

Horiuchi, D., Barkus, R.V., Pilling, A.D., Gassman, A. and Saxton, W.M. (2005) 'APLIP1, a Kinesin Binding JIP-1/JNK Scaffold Protein, Influences the Axonal Transport of Both Vesicles and Mitochondria in Drosophila', *Current Biology*, 15(23), pp. 2137-2141.

Horn, S.R., Thomenius, M.J., Johnson, E.S., Freel, C.D., Wu, J.Q., Coloff, J.L., Yang, C.-S., Tang, W., An, J., Ilkayeva, O.R., Rathmell, J.C., Newgard, C.B. and Kornbluth, S. (2011) 'Regulation of mitochondrial morphology by APC/CCdh1-mediated control of Drp1 stability', *Molecular Biology of the Cell*, 22(8), pp. 1207-1216.

Huang, Q. and Figueiredo-Pereira, M.E. (2010) 'Ubiquitin/proteasome pathway impairment in neurodegeneration: Therapeutic implications', *Apoptosis*, 15(11), pp. 1292-1311.

Huang, T.T., Carlson, E.J., Gillespie, A.M., Shi, Y. Epstein, C.J. (2000) 'Ubiquitous overexpression of CuZn superoxide dismutase does not extendlife span in mice', *The Journals of Gerontology Series A: Biological Sciences and Medical Sciences*, 55(1), pp. B5-B9.

Hurd, D.D. and Saxton, W.M. (1996) 'Kinesin mutations cause motor neuron disease phenotypes by disrupting fast axonal transport in Drosophila', *Genetics*, 144(3), pp. 1075-1085.

Husnjak, K., Elsasser, S., Zhang, N., Chen, X., Randles, L., Shi, Y., Hofmann, K., Walters, K.J., Finley, D. and Dikic, I. (2008) 'Proteasome subunit Rpn13 is a novel ubiquitin receptor', *Nature*, 453(7194), pp. 481-488.

Hussain, S., Foreman, O., Perkins, S.L., Witzig, T.E., Miles, R.R., Van Deursen, J. and Galardy, P.J. (2010) 'The de-ubiquitinase UCH-L1 is an oncogene that drives the development of lymphoma in vivo by deregulating PHLPP1 and Akt signaling', *Leukemia*, 24(9), pp. 1641-1655.

Ichihara, N., Wu, J., Hua Chui, D., Yamazaki, K., Wakabayashi, T. and Kikuchi, T. (1995) 'Axonal degeneration promotes abnormal accumulation of amyloid β-protein in ascending gracile tract of gracile axonal dystrophy (GAD) mouse', *Brain Research*, 695(2), pp. 173-178.

Ihara, Y., Morishima-Kawashima, M. and Nixon, R. (2012) 'The ubiquitin-proteasome system and the autophagic-lysosomal system in Alzheimer disease', *Cold Spring Harbor Perspectives in Medicine*, 2(8).

Ii, K., Ito, H., Tanaka, K. and Hirano, A. (1997) 'Immunocytochemical co-localization of the proteasome in ubiquitinated structures in neurodegenerative diseases and the elderly', *Journal of neuropathology and experimental neurology*, 56(2), pp. 125-131.

Irrcher, I., Aleyasin, H., Seifert, E.L., Hewitt, S.J., Chhabra, S., Phillips, M., Lutz, A.K., Rousseaux, M.W.C., Bevilacqua, L., Jahani-Asl, A., Callaghan, S., MacLaurin, J.G., Winklhofer, K.F., Rizzu, P., Rippstein, P., Kim, R.H., Chen, C.X., Fon, E.A., Slack, R.S., Harper, M.E., McBride, H.M., Mak, T.W. and Park, D.S. (2010) 'Loss of the Parkinson's disease-linked gene DJ-1 perturbs mitochondrial dynamics', *Human Molecular Genetics*, 19(19), pp. 3734-3746.

Ito, M. 978 (2002) 'Historical review of the significance of the cerebellum and the role of purkinje cells in motor learning'. pp. 273-288. Available at: http://www.scopus.com/inward/record.url?eid=2-s2.0-0036964705&partnerID=40&md5=dfbcaed555c86692f036009fa7f2b1d0.

Jacobson, J. and Duchen, M.R. (2004) 'Interplay between mitochondria and cellular calcium signalling', *Molecular and Cellular Biochemistry*, 256-257(1-2), pp. 209-218.

Jahngen-Hodge, J., Obin, M.S., Gong, X., Shang, F., Nowell Jr, T.R., Gong, J., Abasi, H., Blumberg, J. and Taylor, A. (1997) 'Regulation of ubiquitin-conjugating enzymes by glutathione following oxidative stress', *Journal of Biological Chemistry*, 272(45), pp. 28218-28226.

Jahns, H., Callanan, J.J., McElroy, M.C., Sammin, D.J. and Bassett, H.F. (2006) 'Age-related and non-age-related changes in 100 surveyed horse brains', *Veterinary Pathology*, 43(5), pp. 740-750.

James, D.I., Parone, P.A., Mattenberger, Y. and Martinou, J.C. (2003) 'hFis1, a novel component of the mammalian mitochondrial fission machinery', *Journal of Biological Chemistry*, 278(38), pp. 36373-36379.

Jang, M.J., Baek, S.H. and Kim, J.H. (2011) 'UCH-L1 promotes cancer metastasis in prostate cancer cells through EMT induction', *Cancer Letters*, 302(2), pp. 128-135.

Jeong, S.Y. and Seol, D.W. (2008) 'The role of mitochondria in apoptosis', *Journal of Biochemistry and Molecular Biology*, 41(1), pp. 11-22.

Jin, S.M., Lazarou, M., Wang, C., Kane, L.A., Narendra, D.P. and Youle, R.J. (2010) 'Mitochondrial membrane potential regulates PINK1 import and proteolytic destabilization by PARL', *Journal of Cell Biology*, 191(5), pp. 933-942.

Jung, S.H., Jae, S.H., Chang, I. and Kim, S. (2007) 'Age-associated decrease in proteasome content and activities in human dermal fibroblasts: Restoration of normal level of proteasome subunits reduces aging markers in fibroblasts from elderly persons', *Journals of Gerontology - Series A Biological Sciences and Medical Sciences*, 62(5), pp. 490-499.

Jung, T. and Grune, T. (2008) 'The proteasome and its role in the degradation of oxidized proteins', *IUBMB Life*, 60(11), pp. 743-752.

Kabuta, T., Setsuie, R., Mitsui, T., Kinugawa, A., Sakurai, M., Aoki, S., Uchida, K. and Wada, K. (2008) 'Aberrant molecular properties shared by familial Parkinson's disease-associated mutant UCH-L1 and carbonyl-modified UCH-L1', *Human Molecular Genetics*, 17(10), pp. 1482-1496.

Kaether, C., Skehel, P. and Dotti, C.G. (2000) 'Axonal membrane proteins are transported in distinct carriers: A two- color video microscopy study in cultured hippocampal neurons', *Molecular Biology of the Cell*, 11(4), pp. 1213-1224.

Kang, J.-S., Tian, J.-H., Pan, P.-Y., Zald, P., Li, C., Deng, C. and Sheng, Z.-H. (2008) 'Docking of Axonal Mitochondria by Syntaphilin Controls Their Mobility and Affects Short-Term Facilitation', *Cell*, 132(1), pp. 137-148.

Karbowski, M. and Neutzner, A. (2012) 'Neurodegeneration as a consequence of failed mitochondrial maintenance', *Acta Neuropathologica*, 123(2), pp. 157-171.

Karbowski, M., Neutzner, A. and Youle, R.J. (2007) 'The mitochondrial E3 ubiquitin ligase MARCH5 is required for Drp1 dependent mitochondrial division', *Journal of Cell Biology*, 178(1), pp. 71-84.

Kaufman, R.J. and Malhotra, J.D. (2014) 'Calcium trafficking integrates endoplasmic reticulum function with mitochondrial bioenergetics', *Biochimica et Biophysica Acta - Molecular Cell Research*, 1843(10), pp. 2233-2239.

Keller, J.N., Hanni, K.B. and Markesbery, W.R. (2000) 'Impaired proteasome function in Alzheimer's disease', *Journal of Neurochemistry*, 75(1), pp. 436-439.

Kennedy, H.S., Puth, F., Van Hoy, M. and Le Pichon, C. (2011) 'A method for removing the brain and spinal cord as one unit from adult mice and rats', *Lab Animal*, 40(2), pp. 53-57.

Kevei, É. and Hoppe, T. (2014) 'Ubiquitin sets the timer: Impacts on aging and longevity', *Nature Structural and Molecular Biology*, 21(4), pp. 290-292.

Kiernan, J.A., Rajakumar, N. (2013) *Barr's The Human Nervous System: an anatomical viewpoint*. 10 edn.

Kikuchi, T., Mukoyama, M., Yamazaki, K. and Moriya, H. (1990) 'Axonal degeneration of ascending sensory neurons in gracile axonal dystrophy mutant mouse', *Acta Neuropathologica*, 80(2), pp. 145-151.

Kim, Y.C., Li, X., Thompson, D. and Demartino, G.N. (2013) 'ATP binding by proteasomal ATPases regulates cellular assembly and substrate-induced functions of the 26 S proteasome', *Journal of Biological Chemistry*, 288(5), pp. 3334-3345.

Kirino, Y., Yasukawa, T., Ohta, S., Akira, S., Ishihara, K., Watanabe, K. and Suzuki, T. (2004) 'Codon-specific translational defect caused by a wobble modification deficiency in mutant tRNA from a human mitochondrial disease', *Proceedings of the National Academy of Sciences of the United States of America*, 101(42), pp. 15070-15075.

Kish-Trier, E. and Hill, C.P. 42 (2013) 'Structural biology of the proteasome'. pp. 29-49. Available at: http://www.scopus.com/inward/record.url?eid=2-s2.0-84876916040&partnerID=40&md5=39de016cb809e7c7ac1c3fbe19734bac.

Kish, S.J., Bergeron, C., Rajput, A., Dozic, S., Mastrogiacomo, F., Chang, L.J., Wilson, J.M., DiStefano, L.M. and Nobrega, J.N. (1992) 'Brain cytochrome oxidase in Alzheimer's disease', *Journal of Neurochemistry*, 59(2), pp. 776-779.

Kitada, T., Asakawa, S., Hattori, N., Matsumine, H., Yamamura, Y., Minoshima, S., Yokochi, M., Mizuno, Y. and Shimizu, N. (1998) 'Mutations in the parkin gene cause autosomal recessive juvenile parkinsonism', *Nature*, 392(6676), pp. 605-608.

Koga, Y., Povalko, N., Nishioka, J., Katayama, K., Yatsuga, S. and Matsuishi, T. (2012) 'Molecular pathology of MELAS and l-arginine effects', *Biochimica et Biophysica Acta (BBA) - General Subjects*, 1820(5), pp. 608-614.

Kolchinskaya, L.I. and Malysheva, M.K. (2004) 'Activity of calpain in subcellular fractions of the rat brain', *Neurophysiology*, 36(4), pp. 231-237.

Kopek, B.G., Shtengel, G., Xu, C.S., Clayton, D.A. and Hess, H.F. (2012) 'Correlative 3D superresolution fluorescence and electron microscopy reveal the relationship of mitochondrial nucleoids to membranes', *Proceedings of the National Academy of Sciences*, 109(16), pp. 6136-6141.

Koppen, M. and Langer, T. (2007) 'Protein degradation within mitochondria: Versatile activities of AAA proteases and other peptidases', *Critical Reviews in Biochemistry and Molecular Biology*, 42(3), pp. 221-242.

Korhonen, J.A., Gaspari, M. and Falkenberg, M. (2003) 'TWINKLE has 5′ → 3′ DNA helicase activity and is specifically stimulated by mitochondrial single-stranded DNA-binding protein', *Journal of Biological Chemistry*, 278(49), pp. 48627-48632.

Kowald, A. and Kirkwood, T.B.L. (2000) 'Accumulation of defective mitochondria through delayed degradation of damaged organelles and its possible role in the ageing of post-mitotic and dividing cells', *Journal of Theoretical Biology*, 202(2), pp. 145-160.

Kowald, A. and Kirkwood, T.B.L. (2011) 'Evolution of the mitochondrial fusion - Fission cycle and its role in aging', *Proceedings of the National Academy of Sciences of the United States of America*, 108(25), pp. 10237-10242.

Krishnan, K.J., Greaves, L.C., Reeve, A.K. and Turnbull, D. (2007) 'The ageing mitochondrial genome', *Nucleic Acids Research*, 35(22), pp. 7399-7405.

Krishnan, K.J., Ratnaike, T.E., De Gruyter, H.L.M., Jaros, E. and Turnbull, D.M. (2012) 'Mitochondrial DNA deletions cause the biochemical defect observed in Alzheimer's disease', *Neurobiology of Aging*, 33(9), pp. 2210-2214.

Kruegel, U., Robison, B., Dange, T., Kahlert, G., Delaney, J.R., Kotireddy, S., Tsuchiya, M., Tsuchiyama, S., Murakami, C.J., Schleit, J., Sutphin, G., Carr, D., Tar, K., Dittmar, G., Kaeberlein, M., Kennedy, B.K. and Schmidt, M. (2011) 'Elevated proteasome capacity extends replicative lifespan in saccharomyces cerevisiae', *PLoS Genetics*, 7(9).

Kukat, C. and Larsson, N.-G. (2013) 'mtDNA makes a U-turn for the mitochondrial nucleoid', *Trends in Cell Biology*, 23(9), pp. 457-463.

Kuma, A., Hatano, M., Matsui, M., Yamamoto, A., Nakaya, H., Yoshimori, T., Ohsumi, Y., Tokuhisa, T. and Mizushima, N. (2004) 'The role of autophagy during the early neonatal starvation period', *Nature*, 432(7020), pp. 1032-1036.

Kushnareva, Y., Murphy, A.N. and Andreyev, A. (2002) 'Complex I-mediated reactive oxygen species generation: modulation by cytochrome c and NAD(P)+ oxidation-reduction state', *Biochem. J.*, 368(2), pp. 545-553.

Kyriakouli, D.S., Boesch, P., Taylor, R.W. and Lightowlers, R.N. (2008) 'Progress and prospects: gene therapy for mitochondrial DNA disease', *Gene Ther*, 15(14), pp. 1017-1023.

Lam, Y.A., Lawson, T.G., Velayutham, M., Zweler, J.L. and Pickart, C.M. (2002) 'A proteasomal ATPase subunit recognizes the polyubiquitin degradation signal', *Nature*, 416(6882), pp. 763-767.

Lam, Y.A., Pickart, C.M., Alban, A., Landon, M., Jamieson, C., Ramage, R., Mayer, R.J. and Layfield, R. (2000) 'Inhibition of the ubiquitin-proteasome system in Alzheimer's disease', *Proceedings of the National Academy of Sciences of the United States of America*, 97(18), pp. 9902-9906.

Lander, G.C., Estrin, E., Matyskiela, M.E., Bashore, C., Nogales, E. and Martin, A. (2012) 'Complete subunit architecture of the proteasome regulatory particle', *Nature*, 482(7384), pp. 186-191.

Larsell, O. (1952) 'The morphogenesis and adult pattern of the lobules and fissures of the cerebellum of the white rat', *The Journal of Comparative Neurology*, 97(2), pp. 281-356.

Larsen, C.N., Krantz, B.A. and Wilkinson, K.D. (1998) 'Substrate specificity of deubiquitinating enzymes: Ubiquitin C-terminal hydrolases', *Biochemistry*, 37(10), pp. 3358-3368.

Larsen, C.N., Price, J.S. and Wilkinson, K.D. (1996) 'Substrate binding and catalysis by ubiquitin C-terminal hydrolases: Identification of two active site residues', *Biochemistry*, 35(21), pp. 6735-6744.

Larsson, N.G. 79 (2010) 'Somatic mitochondrial DNA mutations in mammalian aging' *Annual Review of Biochemistry*. pp. 683-706. Available at:

http://www.scopus.com/inward/record.url?eid=2-s2.0-77953627194&partnerID=40&md5=ea381cdaf309789b83c0994c2eb20b89.

Lax, N.Z., Hepplewhite, P.D., Reeve, A.K., Nesbitt, V., McFarland, R., Jaros, E., Taylor, R.W. and Turnbull, D.M. (2012) 'Cerebellar ataxia in patients with mitochondrial DNA disease: A molecular clinicopathological study', *Journal of neuropathology and experimental neurology*, 71(2), pp. 148-161.

Leboucher, G.P., Tsai, Y.C., Yang, M., Shaw, K.C., Zhou, M., Veenstra, T.D., Glickman, M.H. and Weissman, A.M. (2012) 'Stress-Induced Phosphorylation and Proteasomal Degradation of Mitofusin 2 Facilitates Mitochondrial Fragmentation and Apoptosis', *Molecular Cell*, 47(4), pp. 547-557.

LeDoux, S.P., Wilson, G.L., Beecham, E.J., Stevnsner, T., Wassermann, K. and Bohr, V.A. (1992) 'Repair of mitochondrial DNA after various types of DNA damage in Chinese hamster ovary cells', *Carcinogenesis*, 13(11), pp. 1967-1973.

Lee, J.Y., Nagano, Y., Taylor, J.P., Lim, K.L. and Yao, T.P. (2010) 'Disease-causing mutations in Parkin impair mitochondrial ubiquitination, aggregation, and HDAC6-dependent mitophagy', *Journal of Cell Biology*, 189(4), pp. 671-679.

Lee, S., Jeong, S.-Y., Lim, W.-C., Kim, S., Park, Y.-Y., Sun, X., Youle, R.J. and Cho, H. (2007) 'Mitochondrial Fission and Fusion Mediators, hFis1 and OPA1, Modulate Cellular Senescence', *Journal of Biological Chemistry*, 282(31), pp. 22977-22983.

Lee, Y.J., Jeong, S.Y., Karbowski, M., Smith, C.L. and Youle, R.J. (2004) 'Roles of the mammalian mitochondrial fission and fusion mediators Fis1, Drp1, Opa1 in apoptosis', *Molecular Biology of the Cell*, 15(11), pp. 5001-5011.

Lennox, G., Lowe, J., Morrell, K., Landon, M. and Mayer, R.J. (1989) 'Anti-ubiquitin immunocytochemistry is more sensitive than conventional techniques in the detection of diffuse Lewy body disease', *Journal of Neurology Neurosurgery and Psychiatry*, 52(1), pp. 67-71.

Lerin, C., Rodgers, J.T., Kalume, D.E., Kim, S.-h., Pandey, A. and Puigserver, P. (2006) 'GCN5 acetyltransferase complex controls glucose metabolism through transcriptional repression of PGC-1α', *Cell Metabolism*, 3(6), pp. 429-438.

Leroy, E., Boyer, R., Auburger, G., Leube, B., Ulm, G., Mezey, E., Harta, G., Brownstein, M.J., Jonnalagada, S., Chernova, T., Dehejia, A., Lavedan, C., Gasser, T., Steinbach, P.J., Wilkinson, K.D. and Polymeropoulos, M.H. (1998) 'The ubiquitin pathway in Parkinson's disease [6]', *Nature*, 395(6701), pp. 451-452.

Li, J.Y. and Conforti, L. (2013) 'Axonopathy in Huntington's disease', *Experimental Neurology*, 246, pp. 62-71.

Li, J.Y. and Dahlström, A. (1997) 'Axonal transport of synaptic vesicle proteins in the rat optic nerve', *Journal of Neurobiology*, 32(2), pp. 237-250.

Li, W., Bengtson, M.H., Ulbrich, A., Matsuda, A., Reddy, V.A., Orth, A., Chanda, S.K., Batalov, S. and Joazeiro, C.A.P. (2008) 'Genome-wide and functional annotation of human E3 ubiquitin ligases identifies MULAN, a mitochondrial E3 that regulates the organelle's dynamics and signaling', *PLoS ONE*, 3(1).

Ligon, L.A. and Steward, O. (2000) 'Movement of mitochondria in the axons and dendrites of cultured hippocampal neurons', *The Journal of Comparative Neurology*, 427(3), pp. 340-350.

Lill, R., Diekert, K., Kaut, A., Lange, H., Pelzer, W., Prohl, C. and Kispal, G. (1999) 'The essential role of mitochondria in the biogenesis of cellular iron-sulfur proteins', *Biological Chemistry*, 380(10), pp. 1157-1166.

Lima, C.F. and Rattan, S.I. (2010) 'Determination of proteasomal activities', *Methods in molecular biology (Clifton, N.J.)*, 648, pp. 183-192.

Lingor, P., Koch, J., Tönges, L. and Bähr, M. (2012) 'Axonal degeneration as a therapeutic target in the CNS', *Cell and Tissue Research*, 349(1), pp. 289-311.

Liu, S., Sawada, T., Lee, S., Yu, W., Silverio, G., Alapatt, P., Millan, I., Shen, A., Saxton, W., Kanao, T., Takahashi, R., Hattori, N., Imai, Y. and Lu, B. (2012) 'Parkinson's disease-associated kinase PINK1 regulates miro protein level and axonal transport of mitochondria', *PLoS Genetics*, 8(3).

Liu, Y., Fallon, L., Lashuel, H.A., Liu, Z. and Lansbury Jr, P.T. (2002) 'The UCH-L1 gene encodes two opposing enzymatic activities that affect α-synuclein degradation and Parkinson's disease susceptibility', *Cell*, 111(2), pp. 209-218.

Liu, Y., Lashuel, H.A., Choi, S., Xing, X., Case, A., Ni, J., Yeh, L.-A., Cuny, G.D., Stein, R.L. and Lansbury Jr, P.T. (2003) 'Discovery of Inhibitors that Elucidate the Role of UCH-L1 Activity in the H1299 Lung Cancer Cell Line', *Chemistry & Biology*, 10(9), pp. 837-846.

Lokireddy, S., Wijesoma, Isuru W., Teng, S., Bonala, S., Gluckman, Peter D., McFarlane, C., Sharma, M. and Kambadur, R. (2012) 'The Ubiquitin Ligase Mul1 Induces Mitophagy in Skeletal Muscle in Response to Muscle-Wasting Stimuli', *Cell Metabolism*, 16(5), pp. 613-624.

Longley, M.J., Prasad, R., Srivastava, D.K., Wilson, S.H. and Copeland, W.C. (1998) 'Identification of 5′ -deoxyribose phosphate lyase activity in human DNA polymerase γ and its role in mitochondrial base excision repair in vitro', *Proceedings of the National Academy of Sciences*, 95(21), pp. 12244-12248.

López-Lluch, G., Irusta, P.M., Navas, P. and de Cabo, R. (2008) 'Mitochondrial biogenesis and healthy aging', *Experimental Gerontology*, 43(9), pp. 813-819.

Löw, P. (2011) 'The role of ubiquitin-proteasome system in ageing', *General and Comparative Endocrinology*, 172(1), pp. 39-43.

Lowe, J., McDermott, H., Landon, M., Mayer, R.J. and Wilkinson, K.D. (1990) 'Ubiquitin carboxyl-terminal hydrolase (PGP 9.5) is selectively present in ubiquitinated inclusion bodies characteristic of human neurodegenerative diseases', *Journal of Pathology*, 161(2), pp. 153-160.

Lowe, J., Stock, D., Jap, B., Zwickl, P., Baumeister, W. and Huber, R. (1995) 'Crystal structure of the 20S proteasome from the archaeon T. acidophilum at 3.4 Å resolution', *Science*, 268(5210), pp. 533-539.

MacAskill, A.F., Brickley, K., Stephenson, F.A. and Kittler, J.T. (2009) 'GTPase dependent recruitment of Grif-1 by Miro1 regulates mitochondrial trafficking in hippocampal neurons', *Molecular and Cellular Neuroscience*, 40(3), pp. 301-312.

Mancall, E.L., Brock, D.G. (2011) *Gray's Clinical Neuroanatomy: The anatomic basis for Clinical Neuroscience*. Saunders.

Mancuso, M., Orsucci, D., Angelini, C., Bertini, E., Carelli, V., Comi, G.P., Minetti, C., Moggio, M., Mongini, T., Servidei, S., Toninc, P., Toscano, A., Uziel, G., Bruno, C., Ienco, E.C., Filosto, M., Lamperti, C., Martinelli, D., Moroni, I., Musumeci, O., Pegoraro, E., Ronchi, D., Santorelli, F.M., Sauchelli, D., Scarpelli, M., Sciacco, M., Spinazzi, M., Valentino, M.L., Vercelli, L., Zeviani, M. and Siciliano, G. (2013) 'Phenotypic heterogeneity of the 8344A>G mtDNA "MERRF" mutation', *Neurology*, 80(22), pp. 2049-2054.

Mandavilli, B.S., Santos, J.H. and Van Houten, B. (2002) 'Mitochondrial DNA repair and aging', *Mutation Research/Fundamental and Molecular Mechanisms of Mutagenesis*, 509(1–2), pp. 127-151.

Mannella, C.A., Lederer, W.J. and Jafri, M.S. (2013) 'The connection between inner membrane topology and mitochondrial function', *Journal of Molecular and Cellular Cardiology*, 62, pp. 51-57.

Maraganore, D.M., Farrer, M.J., Hardy, J.A., Lincoln, S.J., McDonnell, S.K. and Rocca, W.A. (1999) 'Case-control study of the ubiquitin carboxy-terminal hydrolase L1 gene in Parkinson's disease', *Neurology*, 53(8), pp. 1858-1860.

Marangoni, M., Adalbert, R., Janeckova, L., Patrick, J., Kohli, J., Coleman, M.P. and Conforti, L. (2014) 'Age-related axonal swellings precede other neuropathological hallmarks in a knock-in mouse model of Huntington's disease', *Neurobiology of Aging*, 35(10), pp. 2382-2393.

Martins-Branco, D., Esteves, A.R., Santos, D., Arduino, D.M., Swerdlow, R.H., Oliveira, C.R., Januario, C. and Cardoso, S.M. (2012) 'Ubiquitin proteasome system in Parkinson's disease: A keeper or a witness?', *Experimental Neurology*, 238(2), pp. 89-99.

Matsuda, N., Sato, S., Shiba, K., Okatsu, K., Saisho, K., Gautier, C.A., Sou, Y.S., Saiki, S., Kawajiri, S., Sato, F., Kimura, M., Komatsu, M., Hattori, N. and Tanaka, K. (2010) 'PINK1 stabilized by mitochondrial depolarization recruits Parkin to damaged mitochondria and activates latent Parkin for mitophagy', *Journal of Cell Biology*, 189(2), pp. 211-221.

McKeon, T.A. and Lyman, M.L. (1991) 'Calcium ion improves electrophoretic transfer of calmodulin and other small proteins', *Analytical Biochemistry*, 193(1), pp. 125-130.

McNaught, K.S.P., Belizaire, R., Isacson, O., Jenner, P. and Olanow, C.W. (2003) 'Altered proteasomal function in sporadic Parkinson's disease', *Experimental Neurology*, 179(1), pp. 38-46.

McNaught, K.S.P. and Jenner, P. (2001) 'Proteasomal function is impaired in substantia nigra in Parkinson's disease', *Neuroscience Letters*, 297(3), pp. 191-194.

Meray, R.K. and Lansbury Jr, P.T. (2007) 'Reversible monoubiquitination regulates the Parkinson disease-associated ubiquitin hydrolase UCH-L1', *Journal of Biological Chemistry*, 282(14), pp. 10567-10575.

Mermerian, A.H., Case, A., Stein, R.L. and Cuny, G.D. (2007) 'Structure–activity relationship, kinetic mechanism, and selectivity for a new class of ubiquitin C-terminal hydrolase-L1 (UCH-L1) inhibitors', *Bioorganic & Medicinal Chemistry Letters*, 17(13), pp. 3729-3732.

Meyer-Schwesinger, C., Meyer, T.N., Sievert, H., Hoxha, E., Sachs, M., Klupp, E.M., Münster, S., Balabanov, S., Carrier, L., Helmchen, U., Thaiss, F. and Stahl, R.A.K. (2011) 'Ubiquitin C-terminal hydrolase-L1 activity induces polyubiquitin accumulation in podocytes and increases proteinuria in rat membranous nephropathy', *American Journal of Pathology*, 178(5), pp. 2044-2057.

Meyer, H.J. and Rape, M. (2014) 'Enhanced protein degradation by branched ubiquitin chains', *Cell*, 157(4), pp. 910-921.

Mi, W., Beirowski, B., Gillingwater, T.H., Adalbert, R., Wagner, D., Grumme, D., Osaka, H., Conforti, L., Arnhold, S., Addicks, K., Wada, K., Ribchester, R.R. and Coleman, M.P. (2005) 'The slow Wallerian degeneration gene, WldS, inhibits axonal spheroid pathology in gracile axonal dystrophy mice', *Brain*, 128(2), pp. 405-416.

Milenkovic, D., Müller, J., Stojanovski, D., Pfanner, N. and Chacinska, A. (2007) 'Diverse mechanisms and machineries for import of mitochondrial proteins', *Biological Chemistry*, 388(9), pp. 891-897.

Miquel, J., Economos, A.C., Fleming, J. and Johnson Jr, J.E. (1980) 'Mitochondrial role in cell aging', *Experimental Gerontology*, 15(6), pp. 575-591.

Misaka, T., Miyashita, T. and Kubo, Y. (2002) 'Primary structure of a dynamin-related mouse mitochondrial GTPase and its distribution in brain, subcellular localization, and

effect on mitochondrial morphology', *Journal of Biological Chemistry*, 277(18), pp. 15834-15842.

Mitchell, P. (1966) 'CHEMIOSMOTIC COUPLING IN OXIDATIVE AND PHOTOSYNTHETIC PHOSPHORYLATION', *Biological Reviews*, 41(3), pp. 445-501.

Mitchell, P. (1976) 'Possible molecular mechanisms of the protonmotive function of cytochrome systems', *Journal of Theoretical Biology*, 62(2), pp. 327-367.

Miura, H., Oda, K., Endo, C., Yamazaki, K., Shibasaki, H. and Kikuchi, T. (1993) 'Progressive degeneration of motor nerve terminals in GAD mutant mouse with hereditary sensory axonopathy', *Neuropathology and Applied Neurobiology*, 19(1), pp. 41-51.

Miwa, S., Riyahi, K., Partridge, L. and Brand, M.D. (2004) 'Lack of correlation between mitochondrial reactive oxygen species production and life span in Drosophila', in DeGrey, A.D.N. (ed.) *Strategies for Engineered Negligible Senescence: Why Genuine Control of Aging May Be Foreseeable*. pp. 388-391.

Mizushima, N., Levine, B., Cuervo, A.M. and Klionsky, D.J. (2008) 'Autophagy fights disease through cellular self-digestion', *Nature*, 451(7182), pp. 1069-1075.

Montoya, J., Gaines, G.L. and Attardi, G. (1983) 'The pattern of transcription of the human mitochondrial rRNA genes reveals two overlapping transcription units', *Cell*, 34(1), pp. 151-159.

Moraes, C.T., Ricci, E., Petruzzella, V., Shanske, S., DiMauro, S., Schon, E.A. and Bonilla, E. (1992) 'Molecular analysis of the muscle pathology associated with mitochondrial DNA deletions', *Nature Genetics*, 1(5), pp. 359-367.

Moreira, P.I., Cardoso, S.M., Santos, M.S. and Oliveira, C.R. (2006) 'The key role of mitochondria in Alzheimer's disease', *Journal of Alzheimer's Disease*, 9(2), pp. 101-110.

Mori, H., Kondo, J. and Ihara, Y. (1987) 'Ubiquitin is a component of paired helical filaments in Alzheimer's disease', *Science*, 235(4796), pp. 1641-1644.

Mukoyama, M., Yamazaki, K., Kikuchi, T. and Tomita, T. (1989) 'Neuropathology of gracile axonal dystrophy (GAD) mouse. An animal model of central distal axonopathy in primary sensory neurons', *Acta Neuropathologica*, 79(3), pp. 294-299.

Münch, C., Sedlmeier, R., Meyer, T., Homberg, V., Sperfeld, A.D., Kurt, A., Prudlo, J., Peraus, G., Hanemann, C.O., Stumm, G. and Ludolph, A.C. (2004) 'Point mutations of the p150 subunit of dynactin (DCTN1) gene ALS', *Neurology*, 63(4), pp. 724-726.

Nakamura, N. and Hirose, S. (2008) 'Regulation of mitochondrial morphology by USP30, a deubiquitinating enzyme present in the mitochondrial outer membrane', *Molecular Biology of the Cell*, 19(5), pp. 1903-1911.

Nakamura, N., Kimura, Y., Tokuda, M., Honda, S. and Hirose, S. (2006) 'MARCH-V is a novel mitofusin 2- and Drp1-binding protein able to change mitochondrial morphology', *EMBO Reports*, 7(10), pp. 1019-1022.

Nangaku, M., Sato-Yoshitake, R., Okada, Y., Noda, Y., Takemura, R., Yamazaki, H. and Hirokawa, N. (1994) 'KIF1B, a novel microtubule plus end-directed monomeric motor protein for transport of mitochondria', *Cell*, 79(7), pp. 1209-1220.

Narendra, D., Tanaka, A., Suen, D.F. and Youle, R.J. (2008) 'Parkin is recruited selectively to impaired mitochondria and promotes their autophagy', *Journal of Cell Biology*, 183(5), pp. 795-803.

Narendra, D.P., Jin, S.M., Tanaka, A., Suen, D.-F., Gautier, C.A., Shen, J., Cookson, M.R. and Youle, R.J. (2010) 'PINK1 Is Selectively Stabilized on Impaired Mitochondria to Activate Parkin', *PLoS Biol*, 8(1), p. e1000298.

Nass, M.M. (1966) 'The circularity of mitochondrial DNA', *Proceedings of the National Academy of Sciences of the United States of America*, 56(4), pp. 1215-1222.

Nazio, F., Strappazzon, F., Antonioli, M., Bielli, P., Cianfanelli, V., Bordi, M., Gretzmeier, C., Dengjel, J., Piacentini, M., Fimia, G.M. and Cecconi, F. (2013) 'MTOR inhibits autophagy by controlling ULK1 ubiquitylation, self-association and function through AMBRA1 and TRAF6', *Nature Cell Biology*, 15(4), pp. 406-416.

Nesbitt, V. and McFarland, R. (2011) 'Phenotypic spectrum of m.3243A>G mitochondrial DNA mutation in children', *Archives of Disease in Childhood*, 96(Suppl 1), p. A28.

Neutzner, A., Youle, R.J. and Karbowski, M. 287 (2007) 'Outer mitochondrial membrane protein degradation by the proteasome'. pp. 4-14. Available at:

http://www.scopus.com/inward/record.url?eid=2-s2.0-38449107710&partnerID=40&md5=427c8784c1aec15a84c463eb127620a1.

Nijman, S.M.B., Luna-Vargas, M.P.A., Velds, A., Brummelkamp, T.R., Dirac, A.M.G., Sixma, T.K. and Bernards, R. (2005) 'A genomic and functional inventory of deubiquitinating enzymes', *Cell*, 123(5), pp. 773-786.

Nishikawa, K., Li, H., Kawamura, R., Osaka, H., Wang, Y.L., Hara, Y., Hirokawa, T., Manago, Y., Amano, T., Noda, M., Aoki, S. and Wada, K. (2003) 'Alterations of structure and hydrolase activity of parkinsonism-associated human ubiquitin carboxyl-terminal hydrolase L1 variants', *Biochemical and Biophysical Research Communications*, 304(1), pp. 176-183.

Nisoli, E., Clementi, E., Paolucci, C., Cozzi, V., Tonello, C., Sciorati, C., Bracale, R., Valerio, A., Francolini, M., Moncada, S. and Carruba, M.O. (2003) 'Mitochondrial Biogenesis in Mammals: The Role of Endogenous Nitric Oxide', *Science*, 299(5608), pp. 896-899.

Niu, J., Ding, L., Li, J.J., Kim, H., Liu, J., Li, H., Moberly, A., Badea, T.C., Duncan, I.D., Son, Y.J., Scherer, S.S. and Luo, W. (2013) 'Modality-based organization of ascending somatosensory axons in the direct dorsal column pathway', *Journal of Neuroscience*, 33(45), pp. 17691-17709.

Novak, I. and Dikic, I. (2011) 'Autophagy receptors in developmental clearance of mitochondria', *Autophagy*, 7(3), pp. 301-303.

Oda, K., Yamazaki, K., Miura, H., Shibasaki, H. and Kikuchi, T. (1992) 'Dying back type axonal degeneration of sensory nerve terminals in muscle spindles of the gracile axonal dystrophy (GAD) mutant mouse', *Neuropathology and Applied Neurobiology*, 18(3), pp. 265-281.

Ohtsuka, H., Takahashi, R. and Goto, S. (1995) 'Age-related accumulation of high-molecular-weight ubiquitin protein conjugates in mouse brains', *Journals of Gerontology - Series A Biological Sciences and Medical Sciences*, 50(5), pp. B277-B281.

Old, S.L. and Johnson, M.A. (1989) 'Methods of microphotometric assay of succinate dehydrogenase and cytochrome c oxidase activities for use on human skeletal muscle', *Histochemical Journal*, 21(9-10), pp. 545-555.

Opeskin, K. and Anderson, R.M. (1997) 'Suspected MPTP-induced parkinsonism', *Journal of Clinical Neuroscience*, 4(3), pp. 366-370.

Orenstein, S.J. and Cuervo, A.M. (2010) 'Chaperone-mediated autophagy: Molecular mechanisms and physiological relevance', *Seminars in Cell & Developmental Biology*, 21(7), pp. 719-726.

Orrenius, S., Zhivotovsky, B. and Nicotera, P. (2003) 'Regulation of cell death: The calcium-apoptosis link', *Nature Reviews Molecular Cell Biology*, 4(7), pp. 552-565.

Osaka, H., Wang, Y.L., Takada, K., Takizawa, S., Setsuie, R., Li, H., Sato, Y., Nishikawa, K., Sun, Y.J., Sakurai, M., Harada, T., Hara, Y., Kimura, I., Chiba, S., Namikawa, K., Kiyama, H., Noda, M., Aoki, S. and Wada, K. (2003) 'Ubiquitin carboxy-terminal hydrolase L1 binds to and stabilizes monoubiquitin in neuron', *Human Molecular Genetics*, 12(16), pp. 1945-1958.

Otera, H., Wang, C., Cleland, M.M., Setoguchi, K., Yokota, S., Youle, R.J. and Mihara, K. (2010) 'Mff is an essential factor for mitochondrial recruitment of Drp1 during mitochondrial fission in mammalian cells', *The Journal of Cell Biology*, 191(6), pp. 1141-1158.

Ozawa, T. (1997) *Genetic and functional changes in mitochondria associated with aging*.

Ozol, K., Hayden, J.M., Oberdick, J. and Hawkes, R. (1999) 'Transverse zones in the vermis of the mouse cerebellum', *Journal of Comparative Neurology*, 412(1), pp. 95-111.

Pakkenberg, B. and Gundersen, H.J.G. (1997) 'Neocortical neuron number in humans: Effect of sex and age', *The Journal of Comparative Neurology*, 384(2), pp. 312-320.

Palade, G.E. (1953) 'An electron microscope study of the mitochondrial structure', *The journal of histochemistry and cytochemistry : official journal of the Histochemistry Society*, 1(4), pp. 188-211.

Palmer, C.S., Osellame, L.D., Laine, D., Koutsopoulos, O.S., Frazier, A.E. and Ryan, M.T. (2011) 'MiD49 and MiD51, new components of the mitochondrial fission machinery', *EMBO Reports*, 12(6), pp. 565-573.

Papa, S., Martino, P., Capitanio, G., Gaballo, A., De Rasmo, D., Signorile, A. and Petruzzella, V. (2012) 'The Oxidative Phosphorylation System in Mammalian Mitochondria', in Scatena, R., Bottoni, P. and Giardina, B. (eds.) *Advances in Mitochondrial Medicine*. Springer Netherlands, pp. 3-37.

Parikh, H., Nilsson, E., Ling, C., Poulsen, P., Almgren, P., Nittby, H., Eriksson, K.-F., Vaag, A. and Groop, L.C. (2008) *Molecular correlates for maximal oxygen uptake and type 1 fibers*.

Park, Y.-Y. and Cho, H. (2012) 'Mitofusin 1 is degraded at G2/M phase through ubiquitylation by MARCH5', *Cell Division*, 7(25), pp. 1-6.

Park, Y.Y., Lee, S., Karbowski, M., Neutzner, A., Youle, R.J. and Cho, H. (2010) 'Loss of MARCH5 mitochondrial E3 ubiquitin ligase induces cellular senescence through dynamin-related protein 1 and mitofusin 1', *Journal of Cell Science*, 123(4), pp. 619-626.

Parker Jr, W.D., Filley, C.M. and Parks, J.K. (1990) 'Cytochrome oxidase deficiency in Alzheimer's disease', *Neurology*, 40(8), pp. 1302-1303.

Parone, P.A., Da Cruz, S., Tondera, D., Mattenberger, Y., James, D.I., Maechler, P., Barja, F. and Martinou, J.-C. (2008) 'Preventing Mitochondrial Fission Impairs Mitochondrial Function and Leads to Loss of Mitochondrial DNA', *PLoS ONE*, 3(9), p. e3257.

Passmore, L.A. and Barford, D. (2004) 'Getting into position: The catalytic mechanisms of protein of protein ubiquitylation', *Biochemical Journal*, 379(3), pp. 513-525.

Pathare, G.R., Nagy, I., Śledź, P., Anderson, D.J., Zhou, H.J., Pardon, E., Steyaert, J., Förster, F., Bracher, A. and Baumeister, W. (2014) 'Crystal structure of the proteasomal deubiquitylation module Rpn8-Rpn11', *Proceedings of the National Academy of Sciences of the United States of America*, 111(8), pp. 2984-2989.

Pavlakis, S.G., Phillips, P.C., DiMauro, S., De Vivo, D.C. and Rowland, L.P. (1984) 'Mitochondrial myopathy, encephalopathy, lactic acidosis, and strokelike episodes: A distinctive clinical syndrome', *Annals of Neurology*, 16(4), pp. 481-488.

Paxinos, G., Franklin, K.B.J. (2001) *The Mouse Brain in Stereotaxic Coordinates*. Academic Press.

Pearl, R.A. (1928) *The Rate of Living*. New York: Knopf.

Pereira, C., Santos, M.S. and Oliveira, C. (1998) 'Mitochondrial function impairment induced by amyloid β-peptide on PC12 cells', *NeuroReport*, 9(8), pp. 1749-1755.

Petropoulos, I., Conconi, M., Wang, X., Hoenel, B., Brégégère, F., Milner, Y. and Friguet, B. (2000a) 'Increase of oxidatively modified protein is associated with a decrease of proteasome activity and content in aging epidermal cells', *Journals of Gerontology - Series A Biological Sciences and Medical Sciences*, 55(5), pp. B220-B227.

Petropoulos, I., Conconi, M., Wang, X., Hoenel, B., Brégégère, F., Milner, Y. and Friguet, B. (2000b) 'Increase of Oxidatively Modified Protein Is Associated With a Decrease of Proteasome Activity and Content in Aging Epidermal Cells', *The Journals of Gerontology Series A: Biological Sciences and Medical Sciences*, 55(5), pp. B220-B227.

Poole, A.C., Thomas, R.E., Yu, S., Vincow, E.S. and Pallanck, L. (2010) 'The mitochondrial fusion-promoting factor mitofusin is a substrate of the PINK1/parkin pathway', *PLoS ONE*, 5(4).

Powell, S.R., Davies, K.J.A. and Divald, A. (2007) 'Optimal determination of heart tissue 26S-proteasome activity requires maximal stimulating ATP concentrations', *Journal of Molecular and Cellular Cardiology*, 42(1), pp. 265-269.

Prakash, S., Tian, L., Ratliff, K.S., Lehotzky, R.E. and Matouschek, A. (2004) 'An unstructured initiation site is required for efficient proteasome-mediated degradation', *Nature Structural and Molecular Biology*, 11(9), pp. 830-837.

Proctor, C.J., Tangeman, P.J. and Ardley, H.C. (2010) 'Modelling the role of UCH-L1 on protein aggregation in age-related neurodegeneration', *PLoS ONE*, 5(10).

Pruess, J. Available at: http://rsb.info.nih.gov/ij/macros/slice-to-slice%20Difference.txt (Accessed: 20/12).

Rabl, J., Smith, D.M., Yu, Y., Chang, S.C., Goldberg, A.L. and Cheng, Y. (2008) 'Mechanism of Gate Opening in the 20S Proteasome by the Proteasomal ATPases', *Molecular Cell*, 30(3), pp. 360-368.

Rabuel, C., Samuel, J.-L., Lortat-Jacob, B., Marotte, F., Lanone, S., Keyser, C., Lessana, A., Payen, D. and Mebazaa, A. (2010) 'Activation of the ubiquitin proteolytic pathway in human septic heart and diaphragm', *Cardiovascular Pathology*, 19(3), pp. 158-164.

Ragland, M., Hutter, C., Zabetian, C. and Edwards, K. (2009) 'Association between the ubiquitin carboxyl-terminal esterase l1 gene (UCHL1) S18Y variant and parkinson's disease: A huge review and meta-analysis', *American Journal of Epidemiology*, 170(11), pp. 1344-1357.

Rakovic, A., Grünewald, A., Kottwitz, J., Brüggemann, N., Pramstaller, P.P., Lohmann, K. and Klein, C. (2011) 'Mutations in PINK1 and Parkin impair ubiquitination of Mitofusins in human fibroblasts', *PLoS ONE*, 6(3).

Ramaekers, C.H.M.A., van den Beucken, T., Bristow, R.G., Chiu, R.K., Durocher, D. and Wouters, B.G. (2014) 'RNF8-Independent Lys63 Poly-Ubiquitylation Prevents Genomic Instability in Response to Replication-Associated DNA Damage', *PLoS ONE*, 9(2), p. e89997.

Reinheckel, T., Sitte, N., Ullrich, O., Kuckelkorn, U., Davies, K.J. and Grune, T. (1998) 'Comparative resistance of the 20S and 26S proteasome to oxidative stress', *Biochem. J.*, 335(3), pp. 637-642.

Rintoul, G.L., Filiano, A.J., Brocard, J.B., Kress, G.J. and Reynolds, I.J. (2003) 'Glutamate decreases mitochondrial size and movement in primary forebrain neurons', *Journal of Neuroscience*, 23(21), pp. 7881-7888.

Rock, K.L., Gramm, C., Rothstein, L., Clark, K., Stein, R., Dick, L., Hwang, D. and Goldberg, A.L. (1994) 'Inhibitors of the proteasome block the degradation of most cell proteins and the generation of peptides presented on MHC class I molecules', *Cell*, 78(5), pp. 761-771.

Rodriguez, K.A., Edrey, Y.H., Osmulski, P., Gaczynska, M. and Buffenstein, R. (2012) 'Altered composition of liver proteasome assemblies contributes to enhanced proteasome activity in the exceptionally long-lived naked mole-rat', *PLoS ONE*, 7(5).

Rojo, M., Legros, F., Chateau, D. and Lombès, A. (2002) 'Membrane topology and mitochondrial targeting of mitofusins, ubiquitous mammalian homologs of the transmembrane GTPase Fzo', *Journal of Cell Science*, 115(8), pp. 1663-1674.

Rossignol, R., Faustin, B., Rocher, C., Malgat, M., Mazat, J.P. and Letellier, T. (2003) 'Mitochondrial threshold effects', *Biochemical Journal*, 370(3), pp. 751-762.

Rui, Y., Tiwari, P., Xie, Z. and Zheng, J.Q. (2006) 'Acute impairment of mitochondrial trafficking by β-amyloid peptides in hippocampal neurons', *Journal of Neuroscience*, 26(41), pp. 10480-10487.

Rutledge, A.C., Qiu, W., Zhang, R., Urade, R. and Adeli, K. (2013) 'Role of cysteine-protease CGHC motifs of ER-60, a protein disulfide isomerase, in hepatic apolipoprotein B100 degradation', *Archives of Biochemistry and Biophysics*, 537(1), pp. 104-112.

Saigoh, K., Wang, Y.L., Suh, J.G., Yamanishi, T., Sakai, Y., Kiyosawa, H., Harada, T., Ichihara, N., Wakana, S., Kikuchi, T. and Wada, K. (1999) 'Intragenic deletion in the gene encoding ubiquitin carboxy-terminal hydrolase in gad mice', *Nature Genetics*, 23(1), pp. 47-51.

Sakurai, M., Sekiguchi, M., Zushida, K., Yamada, K., Nagamine, S., Kabuta, T. and Wada, K. (2008) 'Reduction in memory in passive avoidance learning, exploratory behaviour and synaptic plasticity in mice with a spontaneous deletion in the ubiquitin C-terminal hydrolase L1 gene', *European Journal of Neuroscience*, 27(3), pp. 691-701.

Sandoval, M.E. (1980) 'Studies on the relationship between Ca2+ efflux from mitochondria and the release of amino acid neurotransmitters', *Brain Research*, 181(2), pp. 357-367.

Santos, D. and Cardoso, S.M. (2012) 'Mitochondrial dynamics and neuronal fate in Parkinson's disease', *Mitochondrion*, 12(4), pp. 428-437.

Sarraf, S.A., Raman, M., Guarani-Pereira, V., Sowa, M.E., Huttlin, E.L., Gygi, S.P. and Harper, J.W. (2013) 'Landscape of the PARKIN-dependent ubiquitylome in response to mitochondrial depolarization', *Nature*, 496(7445), pp. 372-376.

Sasarman, F., Antonicka, H. and Shoubridge, E.A. (2008) 'The A3243G tRNALeu(UUR) MELAS mutation causes amino acid misincorporation and a combined respiratory chain assembly defect partially suppressed by overexpression of EFTu and EFG2', *Human Molecular Genetics*, 17(23), pp. 3697-3707.

Sato, A., Nakada, K. and Hayashi, J.I. (2006) 'Mitochondrial dynamics and aging: Mitochondrial interaction preventing individuals from expression of respiratory deficiency caused by mutant mtDNA', *Biochimica et Biophysica Acta - Molecular Cell Research*, 1763(5-6), pp. 473-481.

Saxena, S. and Caroni, P. (2007) 'Mechanisms of axon degeneration: From development to disease', *Progress in Neurobiology*, 83(3), pp. 174-191.

Scarpulla, R.C. (2002) 'Nuclear activators and coactivators in mammalian mitochondrial biogenesis', *Biochimica et Biophysica Acta - Gene Structure and Expression*, 1576(1-2), pp. 1-14.

Schaefer, A.M., McFarland, R., Blakely, E.L., He, L., Whittaker, R.G., Taylor, R.W., Chinnery, P.F. and Turnbull, D.M. (2008) 'Prevalence of mitochondrial DNA disease in adults', *Annals of Neurology*, 63(1), pp. 35-39.

Schapira, A.H. (2008) 'Mitochondria in the aetiology and pathogenesis of Parkinson's disease', *The Lancet Neurology*, 7(1), pp. 97-109.

Schapira, A.H.V., Cooper, J.M., Dexter, D., Clark, J.B., Jenner, P. and Marsden, C.D. (1990) 'Mitochondrial complex I deficiency in Parkinson's disease', *Journal of Neurochemistry*, 54(3), pp. 823-827.

Schlossmacher, M.G., Frosch, M.P., Gai, W.P., Medina, M., Sharma, N., Forno, L., Ochiishi, T., Shimura, H., Sharon, R., Hattori, N., Langston, J.W., Mizuno, Y., Hyman, B.T., Selkoe, D.J. and Kosik, K.S. (2002) 'Parkin localizes to the Lewy bodies of Parkinson disease and dementia with Lewy bodies', *American Journal of Pathology*, 160(5), pp. 1655-1667.

Schmidtke, G., Aichem, A. and Groettrup, M. (2014) 'FAT10ylation as a signal for proteasomal degradation', *Biochimica et Biophysica Acta - Molecular Cell Research*, 1843(1), pp. 97-102.

Schon, E. and Przedborski, S. (2011) 'Mitochondria: The Next (Neurode)Generation', *Neuron*, 70(6), pp. 1033-1053.

Schreiner, P., Chen, X., Husnjak, K., Randles, L., Zhang, N., Elsasser, S., Finley, D., Dikic, I., Walters, K.J. and Groll, M. (2008) 'Ubiquitin docking at the proteasome through a novel pleckstrin-homology domain interaction', *Nature*, 453(7194), pp. 548-552.

Schulman, B.A. and Wade Harper, J. (2009) 'Ubiquitin-like protein activation by E1 enzymes: The apex for downstream signalling pathways', *Nature Reviews Molecular Cell Biology*, 10(5), pp. 319-331.

Sciacco, M., Bonilla, E., Schon, E.A., DiMauro, S. and Moraes, C.T. (1994) 'Distribution of wild-type and common deletion forms of mtDNA in normal and respiration-deficient muscle fibers from patients with mitochondrial myopathy', *Human Molecular Genetics*, 3(1), pp. 13-19.

Segref, A., Kevei, É., Pokrzywa, W., Schmeisser, K., Mansfeld, J., Livnat-Levanon, N., Ensenauer, R., Glickman, M.H., Ristow, M. and Hoppe, T. (2014) 'Pathogenesis of human mitochondrial diseases is modulated by reduced activity of the ubiquitin/proteasome system', *Cell Metabolism*, 19(4), pp. 642-652.

Seo, A.Y., Joseph, A.M., Dutta, D., Hwang, J.C.Y., Aris, J.P. and Leeuwenburgh, C. (2010) 'New insights into the role of mitochondria in aging: Mitochondrial dynamics and more', *Journal of Cell Science*, 123(15), pp. 2533-2542.

Sgaier, S.K., Lao, Z., Villanueva, M.P., Berenshteyn, F., Stephen, D., Turnbull, R.K. and Joyner, A.L. (2007) 'Genetic subdivision of the tectum and cerebellum into functionally related regions based on differential sensitivity to engrailed proteins', *Development*, 134(12), pp. 2325-2335.

Shabek, N., Herman-Bachinsky, Y., Buchsbaum, S., Lewinson, O., Haj-Yahya, M., Hejjaoui, M., Lashuel, H.A., Sommer, T., Brik, A. and Ciechanover, A. (2012) 'The

Size of the Proteasomal Substrate Determines Whether Its Degradation Will Be Mediated by Mono- or Polyubiquitylation', *Molecular Cell*, 48(1), pp. 87-97.

Sheng, Z.-H. and Cai, Q. (2012) 'Mitochondrial transport in neurons: impact on synaptic homeostasis and neurodegeneration', *Nat Rev Neurosci*, 13(2), pp. 77-93.

Shi, Y., Dierckx, A., Wanrooij, P.H., Wanrooij, S., Larsson, N.G., Wilhelmsson, L.M., Falkenberg, M. and Gustafsson, C.M. (2012) 'Mammalian transcription factor A is a core component of the mitochondrial transcription machinery', *Proceedings of the National Academy of Sciences of the United States of America*, 109(41), pp. 16510-16515.

Shirendeb, U., Reddy, A.P., Manczak, M., Calkins, M.J., Mao, P., Tagle, D.A. and Reddy, P.H. (2011) 'Abnormal mitochondrial dynamics, mitochondrial loss and mutant huntingtin oligomers in Huntington's disease: Implications for selective neuronal damage', *Human Molecular Genetics*, 20(7), pp. 1438-1455.

Shoffner, J.M., Lott, M.T., Lezza, A.M.S., Seibel, P., Ballinger, S.W. and Wallace, D.C. (1990) 'Myoclonic epilepsy and ragged-red fiber disease (MERRF) is associated with a mitochondrial DNA tRNALys mutation', *Cell*, 61(6), pp. 931-937.

Shoshan-Barmatz, V., De Pinto, V., Zweckstetter, M., Raviv, Z., Keinan, N. and Arbel, N. (2010) 'VDAC, a multi-functional mitochondrial protein regulating cell life and death', *Molecular Aspects of Medicine*, 31(3), pp. 227-285.

Shringarpure, R., Grune, T., Mehlhase, J. and Davies, K.J.A. (2003) 'Ubiquitin conjugation is not required for the degradation of oxidized proteins by proteasome', *Journal of Biological Chemistry*, 278(1), pp. 311-318.

Sitte, N., Huber, M., Grune, T., Ladhoff, A., Doecke, W.D., Von Zglinicki, T. and Davies, K.J.A. (2000) 'Proteasome inhibition by lipofuscin/ceroid during postmitotic aging of fibroblasts', *FASEB Journal*, 14(11), pp. 1490-1498.

Smigrodzki, R., Parks, J. and Parker, W.D. (2004) 'High frequency of mitochondrial complex I mutations in Parkinson's disease and aging', *Neurobiology of Aging*, 25(10), pp. 1273-1281.

Smirnova, E., Griparic, L., Shurland, D.L. and Van der Bliek, A.M. (2001) 'Dynamin-related protein Drp1 is required for mitochondrial division in mammalian cells', *Molecular Biology of the Cell*, 12(8), pp. 2245-2256.

Smith, M.J., Pozo, K., Brickley, K. and Stephenson, F.A. (2006) 'Mapping the GRIF-1 binding domain of the kinesin, KIF5C, substantiates a role for GRIF-1 as an adaptor protein in the anterograde trafficking of cargoes', *Journal of Biological Chemistry*, 281(37), pp. 27216-27228.

Snapinn, K.W., Larson, E.B., Kawakami, H., Ujike, H., Borenstein, A.R., Izumi, Y., Kaji, R., Maruyama, H., Mata, I.F., Morino, H., Oda, M., Tsuang, D.W., Yearout, D., Edwards, K.L. and Zabetian, C.P. (2011) 'The UCHL1 S18Y polymorphism and Parkinson's disease in a Japanese population', *Parkinsonism and Related Disorders*, 17(6), pp. 473-475.

Sologub, M., Litonin, D., Anikin, M., Mustaev, A. and Temiakov, D. (2009) 'TFB2 Is a Transient Component of the Catalytic Site of the Human Mitochondrial RNA Polymerase', *Cell*, 139(5), pp. 934-944.

Song, Z., Ghochani, M., McCaffery, J.M., Frey, T.G. and Chan, D.C. (2009) 'Mitofusins and OPA1 mediate sequential steps in mitochondrial membrane fusion', *Molecular Biology of the Cell*, 20(15), pp. 3525-3532.

Sparaco, M., Bonilla, E., Dimauro, S. and Powers, J.M. (1993) 'Neuropathology of mitochondrial encephalomyopathies due to mitochondrial DNA defects', *Journal of neuropathology and experimental neurology*, 52(1), pp. 1-10.

Sparaco, M., Schon, E.A., DiMauro, S. and Bonilla, E. (1995) 'Myoclonic epilepsy with ragged-red fibers (MERRF): An immunohistochemical study of the brain', *Brain Pathology*, 5(2), pp. 125-133.

Spelbrink, J.N., Li, F.-Y., Tiranti, V., Nikali, K., Yuan, Q.-P., Tariq, M., Wanrooij, S., Garrido, N., Comi, G., Morandi, L., Santoro, L., Toscano, A., Fabrizi, G.-M., Somer, H., Croxen, R., Beeson, D., Poulton, J., Suomalainen, A., Jacobs, H.T., Zeviani, M. and Larsson, C. (2001) 'Human mitochondrial DNA deletions associated with mutations in the gene encoding Twinkle, a phage T7 gene 4-like protein localized in mitochondria', *Nat Genet*, 28(3), pp. 223-231.

Stowers, R.S., Megeath, L.J., Górska-Andrzejak, J., Meinertzhagen, I.A. and Schwarz, T.L. (2002) 'Axonal transport of mitochondria to synapses depends on Milton, a novel Drosophila protein', *Neuron*, 36(6), pp. 1063-1077.

Strappazzon, F., Vietri-Rudan, M., Campello, S., Nazio, F., Florenzano, F., Fimia, G.M., Piacentini, M., Levine, B. and Cecconi, F. (2011) 'Mitochondrial BCL-2 inhibits AMBRA1-induced autophagy', *EMBO Journal*, 30(7), pp. 1195-1208.

Su, B., Wang, X., Zheng, L., Perry, G., Smith, M.A. and Zhu, X. (2010) 'Abnormal mitochondrial dynamics and neurodegenerative diseases', *Biochimica et Biophysica Acta (BBA) - Molecular Basis of Disease*, 1802(1), pp. 135-142.

Susin, S.A., Zamzami, N. and Kroemer, G. (1998) 'Mitochondria as regulators of apoptosis: doubt no more', *Biochimica et Biophysica Acta (BBA) - Bioenergetics*, 1366(1–2), pp. 151-165.

Sutovsky, P., Moreno, R.D., Ramalho-Santos, J., Dominko, T., Simerly, C. and Schatten, G. (2000) 'Ubiquitinated sperm mitochondria, selective proteolysis, and the regulation of mitochondrial inheritance in mammalian embryos', *Biology of Reproduction*, 63(2), pp. 582-590.

Swerdlow, R.H., Burns, J.M. and Khan, S.M. (2010) 'The Alzheimer's disease mitochondrial cascade hypothesis', *Journal of Alzheimer's Disease*, 20(SUPPL.2), pp. S265-S279.

Swerdlow, R.H., Burns, J.M. and Khan, S.M. (2014) 'The Alzheimer's disease mitochondrial cascade hypothesis: Progress and perspectives', *Biochimica et Biophysica Acta (BBA) - Molecular Basis of Disease*, 1842(8), pp. 1219-1231.

Takamori, S., Holt, M., Stenius, K., Lemke, E.A., Grønborg, M., Riedel, D., Urlaub, H., Schenck, S., Brügger, B., Ringler, P., Müller, S.A., Rammner, B., Gräter, F., Hub, J.S., De Groot, B.L., Mieskes, G., Moriyama, Y., Klingauf, J., Grubmüller, H., Heuser, J., Wieland, F. and Jahn, R. (2006) 'Molecular Anatomy of a Trafficking Organelle', *Cell*, 127(4), pp. 831-846.

Tan, Y.-Y., Zhou, H.-Y., Wang, Z.-Q. and Chen, S.-D. (2008) 'Endoplasmic reticulum stress contributes to the cell death induced by UCH-L1 inhibitor', *Molecular and Cellular Biochemistry*, 318(1-2), pp. 109-115.

Tanahashi, C., Nakayama, A., Yoshida, M., Ito, M., Mori, N. and Hashizume, Y. (2000) 'MELAS with the mitochondrial DNA 3243 point mutation: a neuropathological study', *Acta Neuropathologica*, 99(1), pp. 31-38.

Tanaka, A., Cleland, M.M., Xu, S., Narendra, D.P., Suen, D.F., Karbowski, M. and Youle, R.J. (2010) 'Proteasome and p97 mediate mitophagy and degradation of mitofusins induced by Parkin', *Journal of Cell Biology*, 191(7), pp. 1367-1380.

Tanaka, K. and Matsuda, N. (2014) 'Proteostasis and neurodegeneration: The roles of proteasomal degradation and autophagy', *Biochimica et Biophysica Acta - Molecular Cell Research*, 1843(1), pp. 197-204.

Tanaka, K., Mizushima, T. and Saeki, Y. (2012) 'The proteasome: Molecular machinery and pathophysiological roles', *Biological Chemistry*, 393(4), pp. 217-234.

Tanaka, K., Sugiura, Y., Ichishita, R., Mihara, K. and Oka, T. (2011) 'KLP6: A newly identified kinesin that regulates the morphology and transport of mitochondria in neuronal cells', *Journal of Cell Science*, 124(14), pp. 2457-2465.

Tanaka, K., Tanahashi, N., Tsurumi, C., Yokota, K.Y. and Shimbara, N. 64 (1997) 'Proteasomes and antigen processing'. pp. 1-38. Available at: http://www.scopus.com/inward/record.url?eid=2-s2.0-0030945333&partnerID=40&md5=9c7c21c9cad0cbb634bf8b9d3a4a54be.

Tanaka, Y., Kanai, Y., Okada, Y., Nonaka, S., Takeda, S., Harada, A. and Hirokawa, N. (1998) 'Targeted disruption of mouse conventional kinesin heavy chain, kif5B, results in abnormal perinuclear clustering of mitochondria', *Cell*, 93(7), pp. 1147-1158.

Thomas, K.J., McCoy, M.K., Blackinton, J., Beilina, A., van der Brug, M., Sandebring, A., Miller, D., Maric, D., Cedazo-Minguez, A. and Cookson, M.R. (2011) 'DJ-1 acts in parallel to the PINK1/parkin pathway to control mitochondrial function and autophagy', *Human Molecular Genetics*, 20(1), pp. 40-50.

Thrower, J.S., Hoffman, L., Rechsteiner, M. and Pickart, C.M. (2000) 'Recognition of the polyubiquitin proteolytic signal', *EMBO Journal*, 19(1), pp. 94-102.

Tomko Jr, R.J., Funakoshi, M., Schneider, K., Wang, J. and Hochstrasser, M. (2010) 'Heterohexameric Ring Arrangement of the Eukaryotic Proteasomal ATPases:

Implications for Proteasome Structure and Assembly', *Molecular Cell*, 38(3), pp. 393-403.

Tomko, R.J. and Hochstrasser, M. (2011) 'Incorporation of the Rpn12 Subunit Couples Completion of Proteasome Regulatory Particle Lid Assembly to Lid-Base Joining', *Molecular Cell*, 44(6), pp. 907-917.

Tonoki, A., Kuranaga, E., Tomioka, T., Hamazaki, J., Murata, S., Tanaka, K. and Miura, M. (2009) 'Genetic evidence linking age-dependent attenuation of the 26S proteasome with the aging process', *Molecular and Cellular Biology*, 29(4), pp. 1095-1106.

Trifunovic, A. and Larsson, N.G. (2008) 'Mitochondrial dysfunction as a cause of ageing', *Journal of Internal Medicine*, 263(2), pp. 167-178.

Trifunovic, A., Wredenberg, A., Falkenberg, M., Spelbrink, J.N., Rovio, A.T., Bruder, C.E., Bohlooly-Y, M., Gidlof, S., Oldfors, A., Wibom, R., Tornell, J., Jacobs, H.T. and Larsson, N.-G. (2004) 'Premature ageing in mice expressing defective mitochondrial DNA polymerase', *Nature*, 429(6990), pp. 417-423.

Tseng, B.P., Green, K.N., Chan, J.L., Blurton-Jones, M. and LaFerla, F.M. (2008) 'Aβ inhibits the proteasome and enhances amyloid and tau accumulation', *Neurobiology of Aging*, 29(11), pp. 1607-1618.

Tsukamoto, S., Kuma, A. and Mizushima, N. (2008) 'The role of autophagy during the oocyte-to-embryo transition', *Autophagy*, 4(8), pp. 1076-1078.

Tuppen, H.A.L., Blakely, E.L., Turnbull, D.M. and Taylor, R.W. (2010) 'Mitochondrial DNA mutations and human disease', *Biochimica et Biophysica Acta - Bioenergetics*, 1797(2), pp. 113-128.

Turco, D.D., Schlaudraff, J., Bonin, M. and Deller, T. (2014) 'Upregulation of APP, ADAM10 and ADAM17 in the denervated mouse dentate gyrus', *PLoS ONE*, 9(1).

Turrens, J.F. and Boveris, A. (1980) 'Generation of superoxide anion by the NADH dehydrogenase of bovine heart mitochondria', *Biochemical Journal*, 191(2), pp. 421-427.

Twig, G., Elorza, A., Molina, A.J.A., Mohamed, H., Wikstrom, J.D., Walzer, G., Stiles, L., Haigh, S.E., Katz, S., Las, G., Alroy, J., Wu, M., Py, B.F., Yuan, J., Deeney, J.T., Corkey, B.E. and Shirihai, O.S. (2008) 'Fission and selective fusion govern

mitochondrial segregation and elimination by autophagy', *EMBO Journal*, 27(2), pp. 433-446.

Twig, G., Graf, S.A., Wikstrom, J.D., Mohamed, H., Haigh, S.E., Elorza, A., Deutsch, M., Zurgil, N., Reynolds, N. and Shirihai, O.S. (2006) 'Tagging and tracking individual networks within a complex mitochondrial web with photoactivatable GFP', *American Journal of Physiology - Cell Physiology*, 291(1), pp. C176-C184.

Unno, M., Mizushima, T., Morimoto, Y., Tomisugi, Y., Tanaka, K., Yasuoka, N. and Tsukihara, T. (2002) 'The structure of the mammalian 20S proteasome at 2.75 Å resolution', *Structure*, 10(5), pp. 609-618.

Valtorta, F., Pennuto, M., Bonanomi, D. and Benfenati, F. (2004) 'Synaptophysin: Leading actor or walk-on role in synaptic vesicle exocytosis?', *BioEssays*, 26(4), pp. 445-453.

Van Bruggen, E.F.J., Borst, P., Ruttenberg, G.J.C.M., Gruber, M. and Kroon, A.M. (1966) 'Circular mitochondrial DNA', *BBA Section Nucleic Acids And Protein Synthesis*, 119(2), pp. 437-439.

Van Den Heuvel, C., Blumbergs, P.C., Finnie, J.W., Manavis, J., Jones, N.R., Reilly, P.L. and Pereira, R.A. (1999) 'Upregulation of amyloid precursor protein messenger RNA in response to traumatic brain injury: An ovine head impact model', *Experimental Neurology*, 159(2), pp. 441-450.

Van den Heuvel, C., Finnie, J.W., Blumbergs, P.C., Manavis, J., Jones, N.R., Reilly, P.L. and Pereira, R.A. (2000) 'Upregulation of neuronal amyloid precursor protein (APP) and APP mRNA following magnesium sulphate (MgSO4) therapy in traumatic brain injury', *Journal of Neurotrauma*, 17(11), pp. 1041-1053.

van Humbeeck, C., Cornelissen, T., Hofkens, H., Mandemakers, W., Gevaert, K., de Strooper, B. and Vandenberghe, W. (2011) 'Parkin interacts with ambra1 to induce mitophagy', *Journal of Neuroscience*, 31(28), pp. 10249-10261.

Van Remmen, H., Ikeno, Y., Hamilton, M., Pahlavani, M., Wolf, N., Thorpe, S.R., Alderson, N.L., Baynes, J.W., Epstein, C.J., Huang, T.-T., Nelson, J., Strong, R. and Richardson, A. (2003) *Life-long reduction in MnSOD activity results in increased DNA damage and higher incidence of cancer but does not accelerate aging*.

Van Remmen, H., Qi, W., Sabia, M., Freeman, G., Estlack, L., Yang, H., Mao Guo, Z., Huang, T.-T., Strong, R., Lee, S., Epstein, C.J. and Richardson, A. (2004) 'Multiple deficiencies in antioxidant enzymes in mice result in a compound increase in sensitivity to oxidative stress', *Free Radical Biology and Medicine*, 36(12), pp. 1625-1634.

Verma, R., Aravind, L., Oania, R., McDonald, W.H., Yates Iii, J.R., Koonin, E.V. and Deshaies, R.J. (2002) 'Role of Rpn11 metalloprotease in deubiquitination and degradation by the 26S proteasome', *Science*, 298(5593), pp. 611-615.

Vilchez, D., Morantte, I., Liu, Z., Douglas, P.M., Merkwirth, C., Rodrigues, A.P.C., Manning, G. and Dillin, A. (2012) 'RPN-6 determines C. elegans longevity under proteotoxic stress conditions', *Nature*, 489(7415), pp. 263-268.

Viteri, G., Carrard, G., Birlouez-Aragón, I., Silva, E. and Friguet, B. (2004) 'Age-dependent protein modifications and declining proteasome activity in the human lens', *Archives of Biochemistry and Biophysics*, 427(2), pp. 197-203.

Vives-Bauza, C., Zhou, C., Huang, Y., Cui, M., De Vries, R.L.A., Kim, J., May, J., Tocilescu, M.A., Liu, W., Ko, H.S., Magrané, J., Moore, D.J., Dawson, V.L., Grailhe, R., Dawson, T.M., Li, C., Tieu, K. and Przedborski, S. (2010) 'PINK1-dependent recruitment of Parkin to mitochondria in mitophagy', *Proceedings of the National Academy of Sciences of the United States of America*, 107(1), pp. 378-383.

Vockley, J. and Ensenauer, R. (2006) 'Isovaleric acidemia: New aspects of genetic and phenotypic heterogeneity', *American Journal of Medical Genetics - Seminars in Medical Genetics*, 142 C(2), pp. 95-103.

Voogd, J. and Glickstein, M. (1998) 'The anatomy of the cerebellum', *Trends in Cognitive Sciences*, 2(9), pp. 307-313.

Vosper, J.M.D., McDowell, G.S., Hindley, C.J., Fiore-Heriche, C.S., Kucerova, R., Horan, I. and Philpott, A. (2009) 'Ubiquitylation on canonical and non-canonical sites targets the transciption factor neurogenin for ubiquitin-mediated proteolysis', *Journal of Biological Chemistry*, 284(23), pp. 15458-15468.

Wagner, B.J. and Margolis, J.W. (1995) 'Age-Dependent Association of Isolated Bovine Lens Multicatalytic Proteinase Complex (Proteasome) with Heat-Shock Protein 90, an Endogenous Inhibitor', *Archives of Biochemistry and Biophysics*, 323(2), pp. 455-462.

Wagner, K., Mick, D.U. and Rehling, P. (2009) 'Protein transport machineries for precursor translocation across the inner mitochondrial membrane', *Biochimica et Biophysica Acta (BBA) - Molecular Cell Research*, 1793(1), pp. 52-59.

Wakabayashi, J., Zhang, Z., Wakabayashi, N., Tamura, Y., Fukaya, M., Kensler, T.W., Iijima, M. and Sesaki, H. (2009) 'The dynamin-related GTPase Drp1 is required for embryonic and brain development in mice', *Journal of Cell Biology*, 186(6), pp. 805-816.

Waller, A. (1850) 'Experiments on the section of the glossopharyngeal and hypoglossal nerves of the frog, and observations of the alterations produced thereby in the structure of their primitive fibres', *Philosphical Transactions of the Royal Society of London Series B: Biological Sciences*.

Walters, B.J., Campbell, S.L., Chen, P.C., Taylor, A.P., Schroeder, D.G., Dobrunz, L.E., Artavanis-Tsakonas, K., Ploegh, H.L., Wilson, J.A., Cox, G.A. and Wilson, S.M. (2008) 'Differential effects of Usp14 and Uch-L1 on the ubiquitin proteasome system and synaptic activity', *Molecular and Cellular Neuroscience*, 39(4), pp. 539-548.

Wang, H., Song, P., Du, L., Tian, W., Yue, W., Liu, M., Li, D., Wang, B., Zhu, Y., Cao, C., Zhou, J. and Chen, Q. (2011a) 'Parkin ubiquitinates Drp1 for proteasome-dependent degradation: Implication of dysregulated mitochondrial dynamics in Parkinson disease', *Journal of Biological Chemistry*, 286(13), pp. 11649-11658.

Wang, L., Guo, J.F., Nie, L.L., Luo, L., Zuo, X., Shen, L., Jiang, H., Yan, X.X., Xia, K., Pan, Q. and Tang, B.S. (2011b) 'Case-control study of the UCH-L1 S18Y variant in sporadic Parkinson's disease in the Chinese population', *Journal of Clinical Neuroscience*, 18(4), pp. 541-544.

Wang, X., Su, B., Fujioka, H. and Zhu, X. (2008) 'Dynamin-like protein 1 reduction underlies mitochondrial morphology and distribution abnormalities in fibroblasts from sporadic Alzheimer's disease patients', *American Journal of Pathology*, 173(2), pp. 470-482.

Wang, X., Su, B., Lee, H.G., Li, X., Perry, G., Smith, M.A. and Zhu, X. (2009) 'Impaired balance of mitochondrial fission and fusion in Alzheimer's disease', *Journal of Neuroscience*, 29(28), pp. 9090-9103.

Wang, X., Winter, D., Ashrafi, G., Schlehe, J., Wong, Yao L., Selkoe, D., Rice, S., Steen, J., LaVoie, Matthew J. and Schwarz, Thomas L. (2011c) 'PINK1 and Parkin Target Miro for Phosphorylation and Degradation to Arrest Mitochondrial Motility', *Cell*, 147(4), pp. 893-906.

Wang, X., Yan, M.H., Fujioka, H., Liu, J., Wilson-delfosse, A., Chen, S.G., Perry, G., Casadesus, G. and Zhu, X. (2012) 'LRRK2 regulates mitochondrial dynamics and function through direct interaction with DLP1', *Human Molecular Genetics*, 21(9), pp. 1931-1944.

Wang, Y.L., Takeda, A., Osaka, H., Hara, Y., Furuta, A., Setsuie, R., Sun, Y.J., Kwon, J., Sato, Y., Sakurai, M., Noda, M., Yoshikawa, Y. and Wada, K. (2004) 'Accumulation of β- and γ-synucleins in the ubiquitin carboxyl-terminal hydrolase L1-deficient gad mouse', *Brain Research*, 1019(1-2), pp. 1-9.

Wanrooij, S. and Falkenberg, M. (2010) 'The human mitochondrial replication fork in health and disease', *Biochimica et Biophysica Acta (BBA) - Bioenergetics*, 1797(8), pp. 1378-1388.

Watson, C. and Harrison, M. (2012a) 'The Location of the Major Ascending and Descending Spinal Cord Tracts in all Spinal Cord Segments in the Mouse: Actual and Extrapolated', *Anatomical Record*, 295(10), pp. 1692-1697.

Watson, C. and Harrison, M. (2012b) 'The Location of the Major Ascending and Descending Spinal Cord Tracts in all Spinal Cord Segments in the Mouse: Actual and Extrapolated', *The Anatomical Record: Advances in Integrative Anatomy and Evolutionary Biology*, 295(10), pp. 1692-1697.

Watson, C., Paxinos, G. and Kayalioglu, G. (2009a) *The Spinal Cord*.

Watson, C., Paxinos, G., Kayalioglu, G. and Heise, C. (2009b) 'Chapter 16 - Atlas of the Mouse Spinal Cord', in Charles, W., George, P., Gulgun KayaliogluA2 - Charles Watson, G.P. and Gulgun, K. (eds.) *The Spinal Cord*. San Diego: Academic Press, pp. 308-379.

Wei, Y.-H. (1998) 'Oxidative Stress and Mitochondrial DNA Mutations in Human Aging', *Experimental Biology and Medicine*, 217(1), pp. 53-63.

Wei, Y.H., Ma, Y.S., Lee, H.C., Lee, C.F. and Lu, C.Y. (2001) 'Mitochondrial theory of aging matures - Roles of mtDNA mutation and oxidative stress in human aging', *Chinese Medical Journal (Taipei)*, 64(5), pp. 259-270.

Weihofen, A., Thomas, K.J., Ostaszewski, B.L., Cookson, M.R. and Selkoe, D.J. (2009) 'Pink1 forms a multiprotein complex with miro and milton, linking Pink1 function to mitochondrial trafficking', *Biochemistry*, 48(9), pp. 2045-2052.

Whitmore, A.V., Lindsten, T., Raff, M.C. and Thompson, C.B. (2003) 'The proapoptotic proteins Bax and Bak are not involved in Wallerian degeneration', *Cell Death Differ*, 10(2), pp. 260-261.

Wickliffe, K.E., Williamson, A., Meyer, H.J., Kelly, A. and Rape, M. (2011) 'K11-linked ubiquitin chains as novel regulators of cell division', *Trends in Cell Biology*, 21(11), pp. 656-663.

Wikström, M. (1984) 'Two protons are pumped from the mitochondrial matrix per electron transferred between NADH and ubiquinone', *FEBS Letters*, 169(2), pp. 300-304.

Wilkinson, K.D., Lee, K., Deshpande, S., Duerksen-Hughes, P., Boss, J.M. and Pohl, J. (1989) 'The neuron-specific protein PGP 9.5 is a ubiquitin carboxyl-terminal hydrolase', *Science*, 246(4930), pp. 670-673.

Wright, D.C., Geiger, P.C., Han, D.H., Jones, T.E. and Holloszy, J.O. (2007) 'Calcium induces increases in peroxisome proliferator-activated receptor γ coactivator-1α and mitochondrial biogenesis by a pathway leading to p38 mitogen-activated protein kinase activation', *Journal of Biological Chemistry*, 282(26), pp. 18793-18799.

Wu, J., Ichihara, N., Chui, D.H., Yamazaki, K., Wakabayashi, T. and Kikuchi, T. (1996) 'Abnormal ubiquitination of dystrophic axons in central nervous system of gracile axonal dystrophy (GAD) mutant mouse', *Alzheimer's Research*, 2(5), pp. 163-167.

Wu, Z., Huang, X., Feng, Y., Handschin, C., Gullicksen, P.S., Bare, O., Labow, M., Spiegelman, B. and Stevenson, S.C. (2006) 'Transducer of regulated CREB-binding proteins (TORCs) induce PGC-1α transcription and mitochondrial biogenesis in muscle cells', *Proceedings of the National Academy of Sciences of the United States of America*, 103(39), pp. 14379-14384.

Xu, C., Fan, C.D. and Wang, X. (2014) 'Regulation of Mdm2 protein stability and the p53 response by NEDD4-1 E3 ligase', *Oncogene*.

Xu, P., Duong, D.M., Seyfried, N.T., Cheng, D., Xie, Y., Robert, J., Rush, J., Hochstrasser, M., Finley, D. and Peng, J. (2009) 'Quantitative Proteomics Reveals the Function of Unconventional Ubiquitin Chains in Proteasomal Degradation', *Cell*, 137(1), pp. 133-145.

Xu, S., Peng, G., Wang, Y., Fang, S. and Karbowsk, M. (2011) 'The AAA-ATPase p97 is essential for outer mitochondrial membrane protein turnover', *Molecular Biology of the Cell*, 22(3), pp. 291-300.

Yakubovskaya, E., Chen, Z., Carrodeguas, J.A., Kisker, C. and Bogenhagen, D.F. (2006) 'Functional human mitochondrial DNA polymerase γ forms a heterotrimer', *Journal of Biological Chemistry*, 281(1), pp. 374-382.

Yakubovskaya, E., Mejia, E., Byrnes, J., Hambardjieva, E. and Garcia-Diaz, M. (2010) 'Helix unwinding and base flipping enable human MTERF1 to terminate mitochondrial transcription', *Cell*, 141(6), pp. 982-993.

Yamazaki, K., Wakasugi, N., Tomita, T., Kikuchi, T., Mukoyama, M. and Ando, K. (1988) 'Gracile axonal dystrophy (GAD), a new neurological mutant in the mouse', *Proceedings of the Society for Experimental Biology and Medicine*, 187(2), pp. 209-215.

Yang, C., Curth, U., Urbanke, C. and Kang, C. (1997) 'Crystal structure of human mitochondrial single-stranded DNA binding protein at 2.4 A resolution', *Nat Struct Mol Biol*, 4(2), pp. 153-157.

Yao, T. and Cohen, R.E. (2002) 'A cryptic protease couples deubiquitination and degradation by the proteasome', *Nature*, 419(6905), pp. 403-407.

Yasukawa, T., Suzuki, T., Ishii, N., Ohta, S. and Watanabe, K. (2001) 'Wobble modification defect in tRNA disturbs codon-anticodon interaction in a mitochondrial disease', *EMBO Journal*, 20(17), pp. 4794-4802.

Yasukawa, T., Suzuki, T., Ohta, S. and Watanabe, K. (2002) 'Wobble modification defect suppresses translational activity of tRNAs with MERRF and MELAS mutations', *Mitochondrion*, 2(1-2), pp. 129-141.

Ye, Y., Scheel, H., Hofmann, K. and Komander, D. (2009) 'Dissection of USP catalytic domains reveals five common insertion points', *Molecular BioSystems*, 5(12), pp. 1797-1808.

Yoboue, E.D., Mougeolle, A., Kaiser, L., Averet, N., Rigoulet, M. and Devin, A. (2014) 'The role of mitochondrial biogenesis and ROS in the control of energy supply in proliferating cells', *Biochimica et Biophysica Acta (BBA) - Bioenergetics*, 1837(7), pp. 1093-1098.

Yonashiro, R., Ishido, S., Kyo, S., Fukuda, T., Goto, E., Matsuki, Y., Ohmura-Hoshino, M., Sada, K., Hotta, H., Yamamura, H., Inatome, R. and Yanagi, S. (2006) 'A novel mitochondrial ubiquitin ligase plays a critical role in mitochondrial dynamics', *EMBO Journal*, 25(15), pp. 3618-3626.

Yonashiro, R., Sugiura, A., Miyachi, M., Fukuda, T., Matsushita, N., Inatome, R., Ogata, Y., Suzuki, T., Dohmae, N. and Yanagi, S. (2009) 'Mitochondrial ubiquitin ligase MITOL ubiquitinates mutant SOD1 and attenuates mutant SOD1-induced reactive oxygen species generation', *Molecular Biology of the Cell*, 20(21), pp. 4524-4530.

Yoon, Y., Krueger, E.W., Oswald, B.J. and McNiven, M.A. (2003) 'The mitochondrial protein hFis1 regulates mitochondrial fission in mammalian cells through an interaction with the dynamin-like protein DLP1', *Molecular and Cellular Biology*, 23(15), pp. 5409-5420.

Young, P., Deveraux, Q., Beal, R.E., Pickart, C.M. and Rechsteiner, M. (1998) 'Characterization of two polyubiquitin binding sites in the 26 S protease subunit 5a', *Journal of Biological Chemistry*, 273(10), pp. 5461-5467.

Yu, W., Sun, Y., Guo, S. and Lu, B. (2011) 'The PINK1/Parkin pathway regulates mitochondrial dynamics and function in mammalian hippocampal and dopaminergic neurons', *Human Molecular Genetics*, 20(16), pp. 3227-3240.

Yue, W., Chen, Z., Liu, H., Yan, C., Chen, M., Feng, D., Yan, C., Wu, H., Du, L., Wang, Y., Liu, J., Huang, X., Xia, L., Liu, L., Wang, X., Jin, H., Wang, J., Song, Z., Hao, X. and Chen, Q. (2014) 'A small natural molecule promotes mitochondrial fusion through inhibition of the deubiquitinase USP30', *Cell Res*, 24(4), pp. 482-496.

Zeng, B.Y., Medhurst, A.D., Jackson, M., Rose, S. and Jenner, P. (2005) 'Proteasomal activity in brain differs between species and brain regions and changes with age', *Mechanisms of Ageing and Development*, 126(6–7), pp. 760-766.

Zeviani, M., Servidei, S., Gellera, C., Bertini, E., DiMauro, S. and DiDonato, S. (1989) 'An autosomal dominant disorder with multiple deletions of mitochondrial DNA starting at the D-loop region', *Nature*, 339(6222), pp. 309-311.

Zhang, J.H., Sampogna, S., Morales, F.R. and Chase, M.H. (1998) 'Age-related intra-axonal accumulation of neurofilaments in the dorsal column nuclei of the cat brainstem: A light and electron microscopic immunohistochemical study', *Brain Research*, 797(2), pp. 333-338.

Zhang, M., Deng, Y., Luo, Y., Zhang, S., Zou, H., Cai, F., Wada, K. and Song, W. (2012) 'Control of BACE1 degradaton and APP processing by ubiquitin carboxyl-terminal hydrolase L1', *Journal of Neurochemistry*, 120(6), pp. 1129-1138.

Zhao, J., Liu, T., Jin, S., Wang, X., Qu, M., Uhlen, P., Tomilin, N., Shupliakov, O., Lendahl, U. and Nister, M. (2011) 'Human MIEF1 recruits Drp1 to mitochondrial outer membranes and promotes mitochondrial fusion rather than fission', *EMBO J*, 30(14), pp. 2762-2778.

Zhao, Q., Wang, J., Levichkin, I.V., Stasinopoulos, S., Ryan, M.T. and Hoogenraad, N.J. (2002) *A mitochondrial specific stress response in mammalian cells*.

Zhao, S. and Ulrich, H.D. (2010) 'Distinct consequences of posttranslational modification by linear versus K63-linked polyubiquitin chains', *Proceedings of the National Academy of Sciences of the United States of America*, 107(17), pp. 7704-7709.

Zhou, Z.R., Zhang, Y.H., Liu, S., Song, A.X. and Hu, H.Y. (2012) 'Length of the active-site crossover loop defines the substrate specificity of ubiquitin C-terminal hydrolases for ubiquitin chains', *Biochemical Journal*, 441(1), pp. 143-149.

Ziviani, E., Tao, R.N. and Whitworth, A.J. (2010) 'Drosophila Parkin requires PINK1 for mitochondrial translocation and ubiquitinates Mitofusin', *Proceedings of the National Academy of Sciences of the United States of America*, 107(11), pp. 5018-5023.